Developing new biomarkers for cardiovascular disease

The prognostic potential of oxidative stress, and perivascular adipose tissue phenotyping

CHRISTOS P. KOTANIDIS

Green Templeton College
West Wing, John Radcliffe Hospital
Radcliffe Department of Medicine
University of Oxford



A thesis presented for the degree of
Doctor of Philosophy in Medical Sciences

Michaelmas Term 2021

I dedicate this to my mother,

who dedicated her life to God and her children.

Copyright © 2021 by Christos P. Kotanidis
All Rights Reserved

Dominus Illuminatio Mea

— Psalm 27

Acknowledgements

I would like to thank my supervisors Charalambos Antoniades and Keith Channon for their mentorship.

I would like to thank the Engineering and Physical Sciences Research Council, the Scatcherd Fund at the University of Oxford, and the Onassis Foundation for funding my studies.

I would like to express my gratitude towards current and past members of the Oxford Translational Cardiovascular Research Group, particularly Ileana Badi, Ioannis Akoumianakis, Evangelos Oikonomou, Muhammad Siddique, Laura Herdman, Sheena Thomas, and Nadia Akawi, cardiac surgeons Rana Sayeed, George Krasopoulos, Vivek Srivastava, and Shakil Farid, and everyone who has contributed to the development and maintenance of the Oxford Heart, Vessels, and Fat Cohort.

I would like to thank West Wing Level 5 Laboratory colleagues Besarta Vrellaku, My-Nhan Nguyen, Daan Paget, Faseeha Ayaz, Jasha Trompf, Naveed Akbar, Jilian Simon, Yiangos Psaras, Lucia Moreira, Neelam Mehta, and Cheryl Tan.

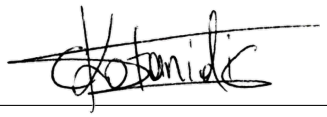
I would like to thank Val, Pavlina, Alina, Antonis, Andy, Nancy, Reuben, Maria, Nikos, Dimitris, Andreas, and Thanos for their friendship.

Finally and most importantly, I want to thank Sevi and Vaso, for helping me keep the faith even when I did not believe.

Declaration

I, Christos P. Kotanidis, declare that this thesis is entirely my own work unless otherwise indicated. It has not been submitted, either wholly or substantially, for another degree at this university, or for a degree at any other institution. I have acknowledged assistance from colleagues and collaborators where relevant.

The word count, exclusive of front matter, figures, tables, bibliography, and appendices, is 41487 . This document contains 72 figures, 15 tables, and 356 references.



23/06/2022

Signature *Date*

Abstract

Despite the fact that cardiovascular disease (CVD) mortality rates have seen major declines during recent years compared to past decades, reflecting advances made in primary and secondary prevention, CVD remains a significant mortality contributor, and the so-called residual cardiovascular risk persists. For the purposes of my thesis, I used the Oxford Fat, Vessels and Fat (Ox-HVF) cohort, which constitutes a uniquely phenotyped cohort, including >1,000 patients undergoing cardiac surgery, with long-term follow-up, to perform observational association studies, functional ex vivo bioassays on human tissue, and discovery transcriptomics combined with radiomics.

In the first part of my thesis, I focused on characterising the prognostic value of arterial and myocardial oxidative stress. I showed that increased production of free radical oxygen species in human arteries and myocardium is associated with a higher risk of future major adverse cardiac events (MACE). I further revealed S100A8 and S100A9 as the most dysregulated genes in the presence of oxidative stress in the vascular wall. Applying discovery network transcriptomics, I unveiled a transcriptomic signature that is redox related and predicts future risk of MACE. Pathways relevant to oxidative phosphorylation, glucose metabolism, and the mitochondrial respiratory chain assembly were enriched and therefore revealed as potential therapeutic targets.

In the second part of my thesis, I developed a method that allows the integration of transcriptomic and radiomic data to produce biologically relevant imaging signatures from radiomic features calculated from segmented three dimensional volumes. I applied this concept to radiomic features of perivascular adipose tissue around the internal mammary artery and thoracic aorta imaged in computed tomography angiography (CTA) to generate an imaging signature that captures vascular inflammation defined by upregulation of key inflammatory pathways in arterial transcription. This signature was validated in the context of vascular inflammation induced by the SARS-CoV-2 virus, and was proven to predict in hospital death, admission to the intensive care unit, response to dexamethasone, and systemic thrombosis.

Taken together, my findings propose oxidative stress, and specific redox-relevant genes and pathways as prognostic and therapeutic targets in CVD. Further, COVID-19 related vascular inflammation can be captured non-invasively by a novel radiotranscriptomic perivascular adipose tissue signature, which can maximise the diagnostic and prognostic yield of CTA.

Keywords— oxidative stress - vascular - myocardial - transcriptomics - perivascular adipose tissue - computed tomography angiography - radiomics - prognosis - biomarkers

Awards

1. **ESC Young Investigator Award in Coronary Pathophysiology and Microcirculation - Winner**
   European Society of Cardiology
   1st prize in the Young Investigator Award Competition in Coronary Pathophysiology and Microcirculation in the European Society of Cardiology (ESC) Congress 2021

2. **Paul Dudley White International Scholar Award**
   American Heart Association
   Highest ranked abstract submitted from the United Kingdom at the American Heart Association Scientific Sessions 2020

3. **BCS/BAS/BSCR Young Investigators Award Competition - Finalist**
   British Cardiovascular Society
   Finalist in the Young Investigators Award Competition at the British Cardiovascular Society Virtual Annual Conference 2021, Manchester

4. **BSCI Young Investigator Award - Finalist**
   British Society of Cardiovascular Imaging
   Finalist in the Young Investigator Award Competition at the British Society of Cardiovascular Imaging Annual Meeting 2021

5. **ICNC-CT 2021 Young Investigator Award - First Runner up**
   European Society of Cardiology
   2nd prize in the Young Investigators Award Competition at the ICNC-CT 2021 Virtual Conference

6. **Melvin Judkins Early Career Investigator Award in Cardiovascular Radiology - Finalist**
   Council on Cardiovascular Radiology and Intervention - American Heart Association
   Finalist in the CVRI Early Career Investigator Award Session of the American Heart Association Scientific Sessions 2020

7. **CVSA Young Investigator Abstract Travel Award**
   Council on Cardiovascular Surgery and Anesthesia, American Heart Association
   Selected to present in the Late Breaking Science Session of the American Heart Association Scientific Sessions 2019

Publications

Akawi, N., Checa, A., Antonopoulos, A. S., Akoumianakis, I., Daskalaki, E., **Kotanidis, C. P.**, Kondo, H., Lee, K., Yesilyurt, D., Badi, I., Polkinghorne, M., Akbar, N., Lundgren, J., Chuaiphichai, S., Choudhury, R., Neubauer, S., Channon, K. M., Torekov, S. S., Wheelock, C. E., & Antoniades, C. (2021). Fat-Secreted Ceramides Regulate Vascular Redox State and Influence Outcomes in Patients With Cardiovascular Disease. *J Am Coll Cardiol*, *77*(20), 2494-2513.

Akoumianakis, I., Sanna, F., Margaritis, M., Badi, I., Akawi, N., Herdman, L., Coutinho, P., Fagan, H., Antonopoulos, A. S., Oikonomou, E. K., Thomas, S., Chiu, A. P., Chuaiphichai, S., **Kotanidis, C. P.**, Christodoulides, C., Petrou, M., Krasopoulos, G., Sayeed, R., Lv, L., Hale, A., Naeimi Kararoudi, M., McNeill, E., Douglas, G., George, S., Tousoulis, D., Channon, K. M., & Antoniades, C. (2019). Adipose tissue-derived WNT5A regulates vascular redox signaling in obesity via USP17/RAC1-mediated activation of NADPH oxidases. *Sci Transl Med*, *11*(510).

Antoniades, C., **Kotanidis, C. P.**, & Berman, D. S. (2019). State-of-the-art review article. Atherosclerosis affecting fat: What can we learn by imaging perivascular adipose tissue? *J Cardiovasc Comput Tomogr*, *13*(5), 288-296.

Ayllon, B. T., Basu, J., Burrage, M., **Kotanidis, C. P.**, Ramirez, J., & Coyle, C. (2021). The British Cardiovascular Society Young Investigator Award 2021. *Heart*.

Kondo, H., Akoumianakis, I., Badi, I., Akawi, N., **Kotanidis, C. P.**, Polkinghorne, M., Stadiotti, I., Sommariva, E., Antonopoulos, A. S., Carena, M. C., Oikonomou, E. K., Reus, E. M., Sayeed, R., Krasopoulos, G., Srivastava, V., Farid, S., Chuaiphichai, S., Shirodaria, C., Channon, K. M., Casadei, B., & Antoniades, C. (2021). Effects of canagliflozin on human myocardial redox signalling: clinical implications. *Eur Heart J*.

Kotanidis, C. P., & Antoniades, C. (2019). Targeting interleukin-1: implications for long-term cardiovascular management following radiotherapy. *Eur Heart J*, *40*(30), 2504-2506.

Kotanidis, C. P., & Antoniades, C. (2020a). Perivascular Adipose Tissue and Atherosclerosis. In G. Iacobellis (Ed.), *Epicardial Adipose Tissue* (p. 91-115). Cham: Springer International Publishing.

Kotanidis, C. P., & Antoniades, C. (2020b). Selfies in cardiovascular medicine: welcome to a new era of medical diagnostics. *Eur Heart J*.

Kotanidis, C. P., & Antoniades, C. (2021). Perivascular Fat Imaging by Computed Tomography: A Virtual Guide. *Br J Pharmacol*.

Nikolaidou, C., **Kotanidis, C. P.**, Wijesurendra, R., Leal-Pelado, J., Kouskouras, K., Vassilikos, V. P., Karvounis, H., Ntusi, N., Antoniades, C., Neubauer, S., & Karamitsos, T. D. (2021). Cardiac Magnetic Resonance to Detect the Underlying Substrate in Patients with Frequent Idiopathic Ventricular Arrhythmias. *Diagnostics (Basel)*, *11*(6).

Oikonomou, E. K., Desai, M. Y., Marwan, M., **Kotanidis, C. P.**, Antonopoulos, A. S., Schottlander, D., Channon, K. M., Neubauer, S., Achenbach, S., & Antoniades, C. (2020). Perivascular Fat Attenuation Index Stratifies Cardiac Risk Associated With High-Risk Plaques in the CRISP-CT Study. *J Am Coll Cardiol*, *76*(6), 755-757.

Oikonomou, E. K., Marwan, M., Desai, M. Y., Mancio, J., Alashi, A., Hutt Centeno, E., Thomas, S., Herdman, L., **Kotanidis, C. P.**, Thomas, K. E., Griffin, B. P., Flamm, S. D., Antonopoulos, A. S., Shirodaria, C., Sabharwal, N., Deanfield, J., Neubauer, S., Hopewell, J. C., Channon, K. M., Achenbach, S., & Antoniades, C. (2018). Non-invasive detection of coronary inflammation using computed tomography and prediction of residual cardiovascular risk (the CRISP CT study): a post-hoc analysis of prospective outcome data. *Lancet*, *392*(10151), 929-939.

Oikonomou, E. K., Williams, M. C., **Kotanidis, C. P.**, Desai, M. Y., Marwan, M., Antonopoulos, A. S., Thomas, K. E., Thomas, S., Akoumianakis, I., Fan, L. M., Kesavan, S., Herdman, L., Alashi, A., Centeno, E. H., Lyasheva, M., Griffin, B. P., Flamm, S. D., Shirodaria, C., Sabharwal, N., Kelion, A., Dweck, M. R., Van Beek, E. J. R., Deanfield, J., Hopewell, J. C., Neubauer, S., Channon, K. M., Achenbach, S., Newby, D. E., & Antoniades, C. (2019). A novel machine learning-derived radiotranscriptomic signature of perivascular fat improves cardiac risk prediction using coronary CT angiography. *Eur Heart J*, *40*(43), 3529-3543.

Conference Presentation Extracts

Akawi, N., Checa, A., Akoumianakis, I., Margaritis, M., **Kotanidis, C. P.**, Daskalakis, E., Kondo, H., Channon, K. M., Wheelock, C., & Antoniades, C. (2019). Adipose Tissue Ceramides Reduces Endothelium-Dependent Vasorelaxation, Amplifies Vascular Oxidative Stress Induces Systemic Inflammation Ultimately Leading To Death In Coronary Artery Disease. *Circulation*, *140*(Suppl$_1$), $A12286 - A12286$.

Akawi, N., Checa, A., **Kotanidis, C. P.**, Akoumianakis, I., Daskalakis, E., Herdamn, L., Wheelock, C., & Antoniades, C. (2019). 5893 Adipose tissue secreted ceramides and related sphingolipids-potential modulators of vascular redox signalling in cardiovascular disease. *European Heart Journal*, *40*(Supplement$_1$), $ehz746.0085$.

Akawi, N., Checa, A., **Kotanidis, C. P.**, Akoumianakis, I., Daskalakis, E., Wheelock, C., & Antoniades, C. (2019). BS32 Untargeted metabolomics interrogation of adipose tissue secretome from participants of the oxford cohort for heart, vessels fat highlighted ceramides as potential adipokines modulating vascular redox signalling in cardiovascular disease. *Heart*.

Antonopoulos, A., Herdman, L., Thomas, S., Akoumianakis, I., **Kotanidis, C. P.**, Thomas, K., Oikonomou, E., Psarros, K., Sayeed, R., & Antoniades, C. (2018). 104 Metabolically healthy obesity is associated with a distinct epicardial fat phenotype and low myocardial oxidative stress. *European Heart Journal*, *39*(suppl$_1$), $ehy564.104$.

Kondo, H., Akoumianakis, I., Akawi, N., Cristina, M., Herdman, L., Badi, I., **Kotanidis, C. P.**, Akbar, N., Antonopoulos, A., & Oikonomou, E. (2019). P6267 Novel direct effects of SGLT2 inhibitor, Canagliflozin, on myocardial redox state in humans. *European Heart Journal*, *40*(Supplement$_1$), $ehz746.0866$.

Kondo, H., Akoumianakis, I., Akawi, N., **Kotanidis, C. P.**, Antonopoulos, A., Carena, M., Badi, I., Oikonomou, E., Reus, E., & Krasopoulos, G. (2020). Direct effects of canagliflozin on human myocardial redox signalling: a novel role for SGLT1 inhibition. *European Heart Journal*, *41*(Supplement$_2$), $ehaa946.3351$.

Kotanidis, C. P., Akawi, N., Thomas, S., Siddique, M., Oikonomou, E., Alashi, A., Akoumianakis, I., Antonopoulos, A., Krasopoulos, G., & Sayeed, R. (2020). A novel arterial redox-specific machine learning-derived radiomic signature of perivascular adipose tissue predicts cardiac mortality from routine CCTA. *European Heart Journal*, *41*(Supplement$_2$), $ehaa946.1372$.

Kotanidis, C. P., Antonopoulos, A., Psarros, C., Akoumianakis, I., Herdman, L., Oikonomou, E., Badi, I., Krasopoulos, G., Sayeed, R., & Petrou, M.

(2019). P6282 Myocardial redox state predicts 3-year mortality in patients undergoing cardiac surgery: the ox-HVF study. *European Heart Journal*, *40*(Supplement$_1$), $ehz746.0880$.

Kotanidis, C. P., Antonopoulos, A. S., Oikonomou, E. K., Akoumianakis, I., Badi, I., Krasopoulos, G., Sayeed, R., Petrou, M., Srivastava, V., & Farid, S. (2019). Oxidative Stress in the Myocardium as a Novel Predictor of Long-Term Outcomes in Patients Undergoing Cardiac Surgery. *Circulation*, *140*(Suppl$_1$), $A14695 - A14695$.

Kotanidis, C. P., Oikonomou, E., Williams, M., Thomas, S., Thomas, K., Lyasheva, M., Antonopoulos, A., Dweck, M., Shirodaria, C., & Neubauer, S. (2020). Pericoronary fat radiomic profile (FRP) predicts long-term cardiac risk in individuals with calcium score below 100 on coronary computed tomography angiography. *European Heart Journal*, *41*(Supplement$_2$), $ehaa946.0181$.

Kotanidis, C. P., Oikonomou, E. K., Marwan, M., Kluener, L., Thomas, K. E., Alashi, A., Antonopoulos, A. S., Shirodaria, C., Neubauer, S., & Channon, K. M. (2020). OP3 Improved cardiac risk stratification in individuals with high risk plaque features using the perivascular fat attenuation index on CCTA. *Heart*.

Kotanidis, C. P., Oikonomou, E. K., Marwan, M., Thomas, K. E., Alashi, A., Antonopoulos, A. S., Shirodaria, C., Neubauer, S., Channon, K. M., & Achenbach, S. (2020). OP4 Perivascular fat attenuation index mapping around the right and left coronary artery independently predict cardiac mortality. *Heart*.

Kotanidis, C. P., Xie, C., Adlam, D., Rodrigues, J. C., Siddique, M., Lockstone, H., Thomas, S., Kotronias, R., Oikonomou, E. K., & Lumley, S. F. (2021). D Radiotranscriptomic analysis of perivascular adipose tissue quantifies vascular inflammation in covid-19 from routine CT angiograms: Stratification of "new UK variant" Infection and prediction of in-hospital outcomes. *Heart*.

Kotanidis, C. P., Xie, C., Kotronias, R., Siddique, M., Thomas, S., Schottlander, D., Channon, K., Neubauer, S., Deanfield, J., & Antoniades, C. (2020). Abstract 16467: A Novel CT-derived Radiotranscriptomic Signature of Perivascular Adipose Tissue Stratifies COVID-19 Vascular Cytokine Burst and Predicts in Hospital Outcomes. *Circulation*, *142*(Suppl$_3$), $A16467 - A16467$.

Nikolaidou, C., **Kotanidis, C. P.**, Leal-Pelado, J., Kouskouras, K., Vassilikos, V., Karvounis, H., & Karamitsos, T. (2021). Incremental value of feature-tracking cardiac magnetic resonance imaging in detecting myocardial dysfunction in patients with idiopathic ventricular arrhythmias. *European Heart Journal-Cardiovascular Imaging*, *22*(Supplement$_1$), $jeaa356.275$.

Oikonomou, E., Schottlander, D., Antonopoulos, A., Marwan, M., **Kotanidis, C. P.**,

Kluner, L., Shirodaria, C., Channon, K., Neubauer, S., & Desai, M. (2021). Standardised quantification of coronary inflammation using cardiac computed tomography: The Fat Attenuation Index Score (FAI-Score). *European Journal of Preventive Cardiology*, *28*(Supplement$_1$), $zwab061.451$.

Oikonomou, E. K., Marwan, M., Mancio, J., **Kotanidis, C. P.**, Thomas, K. E., Alashi, A., Hutt Centeno, E., Antonopoulos, A. S., Shirodaria, C., Neubauer, S., Channon, K. M., Achenbach, S., Desai, M. Y., & Antoniades, C. (2019). 3258Perivascular fat attenuation index stratifies the cardiac risk associated with high-risk plaque features on coronary computed tomography angiography. *European Heart Journal*, *40*(Supplement$_1$).

Table of Contents

Acknowledgements v

Declaration vi

Abstract vii

Awards viii

Publications ix

Conference Presentation Extracts xi

List of Figures xxiii

List of Tables xxiv

List of Abbreviations xxv

1 Introduction 1

1.1 The Need for New Diagnostic Tools in Cardiovascular Disease 1

1.2 Oxidative stress and cardiovascular disease 2

1.2.1 Defining oxidative stress 2

1.2.2 Reactive oxygen species 3

1.2.3 Oxidases in Cardiovascular pathophysiology 5

1.2.3.1 NADPH Oxidases 5

1.2.3.1.1 Structure 6

1.2.3.1.2 Activation 7

1.2.3.1.3 NOX2 or CYBB 8

1.2.3.1.4 NOX1 9

1.2.3.1.5 NOX4 9

1.2.3.1.6 NOX5 10

1.2.3.1.7 DUOX1-2 11
1.2.3.2 Uncoupled eNOS 11
1.2.3.3 Dysfunctional mitochondria 14
1.2.3.4 Xanthine oxidase 16
1.2.4 Oxidase crosstalk in CVD 16
1.2.4.1 NOXs and uncoupled eNOS 17
1.2.4.2 NOXs and mitochondria 18
1.2.4.3 Uncoupled eNOS, xanthine oxidase and mitochondria 19
1.2.5 Contributions of oxidase crosstalk to particular CVDs 20
1.2.5.1 Atherosclerosis 21
1.2.5.2 Heart failure 22
1.2.6 Antioxidant therapeutic strategies 24
1.2.6.1 Vitamins 25
1.2.6.2 Superoxide dismutase - catalase mimics 26
1.2.6.3 NOX inhibitors 27
1.2.6.4 Glutathione peroxidase mimics 29
1.2.6.5 Increasing GSH 30
1.2.6.5.1 N-acetylcysteine 30
1.2.6.5.2 GSH esters 30
1.2.6.6 Inhibiting mitochondrial ROS 31
1.3 Perivascular adipose tissue and cardiovascular disease 32
1.3.1 Atherogenesis and inflammation 32
1.3.2 Defining adiposity in the human body 36
1.3.2.1 Subcutaneous and visceral adipose tissue definition 36
1.3.2.2 Epicardial adipose tissue definition 36
1.3.2.3 Defining perivascular adipose tissue 37
1.3.3 PVAT effects on the vascular wall - Outside to inside signaling 39
1.3.4 Inside-to-outside signals: Vasculature affecting fat 44
1.3.4.1 Systemic Signals 44
1.3.4.2 Regional Signals 49
1.3.5 Imaging perivascular adipose tissue 53

1.3.5.1 Quantitative imaging features . . . 54
1.3.5.2 Qualitative imaging features . . . 54
1.3.5.3 Dual energy X-ray absorptiometry . . . 56
1.3.5.4 Ultrasonography . . . 57
1.3.5.5 Magnetic Resonance Imaging . . . 57
1.3.5.6 Computed Tomography Imaging . . . 57
1.4 Radiomic phenotyping . . . 58
1.4.1 What is radiomics? . . . 58
1.4.2 Radiomics in cardiovascular imaging . . . 59
1.5 Aims and Hypotheses . . . 65

2 Methods **66**
2.1 The Oxford Heart, Vessels,and Fat Cohort . . . 66
2.1.1 Overview . . . 66
2.1.2 Demographic characteristics, risk factor recording, and in-hospital follow-up . . . 69
2.1.3 Sample collection . . . 71
2.1.3.1 Blood sampling . . . 71
2.1.3.2 Tissue collection processing . . . 71
2.2 Long-Term clinical outcome collection . . . 73
2.2.1 Studies involved . . . 74
2.2.2 Processing activities prior to data retrieval . . . 75
2.2.3 Processing activities post data retrieval . . . 78
2.3 Measurement of superoxide production . . . 81
2.3.1 Quantification of baseline superoxide readout . . . 82
2.3.2 Quantification of NADPH-stimulated superoxide readout . . . 83
2.3.3 Quantification of Vas2870-inhibitable superoxide readout . . . 83
2.4 Gene expression studies . . . 85
2.4.1 RNA isolation purification . . . 85
2.4.2 Reverse transcription of RNA - cDNA library creation . . . 86
2.4.3 Gene expression studies using quantitative PCR . . . 86

2.4.4 RNA sequencing . . . 87
2.5 Computed Tomography Angiography Acquisition Protocols . . . 88
2.5.1 Coronary Computed Tomography Angiography (CCTA) Acquisition Protocol . . . 88
2.5.2 Pulmonary Computed Tomography Angiography Acquisition Protocols 89
2.6 Radiomic Characterization . . . 90
2.6.1 Adipose Tissue Segmentation . . . 90
2.6.2 Radiomic Characterization Details . . . 91
2.6.3 Radiomic feature filtering and selection . . . 92
2.7 Statistical analysis . . . 93
2.7.1 Cross-sectional analysis . . . 93
2.7.2 Transcriptomic Data Generation and Processing . . . 93
2.7.3 WGCNA analysis . . . 94
2.7.4 Survival analysis and prognostic models . . . 94
2.7.5 Machine learning models . . . 95

3 Oxidative Stress: Prognostic Potential 96
3.1 Introduction . . . 96
3.2 Methods . . . 98
3.2.1 Study Participants . . . 98
3.2.2 In vivo clinical studies . . . 98
3.2.3 Long-term clinical endpoints data collection . . . 98
3.2.4 Tissue Collection, RNA Isolation and Sequencing Data Analysis . . . 99
3.2.5 Transcriptomic Data Generation and Processing . . . 100
3.2.6 WGCNA analysis . . . 100
3.2.7 Enrichment analyses . . . 101
3.2.8 Whole Genome Genotyping, Quality Checks and Imputation . . . 101
3.2.9 Association Analyses . . . 102
3.2.10 Statistical analysis . . . 102
3.3 Results . . . 103
3.3.1 Vascular NADPH oxidase activity is linked with mortality and MACE . 103

3.3.2 Exploring transcriptional changes in increased vascular oxidative stress 112
3.3.3 Constructing vascular wall transcriptomic signatures 117
3.3.4 A vascular wall transcriptomic signature predicts long-term cardiovascular risk 128
3.3.5 Combining transcriptomic and genomic data reveals OGDH, SRL, and USP13 genes as top genetic candidates of vascular oxidative stress . . . 136
3.3.6 Myocardial oxidative stress and long-term outcomes 138
3.4 Discussion 145
3.4.1 Oxidative stress in atherosclerosis 146
3.4.2 The "antioxidant paradox" 147
3.4.3 Vascular oxidative stress as a predictor of long-term clinical outcomes . 148
3.4.4 Revealing S100A8 and S100A9 as gene targets dysregulated by oxidative stress 150
3.4.5 A transcriptomic signature related with oxidative stress and clinical outcomes 151
3.4.6 Combining transcriptomic with genomic data to reveal redox state-related gene targets 153
3.4.7 Myocardial oxidative stress as a predictor of long-term clinical outcomes 154
3.4.8 Conclusion 154

4 Perivascular Adipose Tissue: Radiotranscriptomic Prognostic Signatures 156
4.1 Introduction 156
4.2 Methods 158
4.2.1 Study Participants 158
4.2.2 Tissue Collection, RNA Isolation and Sequencing Data Analysis 160
4.2.3 Defining Inflammatory-related Genes 162
4.2.4 Clustering and Differential Expression Analysis 163
4.2.5 Coronary and Pulmonary Computed Tomography Angiography Acquisition Protocols 166
4.2.6 Adipose Tissue Segmentation and Radiomic Characterization 168
4.2.7 Radiomic Characterization Details 169

4.2.8 Radiomic feature filtering and selection . . . 169
4.2.9 Viral Genome Sequencing . . . 170
4.2.10 Statistical analysis . . . 171
4.3 Results . . . 173
4.3.1 Designing a platform for developing radiotranscriptomic imaging biomarkers . . . 173
4.3.2 Clustering of inflammatory genes expression within human internal mammary arteries to stratify vascular inflammation . . . 173
4.3.3 Training of C19-RS . . . 176
4.3.4 Exploring the ability of C19-RS to track COVID-19-induced vascular inflammation . . . 178
4.3.5 C19-RS is higher in patients infected with the B.1.1.7 SARS-CoV-2 variant . . . 181
4.3.6 Exploring the prognostic value of C19-RS in COVID-19 . . . 188
4.3.7 C19-RS shows strong correlation with coagulation gene module . . . 194
4.4 Discussion . . . 196
4.4.1 Presenting a custom-made radiotranscriptomic signature . . . 196
4.4.2 C19-RS to guide selection of dexamethasone . . . 198
4.4.3 Identifying the degree of vascular inflammation in COVID-19 . . . 199
4.4.4 Limitations . . . 201
4.4.5 Translational Perspective . . . 202
4.4.6 Conclusions . . . 203

5 Summary, Limitations, and Future Directions 204
5.1 Summary of findings . . . 204
5.1.1 Oxidative stress in cardiovascular disease . . . 204
5.1.2 Perivascular adipose tissue derived radiotranscriptomic signatures: an application in COVID-19 . . . 206
5.2 Limitations . . . 209
5.3 Future directions . . . 211
5.3.1 Time to revisit antioxidant strategies in atherosclerosis . . . 211

5.3.2 Is radiotranscriptomics the future of cardiac imaging? 212
5.3.3 Ox-HVF: What does the future hold? 214

Bibliography **216**

Appendix A Variables in outcomes dataset **270**

Appendix B Radiomic features **273**

Appendix C List of DE genes in Chapter 3 **311**

List of Figures

1.1 ROS interactions . . . 6
1.2 NOX structure-schematic . . . 10
1.3 eNOS structure-schematic . . . 12
1.4 Antioxidant therapeutic strategies . . . 25
1.5 Inflammation is a valid therapeutic target to reduce cardiovascular events . . . 34
1.6 Defining distinct adipose tissue depots . . . 38
1.7 Adipose tissue depots as imaged . . . 39
1.8 Main roles of key adipocytokines secreted by perivascular adipose tissue . . . 40
1.9 Effect of WNT5A on the vasculature . . . 43
1.10 Bi-directional interplay between the vascular wall and PVAT . . . 49
1.11 Adiponectin upregulation caused by vascular oxidative stress . . . 51
1.12 Schematic of PVAT's response to vascular inflammation . . . 53
1.13 What is radiomics? . . . 59
1.14 Radiomic phenotyping to detect biological hallmarks of dysfunctional adipose tissue . . . 63
1.15 Schematic representation of the biology underlying FAI and FRP . . . 64

2.1 The Oxford Heart, Vessels, and Fat (Ox-HVF) cohort . . . 67
2.2 The ORFAN study . . . 69
2.3 AdipoRedOx study: Human samples collection process . . . 73
2.4 The NHS Digital outcomes script GUI . . . 78
2.5 Representative superoxide $O_2^{\bullet -}$ traces . . . 84
2.6 NADPH-stimulated and Vas2870-inhibitable superoxide ($O_2^{\bullet -}$) correlation . . . 85

3.1 Chapter 3 Studies Workflow . . . 99
3.2 Study Arm 1 alluvial plot based on outcome . . . 103
3.3 IMA NADPH oxidase activity as a continuous variable and long-term outcomes: Univariate models . . . 105

3.4 Computing cut-off points for vascular oxidative stress indices . . . 107
3.5 IMA NADPH oxidase activity as a continuous variable and long-term outcomes: Multivariable models . . . 108
3.6 IMA resting oxidative stress Kaplan-Meier plots . . . 109
3.7 IMA NAPDH stimulated oxidative stress Kaplan-Meier plots . . . 110
3.8 IMA Vas2870 inhibitable oxidative stress Kaplan-Meier plots . . . 111
3.9 NADPH oxidase activity tertiles in the Study Arm 2 population . . . 113
3.10 Volcano plot of differential gene expression for all genes sequenced . . . 114
3.11 Volcano plot of differential gene expression for genes in the GO:Inflammatory Response . . . 114
3.12 Validation qPCR for the S100A8 gene . . . 116
3.13 Exploratory experiments in IMA and aortic biopsies . . . 117
3.14 Quality check dendrogram . . . 118
3.15 WGCNA modules . . . 120
3.16 Correlation of gene modules with traditional risk factors . . . 121
3.17 Study Arm 2 alluvial plot based on risk factors and long-term outcomes . . . 129
3.18 Pathway enrichment analysis for the red signature . . . 131
3.19 Prognostic value of the red transcriptomic signature . . . 132
3.20 Intersection plot for pathways in the red signature . . . 133
3.21 Gene Ontology analysis of the red signature: Biological Process . . . 134
3.22 Gene Ontology analysis of the red signature: Molecular Function . . . 135
3.23 Genes in the red signature identified in GWAS in association with IMA NADPH oxidase activity . . . 137
3.24 High OGDH expression in internal mammary arteries is associated with cardiac risk . . . 138
3.25 Study Arm 3 alluvial plot based on outcome . . . 139
3.26 Computing cut-off points for myocardial oxidative stress indices . . . 141
3.27 RAA oxidative stress as a continuous variable and long-term outcomes . . . 142
3.28 RAA NADPH stimulated oxidative stress Kaplan-Meier plots . . . 143
3.29 RAA Vas2870 inhibitable oxidative stress Kaplan-Meier plots . . . 144
3.30 Myocardial oxidative stress and ICU admission . . . 146

3.31 Utilising myocardial oxidative stress as a cardiac risk stratification tool in cardiac surgery . . . 155

4.1 Chapter 4 Workflow Diagram . . . 161
4.2 Building C19-RS: A radiotranscriptomics analysis . . . 164
4.3 Reproducibility analysis of perivascular adipose tissue features . . . 170
4.4 Recursive feature elimination . . . 171
4.5 Unsupervised hierarchical clustering of cytokine production genes . . . 174
4.6 Validation pathway enrichment analysis . . . 176
4.7 C19-RS . . . 177
4.8 C19-RS for COVID-19 detection . . . 180
4.9 C19-RS is higher in COVID-19 . . . 183
4.10 Optimal C19-RS cut-off for COVID-19 detection . . . 183
4.11 Incremental value of C19-RS radiomic features in COVID-19 detection . . . 184
4.12 C19-RS is higher in patients with the B.1.1.7 variant . . . 185
4.13 Image analysis and in-hospital outcomes collection diagram for Study Arms 3 4 186
4.14 Prognostic value of C19-RS. . . . 187
4.15 Identifying the optimal C19-RS cut-off for in-hospital death prediction . . . 189
4.16 Kaplan-Meier plots of C19-RS for in-hospital death . . . 190
4.17 Kaplan-Meier plots of C19-RS for in-hospital death stratified based on dexamethasone treatment . . . 191
4.18 Kaplan-Meier plots of C19-RS for in-hospital death in the external validation cohort . . . 192
4.19 Whole blood gene expression profiles and C19-RS . . . 195
4.20 The proposed imaging biomarker C19-RS . . . 197

List of Tables

1.1 Summary of the effects of inside to outside signals on adipose tissue 45
1.2 Comparison of noninvasive adipose tissue imaging modalities 60

2.1 ICD10 codes included in the cardiovascular mortality endpoint 79
2.2 ICD10 codes included in the cardiac mortality endpoint 80
2.3 List of TaqMan probes used in this thesis 87
2.4 Conversion factors for different CT energies 91

3.1 Study Arm 1 Population Characteristics 104
3.2 Study Arm 2 Population Characteristics 119
3.3 Genes in the 'red' signature 121
3.4 Study Arm 3 Population Characteristics 139

4.1 List of genes chosen for unsupervised clustering in Study Arm 1 162
4.2 Demographic characteristics of the Study Arm 1 population 175
4.3 Demographic characteristics of the Study Arm 2 population 179
4.4 Demographic characteristics of the Study Arm 3 population 182
4.5 Demographic characteristics of the Study Arm 4 population 193

List of Abbreviations

AT . . . . . Adipose Tissue

AAA . . . . . Abdominal aortic aneurysm

ACEi . . . . . Angiotensin-converting-enzyme inhibitor

BH4 . . . . . Tetrahydrobiopterin

CAD . . . . . Coronary artery disease

CCTA . . . . . Coronary computed tomography angiography

CTA . . . . . Computed tomography angiography

CVD . . . . . Cardiovascular disease

EAT . . . . . Epicardial adipose tissue

eNOS . . . . . Endothelial nitric oxide synthase

FAI . . . . . Fat attenuation index

FRP . . . . . Fat radiomic profile

GPX . . . . . Glutathione peroxidase

GSH . . . . . Glutathione

H4B . . . . . Tetrahydrobiopterin

IFNγ . . . . . Interferon gamma

IL-6 . . . . . Interleukin 6

IRI . . . . . Ischemia/reperfusion injury

MACE . . . . . Major adverse cardiovascular event

MI . . . . . Myocardial infarction

mitoKATP . . . . . Mitochondrial ATP-sensitive K^+ channel

NAC . . . . . N-acetylcysteine

NADPH . . . . . Nicotinamide adenine dinucleotide phosphate

NO . . . . . Nitric oxide

NOX . . . . . NADPH-oxidase

PET . . . . . Positron emission tomography

PKC . . . . . Protein kinase C

PVAT . . . . . Perivascular adipose tissue

ROS . . . . . Radical oxygen species

SAT . . . . . Subcutaneous adipose tissue

SOD . . . . . Superoxide dismutase

SPECT . . . . . Single-photon emission computed tomography

TAC . . . . . Transverse aortic constriction

TNFα . . . . . Tumor necrosis factor alpha

VAT . . . . . Visceral adipose tissue

1 | Introduction

1.1 The Need for New Diagnostic Tools in Cardiovascular Disease

Coronary artery disease (CAD) continues to be a leading cause of death in the western world, as demonstrated by the World Health Organization's (WHO) most recent report ("WHO | Disease burden and mortality estimates", 2018). Being responsible for 1 in 7 deaths in the United States of America, killing over 366,800 people a year, it is a major contributor to the ever-increasing medical costs associated with its management, which are projected to amount to 1.1 trillion by 2035 (Dunbar et al., 2018). Despite the fact that mortality rates have seen major declines during recent years compared to past decades, reflecting advances made in primary and secondary prevention (Kalbacher, Waldeyer, Blankenberg, & Westermann, 2018), the disease remains a significant mortality contributor, and the so-called residual cardiovascular risk persists (Ferrari & Catapano, 2016). Indeed, residual cardiovascular risk has been proposed as a promising target in many large clinical trials utilizing novel, effective but at the same time costly therapies, such as anti-PCSK9 monoclonal antibodies (Schmidt et al., 2017) or antibodies targeting chemokines (Ridker et al., 2017). These therapeutic agents have proven to be rather robust and promising, successfully reducing the global inflammatory burden in patients at high cardiovascular risk; however, their high cost hinders the clinical adaptation by healthcare systems, highlighting the imperative need for early and accurate detection of the target populations (Sehested et al., 2019).

As we move further into the era of personalized medicine, the development and deployment of new "companion diagnostics", will enable the detection of the true "vulnerable patient", meaning the patient that is indeed at the greatest risk and will therefore benefit the most out of these new and expensive therapeutics. These applications will revolutionize the prevention of development of clinical cardiovascular disease, including ischemic heart disease, and at the same time prevent the use of unnecessary invasive therapy in patients with severe but stable CAD, who may mistakenly be considered "vulnerable" under current traditional diagnostics.

1.2 Oxidative stress and cardiovascular disease

1.2.1 Defining oxidative stress

Oxidative stress is a term introduced by Helmut Sies in 1985, as an "imbalance between oxidants and antioxidants in favor of oxidants, leading to a disruption of redox signaling and control and/or molecular damage" (Sies, 2015). As of 2021 more than 264,000 PubMed entries can be found in literature for this term. Oxidative stress has been implicated in a wide range of pathologies including atherosclerosis, chronic obstructive pulmonary disease (COPD), Alzheimer disease and cancer (Valko et al., 2007). Multiple and variable mechanisms by which oxidants and their imbalance against antioxidants contribute to cellular damage have been revealed (Valko et al., 2007). Nevertheless, it should be stressed that oxidative stress participates in diseases pathology to a variable extent, such that the effectiveness of antioxidants may be limited in some diseases (Forman & Zhang, 2021).

1.2.2 Reactive oxygen species

Oxidative stress encompasses the chemistry of reactions of reactive species derived from oxygen and nitrogen (ROS and RNS). The term reactive oxygen species (ROS) classically refers to any partially reduced molecule or ion containing one or more unpaired electrons, thus having strong oxidising properties (Mittal, Siddiqui, Tran, Reddy, & Malik, 2014), and includes molecules derived from O_2, such as superoxide ($O_2^{\bullet -}$), hydrogen peroxide (H_2O_2), hydroxyl radical ($^{\bullet}OH$), ozone and singlet oxygen.

Superoxide or $O_2^{\bullet -}$ primarily produced by one-electron reduction of O_2, comes mostly through leakage of electrons from the mitochondrial respiratory chain, particularly from ubisemiquinone ($QH^{\bullet -}$) (Boveris, Cadenas, & Stoppani, 1976):

$$QH^{\bullet -} + O_2 \leftrightarrow Q + O_2^{\bullet -}$$

Superoxide is also produced in excess by NADPH oxidases through the following reaction (Lambeth, 2004):

$$NADPH + 2O_2 \rightarrow NADP^+ + 2O_2^{\bullet -}$$

H_2O_2 is produced by dismutation of $O_2^{\bullet -}$, through a fast reaction that is accelerated by superoxide dismutases:

$$2O_2^{\bullet -} + 2H^+ \rightarrow H_2O_2 + O_2$$

H_2O_2 is reduced enzymatically by catalase and 14 other enzymes (Forman & Zhang, 2021), through the following reaction:

$$2H_2O_2 \rightarrow 2H_2O + O_2$$

H_2O_2 reacts rapidly with transition metals, such as iron to produce hydroxyl radical (Koppenol, 1993):

$$H_2O_2 + Fe^{2+} \rightarrow OH^- + Fe^{3+} + {}^{\bullet}OH$$

The hydroxyl radical ($^{\bullet}OH$) is a very strong oxidant that can oxidize any molecule in its surroundings. The hydroxyl radical ($^{\bullet}OH$) can also initiate the lipid peroxidation chain reaction:

$$LH + {}^{\bullet}OH \rightarrow L^{\bullet} + H_2O$$

$$L^{\bullet} + O_2 \rightarrow LOO^{\bullet}$$

$$LOO^{\bullet} + LH \rightarrow LOOH + L^{\bullet}$$

where LH is a lipid with allylic hydrogens, which are present in polyunsaturated fatty acids including arachidonic acid. The relatively weak oxidant $O_2^{\bullet -}$ contributes to oxidative stress as a precursor of H_2O_2 and peroxynitrite ($ONOO^-$), which is formed in the following reaction:

$$O_2^{\bullet -} + {}^{\bullet}NO \rightarrow ONOO^-$$

The protonated form of peroxynitrite, peroxynitrous acid (ONOOH), is a non-radical and constitutes a very strong oxidant. Both $^{\bullet}NO_2$ and $^{\bullet}OH$ are very rapid in their reactions and do not really discriminate in what they will oxidize. Finally, the hypohalous acids (HOX) are also oxidants, and are formed from H_2O_2 by phagocytic cell myeloperoxidases:

$$H_2O_2 + X^- + H^+ \rightarrow HOX + H_2O$$

where X^- may be Cl^-, Br^- or even SCN^-. They play a major role in tissue damage associated with phagocyte-mediated inflammation (Pattison, Davies, & Hawkins, 2012).

In the plasma membrane superoxide is formed by the transfer of electrons to molec-

ular oxygen through an enzymatic reaction catalyzed by the membrane-bound NOX family of NADPH oxidases. The cytosolic enzyme xanthine oxidase is another well-studied ROS-producing enzyme that catalyzes xanthine and hypoxanthine oxidation to uric acid and transfers monovalent electron to molecular oxygen to produce superoxide. The mitochondria are also a further source of intracellular superoxide. Complex I and complex III in the mitochondrial respiratory electron transport chain are sites involved in $O_2^{\bullet -}$ generation due to electron leakage to molecular oxygen. Once superoxide is generated, it becomes a precursor for the formation of other ROS in the cell. SOD converts superoxide to H_2O_2, which can generate the highly reactive $^{\bullet}OH$ by interacting with transition metal ions (such as Fe and Cu), and the reactive hypochlorous acid, catalyzed by myeloperoxidase (Kaushal, Chandrashekar, & Juncos, 2019). In addition to ROS, cells also generate RNS. The major RNS include nitric oxide radicals, peroxynitrite, and nitrogen dioxide. The $^{\bullet}NO$ radical is produced by three isoforms of nitric oxide synthase (NOS). Increasing $^{\bullet}NO$ levels can further react with $O_2^{\bullet -}$ to produce $ONOO^-$, which can cause protein nitration (Kaushal et al., 2019). All these interactions are seen in Figure 1.1.

1.2.3 Oxidases in Cardiovascular pathophysiology

1.2.3.1 NADPH Oxidases

NADPH-oxidases, also called NOX enzymes, mainly produce superoxide ($O_2^{\bullet -}$), and are amongst the major sources of ROS in the vascular wall (Konior, Schramm, Czesnikiewicz-Guzik, & Guzik, 2014). NADPH-oxidases have seven isoforms: NOX1-5 and dual oxidase proteins 1-2 (DUOX1-2) (Panday, Sahoo, Osorio, & Batra, 2015). Interestingly, NOX3 is expressed predominantly in the inner ear and is involved in the biogenesis of otoconia/otolith, therefore it will not be discussed further (Banfi, Malgrange, et al., 2004). In endothelial cells NOX2 and NOX4 are

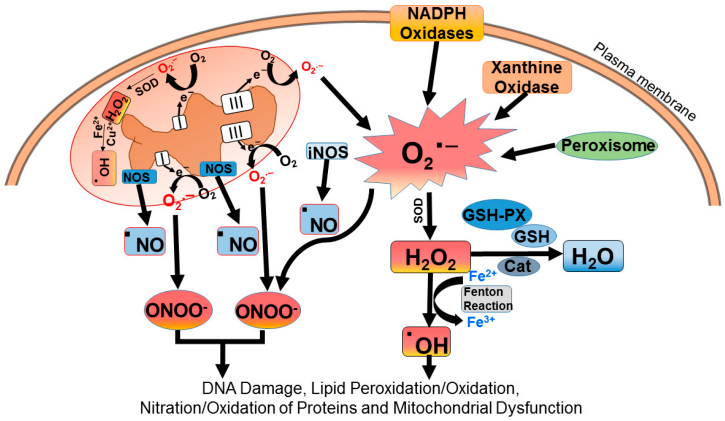


Figure 1.1: ROS interactions. ROS are generated by enzymatic and non-enzymatic redox reactions during cellular metabolism under normal and pathological conditions. Mitochondria, plasma membrane, peroxisomes, and cytosol first generate the superoxide anion ($O_2^{\bullet -}$), which becomes the precursor free radical for the generation of other ROS molecules. Superoxide dismutase dismutates $O_2^{\bullet -}$ to H_2O_2, which yields highly reactive hydroxyl radicals ($^{\bullet}OH$) by interaction with reduced transition metal ions (such as Fe and Cu). In addition to ROS, cells also generate reactive nitrogen species (RNS). The major RNS include nitric oxide ($^{\bullet}NO$), and peroxynitrite ($ONOO^-$). Nitric oxide ($^{\bullet}NO$) is produced by three isoforms of nitric oxide synthase (NOS), all of which are expressed in the kidney. ROS produced cause oxidative damage, including DNA damage, lipid and protein oxidation, protein nitration, and mitochondrial dysfunction. Adapted from (Kaushal et al., 2019).

the major NADPH-oxidase isoforms, while vascular smooth muscle cells mainly express NOX4 and NOX1 (Guzik et al., 2004). Interestingly, NOX1 and NOX2 (also known as CYBB) genes are found on chromosome X, while the rest of the NOX genes are located on autosomes.

1.2.3.1.1 Structure Structurally, NADPH-oxidases have multiple subunits and are transmembrane enzymes (Bedard & Krause, 2007a). NOX1-NOX5 are six-transmembrane proteins, whereas DUOX1 and DUOX2 are seven-transmembrane proteins, with the C-terminus exposed to the cytosol (Y. Zhang, Murugesan, Huang, & Cai, 2020). NADPH-oxidases sequentially transfer electrons from NADPH to FAD, haem groups and finally to molecular oxygen, leading to superoxide production (Gimenez, Schickling, Lopes, & Miller, 2016). Understanding the crystal structures of NOXs has been sought throughout the past decade. In 2009, the crystal

structure of the N-terminal regulatory domain of a plant NOX in rice (a homologue of mammalian NOX2) was reported (Oda et al., 2010). This showed a cytosolic N-terminal region with two Ca^{2+} binding EF hands. These motifs are shared with the human NOX5, DUOX1 and DUOX2 isoforms, but are absent in mammalian NOX2. Next, in 2017, researchers studied NOX5 from Cylindrospermum stagnale to reveal the crystal structures of the FAD-binding and NADPH-binding domains, known as the C-terminal cytosolic dehydrogenase (DH) domain when combined (Magnani et al., 2017). Interestingly, all seven NOX family isoforms contain this common DH domain (Magnani et al., 2017). This C-terminus domain functions as a toggle switch and regulates access of the NADPH to NOX1 (Sies, 2015). NOX2 includes a very similar NADPH-binding domain (RCSB Protein Data Bank, ID: 3A1F).

1.2.3.1.2 Activation All NOX isoforms contain one catalytic subunit and other regulatory subunits, apart from NOX5, which consists of one catalytic subunit only. The catalytic subunit of NOX2 is gp91phox, while the p22phox comprises the catalytic subunit of the other NOX isoforms (Panday et al., 2015). p22phox is required for the stability and activation of the NOX enzymes (Brandes, Weissmann, & Schroder, 2014). NOX2 is the first described prototype NADPH oxidase and its structure is described extensively below. In terms of ROS production, the immediate product of NOX enzymes is superoxide. However, due to spontaneous and enzymatic dismutation, hydrogen peroxide (H_2O_2) is also rapidly generated (Bedard & Krause, 2007b). DUOX1 and DUOX2 exhibit calcium-dependent generation of H_2O_2 produced directly from a superoxide intermediate owing to activity of their unique extracellular peroxidase-like domains (Morand et al., 2009).

1.2.3.1.3 NOX2 or CYBB In phagocytic cells NADPH oxidase is composed of two membrane bound elements: gp91phox and p22phox, three cytosolic proteins: p40phox, p47phox, p67phox and a small G-protein: Rac. Gp91phox and p22phox proteins form a heterodimer linked permanently with the plasma membrane (H. D. Wang et al., 2001; Van Buul, Fernandez-Borja, Anthony, & Hordijk, 2005). Wallach and Segal ((Wallach & Segal, 1997)) first presented the structure of the catalytic subunit gp91phox, also called NOX2. At the resting state, NOX2 and p22phox are located at the membrane as an inactive complex, while the p40phox (also known as neutrophil cytosol factor 4), p67phox (also known as neutrophil cytosol factor 2) and p47phox (also known as neutrophil cytosol factor 1) subunits are found in the cytosol (H. D. Wang et al., 2001; Van Buul et al., 2005). Assembly of the small GTPase p21-RAC1 (also known as Ras-related C3 botulinum toxin substrate 1) on the membrane is required for NOX2 activation and full activity. Upon NOX2 activation, RAC1 is recruited to the membrane, followed by recruitment of other cytosolic components. Afterwards, p47phox is phosphorylated by protein kinase C (PKC) (Fontayne, Dang, Gougerot-Pocidalo, & El Benna, 2002; Kitada et al., 2003; Schulz, Wenzel, Munzel, & Daiber, 2014a) and translocated to the membrane, together with p67phox and p40phox (Figure 1.2). This step leads to a conformational change through which the tandem SRC homology 3 (SH3) domain in p47phox can bind to the proline-rich region in the cytosolic C-terminus of p22phox (Groemping, Lapouge, Smerdon, & Rittinger, 2003). Taken together, all these assembly events result in the activation of NOX2. Through a positive reinforcement loop, the initial ROS production (especially of H_2O_2) activates proto-oncogene tyrosine-protein kinase Src, which transactivates epidermal growth factor receptor (EGFR) and PI3K-dependent activation of RAC1, further amplifying NOX2 activation (Seshiah et al., 2002).

Observations of stimulus-dependent ROS formation in non-phagocytic cells, coupled with the presence of the known NOX component p22phox in almost all cell types, prompted a search for gp91phox homologs. In nonphagocytic cells, the gp91phox component may be replaced by homologous NOX and DUOX proteins (Figure 1.2). NOX1, NOX2, NOX4, and NOX5 have been also identified in vascular tissue (Kleniewska, Piechota, Skibska, & GorÄca, 2012). The main difference between phagocytic gp91phox and other NOX species is that ROS production by phagocytic NOX2 occurs on the external side of the plasma membrane, releasing ROS into phagosomes or the extracellular space, whereas ROS produced by other NOX species are found in the intracellular medium in much smaller quantities (Elbim, 2005).

1.2.3.1.4 NOX1 Similar to NOX2, NOX1 also requires the assembly of multiple subunit in order to reach an activated status (Bedard & Krause, 2007a). NADPH oxidase organizer 1 (NOXO1) and NADPH oxidase activator 1 (NOXA1) are regulators of NOX1 activity, while active Rac1 can also contribute to NOX1 activity via membrane translocation upon its GTP-activation (Panday et al., 2015).

1.2.3.1.5 NOX4 Similarly to NOX3, the activation of NOX4 requires only p22phox. NOX4 is mainly regulated at the expression level (Altenhofer, Radermacher, Kleikers, Wingler, & Schmidt, 2015; Sahoo, Meijles, & Pagano, 2016). In vascular smooth muscle cells polymerase δ-interacting protein 2 (POLDIP2) binds with p22phox and increases NOX4 enzymatic activity and ROS production, leading to increased focal adhesion turnover and migration (Flegal, Kit, Orpana, & Graubard, 2013).

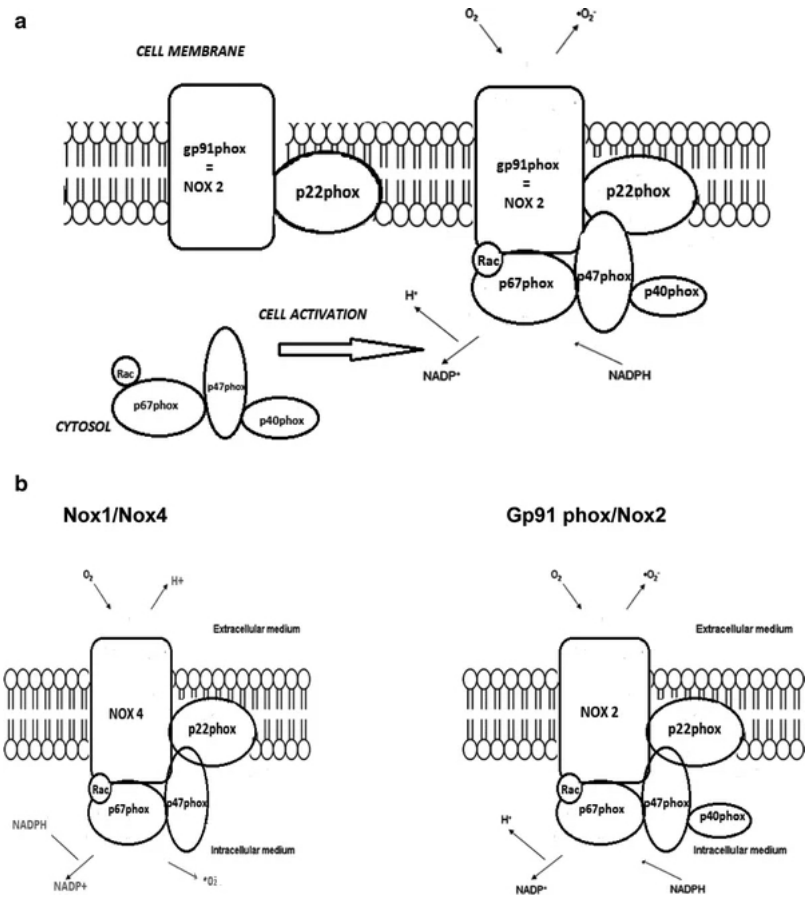


Figure 1.2: NOX structure-schematic. (a) NADPH oxidases are multisubunit membrane proteins that are activated by translocation of the cytosolic subunits p47phox, p67phox, and Rac to the NOX/p22phox complex. (b) The vascular NADPH oxidase complex may contain NOX1 or NOX4 as substitutes for the catalytic gp91phox subunit (NOX2) of the phagocytic oxidase. Superoxide is produced intracellularly (as opposed to NOX2 which produces superoxide extracellularly). The NOX subunit is bound to p22phox in the plasma membrane and they stabilize each other. Adapted with permission from (Kleniewska et al., 2012).

1.2.3.1.6 NOX5 Activation of NOX5 is independent of interactions with known subunits, and it is rather Ca^{2+} realted, owing to an N-terminal calmodulin-like domain with four binding sites for Ca^{2+} (EF hands) (Jha, Watson, Mathew, de Vos, & Jandeleit-Dahm, 2017; F. Chen, Wang, Barman, & Fulton, 2015; BelAiba et al., 2007). Following an increase in Ca^{2+} concentration, the N-terminus of NOX5 undergoes conformational changes that lead to exposure of its hydrophobic patch (Banfi, Tirone, et al., 2004). This patch enables intramolecular interac-

tions between the N-terminus and the C-terminus, resulting in the activation of NOX5 (Banfi, Tirone, et al., 2004). In the C-terminus, NOX5 has a binding site for the Ca^{2+}-modulated and Ca^{2+}-binding protein calmodulin (F. Chen, Yin, Dimitropoulou, & Fulton, 2016). The activity of NOX5 can also be positively regulated through phosphorylation by PKC, Ca^{2+}/calmodulin-dependent protein kinase II (CaMKII) and mitogen-activated protein kinases (MAPKs) (Pandey, Gratton, Rafikov, Black, & Fulton, 2011; Pandey & Fulton, 2011; Montezano et al., 2015).

1.2.3.1.7 DUOX1-2 DUOX1 and DUOX2 are composed of the basic NOX5-like structure, but fused with an additional transmembrane domain and an extracellular N-terminus (Lambeth, Kawahara, & Diebold, 2007). The association of DUOX1 with dual oxidase maturation factor 1 (DUOXA1) and of DUOX2 with DUOXA2 enables the translocation of DUOX1 and DUOX2 from the endoplasmic reticulum to the plasma membrane. DUOX1 and DUOX2 are activated by the binding of Ca^{2+} to their intracellular domain (Lambeth et al., 2007).

1.2.3.2 Uncoupled eNOS

Nitric oxide synthase (NOS) is a homodimeric enzyme with three isoforms: endothelial NOS (eNOS), neuronal NOS (nNOS; also known as NOS1) and inducible NOS (iNOS; also known as NOS2). NOS is tasked with the synthesis of synthesis of NO, for which L-arginine is required as the primary substrate. At the same time molecular oxygen and reduced NADPH (harbouring one extra electron) are also required as co-substrates. eNOS uses Tetrahydrobiopterin (H4B or BH4) as an essential cofactor for the synthesis of NO as it promotes stabilization of the enzyme's dimeric state. L-arginine, H4B, haem and molecular oxygen bind to the N-terminal oxygenase domain of eNOS; NADPH binds to the C-terminal reductase domain (Chalupsky & Cai, 2005a).

In physiological conditions, eNOS catalyses electron transfer from reduced NADPH found in one its monomers to the haem-containing oxygenase domain of the other monomer. Oxygen is then reduced by electrons and incorporated into the terminal guanidine group of L-arginine. The produce of this reaction is NO and L-citrulline. When H4B is available eNOS adopts is normal dimer form, a state called coupled eNOS (Figure 1.3). However, in the absence of H4B, mainly because of oxidative inactivation, eNOS becomes uncoupled, the dimer breaks down, and electrons are transferred to molecular oxygen to generate superoxide instead of NO (Oak & Cai, 2007a).

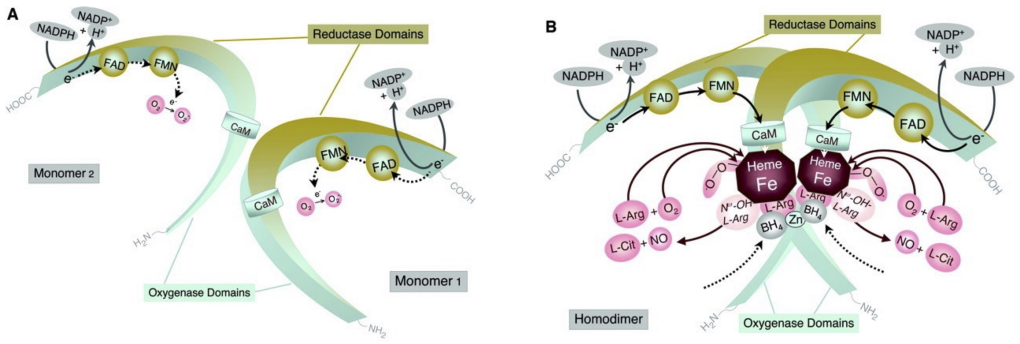


Figure 1.3: eNOS structure-schematic. (A) All NOS enzymes are synthesized from subunits that consist of a reductase domain and an oxygenase domain, which are able to transfer electrons from NADPH to the flavins FAD and FMN and have the capacity to reduce molecular oxygen to $O_2^{\bullet -}$. (B) When sufficient substrate l-arginine and co-factor BH4 are present, intact NOS dimers couple their heme and O_2 reduction to the synthesis of NO. Adapted with permission from (Forstermann & Munzel, 2006).

H4B is produced through two enzymatic pathways: the de novo synthetic pathway and the salvage pathway, in which H4B is regenerated from dihydrobiopterin (H2B) that is its oxidized for. In the de novo synthesis pathway, H4B is generated from GTP sequentially by the enzymes GTP cyclohydrolase 1 (GTPCH1; the rate-limiting synthetic enzyme), 6-pyruvoyl tetrahydrobiopterin synthase and sepiapterin reductase (SPR) (Iacobellis, 2015). H4B can also be regenerated from its oxidized form H2B in a process catalysed by the rate-limiting, salvage

enzyme dihydrofolate reductase (DHFR); H2B can be converted from the exogenous precursor sepiapterin by SPR (Crabtree & Channon, 2011; Thony, Auerbach, & Blau, 2000). The uncoupling of eNOS can be the result of NOX activation, which will produce ROS, that will oxidize H4B and lead to its deficiency (Chalupsky & Cai, 2005a).

The crosstalk and interactions between NOXs and eNOS uncoupling has been implicated in various CVDs, including hypertension and aortic aneurysms (Q. Li et al., 2019), atherosclerosis (Takaya et al., 2007), diabetes mellitus (Faria, Papadimitriou, Silva, de Faria, & de Faria, 2012), cardiac IR injury (Moens et al., 2008) and heart failure (Moens et al., 2011). H4B deficiency and eNOS uncoupling can be induced through DHFR depletion. Indeed, Dhfr$+/-$ mice (the homozygous knockout is embryonically lethal) have reduced H4B levels in the aorta at baseline and a well well-compensated low-level eNOS uncoupling (Kaul et al., 2012), similar to what is observed in Apoe$-/-$ mice (Siu, Miao, & Cai, 2014a). When angiotensin II was infused into Dhfr$+/-$ mice marked hypertension and development of abdominal aortic aneurysm (AAA) was observed (Kaul et al., 2012).

In addition, deficiency of SPR or GTPCH1 can also cause H4B deficiency and eNOS uncoupling, as shown in deoxycorticosterone acetate (DOCA)-salt hypertensive mice (Siu et al., 2014a; Leipsic et al., 2014). Overexpression of GTPCH1 restored the H4B level and let to eNOS neing recoupled in DOCA-salt hypertensive mice. Therefore, modulation of H4B metabolic enzymes and eNOS coupling management might be a therapeutic strategy in CVD.

Apart from H4B deficiency, other mechanisms are also responsible for inducing eNOS uncoupling (Schulz et al., 2014a). Oxidants (such as peroxynitrite and hypochlorous acid) can disrupt the ZnS4 cluster of eNOS and result in eNOS uncoupling (Zou, Shi, & Cohen, 2002).

Additionally, S-glutathionylation of cysteine residues in aortic eNOS has been found to be increased in animal models of hypertension (C. A. Chen et al., 2010), and streptozotocin (STZ)-induced diabetes (Schuhmacher et al., 2011). Normalization of S-glutathionylation in eNOS resulting in coupling of eNOS and improved vasorelaxation.

1.2.3.3 Dysfunctional mitochondria

Mitochondria are tasked with producing cellular energy, through the synthesis of ATP by oxidative phosphorylation (Roger, Munoz-Gomez, & Kamikawa, 2017). Oxidative phosphorylation takes place at the mitochondrial electron transport chain, which consists of a series of enzymatic complexes that pump protons across the mitochondrial inner membrane. These processes generate a proton gradient, that is utilised to produce ATP while transferring electrons from electron donors (NADH or succinate from the citric acid cycle) to oxygen to generate water (Nolfi-Donegan, Braganza, & Shiva, 2020).

In homeostasis, electron transportation in the mitochondria is efficient and the electron leak is maintained at low, physiological levels (Chance, Sies, & Boveris, 1979). Under conditions of oxidative stress, the mitochondrial ATP-sensitive K^+ channel (mitoK_{ATP}) is activated by redox-sensitive PKC to transduce redox signals from the cytosol to the mitochondria (Queliconi, Wojtovich, Nadtochiy, Kowaltowski, & Brookes, 2011). This leads to an influx of potassium into the mitochondrial matrix, which in turn prompts the electron transport chain to produce ROS (Oldenburg, Cohen, Yellon, & Downey, 2002). Inhibition of mitoK_{ATP}, after incubation with 5-hydroxydecanoate, prevented mitochondrial ROS production, suggesting that this potassium influx is crucial in regulating mitochondrial ROS production (Kimura et al., 2005a). Complex I and complex III are the major sites at which superoxide is generated (Madamanchi

& Runge, 2007). Furthermore, oxidative stress results in the production of more electron donors from the citric acid cycle, which are then available to the mitochondrial electron transport chain to generate superoxide through the interaction of electrons with oxygen (Brownlee, 2005; Brand, 2010). Finally, oxidative stress in known to damage DNA, and therefore mitochondrial DNA can also be a target, which causes ROS production and apoptosis (Brownlee, 2005).

ROS produced by dysfunctional mitochondria has been reported to be implicated in hypertension (D. Graham et al., 2009), atherosclerosis (Ballinger et al., 2002), diabetes (E. J. Anderson et al., 2009), heart failure (D. F. Dai, Chen, et al., 2011) and AAA (Q. Li et al., 2019). In mice, inhibiting mitochondrial ROS production with mitochondria-targeted peptide antioxidant SS-31 preserved insulin sensitivity in rats fed a high-fat diet61 and prevented angiotensin II-induced cardiac hypertrophy and diastolic dysfunction (D. F. Dai, Johnson, et al., 2011). Also, the use of the mitochondria-specific antioxidant MitoQ reduced cardiac hypertrophy in stroke-prone spontaneously hypertensive rats (D. Graham et al., 2009) and diminished ROS production in leukocytes isolated from patients with diabetes, hindering leukocyte-endothelial cell interactions (Escribano-Lopez et al., 2016). Further, upregulation of mitochondrial brown fat uncoupling protein 1 (UCP1) completely inhibited hyperglycaemia-induced mitochondrial superoxide production in mice, through disruption of the mitochondrial electron transport chain (Nishikawa et al., 2000). Finally, NOX-derived ROS have been shown to disseminate inside mitochondria and promote electron leak and mitochondrial ROS production, suggesting that dysfunctional mitochondria are a natural consequence of dysfunctional NOXs (Doughan, Harrison, & Dikalov, 2008a).

1.2.3.4 Xanthine oxidase

Xanthine oxidase (XO) is the oxidation product of xanthine dehydrogenase (XDH); both XDH and XO are interconvertible. Xanthine oxidase is part of the purine degradation pathway, converting hypoxanthine to xanthine and ultimately to uric acid (H. Suzuki et al., 1998). In these reactions XO uses oxygen as an electron acceptor and generates superoxide.

Studies have suggested that XO is involved in the athology of various CVDs. In animal model studies inhibiting XO was beneficial for hypertension (Nakazono et al., 1991), myocardial IR injury (G. R. Li & Ferrier, 1992) and chronic heart failure (Engberding et al., 2004). However, in humans use of oxypurinol, an XO inhibitor did not show benefits in patients with chronic heart failure (Hare et al., 2008). A meta-analysis of individual data in hyperuricemic patients with acute myocardial infarction found an improved survival, free from MACE in post-AMI patients treated with a combination of an urate lowering drug with antioxidant activity and an ACEi (Borghi et al., 2018). This suggests that XO inhibition may be rationalised in the context of CVD comorbidity and hyperuricaemia.

1.2.4 Oxidase crosstalk in CVD

Cardiovascular disease pathogenesis involves sustained oxidative stress which is induced by oxidase crosstalk. The most important oxidase system to contribute seems to be activated NOXs, which in turn have the capacity to activate downstream oxidase systems, such as uncoupled eNOS, dysfunctional mitochondria or XO, resulting in further ROS production. These secondary oxidase systems can also activate NOXs and/or each other. The interactions between these oxidases in the cardiovascular system are introduced below.

1.2.4.1 NOXs and uncoupled eNOS

Bovine endothelial cell exposure to angiotensin II in vitro increased the production of superoxide, which was attenuated by the RAC1 inhibitor NSC23766, indicating NOX-derived ROS production. However, following 24-hour angiotensin II infusion, superoxide production was entirely blocked by administration of L-NAME (a NOS inhibitor), while NSC23766 did not significantly reduce superoxide production, suggesting that uncoupled eNOS is predominantly responsible for ROS production after prolonged exposure of endothelial cells to angiotensin II, and that eNOS uncoupling occurs as a consequence of angiotensin II-induced activation of NOX (Chalupsky & Cai, 2005b).

eNOS uncoupling is induced after NOX activation through E2F1-dependent, E2F2-dependent or E2F3a-dependent downregulation of Dhfr expression. NOX derived H_2O_2 downregulated the expression of E2F1, E2F2 and E2F3a, the main transcription factors required to activate Dhfr transcription in endothelial cells (H. Li et al., 2019). Attenuating expression and activity of Dhfr lead to BH4 deficiency and consequently eNOS uncoupling. In vivo transfection of Dhfr or oral folic acid administration restored endothelial DHFR expression and activity, recoupled eNOS and improved NO bioavailability in angiotensin II-infused animals (Siu, Miao, & Cai, 2014b). In addition, overexpression of E2F1 in mice increased DHFR levels, leading to more BH4 available and eNOS coupling. NO bioavailability was improved resulting in reduced blood pressure (H. Li et al., 2019). These data reveal a crosstalk across NOX-H_2O_2-E2F-DHFR-BH4 that regulates eNOS uncoupling.

Furthermore, in DOCA-salt hypertensive mice and rats eNOS uncoupling has been shown to result from decreased SPR expression and GTPCH1 activity, both of which lead to impaired

BH4 bioavailability (Gimenez, Schickling, Lopes, & Miller Jr, 2016). NOX activity was also reported to be upregulated in DOCA-salt hypertensive mice with administration of the NOX inhibitor 4'-hydroxy-3'-methoxyacetophenone (apocynin) or deletion of p47phox restoring BH4 bioavailability and eNOS coupling in DOCA-salt hypertensive mice (J. Y. Youn et al., 2012). These data demonstrate an upstream role of NOXs in eNOS uncoupling in a salt-sensitive model of hypertension. Of note, different H4B metabolic enzymes are involved in different types of hypertension, with DHFR deficiency underlying eNOS uncoupling and hypertension in angiotensin II-infused mice, and SPR and GTPCH1 deficiency accounting for hypertension in DOCAâsalt hypertensive animals.

The interaction between NOXs and uncoupled eNOS has also been studied in streptozotocin (STZ)-injected type 1 diabetic animals. STZ injection in mice downregulated aortic DHFR expression and BH4 bioavailability, resulting in eNOS uncoupling (J. Youn, Gao, & Cai, 2012). Administration of the angiotensin II receptor type 1 blocker candesartan or the ACE inhibitor captopril recoupled eNOS through inhibition of NOX activity and restoration of DHFR protein expression (Oak & Cai, 2007b). Knocking out either Nox1 or Ncf1 (encoding p47phox) improved endothelium-dependent vasodilatation in STZ-induced diabetic mice through recoupling of eNOS as a result of the restoration of DHFR function and BH4 bioavailability (J. Youn et al., 2012). Therefore NOX1 in particular is strongly involved in NOX-dependent uncoupling of eNOS through NOX-derived ROS production and oxidation of BH4.

1.2.4.2 NOXs and mitochondria

NOX activation has been implicated in mitochondrial ROS production and dysfunction in endothelial cells (Doughan, Harrison, & Dikalov, 2008b). Using apocynin or small interfering

RNA (siRNA) targeted to Cyba (encoding p22phox) in bovine endothelial cells in vitro researchers have shown a reduction in angiotensin II-provoked mitochondrial ROS production, indicating NOX-dependent modulation of mitochondrial dysfunction (Lassegue & Griendling, 2010). Further, administration of L-NAME prevented angiotensin II-induced mitochondrial dysfunction, suggesting that the NOX modulation of mitochondrial ROS is mediated by uncoupling of eNOS (Doughan et al., 2008b). Another suggested pathway for this modulation is the reported involvement of angiotensin II-stimulated mitochondrial ROS production in the opening of mitoK$_{ATP}$ in both endothelial cells and vascular smooth muscle cells (Kimura et al., 2005b).

Conversely, mitochondrial ROS can in turn regulate NOX activity. Treatment with diazoxide leads to mitoK$_{ATP}$ opening and results in NOX activation (Kimura et al., 2005b). Moreover, the mitoK$_{ATP}$-specific inhibitor 5-hydroxydecanoate reduced superoxide production by NOX and uncoupled eNOS in angiotensin II-treated endothelial cells in vitro, suggesting feedback regulation of NOX and eNOS activity by mitoK$_{ATP}$ (Schulz, Wenzel, Munzel, & Daiber, 2014b). Finally, in mice where mitochondrial superoxide was eliminated by either overexpression of SOD2 or administration of the mitochondria-targeted antioxidant MitoTEMPO, NOX activity was inhibited in endothelial cells, but only after angiotensin II stimulation, with basal NOX activity remaining intact (Dikalova et al., 2010).

1.2.4.3 Uncoupled eNOS, xanthine oxidase and mitochondria

Superoxide reacts with NO to form peroxynitrite, which oxidises membrane lipids and electron transport chain complexes and damages mitochondria (Rubbo et al., 1994). Uric acid, a peroxynitrite scavenger, or L-NAME protected against mitochondrial dysfunction induced by angiotensin II in cultured endothelial cells, proposing that an eNOS-dependent mitochondrial

dysfunction exists (Doughan et al., 2008b). Of note, in Dhfr+/â mice mitochondrial superoxide production in the aorta significantly increased following angiotensin II infusion, suggesting that eNOS uncoupling in DHFR deficiency induces mitochondrial dysfunction (H. Li et al., 2019). In the myocardium, uncoupling eNOS by treatment of mice with 2,4-diamino-6-hydroxypyrimidine (DAHP: an inhibitor of GTPCH1) resulted in impaired mitochondrial function, and cardiac contractile dysfunction (Ceylan-Isik et al., 2009). Treatment with sepiapterin (a precursor of BH4) in mice with cardiac IR injury recoupled eNOS, reduced mitochondrial superoxide production, and resulted in preserved cardiac function (Siu, Lotz, Ping, & Cai, 2015). On the other hand, in patients with Type II diabetes and dyslipidaemia supplementation with antioxidant coenzyme Q10 recoupled eNOS and improved endothelial function of conduit arteries of the peripheral circulation (Watts et al., 2002).

As for XO, in a rat model of cocaine-induced cardiac dysfunction, treatment with allopurinol, an XO inhibitor, significantly reduced mitochondrial ROS production and improved cardiac function (Vergeade et al., 2012). Conversely, hypoxanthine, which is a metabolic product of ADP and AMP, both of which are produced during ATP breakdown in the mitochondria, has been proposed to react with XO to produce superoxide, which in turn causes damage to mitochondria (Gladden et al., 2011), indicating the presence of an "oxidative loop" between XO and mitochondria.

1.2.5 Contributions of oxidase crosstalk to particular CVDs

For the purposes of this thesis the detailed molecular pathways and pathophysiological relevance of the oxidase crosstalk in atherosclerosis and heart failure are discussed below.

1.2.5.1 Atherosclerosis

NOX-derived ROS have been implicated as a major mediator of atherosclerosis (Streeter, Thiel, Brieger, & Miller, 2013). Firstly, ROS can oxidise LDL which is a central event in the natural history of atherosclerosis (Aviram, Rosenblat, Etzioni, & Levy, 1996).

In Apoe$-/-$ mice, knockout of the Ncf1 gene, which encodes the p47phox subunit, prevented vascular lesion formation, which suggests that either NOX1 or NOX2 are required for the development of atherosclerosis (Barry-Lane et al., 2001). Indeed in later experiments, Nox1 knockout in Apoe$-/-$ mice reduced aortic superoxide production, macrophage infiltration and lesion formation (Gray et al., 2013). Similarly, inhibiting Nox1 and Nox4 with GKT137831 (a dual inhibitor of both NOX1 and NOX4) led to the same effect in Apoe$-/-$ mice (Gray et al., 2013). Also, deletion of Nox2 in the same mouse model resulted in decreased aortic superoxide production, reduced lesion formation and increased NO bioavailability (Judkins et al., 2010). Interestingly, overexpression of NOX2 in endothelial cells did not lead to rapid progression of atherosclerosis, despite the fact that superoxide production and macrophage recruitment were increased (Douglas et al., 2012). Therefore, the cell type is also an important factor when studying the clear effect NOX1 and NOX2 have in atherogenesis.

NOX4 on the other hand has been shown by several studies to exert a protective effect in atherosclerosis (Gray et al., 2016). Global Nox4 knockout or induced deletion of Nox4 increased atherosclerosis in Apoe$-/-$ mice, despite the fact that H_2O_2 production was reduced, propmpting the researchers to speculate that NOX4-produced H_2O_2 has anti-atherosclerotic functions (Schurmann et al., 2015). Likewise, overexpression of NOX4 in endothelial cells of Apoe$-/-$ mice prevented the formation of atherosclerotic lesions, primarily through attenu-

ated inflammatory responses81. Similar deleterious effects of Nox4-produced H_2O_2 deficiency were observed in Ldlr$-/-$ mice (Langbein et al., 2016). In humans, NOX4 transcription was decreased as opposed to upregulated NOX1 in endarterectomy specimens from patients with CVDs or diabetes (Gray et al., 2016). Al these highlight that NOX4-derived H_2O_2 may exert beneficial effects in atherosclerosis through inhibition of inflammation.

Expression levels of NOX5 in the coronaries have been found increased in the presence of coronary artery disease in patients undergoing cardiac transplantation (Guzik et al., 2008). NOX5 has also been shown to increase vascular smooth muscle cell proliferation (Jay et al., 2008). NOX5 is localized in the lesion area, both in endothelial and vascular smooth muscle cells, in the coronary arteries and seems to be an important source of ROS in atherosclerosis.

As for eNOS, in Apoe$-/-$ mice increased uncoupling led to the formation of atherosclerotic lesions (Takaya et al., 2007). Reversing this, either by supplementation with H4B or with endothelial-specific overexpression of GTPCH1, decreased superoxide production, improved vasorelaxation and NO bioavailability, and significantly reduced lesion formation in Apoe$-/-$ mice (Ozaki et al., 2002). In addition, NOX activation and NOX-derived ROS were found to mediate angiotensin II-induced eNOS uncoupling in hph-1 mice (hph-1 mice have a mutation in the GTPCH1 encoding Gch1 gene and have a phenotype of modest eNOS uncoupling), leading to hypertension and AAA (Siu et al., 2017).

1.2.5.2 Heart failure

The role of different NOX isoforms in the development of cardiac hypertrophy and heart failure has been assessed in animal models, particularly for NOX2 and NOX4 (Maejima, Kuroda, Matsushima, Ago, & Sadoshima, 2011). Following pressure overload, induced either by trans-

verse aortic constriction (TAC) or after phenylephrine/angiotensin II infusion, NOX4 expression in the heart was upregulated (M. Zhang et al., 2010). Cardiac-specific knockout of Nox4 prevented cardiac hypertrophy after TAC or phenylephrine/angiotensin II infusion, while the opposite (i.e. hypertrophy) was observed in cardiac-specific overexpression of Nox4 (Matsushima et al., 2013). NOX4 overexpression and activation is believed to lead to increased mitochondrial superoxide production, resulting in apoptosis and cardiac dysfunction (Kuroda et al., 2010). However, at the same time global knockout of Nox4 has also been shown to induce hypertrophy during exposure to chronic pressure overload with 6 weeks of suprarenal aortic constriction, through inhibition of Hif1a and Vegf, which resulted in angiogenesis of myocardial capillaries and hypertrophy (M. Zhang et al., 2010). These opposing results underline the potential importance of the role of different cell types in the development of hypertrophy, which warrant further investigation.

The role of NOX2 in the development of cardiac hypertrophy has also been studied. Following angiotensin II induced cardiac hypertrophy protein levels of Nox2 were increased and increased ROS production reported (Zhao et al., 2015). NOX2 was also upregulated after aortic banding (Parajuli, Patel, Wang, Basu, & Oudit, 2014) or MI (Looi et al., 2008). In addition, NOX2 protein levels in human biopsies of the left ventricle were elevated in patients with end-stage heart failure and dilated cardiomyopathy compared with that of individuals without heart failure (Parajuli et al., 2014).

eNOS uncoupling in the heart has also been observed in mice in response to TAC (Takimoto & Kass, 2007). Also, ROS production in excess from the mitochondria has been shown to contribute to heart failure (S. Dey, DeMazumder, Sidor, Foster, & O'Rourke, 2018). Myocardial ROS and left ventricular contractile dysfunction have been shown to be correlated (Ide et

al., 2000). Levels of both cytoplasmic and mitochondrial ROS were significantly increased in freshly isolated cardiomyocytes from failing hearts compared with cardiomyocytes from control hearts (Meyer & Dick, 2010). Administration of the mitochondria-targeted antioxidant MitoTEMPO brought both cytoplasmic and mitochondrial ROS in cardiomyocytes from failing hearts back to normal (S. Dey et al., 2018).

1.2.6 Antioxidant therapeutic strategies

Oxidative stress has been causally linked with cardiovascular disease, but not with cardiovascular events. Multiple antioxidant therapeutic strategies are being explored, some of which are currently undergoing clinical trials (Figure 1.4). These include:

- Targeting ROS sources

  NOXs inhibition

  mitochondrial antioxidants

- Targetting ROS itself

  targeting $O_2^{\bullet -}$ before it can react with $^{\bullet}NO$ to form $ONOO^-$

  targeting H_2O_2 before it can form $^{\bullet}OH$ or HOX

- ROS scavenging

  increasing GSH

  increasing synthesis of antioxidant enzymes, through NRF2 activation

  antioxidant supplements in the diet

- Inhibition of aberrant redox signalling

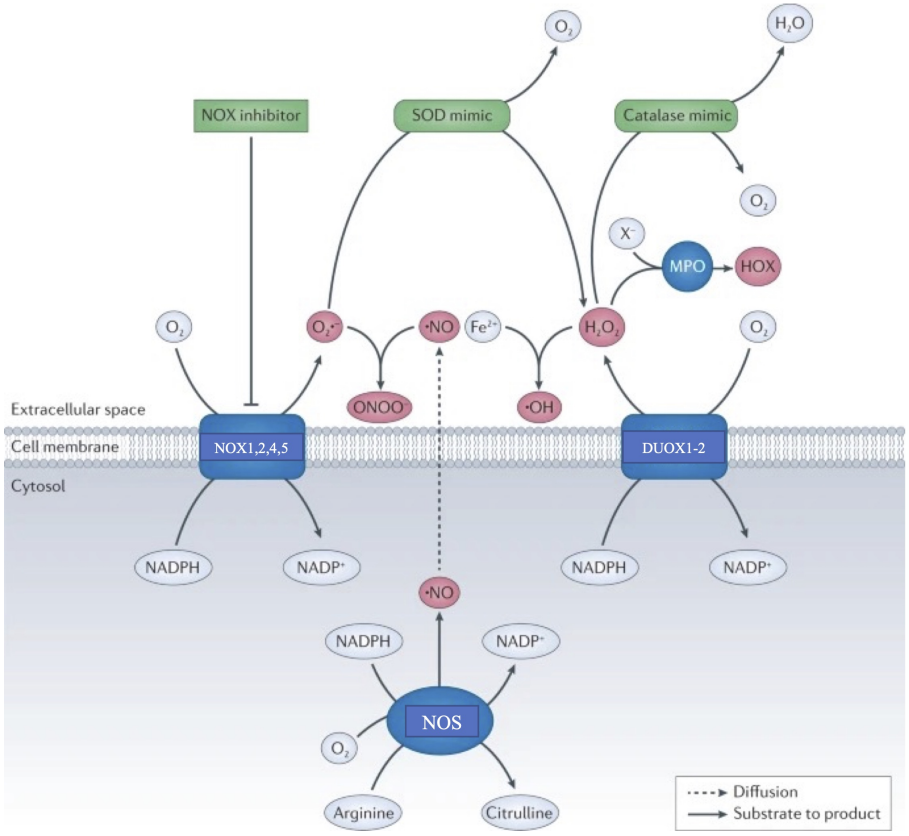


Figure 1.4: Antioxidant therapeutic strategies. Plasma membrane NADPH oxidase (NOX) production of superoxide ($O_2^{\bullet -}$) outside cells may be prevented by NOX inhibitors. Dismutation of $O_2^{\bullet -}$ to hydrogen peroxide (H_2O_2) is accelerated by superoxide dismutase (SOD) mimics, preventing the formation of peroxynitrite ($ONOO^-$), which spares nitric oxide ($^{\bullet}NO$). Reduction of H_2O_2 is accelerated by catalase mimics, preventing the formation of hypohalous acids (HOX) by myeloperoxidase (MPO) and hydroxyl radical ($^{\bullet}OH$) production via the Fenton reaction. Most SOD mimics appear to have catalase activity. Although NOX4, which is primarily in intracellular organelle membranes, has also been found in the plasma membrane, this has only been reported for one cell type and so its extracellular location remains debatable (indicated by the question mark). NOS: nitric oxide synthase. Reproduced from (Forman & Zhang, 2021).

1.2.6.1 Vitamins

Many prospective epidemiological studies have looked into whether consumption of fruit and vegetables, which are abundant in antioxidant vitamins, is associated with reduced risk of cardiovascular diseases. The role of such antioxidant vitamins (including vitamins C, E, and β-carotene) in prevention and treatment of cardiovascular disease has been a subject of intensive

investigation over the past several decades. A large systematic review with a total of 15 cohort studies involving a total of 7,415 incident coronary heart disease cases and 374,488 participants showed non significant association in the dose response meta-analysis for vitamins C, and β-carotene (Ye & Song, 2008). For vitamin E there was an inverse association with CVD risk, with each 30 IU/day increase in vitamin E intake related to a decrease in risk by 4%. A more recent 22-years population-based prospective study in chinese populations including 875 participants showed that dietary intake of anti-oxidant vitamins A, C, and E reduced the risk of adverse cardiovascular outcomes (C.-H. Lee et al., 2018).

1.2.6.2 Superoxide dismutase - catalase mimics

Superoxide dismutase mimics are not specific and target superoxide and other reactive oxygen or nitrogen species such as $ONOO^{-}$, peroxyl radical, H_2O_2 and $CO_3^{\bullet -}$ (Batinic-Haberle, Tovmasyan, & Spasojevic, 2015). However, some SOD mimics, can also act as pro-oxidants and react with thiols, ascorbate and tetrahydrobiopterin, thereby affecting redox-sensitive signalling pathways and cellular transcription (Batinic-Haberle et al., 2012). Therefore, the protective mechanism of SOD mimics may not be attributable to their SOD analogue ability.

The class of SOD mimics with most citations to date is the Mn porphyrins. Various Mn porphyrin compounds have been synthesized to exert dismutation activity, with MnTM-2-pYp^{5+} and MnTE-2-pYp^{5+} showing very high SOD activity. The protective and therapeutic effects of many Mn porphyrins such as MnTE-2-pYp^{5+} and MnTDE-2-ImP^{5+} have been demonstrated in non-human animal models of diseases, including stroke (Mackensen et al., 2001), diabetes (Piganelli et al., 2002) and cardiovascular system damage (Ganesh et al., 2016).

GC4419 is a novel, highly stable Mn(II)-containing penta-azamacrocyclic, which selec-

tively removes superoxide anions without reacting with other oxidants (Aston et al., 2001). In a recent phase I clinical trial in oropharyngeal cancer patients with chemoradiotherapy-induced oral mucositis GC4419 was shown to be safe for human use (C. M. Anderson et al., 2018). In addition, GC4419 has exhibited therapeutic effects in several animal models of inflammation (Salvemini, Mazzon, Dugo, Riley, et al., 2001), joint disease (Salvemini, Mazzon, Dugo, Serraino, et al., 2001) and myocardial IRI (Masini et al., 2002). A recent phase I clinical trial in severe oral mucositis of oropharyngeal cancer with radiation and chemotherapy indicates that the safety of GC4419 in patients is acceptable (C. M. Anderson et al., 2018).

1.2.6.3 NOX inhibitors

As evidenced above, NOXs are a clear contributor in the pathogenesis of CVDs. Therefore, targeting these enzymes has been studied, in the quest for new therapeutic strategies. The first two molecules to be investigated were diphenyleneiodonium (DPI) and apocynin (Y. Suzuki, Wang, Vu, & Raffin, 1992; Simons, A't Hart, Ching, Van Dijk, & Labadie, 1990). DPI is a general, nonreversible inhibitor of all NOX isoforms, but can also inhibits other ROS-generating systems, including XO, NOS and the mitochondrial electron transport chain (Altenhofer et al., 2012). Apocynin inhibits the membrane translocation of p47phox and p67phox in leukocytes and inhibits all flavin-containing enzymes (Williams & Griendling, 2007). Although not activated in endothelial and smooth muscle cells, apocynin has intrinsic antioxidant activity as a ROS scavenger, and can still lower ROS levels in endothelial cells and smooth muscle cells (Drummond, Selemidis, Griendling, & Sobey, 2011). 4-(2-Aminoethyl)-benzenesulfonyl fluoride, is a nonspecific inhibitor, that is weaker in inhibiting NOX compared with DPI (10 μmol/l) and is, therefore, not frequently used (Wartenberg et al., 2005). S17834 is a synthetic polyphe-

nol, which targets 5' AMP-activated protein kinase, and reduced tumour necrosis factor-induced NOX activity in endothelial cells and inhibited atherosclerotic lesion formation in the aortas of ApoE$-/-$ and Ldlr$-/-$ mice (Zang et al., 2006). One of the pleiotropic effects of statins (inhibitors of 3-hydroxy-3-methylglutaryl-coenzyme A reductase) is NOX inhibition by targeting RAC1 (Kwok, Ma, & Ma, 2013).

More recently, high throughput chemical screening has been use to identify novel NOX inhibitors. In 2015, GLX351322 was reported to inhibit NOX1, NOX2, NOX4 and NOX5 (Anvari, Wikstrom, Walum, & Welsh, 2015), but due to limited specificity it was not widely studied, although it was shown in 2018 to reverse Aβ11421-induced neuronal death, decrease oxidative stress and attenuate memory deficits and synaptic dysfunction in APP/PS1 mice (X. Wang et al., 2018). In 2018, GLX7013114, the first-reported highly selective inhibitor of NOX4, was shown to protect islet cells against high glucose+palmitate and cytokine-induced cell death. However, GLX7013114 did not show activity as a direct ROS scavenger or as an inhibitor of XO or glucose oxidase (X. Wang et al., 2018). In 2017, ML171, a Nox1 inhibitor, was shown to reduce NADPH-dependent ROS production in VSMCs from SHRSP rats (Harvey et al., 2017). Further, a nonspecific NOX inhibitor, APX-115, has been shown in 2018 to protect against kidney injury in animal models of T1DM and T2DM (Dorotea et al., 2018).

In addition, methylation-dependent and acetylation-dependent regulation of NOX gene expression has also been studied. Inhibition of histone deacetylases with pharmacological inhibitors, such as scriptaid, suberoylanilide hydroxamic acid, trichostatin A and valproic acid, has been shown in recent years to reduce NAPDPH oxidases mRNA levels and ROS production (F. Chen, Li, et al., 2016). In particular, suberoylanilide hydroxamic acid was shown to reverse STZ-induced upregulation of Nox1, Nox2 and Nox4 as well as ROS production in mouse

aorta (Manea et al., 2018). Moreover, in 2018 researchers noted that macrophage expression of myocardin-related transcription factor A recruited the histone acetyltransferase KAT8 to the promoters of Nox1, Nox2 and Nox4 to activate transcription in an animal model of cardiac IR injury. They therefore used the KAT8 inhibitor and observed significant downregulation of Nox1 and Nox4 expression, with reduction in ROS production and restoration of myocardial function (Yu et al., 2018).

Despite a lot of interest in NOX inhibition, several limitations remain. Firstly, developing isoform-specific inhibitors for NOXs has proven very challenging as only a handful of lead compounds described actually target Nox activity specifically. Secondly, it is important to underline that basal ROS production is required for many physiological processes, and thus interference has the potential to compromise the physiological equilibrium. Furthermore, tissue-specific or cell-specific roles of NOX isoforms need to be targeted in different cardiovascular conditions. Therefore, details of NOX inhibitor application, including timing, dosing and cell-specific or tissue-specific targeting, are of essential importance in the prevention and treatment of CVDs.

1.2.6.4 Glutathione peroxidase mimics

Among the large variety of glutathione peroxidase (GPX) mimetics that have been developed over the years, the selenoorganic compound ebselen (2-phenyl-1,2-benzisoselenazol-3(2H)-one) is best known, primarily for its wide range of specificity for smaller organic hydroperoxides to membrane-bound phospholipid and cholesterol hydroperoxides (Day, 2009). Ebselen reduced oxidative stress and decreases inflammation in animal studies (Nakamura et al., 2002; Garland et al., 2020). In clinical trials oral administration of ebselen was well tolerated and exerted therapeutic effects after complete occlusion of the middle cerebral artery (Ogawa et al., 1999),

and acute ischaemic stroke (Yamaguchi et al., 1998). ALT-2074 (BXT-51072), an analogue of ebselen, reduced infarct size in a mouse model of heart ischaemia-reperfusion (Blum et al., 2007). Human data from clinical trials in diabetes and coronary artery disease have yet to be published (Phase II clinical trial - NCT00491543).

1.2.6.5 Increasing GSH

Oxidative stress significantly reduces GSH, therefore strategies to maintain its levels using GSH esters or agents that contain its precursor, cysteine have been explored.

1.2.6.5.1 N-acetylcysteine N-acetylcysteine (NAC) is a water soluble, quickly absorbed antioxidant agent (Raftos, Whillier, Chapman, & Kuchel, 2007), that replenishes GSH (Rushworth & Megson, 2014). It has been investigated in the treatment of many pathologies with conflicting results. It has been used therapeutically in liver paracetamol toxicity (Smilkstein, Knapp, Kulig, & Rumack, 1988) , and cystic fibrosis (Conrad et al., 2015).

1.2.6.5.2 GSH esters Ester derivatives of GSH, such as monomethyl (GSH-OMe), monoethyl (GSH-MEE), diethyl (GSH-DEE) and isopropyl esters have been synthesized and evaluated for the efficiency of GSH supplementation (Wendel & Cikryt, 1980). Inside cells, GSH esters are rapidly hydrolysed by nonspecific esterases to form GSH (Levy, Anderson, & Meister, 1993). Subcutaneous or intraperitoneal injection of GSH esters into animals increased GSH levels in various tissues including the heart (M. E. Anderson, Powrie, Puri, & Meister, 1985). Although GSH esters do increase GSH levels and reduce oxidative stress in cells and non-human animals, no clinical trials to date have been conducted to test their efficacy in humans.

1.2.6.6 Inhibiting mitochondrial ROS

Interfering with the respiratory chain which is the main site of superoxide production in the mitochondria can be challenging, because of the consequences such an approach can have on ATP production. OP2113 is a drug that can be used in humans, which inhibits complex I and does not interfere with ATP production (Detaille, Pasdois, Semont, Dos Santos, & Diolez, 2019). However, it has yet to be studied in human clinical trials. Ebselen also enters the mitochondria but has been reported to lead to unexpected toxicity (Pavon, Correa, Buelna-Chontal, Hernandez-Esquivel, & Chavez, 2015).

1.3 Perivascular adipose tissue and cardiovascular disease

Elements of this section are taken from the following published material:

Kotanidis CP, Antoniades C. Perivascular fat imaging by computed tomography (CT): a virtual guide. Br J Pharmacol. 2021 Jul 23. doi: 10.1111/bph.15634.

Kotanidis, C. P. Antoniades, C. in Epicardial Adipose Tissue: From Cell to Clinic (ed Gianluca Iacobellis) 91-115 (Springer International Publishing, 2020).

1.3.1 Atherogenesis and inflammation

Inflammation is a key player in the natural history of atherogenesis, especially the development of the vulnerable atherosclerotic plaque (Antonopoulos, Margaritis, Lee, Channon, & Antoniades, 2012). The links between inflammatory processes and atherosclerosis are well established, with both innate and adaptive immunity involved in a complex network of molecular and cellular interactions (Libby, Ridker, Hansson, & Leducq Transatlantic Network on, 2009; Tousoulis et al., 2014). Components of the innate arm of immunity can be triggered by pathogens in a non-specific manner, leading to the activation of mast cells, neutrophils, macrophages (respiratory burst) and the complement (Tousoulis et al., 2014). At the same time, antigen-presenting cells are activated by toll-like receptors (TLRs), leading to pro-inflammatory signaling responses, and cross-linking with adaptive immunity, which is highly organized and more relevant to atherogenesis. T-cell activation, antibody production, and secretion of a range of pro-inflammatory cytokines, such as IFN-γ, IL-1, IL-6, are all responses related to the state of systemic low-grade

inflammation inherent to atherosclerosis. This state still accounts for residual risk for cardiovascular events in the population (Harrington, 2017). Low-grade inflammation is induced by the release of pro-inflammatory cytokines that lead to endothelial dysfunction, depletion of nitric oxide bioavailability, and accumulation of cell adhesion molecules to the vascular bed, which attract circulating leukocytes into the arterial intima (Souilhol et al., 2020). Reactive oxygen species produced in the sub-endothelial space, as part of the localized inflammatory cascade, oxidise LDL, which is taken up by macrophages, turning them into foam cells and initiating plaque development (Antoniades, Bakogiannis, Tousoulis, Antonopoulos, & Stefanadis, 2009). Activated T-lymphocytes are brought into action, while vascular smooth muscle cells (VSMCs) exhibit an increase in proliferation and migration, reaching the intima and differentiating into osteoblasts, contributing to the local deposition of calcium and overall stabilization of the plaque (Durham, Speer, Scatena, Giachelli, & Shanahan, 2018). Nevertheless, perpetuating excess local inflammation and sheer stress, induce metalloproteinases and lead to extracellular matrix degradation, remodeling and ultimately destabilization of the plaque, resulting in fissures, erosion, rupture, occlusive thrombosis and fatal complications (Souilhol et al., 2020; Antoniades et al., 2009). The inflammatory hypothesis in atherosclerosis development and progression has ignited the search for inflammation markers used as surrogate markers of presence and prognosis of cardiovascular disease. Systemic indices, mainly high sensitivity C-reactive protein (hsCRP) and proinflammatory cytokines in the plasma, have been associated with cardiovascular risk prediction, beyond traditional cardiovascular risk factors, supporting the concept of residual inflammatory risk (Ridker, 2007). This hypothesis became ever more prominent when large trials such as the JUPITER and CANTOS trials were reported. JUPITER (Ridker et al., 2008) showcased a reduction in cardiovascular risk in individuals with elevated hsCRP following treatment

with the statin rosuvastatin (Figure 1.5).

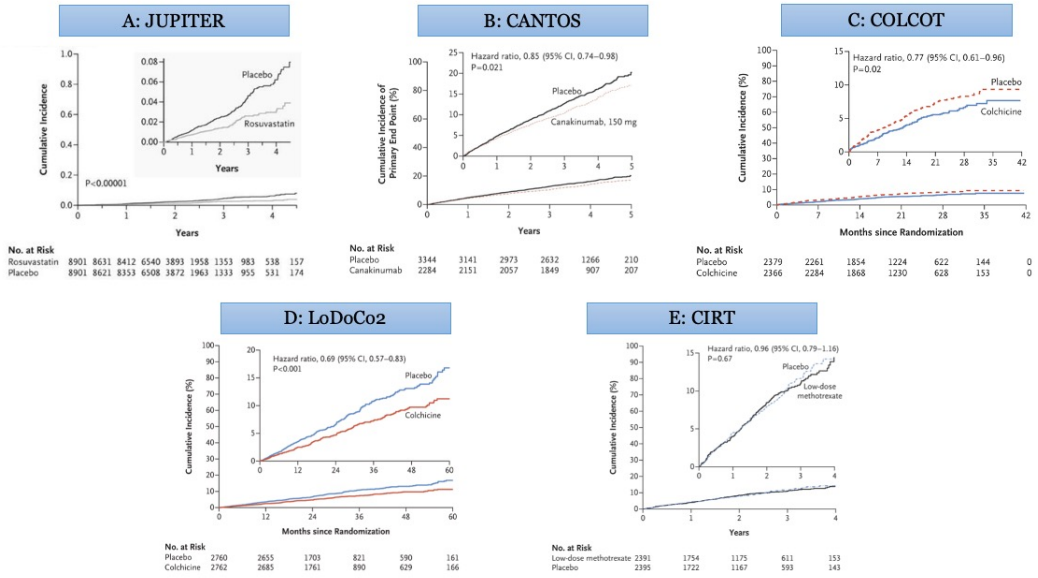


Figure 1.5: Inflammation is a valid therapeutic target to reduce cardiovascular events. (a) JUPITER trial: Rosuvastatin reduced the primary outcome defined as nonfatal myocardial infarction, nonfatal stroke, hospitalization for unstable angina, an arterial revascularization procedure, or confirmed death from cardiovascular causes. Adapted from (Ridker et al., 2008). (b) CANTOS trial: Canakinumab reduced the primary end point of nonfatal myocardial infarction, nonfatal stroke, or cardiovascular death. Adapted from (Ridker et al., 2017). (c) COLCOT trial: KaplanâMeier curve for the primary composite endpoint of death from cardiovascular causes, resuscitated cardiac arrest, myocardial infarction, stroke, or urgent hospitalization for angina leading to coronary revascularization in the colchicine group versus the placebo group. Adapted from (Tardif et al., 2019). (d) LoDoCo2 trial: Colchicine reduced the cumulative incidence of the primary composite end point of cardiovascular death, myocardial infarction, ischemic stroke, or ischemia-driven coronary revascularization. Adapted from (Nidorf et al., 2020). (e) CIRT trial: Low dose methotrexate failed to reduce the cumulative incidence of the final primary end point of major adverse cardiovascular events (nonfatal myocardial infarction, nonfatal stroke, or cardiovascular death) or hospitalization for unstable angina that led to urgent revascularization. Adapted from (Ridker, Everett, et al., 2019).

However, the full extent of rosuvastatin's pleiotropic anti-inflammatory effects was not fully documented, as LDL levels were also reduced in line with the risk reduction observed, obscuring the true size effect. A few years later, the CANTOS trial (Ridker et al., 2017) reported for the first time in humans that targeting IL-1β using the monoclonal antibody canakinumab

reduces the risk for cardiovascular events. However, fatal infections and sepsis were observed more frequently in the treatment group, raising safety concerns regarding the targeting of central key players of innate immunity. Importantly, inflammation should not be perceived as a singular therapeutic target, but rather as a spectrum of signaling pathways, each one constituting a singular target with variant therapeutic potential. This remark was underlined by the Cardiovascular Inflammation Reduction Trial (CIRT) (Ridker, Everett, et al., 2019), in which low-dose methotrexate failed to reduce events versus placebo as well as by a post-hoc analysis of the CANTOS trial data which showed that substantial residual inflammatory risk related to both IL-18 and IL-6 remains after IL-1β inhibition with canakinumab (Ridker, MacFadyen, Thuren, & Libby, 2019). It is consequently evident that, despite its well-established connection with vascular disease pathogenesis, inflammation needs to be further studied, both as a marker aiding the selection of the vulnerable patient, who would benefit the most from novel expensive therapies, and at the same time as a consistent therapeutic target (Passacquale, Di Giosia, & Ferro, 2016). Circulating biomarkers, like hsCRP or IL6, have excellent capacity in detecting systemic inflammation, but are often driven by other systemic (obesity, diabetes, cancer) or local inflammatory conditions (arthritis, infection), that usually co-exist with coronary inflammation (Margaritis et al., 2013). Therefore, unveiling the role of inflammation in atherogenesis to its full extent, both from a diagnostic as well as a therapeutic point of view, is of key importance. Studying in particular the localized inflammation-induced changes in the human arteries as well as in their perivascular space, may lead to the development of new, local biomarkers of inflammation, driving restratification protocols and revolutionizing the management of CAD. Perivascular adipose tissue -its biology and imaging- has recently emerged as a promising player, projected to provide reliable and promising insight into the detection of vascular inflammation, in a localized

and specific manner.

1.3.2 Defining adiposity in the human body

1.3.2.1 Subcutaneous and visceral adipose tissue definition

Adiposity in the human body is distributed anatomically into two major compartments, subcutaneous fat (SAT) and visceral fat (VAT). In terms of functionality, adipose tissue can be categorized into three depots: white, brown and 'beige' or 'brite' (Oikonomou & Antoniades, 2019). White adipose tissue acts mainly as metabolic energy storage, brown adipose tissue is primarily tasked with non-shivering thermogenesis, whereas the term 'beige' refers to brown-like adipocytes inside white adipose tissue that present the ability to produce heat via uncoupling of mitochondrial respiration (Mancio, Oikonomou, & Antoniades, 2018).

1.3.2.2 Epicardial adipose tissue definition

The term epicardial adipose tissue (EAT) refers to white adipose tissue located between the myocardium and the visceral layer of the pericardium. It differs embryologically from pericardial (or paracardial) fat, which is the part of intrathoracic visceral adipose tissue attached to the outside of the parietal layer of the pericardium (Iacobellis, 2015). EAT derives from the splachnopleuric mesoderm, as does the heart, and is supplied with blood by the coronary circulation (Antonopoulos & Antoniades, 2017). On the other hand, intrathoracic VAT, originates from the primitive thoracic mesenchyme, and is vascularized by noncoronary arteries (Iacobellis, 2015). In addition, EAT differs greatly from VAT and SAT at a functional level. Low expression levels of adiponectin and high levels of IL-6 and C-C motif chemokine ligand 2 (CCL2) have been associated with higher infiltration of macrophages in coronary artery disease

and also linked to other phenotypes such as hypertension (Baker et al., 2006). Furthermore, macroscopic measures of EAT, such as thickness and volume, are considered surrogates for metabolically unhealthy obesity and have been used for cardiovascular risk stratification (Sarin et al., 2008).

1.3.2.3 Defining perivascular adipose tissue

The need for a separate and clear definition for adipose tissue around the human arteries, originated from the observation that the part of EAT in close proximity to the coronary arteries has different morphological and functional characteristics compared to the rest of the depot (Antonopoulos et al., 2017). In bulk literature, PVAT is vaguely defined as adipose tissue surrounding the blood vessels. However, recently a series of experiments examining the molecular phenotype of pericoronary fat at increasing distances from the coronary artery wall, revealed regional variability, resulting from complex, paracrine vessel-PVAT interactions (Antonopoulos et al., 2017). This led to the proposal of a new robust definition of pericoronary fat -and by extension PVAT in general- as any adipose tissue located within a radial distance from the outer vessel wall equal to the whole vessel diameter of the adjacent coronary artery (Antonopoulos et al., 2017). This definition highlights the importance of biology, as opposed to a crude anatomical borders, in defining distinct fat depots and has the potential to address the contradicting variable definitions of PVAT that have appeared in literature so far (Figure 1.6).

Perivascular adipose tissue (PVAT) is a highly dynamic and metabolically active tissue surrounding most vascular beds in the human body, except for neural and pulmonary vasculature (Aghamohammadzadeh et al., 2012). In large vessels PVAT is contiguous with the adventitial layer, whereas in small vessels and microvessels PVAT adipocytes are an integral part of the

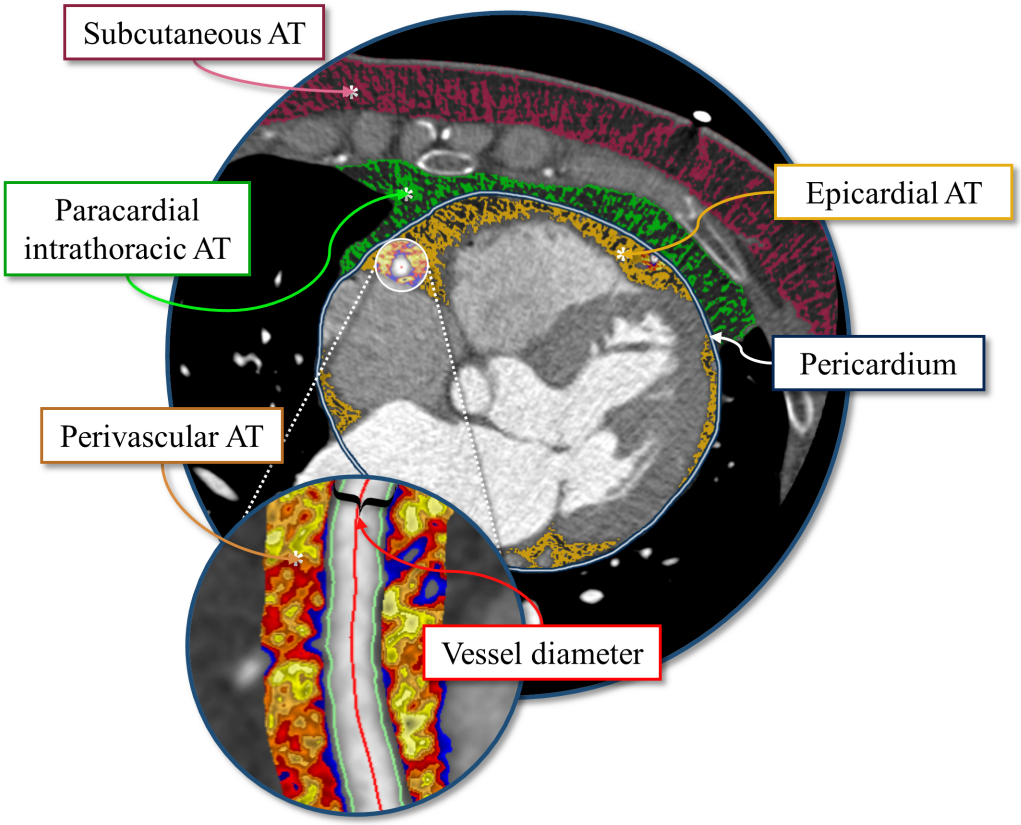
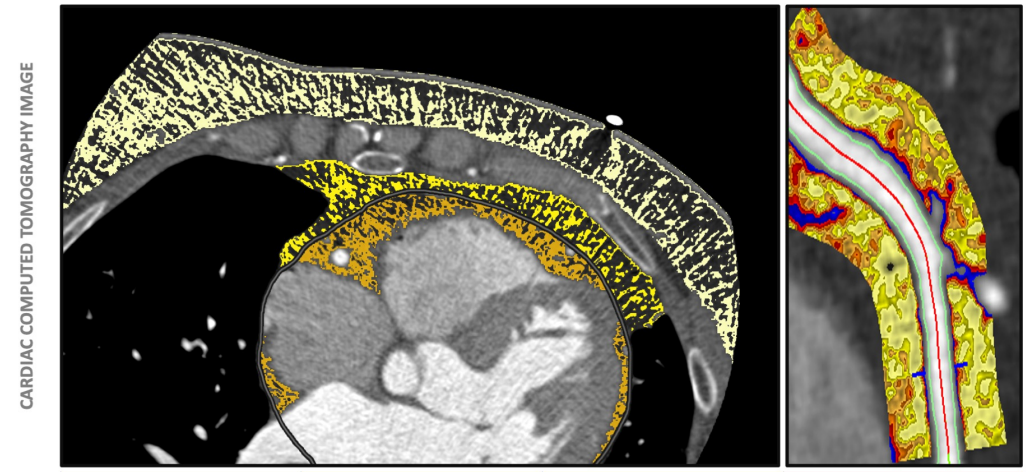


Figure 1.6: Defining distinct adipose tissue depots. Axial cross sectional slice of a coronary CTA, depicting the distinct adipose tissue (AT) depots within the thorax. Adiposity in the human body is distributed anatomically into two major compartments, subcutaneous fat (SAT) and visceral fat (VAT). VAT within the thoracic cavity can be further divided into paracardial or pericardial fat, which is the part of intrathoracic visceral adipose tissue located outside of the parietal layer of the pericardium and epicardial fat which is located between the myocardium and the visceral layer of the pericardium. PVAT is defined as any adipose tissue located within a radial distance from the outer vessel wall equal to the whole vessel diameter of the adjacent coronary artery. Adapted from (Kotanidis & Antoniades, 2020a).

vascular wall itself (Akoumianakis & Antoniades, 2017). Typically, healthy PVAT comprises adipocytes, microvasculature, nerves, stem cells, and inflammatory cells, although the exact phenotype depends on anatomical location and will vary significantly with pathogenesis (Szasz & Webb, 2012). Also, despite containing predominantly WAT, it has been reported to exert BAT thermogenic capabilities after exposure to cold (Akoumianakis & Antoniades, 2017). Within a cardiac CT image, we come across four distinct types of thoracic adipose tissue: subcutaneous,

paracardial, epicardial, and perivascular (Figure 1.7).



	SUBCUTANEOUS	PARACARDIAL	EPICARDIAL	PERIVASCULAR
ANATOMICAL LOCATION	Between dermis and thoracic wall	Within thoracic cavity Outside the pericardium	Inside the pericardium	Within a radial distance from outer vascular wall
BLOOD SUPPLY	Subcutaneous arteries	Mediastinal branches of internal thoracic artery and thoracic aorta	Coronary arteries	Adjacent vessel
EMBRYONIC ORIGIN	Primitive thoracic mesenchyme Neural crest stem cells	Primitive thoracic mesenchyme	Splachnopleuric mesoderm	Variable

Figure 1.7: Adipose tissue depots as imaged. Presentation of the four different adipose tissue depots within the thorax from an axial cross-sectional slice taken from a coronary CT angiogram image. Adapted from (Kotanidis & Antoniades, 2021).

1.3.3 PVAT effects on the vascular wall - Outside to inside signaling

Adipose tissue produces a wide variety of bioactive molecules, including adipokines (such as adiponectin, leptin, apelin) and inflammatory cytokines, jointly referred to as adipocytokines. PVAT further secrets micro-RNAs, microvesicles, inorganic molecules such as hydrogen sulfide, reactive oxygen species, fatty acid metabolites and others (Figure 1.8).

Products from remote depots, such as the subcutaneous adipose tissue, act on distant sites

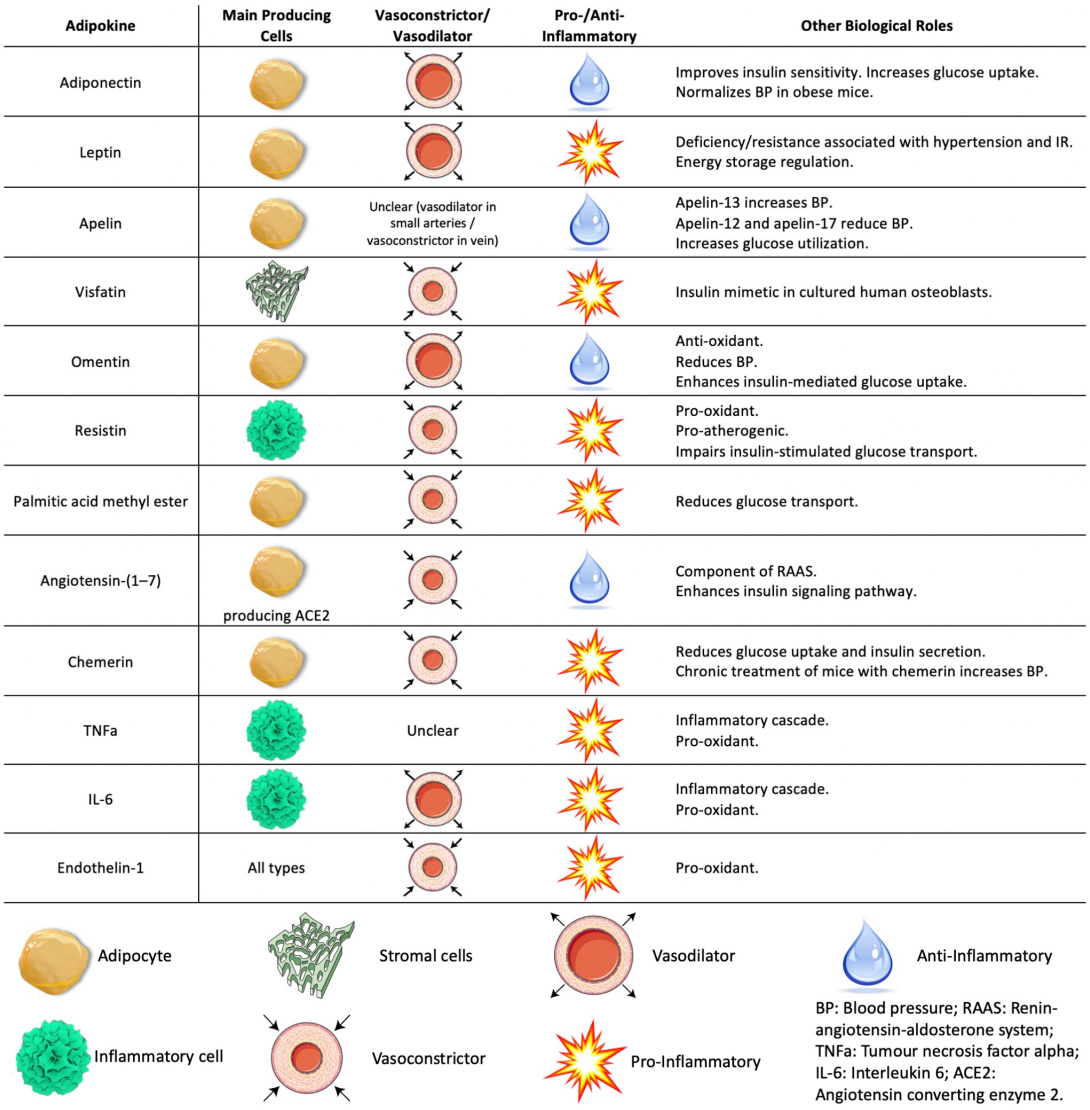


Figure 1.8: Main roles of key adipocytokines secreted by perivascular adipose tissue. Adapted from (Kotanidis & Antoniades, 2021).

of the cardiovascular system in an endocrine manner, after being released into the bloodstream through the adipose tissue microvessels (Oikonomou & Antoniades, 2019). Perivascular fat, on the other hand, can utilize other, more direct routes, so as to affect vascular biology. Given its close anatomical affinity with vessels, PVAT has the unique ability to exert direct effects on the adjacent vascular wall through the paracrine release of bioactive mediators. Furthermore,

PVAT is implicated in a third form of signaling, vasocrine signaling, in which PVAT-derived adipokines can travel through the underlying vascular wall and reach the lumen, thereby being able to circulate in downstream microcirculation and potentially act upon entire vascular beds (Yudkin, Eringa, & Stehouwer, 2005).

Regardless of the route they employ, adipose tissue-derived products influence many aspects of vascular biology, including vascular tone, inflammation, vascular smooth muscle cell migration, endothelial function and vascular redox state (Oikonomou & Antoniades, 2018). It has been shown that the secretome of PVAT contains anti-inflammatory and anti-oxidant components, and it may host defense mechanisms for the vascular wall (Antoniades et al., 2006; Margaritis et al., 2017). Adiponectin induces 5-AMP-activated protein kinase (AMPK) or RACα serine/threonine-protein kinase (AKT)-mediated endothelial nitric oxide synthase (eNOS) phosphorylation acting as a vasorelaxant (Margaritis et al., 2013). Hydrogen sulfide (H_2S) and palmitic acid methyl ester also influence vascular tone, by activating ATP-regulated and voltage-gated potassium channels, respectively (Y. C. Lee et al., 2011; King et al., 2014). PVAT also regulates angiotensinogen expression and the ensuing increase in angiotensin II, which acts on smooth muscle cells in the vessel walls to regulate vasoactivity and blood pressure in a circadian fashion, through the production of the aryl hydrocarbon receptor nuclear translocator-like protein 1 (known as BMAL1) in brown adipocytes (Chang et al., 2018). The anticontractile effects of PVAT include also the uptake and metabolism of vasoactive amines, such as norepinephrine (Ayala-Lopez, Thompson, & Watts, 2017), whereas the gaseous messenger nitric oxide (NO), which is produced by adipocyte or macrophage NOS, exerts paracrine anti-inflammatory effects (D. B. Graham et al., 2018). Finally, adipokines adiponectin and omentin act as antioxidants by inhibiting the activity of the NOX1 and NOX2 isoforms of NADPH oxidase in the vascular

wall, by preventing the activation and membrane translocation of RAC1 and by downregulating the p22phox (also known as CYBA) regulatory protein, consequently reducing superoxide production (Antonopoulos et al., 2015).

On the other hand, PVAT may also contribute to inflammatory processes. Pro-oxidant adipokines such as leptin and resistin, promote activation of NADPH oxidase isoforms and lead to increased vascular oxidative stress, which is a key contributor of vascular inflammation and has been linked with senescence and adverse clinical outcomes (Margaritis et al., 2017). eNOS coupling status may also be modulated by adipose tissue, leading either to the beneficiary production of NO, or to the damaging production of superoxide; chemerin in particular reduces the bioavailability of the enzyme's cofactor tetrahydrobiopterin (BH4) promoting the enzyme's uncoupling and decreasing nitric oxide (NO) production in favor of superoxide (Antoniades et al., 2006; Neves et al., 2014). Vascular inflammation can be promoted further by expression of endothelial cell adhesion molecules, which is induced by adipokines such as visfatin and adipose tissue-derived pro-inflammatory cytokines such as IL-1β and tumor necrosis factor (Oikonomou & Antoniades, 2019). The nuclear factor-κB pathway is yet again implicated as a central signaling pathway exerting a critical role in orchestrating the wide range of pro-atherogenic effects from the PVAT to the vascular wall (Taube, Schlich, Sell, Eckardt, & Eckel, 2012). Moreover, the migration of inflammatory cells into the adventitia, promotes the deposit of collagen and leads to localized upregulation of inflammatory chemokines, TGF-β dependent differentiation of fibroblasts to migratory myofibroblasts and increased vasa vasorum neovascularization (Maiellaro & Taylor, 2007). Also, we have recently shown that WNT5A, a wingless-related integration site (WNT) signaling pathway molecule, secreted by PVAT is implicated in vascular redox signaling in obesity. Circulating WNT5A is increased in obese individuals, who also

present with increased release of WNT5A from PVAT and up-regulation of WNT5A receptors in the arterial wall. These receptors increase arterial sensitivity to the noncanonical WNT signaling pathway and enhance arterial NADPH oxidase activity, increasing superoxide generation and inducing endothelial dysfunction and eNOS uncoupling (Akoumianakis et al., 2019) (Figure 1.9).

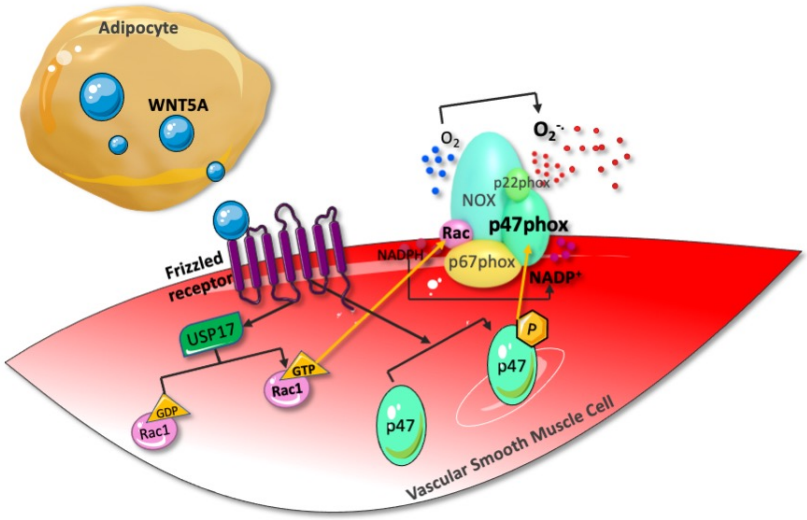


Figure 1.9: Effect of WNT5A on the vasculature. WNT5A is released from PVAT and binds to Frizzled receptors on the arterial wall, activating the noncanonical WNT signaling pathway. This leads to a USP17/RAC1-mediated increase in NADPH oxidase activity and superoxide generation and induces endothelial dysfunction via eNOS uncoupling. Adapted from (Kotanidis & Antoniades, 2021).

In addition, microRNAs, which comprise a vast spectrum of small RNA molecules involved in post-transcriptional regulation, are also produced by PVAT. MicroRNAs have been implicated in several processes, ranging from the recruitment of inflammatory cells, to adipose tissue browning, myocardial fibrosis, atherosclerosis and vascular smooth muscle cell activation,

and their profile changes in response to obesity, insulin resistance and coronary artery disease (Fischer et al., 2017). Furthermore, PVAT-derived exosomes have been shown to promote M1 pro-inflammatory polarization of macrophages and to accelerate atherosclerosis in ApoE$-/-$ mice (Xie et al., 2018). The differential regulation of adipose tissue-derived exosomes and microRNAs in obesity and diabetes mellitus, as well as the proven effects of weight loss and exercise on the levels of specific micro-RNAs in the adipose tissue, has highlighted microRNAs as potential therapeutic targets in obesity-related CVD.

Finally, the immunologic state of adipose tissue, mainly macrophage infiltration and polarization, is described as a crucial regulator of its function, as PVAT inflammation, through the release of a range of cytokines and chemokines, is associated with vascular dysfunction (Lumeng, Bodzin, & Saltiel, 2007). It is becoming evident that adipose tissue, with its highly diverse secretome, can be critical to both health and disease. PVAT exerts anticontractile, anti-inflammatory and antioxidant effects to the adjacent vasculature, while at the same time retaining the ability to undergo remodeling, and adapt an inflamed, pro-oxidant profile, shifting its phenotype from protective to detrimental for the vessels (Kotanidis & Antoniades, 2020a).

1.3.4 Inside-to-outside signals: Vasculature affecting fat

1.3.4.1 Systemic Signals

The concept that adipose tissue is a dynamic tissue that interacts with other systems in the human body is well-known, particularly when it comes to systemic signals (Table 1.1).

Shifts in adipose tissue phenotype and biology are observed in the presence of cardiometabolic disease, including obesity, insulin resistance, diabetes mellitus and inflammation (Fuster, Ouchi,

Table 1.1: Summary of the effects of inside to outside signals on adipose tissue

Systemic Signals

Signal	Effect on adipose tissue	Study
Cardiometabolic disease	Hyperplasia Hypertrophy	(Fuster et al., 2016)
	Adipocytes acquire a dysfunctional, lipid-laden phenotype	(Ketelhuth et al., 2019)
	Inflammatory cells infiltration Macrophage polarisation towards the M1 pro-inflammatory phenotype	(Rutkowski et al., 2015)
	Pericyte activation Secretion of platelet-derived growth factor-b Localised neoangiogenesis	(Onogi et al., 2017)
	Vasomotor dysfunction Capillary rarefaction	(Chadderdon et al., 2014)
	Hypoxia Increased expression of hypoxia-inducible factor 1a Fibrosis	(Pasarica et al., 2009)
	Brown adipose tissue depletion	(Franssens, Nathoe, et al., 2017)

Regional Signals

Regional signal	Model	Effect on perivascular adipose tissue	Study
Endovascular injury	Rodent	Upregulation of MCP-1, TNF-a, IL-6 and downregulation of adiponectin in periadventitial fat 1 day after the injury Accummulation of F4 80-positive macrophages and CD3-positive T cells in periadventitial fat	(Takaoka et al., 2010)
Oxidative stress and release of peroxidation products	Human	Upregulation of PPAR-g and adiponectin in perivascular adipose tissue around saphenous veins and internal mammary arteries	(Margaritis et al., 2013)
Angiotensin II-induced upregulation of IL-6, TNF-a, and IFN-g	Human	Inhibition of preadipocyte differentiation Proliferation of preadipocytes Lower intracellular accumulation of lipid droplets Attenuation shifts in CT imaging	(Antonopoulos et al., 2017)
Drug-eluting stent-induced hyperconstriction	Porcine	Reduced adipocyte diameter Increased CD68-positive and IL-1b positive cells Increased 18F-FDG uptake in in-vivo PET CT imaging	(Ohyama et al., 2017)

Gokce, & Walsh, 2016). The nature of these changes dictates whether adiposity will exert protective or adverse effects in the course of cardiovascular disease pathogenesis. Obesity is characterized by excessive calorie uptake, in response to which the adipose tissue undergoes an increase in adipocytes number (hyperplasia) and/or size (hypertrophy) (Krotkiewski, Bjorntorp, Sjostrom, & Smith, 1983). Pre-adipocytes are mobilized and differentiated into mature adipocytes as part of a traditionally considered healthy mechanism of adipose tissue expansion, whereas at the same time hypertrophy causes adipocytes to acquire a more dysfunctional, lipid-laden phenotype in the setting of adipose tissue inflammation (Rutkowski, Stern, & Scherer, 2015). The latter happens in many chronic diseases such as obesity, diabetes mellitus and atherosclerosis, where the adipose tissue is infiltrated by increasing populations of inflammatory cells, such as lymphocytes (including T helper 1 (TH1) cells and B cells), neutrophils, macrophages and mast cells, whereas the population of eosinophils, TH2 cells and regulatory T cells remains unchanged or reduces (Rutkowski et al., 2015). This balance between the different types of inflammatory cells and immune responses affects also macrophage polarization, with TH2 cytokines promoting the M2 anti-inflammatory macrophage phenotype, while the dominant production of TH1 cytokines (mainly IFN-γ shifts the macrophage phenotype towards the M1 pro-inflammatory type (Fujisaka et al., 2009). The M1 phenotype is also involved in localized neoangiogenesis through secretion of platelet-derived growth factor-β, which activates pericytes (Onogi et al., 2017).

Dysfunction of the expanded adipose tissue in obesity is further characterized by endothelial cell activation with increased expression of adhesion molecules (P-selectin and E-selectin) that promote inflammatory cell infiltration, and vasomotor dysfunction of the vasculature, resulting in capillary rarefaction. The reduced delivery of nutrients and oxygen to the adipose tissue

creates a hypoxic microenvironment that triggers adipose tissue fibrosis, through increased expression of the hypoxia-inducible factor 1α, and eventually promotes further its dysfunction and insulin resistance (Chadderdon et al., 2014; Pasarica et al., 2009). In addition, the escape of chyle from lymphatic vessels into the dysfunctional adipose tissue has been implicated in its phenotypic shifts. Lipids are known to be adipogenic and the leakage of lipid-rich lymph in visceral adipose tissue has been shown to stimulate adipose tissue hypertrophy and ectopic adipose tissue expansion (Escobedo et al., 2016).

Metabolic disease may also alter adipose tissue qualitative composition between the relatively protective BAT and beige adipose tissue phenotypes and the deleterious WAT phenotype. BAT is characterized by increased metabolic activity, thermogenic capacity, and the release of BAT-specific adipokines, which exert beneficial autocrine, paracrine and endocrine effects on peripheral tissues, including the cardiovascular system (Villarroya, Cereijo, Villarroya, & Giralt, 2017). Obesity is associated with lower BAT volumes (Franssens, Hoogduin, Leiner, van der Graaf, & Visseren, 2017). Beiging of WAT - characterized by increased expression of mitochondrial brown fat uncoupling protein 1 (UCP1) in adipocytes - is associated with weight loss and improved insulin resistance, whereas its downregulation in human epicardial adipose tissue leads to increased adipose tissue oxidative stress and dysfunction (Chechi et al., 2017).

Finally, the secretome of adipose tissue is another factor undergoing changes in response to signals from the periphery. Obesity, insulin resistance and diabetes mellitus are linked to a secretory and biochemical profile, consistent with a shift towards a more pro-inflammatory phenotype (Antoniades, Kotanidis, & Berman, 2019). Higher circulating levels of visfatin, chemerin, vaspin and resistin and lower levels of omentin and adiponectin are between the changes occurring. It should be noted though that circulating adipokine levels are not always correlated with

the expression levels in the adipose tissue itself, underlying the existence of complex paracrine mechanisms governing cross-talks in the adipo-vascular axis (Margaritis et al., 2013).

Overall, it becomes evident that adipose tissue has the ability to sense and respond to signals originating from other tissue's pathologies. Diseases with chronicity, such as cancer, congestive heart failure, infectious and inflammatory disease (i.e. tuberculosis, rheumatoid arthritis, Crohn's disease, etc.), as well as advanced age, are characterized by cachexia (Tisdale, 2002). Cachexia refers to a state of chronic low grade inflammation, characterized by a hypercatabolic state leading to unintentional weight loss though lipolysis of adipose tissue (Han, Meng, Shen, & Wu, 2018). Systemic low-grade inflammation suppresses adipose-tissue produced adiponectin levels and abolishes its insulin-sensitizing and anti-atherogenic properties, in humans with or without significant cardiovascular disease (Antonopoulos et al., 2014). Therefore, it is apparent that adipose tissue undergoes changes, ranging from expansion in the presence of high calorie intake in obesity, to atrophy seen in many conditions presenting with cachexia, to transcriptome changes driven by circulating inflammatory molecules. This perception of fat is being highlighted by the so-called obesity paradox. A large-scale meta-analysis including over 30 million individuals showed that the association between BMI and all-cause mortality in the general population can be described as U-shaped or J-shaped (Flegal et al., 2013). The obesity paradox can easily be explained if we take into consideration that despite the fact that excess adipose tissue is associated with reduced survival, significantly reduced adipose tissue in chronic disease (such as cancer, heart failure, renal failure, chronic inflammatory diseases and other conditions) will also lead to poor survival rates. The concept that there is only a positive association between BMI and short-term (5-10 years) survival in the general population is therefore misleading, as it ignores the negative effects of the reduced and dysfunctional adipose tissue in the presence of

chronic disease (Antonopoulos & Tousoulis, 2017; Aune et al., 2016).

1.3.4.2 Regional Signals

Apart from systemic signals, inside-to-outside signalling can occur in a localised manner via a bidirectional cross-talk loop between PVAT and the underlying vascular wall (Table 1.1). This concept has been introduced lately with important implications in our understanding of CVD pathogenesis and diagnosis (Figure 1.10).

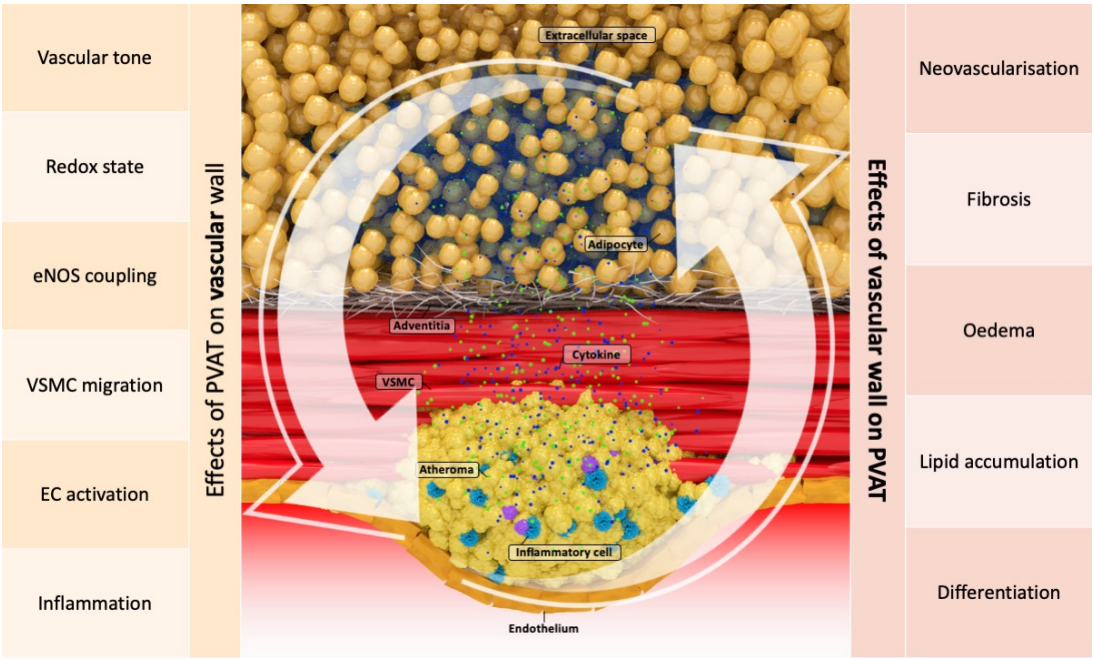


Figure 1.10: Bi-directional interplay between the vascular wall and PVAT. Illustration of the major components of the bi-directional interplay between the vascular wall and fat in the perivascular space. PVAT=perivascular adipose tissue; eNOS=endothelial nitric oxide synthase; VSMC=Vascular smooth muscle cell; EC= Endothelial cell. Adapted from (Kotanidis & Antoniades, 2021).

Early studies underlined that overxpression of p22phox - a subunit of the NOX1, NOX2, and NOX4 isoforms of NADPH oxidase - in vascular smooth muscle cells (VSMC) exaggerates obesity and insulin resistance in mice with high-fat feeding (J. Y. Youn et al., 2014). Intravascular injury, balloon-induced or wire-induced, in mice has been described to produce rapid

phenotypic modifications of the perivascular adipose tissue, through the upregulation of proinflammatory adipocytokines, primarily TNFa (Takaoka et al., 2010). Following these initial observations, we found that increased vascular oxidative stress induces the release of products of lipid peroxidation, such as 4-hydroxynonenal (4-HNE), that diffuse into the perivascular space; adipocytes within PVAT receive these signals, through a process termed "adipose tissue sensing", and upregulate adiponectin's ADIPOQ gene via a peroxisome proliferator-activated receptor-γ (PPARγ) dependent mechanism (Figure 1.11).

Subsequently, adiponectin is released back to the vessel wall, exerting its beneficiary antioxidant and vasoprotective effects, in a protective loop, that concludes a defense mechanism within the proposed bidirectional cross-talk between PVAT and vasculature (Margaritis et al., 2013). Similar links have also been suggested to govern interactions between the myocardium and epicardial adipose tissue. As in vessels, oxidation products from the myocardium lead to PPARγ-mediated upregulation of adiponectin expression and release in the adjacent epicardial fat, which then exerts antioxidant effects on the cardiomyocytes (Aghamohammadzadeh et al., 2012).

In addition, we have more recently reported that inflammation in the human vascular wall triggers the release of inflammatory cytokines, such as TNFα, IL-6 and IFNγ, which also diffuse into the perivascular space. PVAT responds by adopting a "cachexia-type" sequence of biologic events within adipocytes; differentiation becomes suppressed and intracellular lipid formation decreases. Adipocytes get smaller in size as their intracellular lipid content depletes due to an increase in lipolysis and simultaneous decrease in adipogenesis, both resulting from the adverse microenvironment inside the perivascular space caused by vascular inflammation (Antonopoulos et al., 2017). Further to lipolysis and reduced adipogenesis, perivascular edema

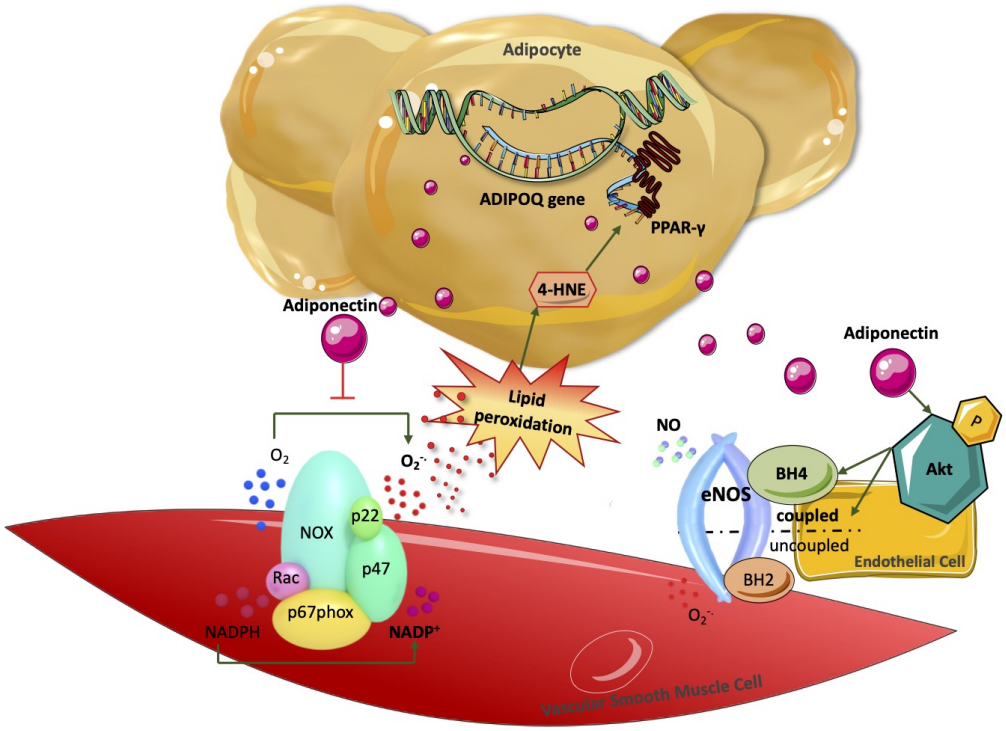


Figure 1.11: Adiponectin upregulation caused by vascular oxidative stress. Enhanced production of superoxide leads to increased local production of lipid peroxidation products such as 4-HNE, which travel into PVAT and up-regulate adiponectin's gene expression via a PPARγ-mediated mechanism. Adiponectin, in turn, is secreted and acts on vascular smooth muscle cells and endothelial cells by inhibiting the activity of NADPH-oxidases as well as through Akt-mediated stimulation of eNOS activity and coupling, resulting in increased production of NO and reduced oxidative stress. PVAT=perivascular adipose tissue; NADPH=nicotinamide adenine dinucleotide phosphate; eNOS=endothelial nitric oxide synthase; BH4=tetrahydrobiopterin; BH2=dihydrobiopterin; NO=nitric oxide; $O_2^{\bullet -}$=superoxide; 4HNE=4-hydroxynonenal; PPARγ=peroxisome proliferator-activated receptor gamma; ADIPOQ=adiponectin. Adapted from (Kotanidis & Antoniades, 2021).

may also appear around the inflamed artery as a result of increased inflammation-induced permeability in the microcirculation and expansion of the interstitial space in the perivascular space. Finally, vascular inflammation has the potential to induce more permanent changes in the surrounding fat, such as fibrosis and neoangiogenesis, which are known to occur in the setting of chronic inflammation (Crewe, An, & Scherer, 2017). Indeed, inflammatory changes of coro-

nary PVAT, as assessed in vivo by 18F-fluorodeoxyglucose positron emission tomography (^{18}F-FDG PET), were significantly enhanced at sites of coronary injury caused by everolimus-eluting stents as compared to untouched control sites in an in vivo porcine model (Ohyama et al., 2017).

All these biological modifications result in the development of a gradient of adipocyte size around the inflamed human coronary artery, with smaller adipocytes closer to the vessel wall that gradually increase to match the baseline size of the rest of epicardial fat adipocytes moving further away from the vessel. At a macroscopic level, these changes can be identified as a gradual shift in the balance between the lipid and aqueous phase in the adipose tissue directly adjacent to the inflamed artery (Antonopoulos et al., 2017). As adipocytes get smaller in size through suppression of differentiation and decrease in intracellular lipid content, the lipid phase of the tissue starts to become depleted and gradually the aqueous phase reflecting localised edema and increased interstitial space becomes more apparent (Figure 1.12). It should be noted though that, although these changes are dynamic and subject to the degree of coronary inflammation, their kinetics are not entirely understood.

However, these observations about macroscopic changes in the PVAT in response to the presence of coronary inflammation and therefore atherosclerosis, have had a substantial impact in highlighting this otherwise neglected adipose tissue depot as a very promising and applicable marker of disease presence in the clinical setting. Taking into account all the above it becomes evident that vascular inflammation is being communicated to the PVAT close to it, which in turn adjusts its biology by entering a state of hypercatabolism and suppressed adipogenesis, leading ultimately to macroscopic phenotypic alterations. The possibility to detect these molecular changes around the inflamed human artery using non-invasive imaging brings up new potential in using PVAT as a "thermometer", to detect and quantify coronary inflammation.

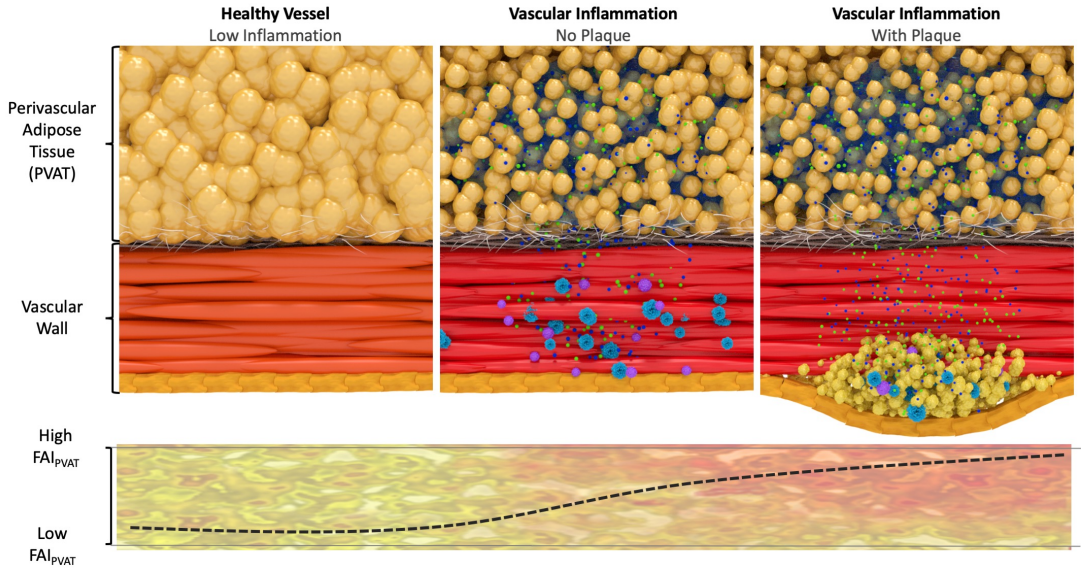


Figure 1.12: Schematic of PVAT's response to vascular inflammation. Morphological appearance of perivascular adipose tissue surrounding healthy and inflamed coronary arteries, depicting the gradient of adipocyte size induced by exogenous vascular inflammation. Adapted from (Kotanidis & Antoniades, 2020b)

1.3.5 Imaging perivascular adipose tissue

Taking into account the fact that it was only until recently that PVAT acquired a clear anatomic definition and more knowledge about its biology became available, this adipose tissue depot has been mainly studied in literature so far as part of epicardial adipose tissue. However, during the last few years interest in this area by the imaging community has sparked and novel techniques and methodologies are being proposed. Adipose tissue imaging has been used for patient risk stratification in clinics and can be visualized by exploiting a wide and diverse range of imaging modalities, which provide quantitative and qualitative information on adipose tissue anatomy.

1.3.5.1 Quantitative imaging features

EAT thickness has been consistently associated with the metabolic syndrome and relative clinical features such as high blood pressure, high levels of low-density lipoprotein cholesterol and insulin resistance (Pierdomenico, Pierdomenico, Cuccurullo, & Iacobellis, 2013). However, the most studied quantitative index is EAT volume, with several large-scale cohorts exploring its significance in atherosclerosis. In low-risk asymptomatic populations, EAT volume, measured on non-contrast CT scans, was associated with the presence of ischemic heart disease, coronary calcification and progression (Mahabadi et al., 2017, 2014). In cohorts consisting of individuals with intermediate cardiovascular risk, higher EAT volume was described to be associated with coronary stenosis, ischemia, and high-risk plaque features (Versteylen et al., 2012; Ito et al., 2013; Bos et al., 2015). Nonetheless, when analyzing data from subjects in high cardiovascular risk, Tanami et al found no correlation between EAT volume and obstructive coronary artery disease or coronary calcification (Tanami et al., 2015), highlighting the fact that the significance of EAT volume in characterizing atherosclerosis is highly dependent on the subject's baseline risk profile and the stage of disease progression. Of note, the SMART (Secondary Manifestations of ARTerial disease) study reported that low EAT attenuation, independently of EAT volume, on CT was associated with coronary artery calcification, indicating that quality features of the adipose tissue are also of importance, bearing the potential to add complementary information to that provided by quantitative measures (Franssens, Hoogduin, et al., 2017).

1.3.5.2 Qualitative imaging features

Evaluation of PVAT inflammation assessed by FDG uptake using positron emission tomography (PET), showed greater standardized uptake values (SUV) in pericoronary fat compared with

other fat depots, while in overweight patients with CAD, a positive correlation between PVAT SUV and respective coronary artery stenosis was described (Mazurek et al., 2017). However, low spatial resolution, high background noise, high exposure to radiation, and low clinical availability are limiting factors for PET imaging, and may restrict its extensive use in low risk populations. Conventional cardiac CT angiography is able to provide information on adipose tissue quality, by analyzing attenuation shifts. In the SMART study, Franssens et al found a negative association between EAT attenuation and age, BMI, waist circumference, visceral abdominal AT, fasting glucose and insulin resistance (Franssens, Hoogduin, et al., 2017). Similarly, in 609 asymptomatic low to intermediate-risk patients, Abazid et al observed a negative correlation between EAT density and coronary calcification independently of EAT volume (Abazid et al., 2017). On the contrary, in a cross-sectional analysis of patients with acute myocardial infarction (MI) and stable CAD controls, Mahabadi et al observed a positive association between EAT attenuation and type I acute MI (Mahabadi et al., 2017), while Hell et al did not report a link between EAT attenuation and myocardial ischemia on SPECT (Hell et al., 2016). These contradictory findings can be attributed to a number of factors, such as small sample size, selection bias and methodological limitations, but the most significant point to be noted here would be that all aforementioned studies derive attenuation data by analyzing EAT as a whole, without taking into account the regional biological - and therefore imaging - variability of adipose tissue in close proximity to the coronaries, stressing the critical need for a standardized CT-based approach for qualitative analysis of PVAT. Towards that end, phenotypic mapping of PVAT has been recently introduced utilizing algorithms constantly evolving though artificial intelligence processes to capture non-invasively PVAT phenotypic alterations, such as reduction in adipocyte size, edema, fibrosis and neovascularization, which have been shown to chaperon

coronary inflammation (Antonopoulos et al., 2017). Fat attenuation index (FAI) mapping, first described in 2017, was derived from studies which demonstrated that inflammatory molecules released from the human vascular wall inhibit adipogenesis and stimulate lipolysis in the adjacent PVAT (Antonopoulos et al., 2017). Several clinical studies have assessed the diagnostic and prognostic utility of FAI in a range of clinical scenarios. In the largest of these studies, which included 3,912 patients undergoing clinically indicated CCTA (CRISP-CT study), FAI mapping improved the prediction of adverse cardiac events beyond traditional risk factors and CCTA metrics, such as the extent of coronary atherosclerosis, coronary calcium score (CCS), and presence of high-risk plaque features (Oikonomou et al., 2018). Further studies have shown that PVAT attenuation can identify culprit lesions in patients presenting with acute myocardial infarction (Antonopoulos et al., 2017), and reliably identify areas of microcalcification and inflammation (Kwiecinski et al., 2019). A new medical device, CaRi-Heart (Caristo Diagnostics, Oxford, UK), has been developed to enable standardization and integrate information on clinical risk factors, coronary plaques, and the degree of coronary inflammation in a way that enables individualized estimation of a patientâs cardiac risk. The prognostic output produced by CaRi-Heart, the FAI-score, demonstrates significant net clinical benefit in two large and independent CCTA populations over and above traditional cardiovascular risk factors (Oikonomou et al., 2021).

1.3.5.3 Dual energy X-ray absorptiometry

Dual energy X-ray absorptiometry (DXA) is a method for measuring bone mineral density and soft tissue composition and is commonly used to calculate body fat mass. It utilizes the absorption of two X-ray beams at different energy levels. Although it is a fairly easy, widely available

and cheap modality, used a method of choice for measuring body composition in athletes, DXA cannot easily provide detailed information on adipose tissue distribution and specific adipose tissue depots (Kaul et al., 2012).

1.3.5.4 Ultrasonography

Echocardiography is an easy, low-cost method for evaluating the thickness of adipose tissue depots accessible to the ultrasound beam. It can provide an easy assessment of epicardial adipose tissue thickness, it is readily accessible in routine clinical practice, but is heavily operator dependent and limited to the two dimensional plane (Iacobellis et al., 2003).

1.3.5.5 Magnetic Resonance Imaging

MRI includes a range of sequences that provide excellent 3D quantification, while combination with proton spectroscopy can give further characterization of adipose tissue. It avoids radiation exposure but involves long scanning times, complex protocols and expensive equipment that may not always be available (Krumm et al., 2018). Importantly its spatial resolution is not enough to allow accurate quantification of epicardial adipose tissue, while it cannot visualize peri-coronary adipose tissue in humans (Nelson et al., 2009).

1.3.5.6 Computed Tomography Imaging

Computed tomography is considered to be the gold standard for three dimensional phenotyping of adiposity, with excellent computer-processed algorithms for segmentation and adipose tissue characterization. It can be combined with CT angiography for PVAT phenotyping and also with PET imaging for quantification of radiotracer uptake and provision of functional information on

inflammatory and metabolic tissue activity. It is widely used and commonly available in clinical practice, and has received a Class I indication by the European Society of Cardiology (ESC) guidelines as a first line investigation of suspected CAD (Knuuti et al., 2020), but it involves radiation exposure (Davidovich, Gastaldelli, & Sicari, 2013). (Table 1.2) presents a comparison of the most commonly used non-invasive modalities for imaging PVAT.

1.4 Radiomic phenotyping

1.4.1 What is radiomics?

As we slowly move towards a big-data dominated era across all facets of scientific research, advances in computational and imaging processing methodologies have rendered medical imaging an ideal field that offers a promising pool of large datasets and registries. Imaging studies in oncology have introduced radiomics to the medical research world with their presence in publication records within cardiovascular research steadily increasing. Radiomics refers to the big data field that focuses on extraction of large amounts of quantitative data from images and their use for machine-learning modelling. Specialized data-characterization algorithms are able to identify patterns of data behavior within the dataset of numbers that comprise an image or a segmented volume, which cannot possibly be perceived by the human naked eye (Gillies, Kinahan, & Hricak, 2015). These patterns are not abstract but rather may be linked with underlying pathology. Imaging studies in cancer patients have linked specific shape- and texture-related patterns within the volume of the tumor to its phenotype and also overall clinical prognosis (Aerts et al., 2014). Figure 1.13 presents a schematic of basic radiomic features and analytical techniques employed in radiomics (Oikonomou, Siddique, & Antoniades, 2020).

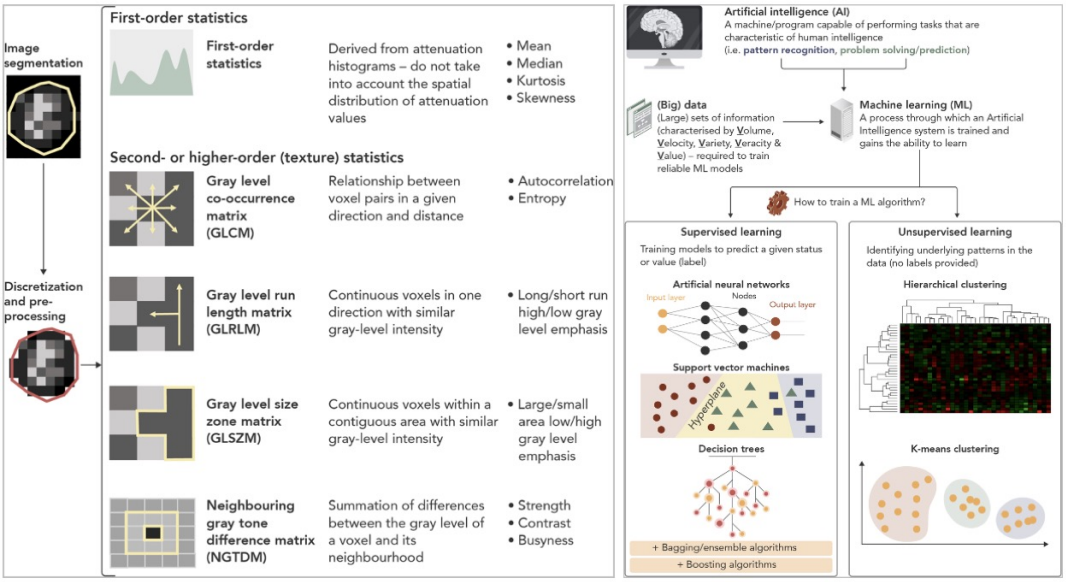


Figure 1.13: What is radiomics? Schematic presenting the different categories of radiomic features extracted from a segmented volume of interest and basic big-data terminology. Higher-order features reflect the unique spatial arrangement of voxels, rather than simple voxel attenuation distribution derived from histogram-based first-order features. Artificial intelligence (AI) describes a programme that mimics "cognitive" functions that are associated with natural intelligence displayed by humans and animals. Machine learning refers to the process through which an AI system is trained to perform "cognitive" functions. There are two broad types of learning used in medicine: supervised, in which different algorithms are used to predict the class or value of a known label, and unsupervised, in which the algorithm itself selects and attributes classes based on the dataset patterns. Reproduced with permission from (Oikonomou et al., 2020)

.

1.4.2 Radiomics in cardiovascular imaging

Cardiac imaging research has also started utilising tools offered by radiomics (D. Dey & Commandeur, 2017). A recent study focusing on vascular wall and plaque characterisation has shown that the metabolic activity of lesions with the napkin-ring HRP can be stratified by radiomic features within the arterial (Kolossvary et al., 2017). We recently performed a large radiotrancriptomic experiment (Figure 1.14) with human adipose tissue biopsies so as to validate the link between radiomics and biology. We tested a range of radiomic features and how

Table 1.2: Comparison of noninvasive adipose tissue imaging modalities

Imaging Modality	Quantitative measures	Qualitative measures	Advantages	Disadvantages
Echocardiography	Thickness		Low cost Wide clinical availability Ease of use	2D-not volumentric High operator dependence No PVAT assessment
CT	Thickness Area Volume	FAI_{PVAT}	High spatial resolution 3D volume Wide clinical availability Coronary CT angiography PVAT characterization	Radiation (and contrast agent) exposure
MRI	Thickness Area Volume	Proton density fat fraction	High spatial resolution 3D volume possible No radiation Proton spectroscopy for functional characterisations	Long scanning duration High cost Low clinical availability No PVAT assessment
^{18}F-FDG PET	SUV		Functional assessment of inflammatory activity	Low spatial resolution Variable myocardial suppression High cost Radiation exposure Low clinical availability

CT: Computed tomography; MRI: Magnetic resonance imaging; 18F-FDG PET: 18F-fluorodeoxyglucose positron emission tomography; SUV: standardized uptake values; 2D: two-dimensional; FAI_{PVAT}: Perivascular adipose tissue fat attenuation index

they correlate with three major aspects of adipose tissue biology: inflammation - using the expression of TNFa gene as marker, fibrosis - evidenced by collagen (COL1A1 gene) expression, and vascularity - reflected by the expression of endothelial marker CD31 (PECAM1 gene). As expected, TNFa expression was most significantly linked with features related mostly to tissue attenuation (captured by the FAI), confirming the concept that attenuation first-order metrics are descriptive of inflammation. Fibrosis and microvascular remodeling were also found to correlate with differential groups of radiomic features mostly inherent to tissue homogeneity and texture, suggesting that radiomic phenotyping can provide a comprehensive evaluation of the biological variation within adipose tissue (Oikonomou et al., 2019).

With these initial observations in mind, we developed a CT specific radiomic signature within the imaging profile of coronary PVAT that incorporates elements not only of inflammation but also permanent fibrotic and microvascular changes, that would enable increased cardiac risk detection. We then applied this new signature, referred to as the Fat Radiomic Profile (FRP), to a population of 1,575 individuals from the CCTA arm of the SCOT-HEART trial. Interestingly, patients with high FRP had a striking 11-fold higher risk for major adverse cardiovascular events, independently of traditional risk factors, presence of coronary artery disease ($\geq$50% stenosis), presence of HRP features, Agatston coronary calcium scoring, and scanner type (Oikonomou et al., 2019). Importantly, FRP was able to capture residual cardiovascular risk in this population offering incremental prognostic information beyond current CCTA-based tools (including Agatston CCS, HRP features and luminal stenosis). Testing FRP on serial CCTA scans from patients with an acute event, it was shown that 6 months after the index event FRP remained unchanged with FAI significantly decreasing towards baseline values (Figure 1.15), as discussed above, suggesting that while FAI is a dynamic inflammatory burden marker,

FRP can detect more permanent structural changes in PVAT (Oikonomou et al., 2019).

However, as with FAI, the reversible or modifiable nature of FRP has yet to be determined in clinical trials or observational studies. Treatment with biologics or even standard of care may have the potential to reverse aforementioned changes in PVAT.

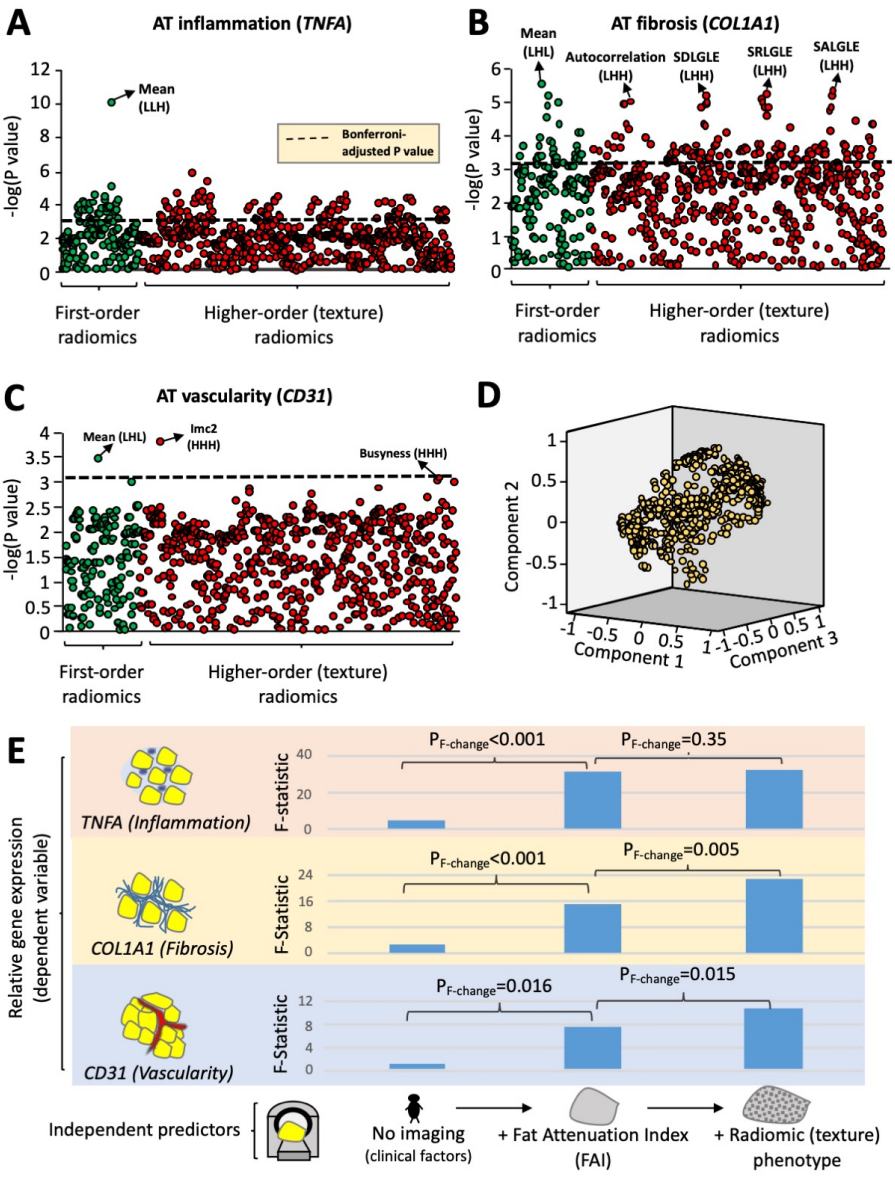


Figure 1.14: Radiomic phenotyping to detect biological hallmarks of dysfunctional adipose tissue. Manhattan plots presenting the strength of association between adipose tissue radiomic features and the relative gene expression of TNFa (inflammation), COL1A1 (fibrosis), and CD31 (vascularity). (D) Component plot of the three principal components of the adipose tissue radiome. (E) Comparison of nested linear regression models with relative gene expression as the dependent variable and (i) clinical risk factors alone (Model 1: age, sex, hypertension, hypercholesterolaemia, diabetes mellitus, and body mass index); (ii) Model 1 + mean attenuation (Model 2); and (iii) Model 2 + PVAT radiome (first three principal components) as the independent predictors. Imc, informational measure of correlation 2; L/H, low/high wavelet transformation; SALGLE, small area low grey-level emphasis; SDLGLE, small dependence low grey-level emphasis; SRLGLE, short-run low grey-level emphasis. Reproduced with permission from (Oikonomou et al., 2019)

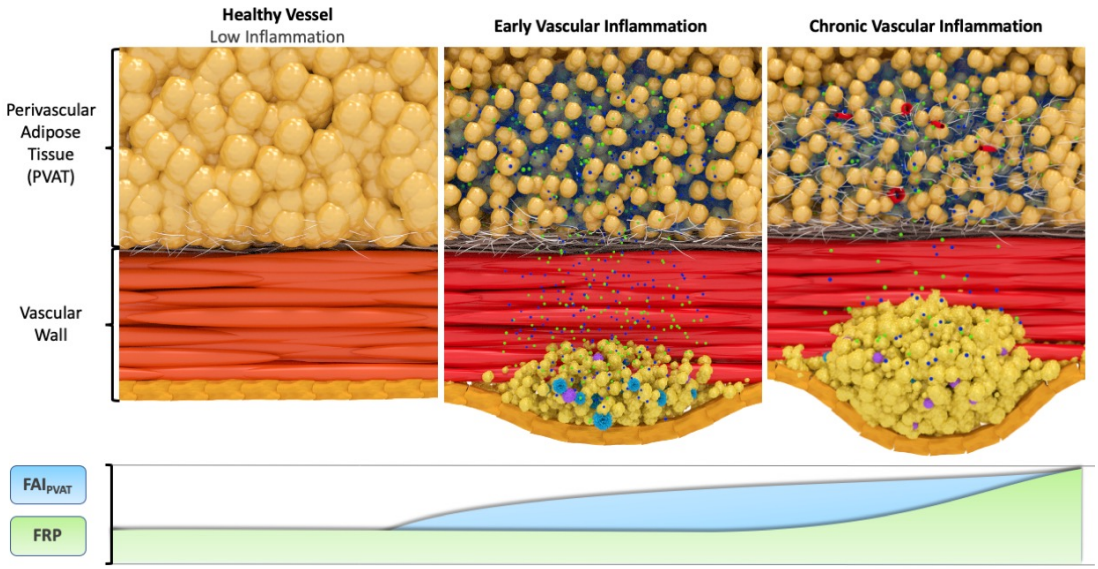


Figure 1.15: Schematic representation of the biology underlying FAI and FRP. Coronary inflammation drives phenotypic changes in perivascular adipose tissue (PVAT), including decreased adipocyte size, differentiation and intracellular lipid content. The novel CT-derived Fat Attenuation Index (FAI), captures weighted three-dimensional attenuation values reflecting biological phenotypic gradients inherent to coronary inflammation. Persistence of vascular inflammation and atherosclerotic disease may lead to further changes in PVAT composition, characterised by increased extracellular fibrosis and neomicrovascularisation. Those changes can be detected by radiomic phenotyping of PVAT using the novel signature Fat Radiomic Profile (FRP). Reproduced with permission from (Kotanidis & Antoniades, 2020b)

.

1.5 Aims and Hypotheses

This thesis is divided in two large sections that attempt to tackle the following two hypotheses:

- Explore the prognostic value of cardiovascular redox state in patients with advanced atherosclerosis.

  More specifically, Chapter 3 aims to:

  - Explore the prognostic value of arterial and myocardial oxidative stress markers in long-term clinical outcomes and all-cause and cardiovascular mortality in patients undergoing cardiac surgery.
  - Investigate the transcriptional profile of human internal mammary arteries to link transcriptional signatures within the vascular wall with redox state and outcome prediction.

- Build a library for quantitative radiotranscriptomics aligning radiomics information of PVAT with vascular inflammation and test it in COVID-19.

  More specifically, Chapter 4 aims to:

  - Utilise radiotranscriptomics to train a radiomic signature in the perivascular space around the aorta and internal mammary arteries visualised in CTA, to reflect the degree of arterial inflammation, as defined by activation of the respective molecular pathways mapped by RNA sequencing in arterial biopsies.
  - Examine the ability of this new radiotranscriptomic signature to quantify the degree of vascular inflammation in COVID-19, together with its prognostic value in detecting the patients at risk for poor in-hospital outcomes.

2 | Methods

This chapter discusses the overview of the study population, participant recruitment process, demographic characteristics of patients enrolled, as well as the background and details of the experimental and data analysis procedures used for this thesis. More extensive details are provided in subsequent chapters regarding the relevant methods and study subsets used for individual parts of this thesis.

2.1 The Oxford Heart, Vessels,and Fat Cohort

2.1.1 Overview

For the purposes of the experimental procedures described in this thesis, I used human samples from the Oxford Heart, Vessels, and Fat (Ox-HVF) cohort. The Ox-HVF cohort consists of a cluster of clinical studies (namely ART Vascular, Bypass Grafts, AdipoRedOx, and ORFAN), which provide synergistic results allowing the deployment of a multi-level strategy to understand the mechanisms of cardiovascular diseases. As each one of the individual studies approaches the issue of cardiovascular disease pathogenesis from a different angle, the Ox-HVF cohort provides a unique and powerful platform. The strength of the cohort is the direct access to human tissue (vessels, myocardial and fat biopsies, DNA, plasma and others), in combination with extensive non-invasive cardiovascular phenotyping that includes cardiovascular computed tomography angiography, ultrasound and others (Figure 2.2).

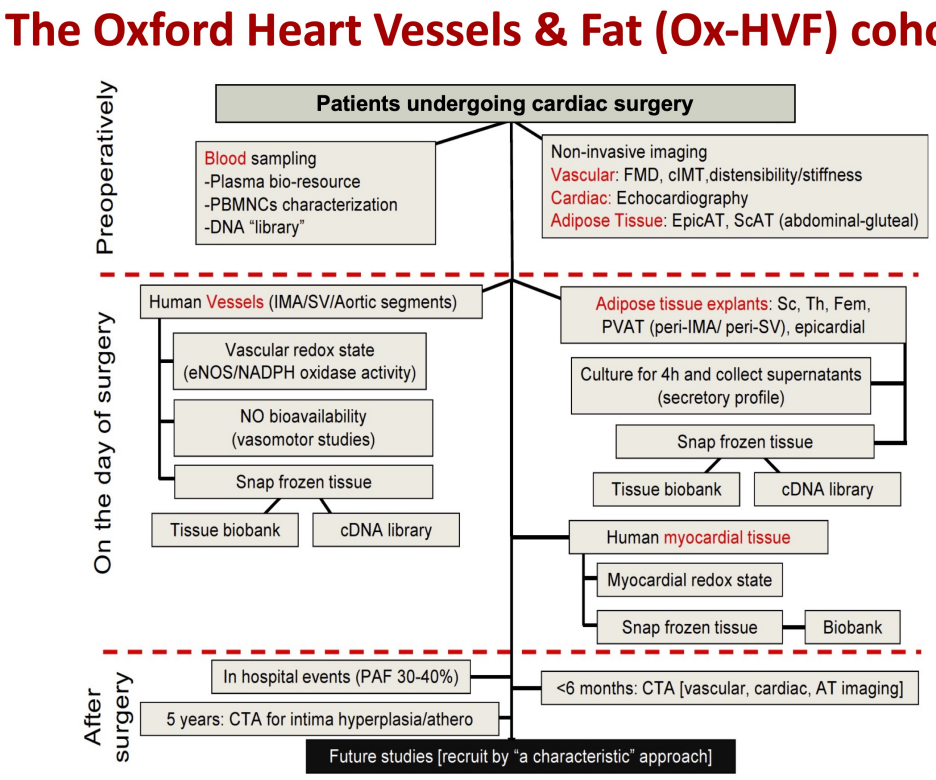


Figure 2.1: The Oxford Heart, Vessels, and Fat (Ox-HVF) cohort. More information about the Ox-HVF cohort can be found on the domain https://oxhvf.com

In this thesis, I mainly used biological material and data from the AdipoRedOx study (REC 11/SC/0140), and imaging and data from the Oxford Risk Factors and Fon-invasive imaging (ORFAN) study (REC 15/SC/0545).

The AdipoRedOx study includes male or female patients aged 18 years or above, diagnosed with cardiac disease and scheduled for coronary artery bypass graft (CABG) surgery or valve replacement/repair surgery, who are willing and able to give informed consent for participation in the study. Exclusion criteria included the presence of active infectious diseases (e.g., hepatitis, HIV), active auto-immune or idiopathic diseases (e.g., rheumatoid arthritis, inflammatory bowel disease, psoriasis), active malignancy, end-stage liver or renal failure (requiring

dialysis) and recent unstable coronary syndrome (within the previous 8 weeks). Patients receiving non-steroidal anti-inflammatory drugs, dietary supplements or antioxidant vitamins were also excluded from the study. The recruitment process can be summarised as follows. Written informed consent is sought from all participants, which is followed by documentation of a full medical history with emphasis on cardiovascular diseases. Non-invasive echo-based imaging studies are also performed upon recruitment for all patients. Prior to surgery, fasting blood is collected and used for plasma and serum isolation, which are then aliquoted and snap-frozen at -80^{o}C for subsequent experiments. During surgery, adipose tissue, vascular and myocardial samples are collected, transferred to the lab as soon as possible and processed on the same day for various bio-assays routinely performed with fresh vascular and adipose tissue samples. Additional tissue samples and blood are snap-frozen and stored at -80^{o}C for future experiments. Surplus fresh tissue is used for specific ex vivo experiments as required.

The ORFAN study recruits healthy individuals aged between 18-99 years, who have been asked by their clinical care team to undergo a cardiac computed tomography (CT) scan at various hospital NHS sites throughout the UK and those who have previously had a clinical cardiac CT scan within the last five years. It also aims to retrospectively collect fully anonymised datasets of CT scans in order to develop new image analysis algorithms and software tools (using artificial intelligence and other approaches) to allow automation of the image analysis processes. All participants have their first CT scan at one of the Radiology Departments of the various selected NHS sites (Oxford University Hospitals NHS Foundation Trust, University Hospital of Leicester NHS Trust, Milton Keynes University Hospital, Royal Brompton and Harefield NHS Trust) as part of their routine clinical care. At this visit a blood sample will be taken for research purposes to measure for blood biomarkers. A second CT scan is then scheduled 3-5 years after the initial

scan at one of the CT scanners within the selected NHS sites. At this visit another CT scan is performed and another blood sample is taken. Study investigators are then be able to make comparisons between the two sets of images and two sets of blood samples to see if there have been any changes overtime.

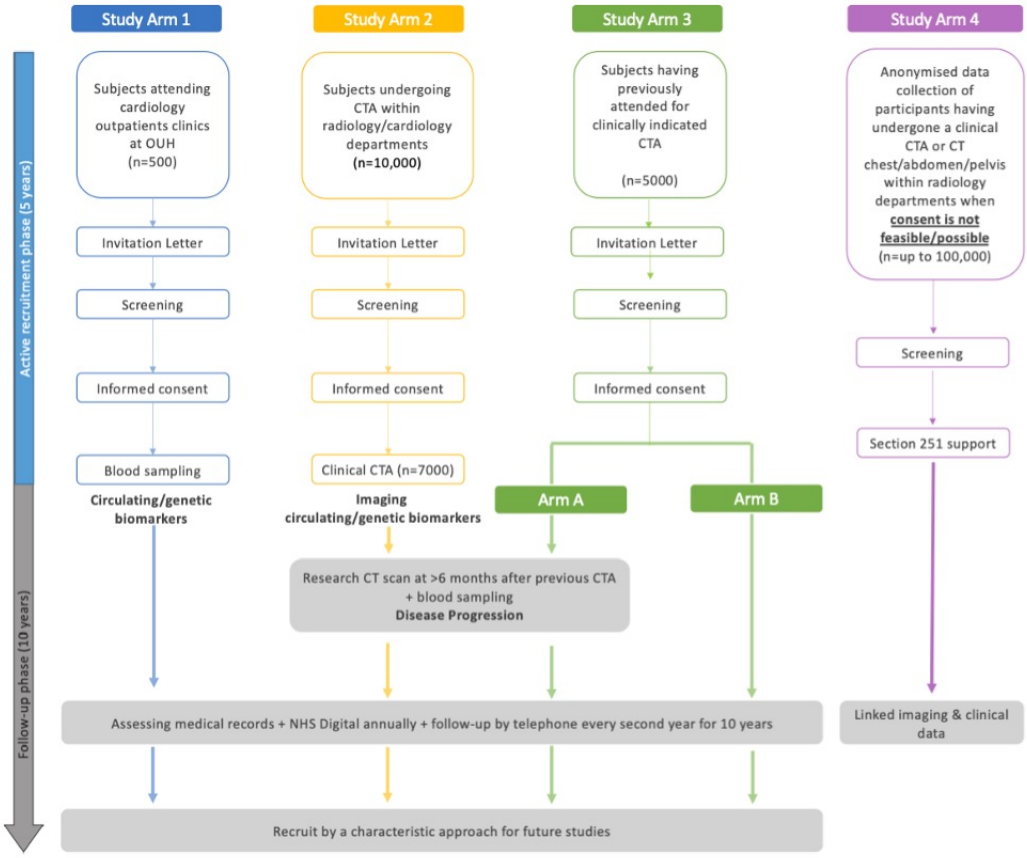


Figure 2.2: The ORFAN study. Flowchart of the ORFAN study. In this thesis, I mainly used data from Arm 4 of the ORFAN study. Adapted from the study's protocol.

2.1.2 Demographic characteristics, risk factor recording, and in-hospital follow-up

Different subsets of the AdipoRedOx and ORFAN studies been used in individual chapters of my thesis. This is due to the fact that not all tissue samples, imaging, or data were available for

all patients and for all types of experiments and analyses. Detailed tables of demographics are provided in subsequent chapters for the study subsets used in each individual chapter.

As part of the routine recruitment process, full cardiovascular history is recorded, including information regarding traditional risk factors for cardiovascular disease (i.e., hyperlipidaemia, diabetes mellitus, smoking status and hypertension), family history of cardiovascular disease, New York Heart Association (NYHA) classification of heart failure, Canadian Cardiovascular Society grading of angina pectoris and cardiovascular medication profile. These are obtained either through the patients' medical records or through direct discussion with the participants. Additional information is sought in medical notes with regards to the angiographic extent of coronary artery disease, left ventricular ejection fraction, previous myocardial infarctions and their territories, previous transient ischaemic attacks (TIA) or stroke, presence of peripheral vascular disease (PVD), previous percutaneous transluminal coronary angioplasty (PTCA) and any other relevant medical conditions. In addition, measurements of body mass index (BMI), waist and hip circumference are performed by nursing staff or the researcher obtaining consent. Following surgery, information regarding Euroscore II, on- or off-pump CABG, clamp/total bypass time (in case of on-pump), number of vein and number of arterial grafts used are routinely obtained from the operative notes filed in the medical records. Participants are also followed-up during their hospitalisation for events such as post-operative atrial fibrillation, need for inotropic support and need for blood transfusion or administration of frozen plasma and platelets. Days spent in the cardiothoracic critical care unit as well as total length of stay are also recorded.

2.1.3 Sample collection

2.1.3.1 Blood sampling

Venous blood samples were obtained from the central line cannula after 8 hours of fasting, on the morning of surgery. The samples were immediately distributed to standard BD Vacutainer tubes. Orange Serum Separator Tubes were used for serum collection, while various anti-coagulants were sued for plasma collections (i.e., Li+/heparin - green, citrate - blue, and K2EDTA - purple). The blood samples were immediately transferred to the Cardiovascular Clinical Research Facility (CCRF) laboratory, Division of Cardiovascular Medicine, University of Oxford, located on Level 1, Heart Centre, main John Radcliffe Hospital. Two K2EDTA vials of whole blood were frozen at -80^{o}C for future DNA extraction. The remainder of the plasma vials were spun at 3,000 g at 4^{o}C for 15 minutes in a Labofuge 400R (Heraeus Instruments) centrifuge. Serum vials were kept at room temperature for 30 min, to allow blood to clot according to serum collection protocol, and were subsequently processed similarly to the plasma tubes after 30min, the tubes were spun at 3,000 g for 15min and serum was collected. Plasma and serum were split into aliquots in barcode-labelled vials and kept at -80^{o}C until further processing.

2.1.3.2 Tissue collection processing

Tissue samples were harvested by the surgeon performing the procedure and transferred in sterile ice-cold Krebs Henseleit buffer (NaCl 120mM, KCl 4.7mM, $CaCl_2$ 2.5mM, $MgSO_4$ 1.2mM, KH_2PO_4 1.2mM, $NaHCO_3$ 25mM, glucose 5.5mM, pH=7.4, oxygenated for 5 min (95% O_2/5% CO_2)).

The following types of samples were collected:

- Pedicle left IMA, with its perivascular adipose tissue (peri-IMA PVAT) attached.
- Long saphenous vein (SV), with its perivascular adipose tissue (peri-SV PVAT) attached.
- Subcutaneous adipose tissue (ScAT), obtained from the site of the sternotomy.
- Thoracic adipose tissue (ThAT), excised from the mediastinal cavity, outside the pericardial sac.
- Femoral adipose tissue (FemAT), which was obtained from the subcutaneous region of the leg incision site.
- Right atrium appendage (RAA), if excised during on-pump CABG or valve procedures.

All surgical samples were obtained before cannulation of the right atrium and before heparin administration. Each sample was always obtained at the same stage of the operation to limit inter-patient variability. All samples were kept on ice during the process and immediately transferred to the laboratory once sample collection was completed. A graphic of human sample collection during CABG surgery is given in Figure 2.3.

IMA samples were placed in a petri dish with a small amount of KHLB and gently flushed with sterile saline using a 25G needle and syringe to remove residual blood and clots. The perivascular adipose tissue surrounding the vessel was carefully dissected using sterile forceps and scalpel. Vessels were carefully cut into rings with a single slice using a 15 scalpel blade. Two IMA rings were used for luminometry experiments to estimate superoxide generation and the specific contribution of NADPH-oxidases and uncoupled eNOS as described later. These experiments were performed on the same day as tissue collection. All adipose tissue samples were cut into separate pieces using sterile scissors and/or scalpel. The pieces were washed in

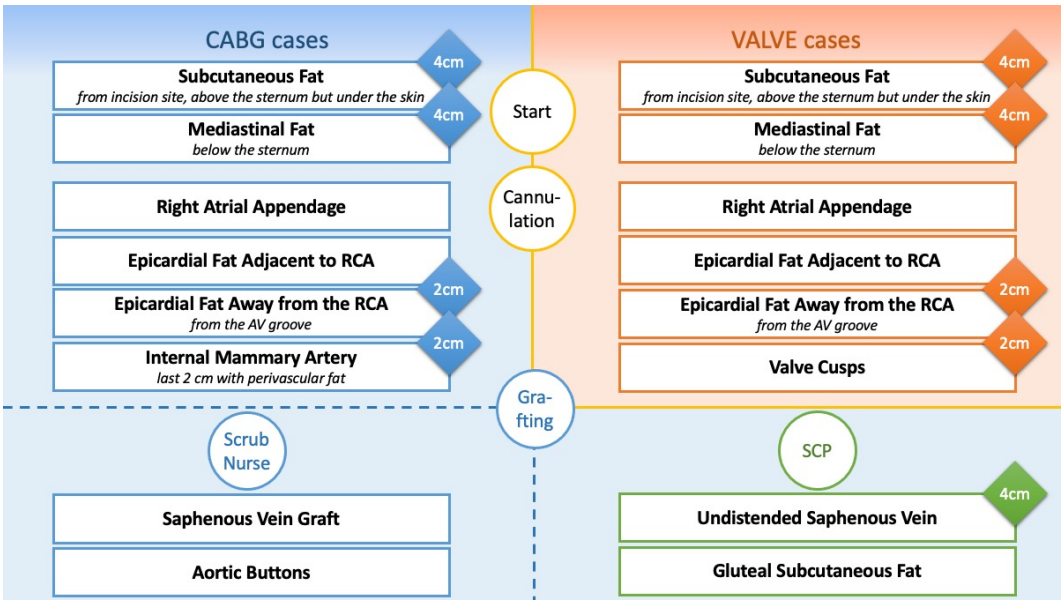


Figure 2.3: AdipoRedOx study: Human samples collection process.

sterile phosphate buffered saline (PBS). Adventitia and connective tissue were removed and discarded. Additional IMA and adipose tissue pieces were kept at -80^{o}C in 1mL phenol (TRI reagent, Sigma) in order to be processed at a later stage for RNA isolation as explained later. Efforts were made to ensure a full set of tissue collection for every patient recruited in the study. However, this was not always achieved, as surgeons were not able to provide samples in certain instances or the samples provided were too small for accurate processing. The different subsets that appear throughout this thesis are a result of this. When adequate samples were provided, processing was always performed and no patients were excluded on this basis.

2.2 Long-Term clinical outcome collection

In order to collect long-term clinical outcome data on the Ox-HVF cohort, I led and coordinated an application for a Data Sharing Agreement between the University of Oxford and NHS Digital. NHS Digital is the trading name of the Health and Social Care Information Centre, which is the

national provider of information, data and IT systems for commissioners, analysts and clinicians in health and social care in England, particularly those involved with the National Health Service of England. Three patients from the Ox-HVF cohort were lost to long term follow up because they either withdrew or had not initially consented to their information being processed for long-term follow-up by NHS Digital.

2.2.1 Studies involved

I worked on a DSA application all studies involved in the Ox-HVF cohort cluster. More specifiacally, those include:

i. The Arterial Revascularisation Trial: Vascular sub-study (ART Vasc) (November 2004 to 2017; REC: MREC04/03/006) compares coronary artery bypass grafting with a single internal mammary artery (IMA) to surgery with bilateral internal mammary arteries. 258 patients undergoing coronary artery bypass grafting surgery at the John Radcliffe Hospital, Oxford were enrolled to the study. ART Vasc study is no longer recruiting. Data collection continues through access to patient's medical records, extracting data from both the local Hospital archive and the NHS Digital records.

ii. The Vascular Properties of Bypass Grafts (Bypass Vascular study) (January 2005 to current; REC: 04/Q1605/95) aims to compare measures of vascular function with post-operative clinical outcome after cardiac surgery. The inner lining of a person's arteries is made up of cells (specifically endothelial cells) that can control how the artery stretches or dilates. The measure of how well this mechanism works is called "endothelial function". The term "endothelial dysfunction" is used to describe changes in the in the inner lining of the artery

to a state that can lead to disease progression and atherosclerosis.

iii. The Bypass Vascular Study invited patients undergoing coronary artery bypass graft surgery at the John Radcliffe Hospital to participate in further investigation of their endothelial function to help better understand why some bypass grafts work better than others and how the function of them could possibly be improved in the future. 231 patients were successfully enrolled to the study. The Bypass Vascular Study is no longer recruiting. Data collection continues through access to the patient's medical records and extracting data from NHS Digital.

iv. The AdipoRedOx study (15/09/2011 to current; REC: 11/SC/140), aims to investigate the mechanisms by which the fat tissue, the vascular tissue and the heart muscle interact and the University of Oxford aim to explore whether aspects of this interaction can predict the outcomes of coronary artery bypass grafting operation (CABG). The AdipoRedOx study is actively recruiting until 2020 and will follow participants up until 2030.

v. The controls of the cohort come from the ORFAN sub-study (11/10/2015 to current; REC: 15/SC/0545). This aims to recruit individuals with risk factors but not advanced coronary artery disease, serving as controls to the heavily diseased populations of the other three sub-studies, and ultimately as the validation cohort for the predictive and prognostic value of any biomarker developed for early cardiovascular disease detection.

2.2.2 Processing activities prior to data retrieval

I include in this subsection an extract from the DSA drafted by myself. The "University of Oxford" party reflects my research group:

"The University of Oxford will send a single request file containing the whole Ox-HVF cohort whose HES-Mortality linked data is being requested. This will be done via the NHS Digital Secure Electronic File Transfer System (SEFT). This request file will contain study participant's identifying information including NHS numbers, date of birth and postcodes (minimum data required for high accuracy HES-Mortality linkage) along with the University study ID that was assigned to them on enrolment to the relevant study. This University study ID contains no personal data and is not directly identifying in isolation, for example 'R123', however as this is a linking file it will be stored on the Medical Sciences Division, University of Oxford High Compliance System that has restricted access and numerous levels of security in place.

NHS Digital will send back identifiable data, whereby the requested outcome data will be returned without the study ID but with a newly assigned NHS Digital ID. NHS Digital will provide a separate code break/bridging file that matches their NHS Digital ID to the internal University study ID to enable the Chief Investigator to identify participants to each study and will not contain identifying data such as names, hospital numbers or date of birth. This system reduces the risk of re-identification as no identifying data is being received with the outcome data. Furthermore, when the data is received from NHS Digital the Chief Investigator will delete the linking request table that was originally sent to NHS Digital and the code break/bridging file. At this point the analysts will only have access to the pseudonymised output data with no ability to link it back to the study participants identifying information held on the high compliance server.

Any computer with access to the aforementioned high compliance network that contains the linking database/request table is not only password protected but also situated in a swipe card-secured area of the Department (with restricted access to authorised individuals and it is

carefully controlled). Users' activity on the high compliance network is monitored and actions such as copying, pasting, screenshotting, and printing are prohibited, so as to maximise security and data protection. No record-level data is being provided to a third party and only aggregated data will be publicised/provided to third parties. No patient identifiable information is extracted out of the high compliance network.

If applicable, information stored on laptop computers of the study investigators will contain additional password protection pertaining to relevant documents; this will be in addition to all computers being password protected. All data received from NHS Digital will not contain subject-identifiable material, and will be stored in a pseudonymised form.

Access to the data provided will be given only to the study investigators, within the University of Oxford, and no third parties will have access to this information. The Investigators will be involved in reviewing drafts of the manuscripts, abstracts, press releases and any other publications arising from the study. The data will be used for research only and not be used to create indicators showing the performance of any organisation. All outputs will only contain aggregated data with small numbers suppressed in adherence to the HES analysis guide.

All organisations party to this agreement must comply with the Data Sharing Framework Contract requirements, including those regarding the use (and purposes of that use) by "Personnel" (as defined within the Data Sharing Framework Contract i.e. : employees, agents and contractors of the Data Recipient who may have access to that data). The data will only be used for the purposes described in this agreement. No data will be shared with 3rd parties. No data will be used for commercial purposes."

2.2.3 Processing activities post data retrieval

Following the secure retrieval of raw data files by NHS Digital, I went throught a list of processing steps so as to convert the data to an analysable format. First, I quality checked all files to ensure inclusion of all cohort patients. Then, I developed scripts that enabled me to match the study IDs with the unique entry identifiers used by NHS Digital.

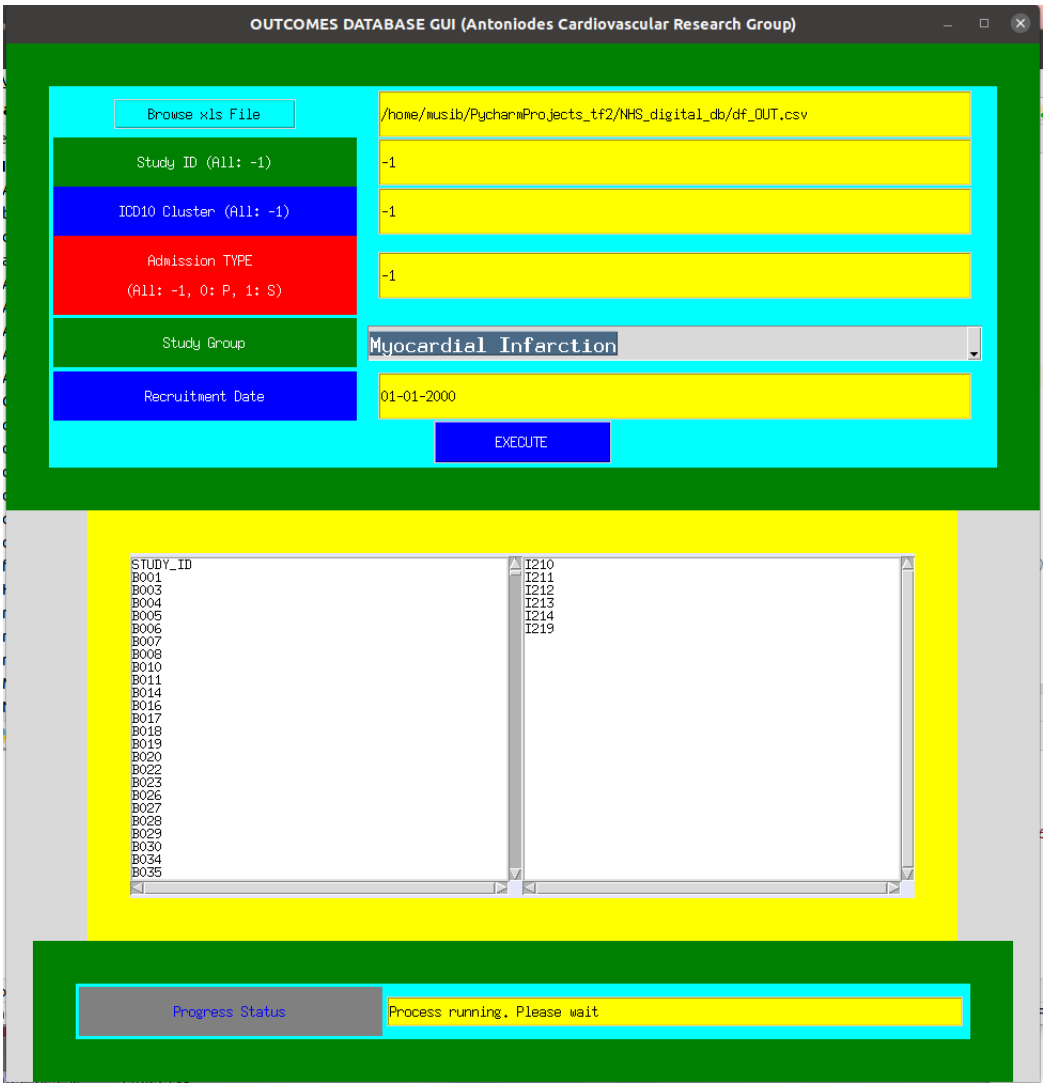


Figure 2.4: The NHS Digital outcomes script GUI. Screenshot of the graphical user interface (GUI) for the script enabling extraction of every possible ICD10 code. Provided by Musib Siddique.

In order to code disease NHS Digital uses the ICD10 coding system. For the mortality dataset I extracted the reason for death in the form of an ICD10 code and used the lists available in Table 2.1 and Table 2.2 to determine the cardiovascular and cardiac mortality endpoints respectively. Date of surgery was used as the date of recruitment to each study. Censoring was done either at the date of an event, or at the date of death, or at 14 March 2020, which is the last date of available data received. These dates were then used to calculate the follow-up time for each desired endpoint, simply by subtracting the most recent from the earliest date.

Table 2.1: ICD10 codes included in the cardiovascular mortality endpoint

ICD10 code	Explanation
I059	Mitral valve disease, unspecified
I119	Hypertensive heart disease without (congestive) heart failure
I120	Hypertensive renal disease
I219	Acute myocardial infarction, unspecified
I249	Acute ischaemic heart disease, unspecified
I251	Atherosclerotic heart disease
I255	Ischaemic cardiomyopathy
I259	Chronic ischaemic heart disease, unspecified
I269	Pulmonary embolism without mention of acute cor pulmonale
I272	Other secondary pulmonary hypertension
I330	Acute and subacute infective endocarditis
I340	Mitral (valve) insufficiency
I350	Nonrheumatic aortic valve disorders
I359	Aortic valve disorder, unspecified
I48	Atrial fibrillation and flutter
I489	Unspecified atrial fibrillation and atrial flutter
I509	Heart failure, unspecified
I619	Intracerebral haemorrhage, unspecified
I639	Cerebral infarction, unspecified
I64	Stroke, not specified as haemorrhage or infarction
I710	Dissection of aorta [any part]
I713	Abdominal aortic aneurysm, ruptured
I739	Peripheral vascular disease, unspecified
I803	Phlebitis and thrombophlebitis of lower extremities, unspecified

For the admitted patient care datasets I developed a script with colleague Musib Siddique

Table 2.2: ICD10 codes included in the cardiac mortality endpoint

ICD10 code	Explanation
I059	Mitral valve disease, unspecified
I119	Hypertensive heart disease without (congestive) heart failure
I219	Acute myocardial infarction, unspecified
I249	Acute ischaemic heart disease, unspecified
I251	Atherosclerotic heart disease
I255	Ischaemic cardiomyopathy
I259	Chronic ischaemic heart disease, unspecified
I330	Acute and subacute infective endocarditis
I340	Mitral (valve) insufficiency
I350	Nonrheumatic aortic valve disorders
I359	Aortic valve disorder, unspecified
I48	Atrial fibrillation and flutter
I489	Unspecified atrial fibrillation and atrial flutter
I509	Heart failure, unspecified

that enabled me to identify each individual hospital spell for each patient, and determine the date of the spell as the censoring date for each particular diagnostic ICD10 code. The field "DIAG01" was used as the primary admission diagnosis to signify the reason for each spell. A list of all available variables in the raw datasets is available in Appendix A. A screenshot of the graphical user interface (GUI) of the script enabling extraction of combinations of diagnostic codes from the database is available in Figure 2.4.

Despite creating a database for the Ox-HVF cohort that includes every possible ICD10 code admission, for the purposes of this thesis, I focused on three particular diagnostic groups: myocardial infarction, stroke, and heart failure. More specifically, the following ICD10 codes were used:

- Myocardial infarction: I21 and all derivatives (I21.0 to I21.9)
- Heart failure: I50 and all derivatives (I50.0 to I50.9)

- Stroke: I61, I63, I64 and all their derivatives

Combining this information with mortality data I was able to construct a series of composite endpoints that are presented throughout this thesis, with the overarching on being MACE, which included cardiovascular mortality, non fatal myocardial infarction, non fatal stroke, and first admission for heart failure.

As for the critical care datasets, I first wrote a script to connect each hospital admission to any possible accompanying admission to the intensive care unit (ICU), and then identified the ICU admissions that were unplanned (i.e. not part of post-surgical care for example) to include in my downstream analyses.

2.3 Measurement of superoxide production

Vascular $O_2^{\bullet -}$ was routinely measured in intact, longitudinally opened vascular rings by lucigenin (5μM) enhanced chemiluminescence based on previously published methods (Margaritis et al., 2013). Lucigenin is able to produce chemiluminescence upon reacting with $O_2^{\bullet -}$ anions, and measurement of this chemiluminescence can be used as a surrogate of $O_2^{\bullet -}$ levels in the system measured (Munzel, 2002). The underlying mechanism is believed to include one-electron reduction of lucigenin (LC^{2+}) to lucigenin cation radical $LC^{\bullet +}$, which then reacts with $O_2^{\bullet -}$ to generate light (Vasquez-Vivar, 1996):

- $LC^{2+} + e^- \rightarrow LC^{\bullet +}$
- $LC^{\bullet +} + O_2^{\bullet -} \rightarrow \text{products} + \text{chemiluminescence}$

Multiple studies have concluded that lucigenin chemiluminescence is one of the most

sensitive methods of $O_2^{\bullet -}$ quantification (Munzel, 2002). On the other hand, the specificity of this method has been questioned because of the potential ability of lucigenin itself to generate $O_2^{\bullet -}$ via a mechanism described as redox cycling, where lucigenin (in concentrations greater than 20μM) reacts with oxygen to produce $O_2^{\bullet -}$ (Munzel, 2002; Guzik & Channon, 2005). However, its usefulness as a means of $O_2^{\bullet -}$ quantification when used at low concentrations (such as 5μM) has since been confirmed (Guzik & Channon, 2005). Therefore, lucigenin enhanced chemiluminescence with 5μM lucigenin remains a sensitive and specific method of $O_2^{\bullet -}$ quantification where the redox cycling phenomenon is not relevant.

The use of intact vascular segments instead of homogenates was selected on the basis of validation experiments previously run in my group reporting a strong correlation of the readouts recorded in intact tissue versus homogenates from same patients (Antonopoulos et al., 2015), with the additional benefit of preserving the structural heterogeneity and cell type separation observed within the vascular wall, yielding more physiological responses.

2.3.1 Quantification of baseline superoxide readout

In this thesis, lucigenin (5μM) enhanced chemiluminescence was the main vascular $O_2^{\bullet -}$ quantification method used routinely for both the baseline phenotyping of vascular redox state in Ox-HVF patients. This was achieved on a single-tube FB12 luminometer set to 37^{o}C to mimic the in vivo situation. Vascular segments were equilibrated in Krebs HEPES buffer (KHB, NaCl 99mM, KCl 4.7mM, $MgSO_4$ 1.2mM, KH_2PO_4 1mM, $CaCl_2$ 1.9mM, $NaHCO_3$ 25mM, Glucose 11.1mM, NaHEPES 20mM) at 37^{o}C with 95% O_2/5% CO_2 for a pre-determined duration of 20 minutes. KHB with lucigenin was added in the luminometry vial and the stable background instrument signal was recorded. Vascular rings were then added in the luminometry vial and

the new stable signal was recorded after plateau achievement. The final readout was calculated after subtracting the background signal from the baseline signal and expressed per mg of tissue. This signal reflects the baseline vascular $O_2^{\bullet -}$ production.

2.3.2 Quantification of NADPH-stimulated superoxide readout

To further increase the specificity of the assay and separate the isolated contributions of individual enzymatic $O_2^{\bullet -}$ sources to the overall baseline vascular $O_2^{\bullet -}$ production, additional stimulation and/or inhibition techniques were employed as described previously (Margaritis et al., 2013). To evaluate the contribution of NADPH-oxidases, I stimulated the vascular segments with NADPH at a supra-physiological concentration of 100μM after recording the baseline signal, resulting to saturation of the NADPH-oxidases molecules. The recorded luminescence signal was drastically amplified with this intervention, acting as a chemical surrogate marker of NADPH-oxidases activity. The final NADPH-stimulated readout was calculated after subtracting the background signal and expressed per mg of tissue.

2.3.3 Quantification of Vas2870-inhibitable superoxide readout

NADPH is a substrate mainly, but not only, for NADPH-oxidases. Therefore, I also routinely used Vas2870 400μM 30min, an established irreversible inhibitor of NADPH-oxidases, to inhibit the NADPH-stimulated signal (Figure 2.5). This intervention typically resulted in a 65% inhibition of the NADPH-stimulated signal. The Vas2870-readout was calculated by subtracting the Vas2870 30min signal from the NADPH-stimulated plateau and expressed per mg of tissue.

The vascular NADPH-stimulated and Vas2870-inhibitable signals are highly correlated in AdipoRedOx cohort (Figure 2.6), confirming that NADPH-oxidases are not the only, but the

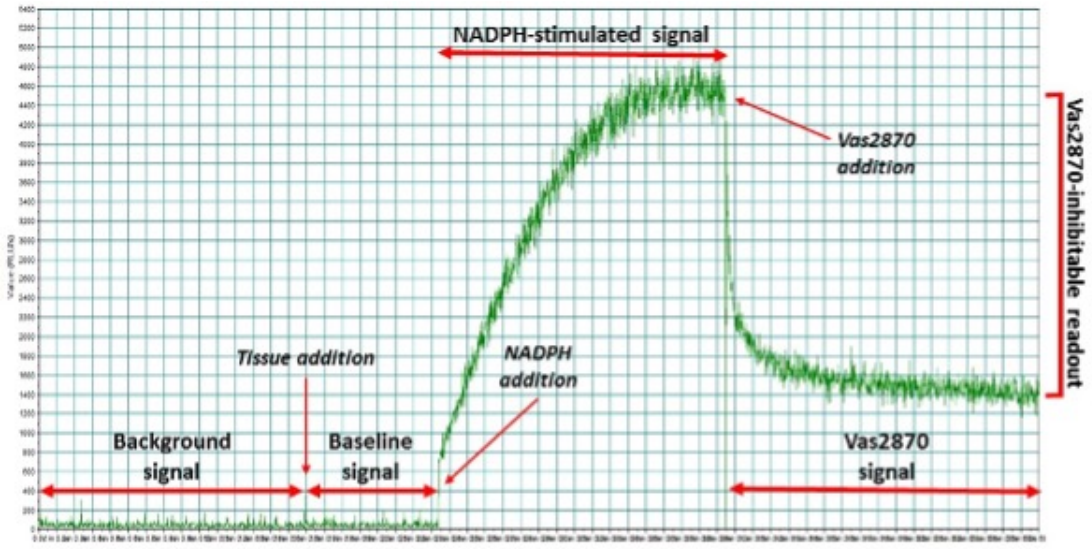


Figure 2.5: Representative superoxide $O_2^{\cdot -}$ traces. The background signal is first recorded, which contains krebs hepes buffer plus lucigenin 5μM in the luminescence vial. Vascular tissue addition results in a signal increase, which corresponds to the baseline (unstimulated) tissue signal. Subtraction of the background from the tissue signal yields the baseline readout, which upon tissue mass correction reflects the baseline production of $O_2^{\cdot -}$ produced per mg of human vascular tissue. Following the recording of the background and the baseline tissue signal, NADPH 100μM is added in the reaction vial. This supra-physiological concentration saturates all NADPH-utilising catalytic enzyme sites, resulting in a massive increase of $O_2^{\cdot -}$. This corresponds to the NADPH-stimulated signal. The corrected NADPH-stimulated readout is then calculated by subtracting the background from the NADPH-stimulated signal, and is finally expressed per mg of vascular tissue. Considering that NADPH-oxidases are the main enzymes utilising NADPH, this readout is believed to reflect the activity of NADPH-oxidases in the human tissue sample tested. After, Vas2870 400μM is added in the reaction vial to specifically inhibit NADPH-oxidases. This results in a reduction of the real-time from its NADPH plateau, corresponding to the Vas2870 signal. Subtraction of the Vas2870 30min signal from the NADPH-plateau corresponds to the Vas2870-inhibitable readout, namely the fraction of the NADPH-stimulated signal that is inhibited by Vas2870 and thus comes directly from NADPH-oxidases. This is expressed per mg of tissue and reflects the vascular NADPH-oxidases activity. Reproduced from (Akoumianakis, 2019)

single most important enzymes using NADPH as a substrate in human vascular tissue.

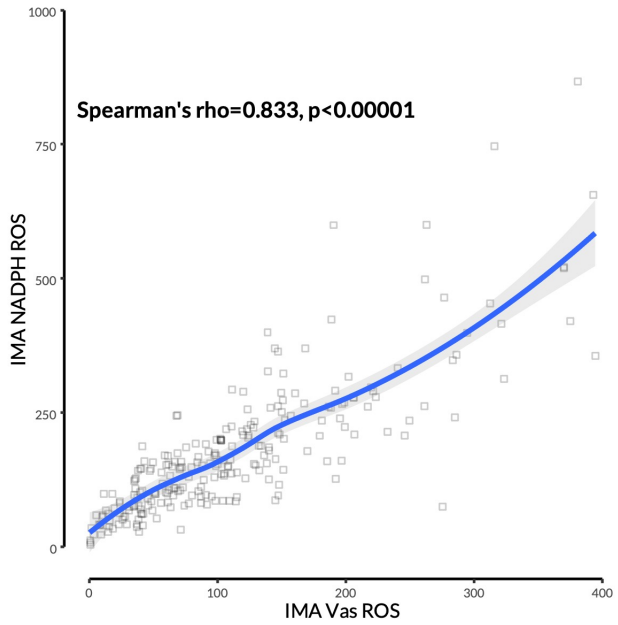


Figure 2.6: NADPH-stimulated and Vas2870-inhibitable superoxide ($O_2^{\cdot -}$) correlation. The NADPH-stim. readout was significantly and strongly correlated with the Vas2870-inh. readout in internal mammary artery. ROS: Radical oxygen species ($O_2^{\cdot -}$).

2.4 Gene expression studies

2.4.1 RNA isolation purification

Samples were kept in 1mL phenol (TRI reagent, Sigma) at -80^{o}C until processed. RNA was separated by phenol:chloroform extraction and purified by an automated magnetic beads based method, using the MagMAX MirVana total RNA isolation kit (Thermo Fisher Scientific) on a KingFisher flex magnetic particle processor.

Samples were thawed on ice and homogenised for 1min using a pre-cooled Polytron homogeniser (Kinematica AG) or for 3min using a bead shaker. Chloroform was added to the homogenates (200μL for a 1:5 chloroform:phenol ratio). Samples were vigorously shaken by hand for 1min, then left to rest at room temperature for 3min, and finally spun at 13,300 rpm

for 15 min, at 4^{o}C. 500μL of the clear, aqueous phase containing the RNA were then transferred in deep 96-well plates and mixed with 300μL of isopropanol and 20μL of beads binding mix. Additional 96-well plates were prepared for washing, DNase treatment, release of RNA from the magnetic beads and elution. All plates were mounted on the KingFisher flex magnetic particle processor and RNA purification was performed in an automated way. At the end of the process, purified RNA quality and quantity were determined using a Nanodrop© ND-1000 Spectrophotometer.

2.4.2 Reverse transcription of RNA - cDNA library creation

RNA was reverse-transcribed to cDNA using the SuperScript VILO master mix (Thermo Fisher Scientific) according to the manufacturer's instructions. Up to 1μg of RNA was reverse-transcribed at every reaction. Reaction conditions were as follows: 25^{o}C for 10 minutes (primer extension step), 42^{o}C for 2 hours (cDNA synthesis step) and finally 5 min at 85^{o}C (reverse transcriptase inactivation step). Part of the cDNA was used to create 100Î¼L of diluted working cDNA plates that were subsequently used for gene expression assays. TE buffer (10mM Tris HCl, 1mM EDTA, pH=8.0) was used as diluent and the working plate cDNA concentration was 1.85ng/μL. Another part of the cDNA of all samples across the library was pulled together to generate a standard sample which was then used for the analysis of the gene expression assays as described below. The remainder of the cDNA was snap-frozen at -80^{o}C and stored as stock.

2.4.3 Gene expression studies using quantitative PCR

Gene expression assays were performed by inventoried TaqMan probes (Applied Biosystems). Quantitative PCR reactions were run in triplicates in 384 well plates using 5ng of cDNA per

reaction (2.7μL of cDNA, 3.0μL of TaqMan gene expression master mix and 0.3μL of TaqMan probe per reaction). A standard curve with serial dilutions (1:10, 1:25, 1:50, 1:100 and 1:200) of the cDNA standard mentioned previously was run in individual plates to calculate the plate amplification efficiency. Runs were performed on a QuantStudio 7 Flex real-time PCR system (Thermo Fisher Scientific). The analysis of the results was performed using the Pfaffl method (Pfaffl, 2001), where the target gene expression was corrected for an endogenous normalising gene and finally expressed relative to the highest standard which was run on every plate, minimising the between-plates variability. All probes displayed an efficiency ranging from 1.85-2.05 and all standard curves had R^2>0.97 upon linear curve fitting. Table 2.3 presents a list of all probes used for this thesis.

Table 2.3: List of TaqMan probes used in this thesis

Target Gene	TaqMan Probe ID
Human TNF	Hs00174128_m1
Human COL1A1	Hs00164004_m1
Human CD31	Hs01065279_m1
Human S100A8	Hs00374264_g1
Human S100A9	Hs00610058_m1
Human TNFAIP3	Hs00234713_m1

2.4.4 RNA sequencing

For RNA sequencing, the QuantSeq 3' mRNA (Lexogen) library preparation kit was used. All samples were sequenced as part of a large multiplex pool on an Illumina NovaSeq 6000 system producing 150bp paired-end reads. RNAseq read pairs were split and only read 1 was used for alignment and quantification, appropriate for the library preparation protocol used. After initial poor mapping results with full-length 150bp reads, reads reduced to 75bp and trimmed for adapter and low-complexity sequence using fqtrim v0.9.5 (Pertea, 2015) were aligned to

Homo sapiens reference genome, GRCh37 using Hisat2 version-2.0.4 (Kim, Langmead, & Salzberg, 2015). Gene annotation files were downloaded in GTF format from Ensembl, release 76 (Cunningham et al., 2015). Reads mapping to annotated exon features were quantified with featureCounts (Liao, Smyth, & Shi, 2014), part of subread-v1.5.0 (Liao, Smyth, & Shi, 2013), using default parameters and keeping all aligned reads including potential duplicates (due to the 3' protocol). Quality metrics for aligned reads were estimated using CollectRnaSeqMetrics, implemented in Picard tools v1.92 (*Web Page*, version at 10.01.2016). The raw count tables produced by featureCounts were imported in R Statistical Software (*Computer Program*, 2013) for further processing and analysis using in-built functionality and relevant packages as detailed below.

2.5 Computed Tomography Angiography Acquisition Protocols

2.5.1 Coronary Computed Tomography Angiography (CCTA) Acquisition Protocol

Participants underwent CCTA using a 64-slice scanner (LightSpeed Ultra, General Electric), as previously described (Antonopoulos et al., 2017). Heart rate was optimised using intravenous injection of beta-blockers and sublingual glyceryl-trinitrate (800ug) was also administered to achieve maximum coronary vasodilatation. A non-contrast prospectively ECG triggered axial acquisition CT scan was obtained (0.35 sec rotation time, 2.5 mm axial slice thickness, 20 mm detector coverage, tube energy of 120 kV and 200 mA) with the carina and the diaphragm used

as cranial and caudal landmarks respectively. Lung field of view was extended to cover the entire thoracic soft tissue (for subcutaneous adipose tissue analysis). CCTA was performed following intravenous injection of 95ml of iodine based contrast medium (Niopam 370, BRACCO) at a flow rate rate of 6mL/sec (tube energy of 120 kVp, axial slice thickness of 0.625 mm, rotation time of 0.35 sec, detector coverage of 40 mm). Prospective image acquisition was used by ECG-gating at 75% of cardiac cycle (with 100 msec padding for optimal imaging of the right coronary artery if required).

2.5.2 Pulmonary Computed Tomography Angiography Acquisition Protocols

At Oxford University Hospitals participants underwent pulmonary CTA (CTPA) performed on the GE Revolution HD CT scanner. During the initial phase of the pandemic, suspected cases of COVID-19 pneumonia had standard CTPA or dual energy CTPA (DECTPA) (Lang et al., 2020). The single energy CTPA were perform using 80-120kV and contrast 70-100mL at 4 mL/s dependent on body size. DECTPA were performed using rapid kV switching to optimise contrast and thrombus visualisation. These scans were all non-ECG gated. Scans from University Hospitals of Leicester were performed on a Siemens Somatom Definition Flash CT scanner, using a FLASH protocol with the following scan parameters: dose modulation on, quality reference kVp 100, ref mAs 100, pitch: 2.1, rotation time 0.28s, detector configuration $128x$0.6mm, suspended respiration scan from lung apices to lung bases, using a pre monitoring slice at the level of the pulmonary artery for optimal contrast enhancement of the pulmonary arteries, contrast agent: omnipaque 350, 50mls at 4ml/sec plus 50mls saline flush. Scans from the Royal United Hospitals Bath were performed on either Siemens Somatom Definition Edge scanner with the

following scan parameters: dose modulation on, quality reference kVp 120, ref mAs 145, pitch 1.2, rotation time 0.5s, detector configuration 128x0.6mm, suspended respiration scan from lung apices to lung bases, using a bolus-tracking method with threshold of 100 HU in an ROI in a slice at the level of the main pulmonary artery and a 4 second delay after triggering, contrast agent: omnipaque 350, 60mls at 5ml/s plus 50mls 0.9% saline flush at 5ml/sec or Siemens Somatom Drive scanner with the following scan parameters: dose modulation on, dual source dual energy 80 kVp / ref mAs 141 and Sn-filter 140 kVp / ref mAs 60, pitch 1.2, rotation time 0.5s, detector configuration 128x0.6mm, suspended respiration scan from lung apices to lung bases, using a bolus-tracking method with threshold of 100 HU in an ROI in a slice at the level of the main pulmonary artery and a 9 second delay after triggering, contrast agent: omnipaque 350, 75mls at 5ml/s plus 25mls 50:50 mix omnipaque 350 / 0.9% saline flush at 5ml/sec.

2.6 Radiomic Characterization

2.6.1 Adipose Tissue Segmentation

Perivascular adipose tissue segmentation was performed manually around the right IMA from the level of the aortic arch to 120mm caudally. Perivascular space was defined as the space within a radial distance from the outer vessel wall equal to the diameter of the respective vessel, as previously described (Oikonomou et al., 2018). Perivascular adipose tissue segmentation around the descending thoracic aorta was performed manually from the level of the pulmonary artery bifurcation to 67.5mm caudally, as previously described (Schlett et al., 2009). Perivascular space was defined as the space within a cylindrical layer that is expanded beyond the vessel borders by a distance equal to 10mm. In order to avoid lung tissue and any COVID-19

related lesions peri-aortic adipose tissue directly adjacent to the left lateral side of the descending thoracic aorta that is in close proximity to. All analyses were performed using the standard operating procedures of the Oxford Academic Cardiovascular CT (OXACCT) core lab and for C19-RS measurements inter-observer agreement amongst two independent operators was excellent [ICC: 0.914 (95% CI: 0.769-0.968), p<0.001]. All segmentations were performed using 3D Slicer (v.4.10.2) (Fedorov et al., 2012). Given the heterogeneity of tube voltage and effective energies used in the various imaging protocols in Studies 1 and 2, we rescaled all images using 100kVp as reference. Conversion factors (Table 2.4) for tube voltage 120kVp and effective energies 55, 58, and 70 keVs were calculated from data previously validated (Okayama et al., 2012).

Table 2.4: Conversion factors for different CT energies

	Conversion Factor for Adipose Tissue
100 kVp (tube voltage)	1 (reference)
110 kVp (tube voltage)	1.054740019
120 kVp (tube voltage)	1.114849188
70keV (effective energy)	0.988683128
58 keV (effective energy)	0.817537672
55 keV (effective energy)	0.771195642

2.6.2 Radiomic Characterization Details

Image processing and extraction of radiomic features was performed using the CaRi-Research toolbox (Caristo Diagnostics, Oxford UK) and pyradiomics (van Griethuysen et al., 2017). A total of 1,655 radiomic features were extracted from each segmented PVAT volume. A total of 1,655 radiomic features were extracted from each segmented PVAT volume (full list of radiomic features extracted is available in Appendix B). Briefly, the radiomic features obtained were based on shape-based analysis, first order statistics, grey level co-occurrence matrix (glcm),

grey level run length matrix (glrlm), grey level size zone matrix (glszm), grey level dependence matrix (gldm), neighbouring grey tone difference matrix (ngtdm). All these features were calculated on the original images and after applying transformations on the images. The transformations included Laplacian of Gaussian (log) with various sigma (1, 2, 3, 4, 5 mm), wavelet-LLH , wavelet-LHL, wavelet-LHH, wavelet-HLL, wavelet-HLH, wavelet-HHL, square, square root, logarithm and exponential. The bin width was kept at 25. More details are provided in the individual chapters, alongside a full list of radiomics features extracted.

2.6.3 Radiomic feature filtering and selection

Firstly, I performed a stability assessment of all 3,310 different radiomic features. For this purpose I used 24 Lung CT scans (12 paired scans, performed 15 minutes apart) from the RIDER dataset ("RIDER. The Reference Image Database to Evaluate Therapy Response", 2013) to assess the scan-rescan ICC of each radiomic feature. Only radiomic features with ICC$\geq$0.90 were included in further analyses. I next filtered out redundant radiomic features with Spearman's rho coefficient lower than an absolute value of 0.9, using the "findCorrelation" function of the "caret" package in R (n=497). For further filtering of radiomic features I removed features significantly correlated with BMI and total intrathoracic adipose tissue, using a threshold of 0.05 in the Spearman's rho correlation p value. Further details may be found in individual chapters.

2.7 Statistical analysis

2.7.1 Cross-sectional analysis

Continuous variables are presented as mean±standard deviation or median [range], as appropriate. Categorical variables between two or more groups were compared by Chi-square test, whereas continuous variables between groups were compared by unpaired Student's t-test or non-parametric Mann-Whitney test (for two groups) and one-way ANOVA (for three groups or more). Correlations between continuous variables were tested by univariate analysis using Pearson's r or Spearman's rho coefficient as appropriate. For comparisons between paired data, the Wilcoxon signed-rank test was used.

2.7.2 Transcriptomic Data Generation and Processing

RNAseq read pairs were split and only read 1 was used for alignment and quantification, appropriate for the library preparation protocol used. After initial poor mapping results with full-length 150bp reads, reads reduced to 75bp and trimmed for adapter and low-complexity sequence using fqtrim v0.9.515 were aligned to Homo sapiens reference genome, GRCh37 using Hisat2 version-2.0.4 (Kim et al., 2015). Gene annotation files were downloaded in GTF format from Ensembl, release 76 (Cunningham et al., 2015). Reads mapping to annotated exon features were quantified with featureCounts (Liao et al., 2014), part of subread-v1.5.0 (Liao et al., 2013), using default parameters and keeping all aligned reads including potential duplicates (due to the 3' protocol). Quality metrics for aligned reads were estimated using CollectRnaSeqMetrics, implemented in Picard tools v1.92 (*Web Page*, version at 10.01.2016). The raw count tables

produced by featureCounts were imported in R Statistical Software for further processing and analysis using in-built functionality and relevant packages as detailed below. Differential gene expression analyses were performed using the edgeR package.

2.7.3 WGCNA analysis

Unsupervised identification of co-correlated genes was undertaken using the Weighted Gene Coexpression Network Analysis Bioconductor package in R (Langfelder & Horvath, 2008). Transcripts per million expression data were filtered using a threshold of at least 0.25 in at least 100 samples and a soft thresholding power was chosen based on the criterion of approximate scale-free topology. Gene networks were constructed, and modules identified from the resulting topological overlap matrix with a dissimilarity correlation threshold of 0.01 used to merge module boundaries with a specified minimum module size of n=50. Modules were summarised as a network of modular eigengenes, which were then correlated with a matrix of clinical variables. Significance of correlation between a given clinical trait and a modular eigengene was assessed using linear regression with Bonferroni adjustment to correct for multiple testing. Hierarchical clustering was performed using a Pearson correlation distance metric and average linkage analysis performed using Genepattern.

2.7.4 Survival analysis and prognostic models

Time-to-event data were assessed using univariate and multivariable Cox regression models, while Kaplan-Meier curves were plotted and compared by the log-rank test. Fractional polynomials were also used to model non-linear relationships and the best-fitting fractional polynomial model was chosen and graphically presented. Optimal cut-off points were selected using the

maximally selected rank statistic (Lausen & Schumacher, 1992). Further details can be found in the methods sections of individual chapters.

2.7.5 Machine learning models

For generation of imaging signatures I considered a series of machine learning methodologies to use in my datasets, including decision trees, and random forest algorithms. Extreme gradient boosting with method "gbtree" was the method with the best performance. I therefore decided to choose extreme gradient boosting, also because this is the de facto standard algorithm for getting accurate results from predictive modelling with machine learning. It is the fastest gradient-boosting library with very high accuracy. It is understood to perform well in many applications with a fair amount of data and can detect and learn from non-linear data patterns (Kadiyala & Kumar, 2018). To avoid overfitting issue, I used 5-fold cross validation and tuned the hyperparameters by optimising step size shrinkage, L2 regularization parameter and learning rate. I used early stopping technique that works by monitoring the performance of the model that is being trained on a separate test dataset and stopping the training procedure once the performance on the test dataset has not improved after a fixed number of training iterations. It avoids overfitting by attempting to automatically select the inflection point where performance on the test dataset starts to decrease while performance on the training dataset continues to improve as the model starts to overfit. Although modest number of samples were used during training step of model development, the accuracy of the model was not degraded on external validation data suggesting that model was not overfitted.

3 | Oxidative Stress: Prognostic Potential

3.1 Introduction

Inflammation is a key player in the natural history of atherogenesis, especially the development of the vulnerable atherosclerotic plaque (Antonopoulos et al., 2012). The links between inflammatory processes and atherosclerosis are well established, with both innate and adaptive immunity involved in a complex network of molecular and cellular interactions (Libby et al., 2009; Tousoulis et al., 2014). Components of the innate arm of immunity can be triggered by pathogens in a non-specific manner, leading to the activation of mast cells, neutrophils, macrophages (respiratory burst) and the complement (Tousoulis et al., 2014). At the same time, antigen-presenting cells are activated by toll-like receptors (TLRs), leading to pro-inflammatory signalling responses, and cross-linking with adaptive immunity, which is highly organized and more relevant to atherogenesis. T-cell activation, antibody production, and secretion of a range of pro-inflammatory cytokines, such as IFN-γ, IL-1, IL-6, are all responses related to the state of systemic low-grade inflammation inherent to atherosclerosis.

Vascular redox state is an important feature of vascular homeostasis, with increased reactive oxygen species (ROS) production implicated in the pathogenesis of hypertension, aortic aneurysm, hypercholesterolaemia, atherosclerosis, diabetic vascular complications, cardiac ischaemia-reperfusion injury, myocardial infarction, heart failure and cardiac arrhythmias (Y. Zhang et al., 2020). Interactions between different oxidases or oxidase systems have been intensively

investigated for their roles in inducing sustained oxidative stress. Accumulating evidence indicates that the major enzymatic sources of reactive oxygen species (ROS) in the cardiovascular system are NADPH oxidase (NOX), uncoupled endothelial nitric oxide synthase (eNOS), mitochondria and xanthine oxidase (XO) (Cai & Harrison, 2000). NOX is distinct from other enzymatic sources because its primary function is to produce ROS. Low levels of ROS produced by certain NOX isoforms (such as NOX2) have been implicated in physiological processes, including cell proliferation, migration, differentiation and cytoskeletal organization (Brown & Griendling, 2015). However, excessive production of ROS from activated NOXs contributes to cardiovascular pathogenesis. Of note, NOX-derived ROS, such as superoxide and hydrogen peroxide (H_2O_2), can trigger ROS production through the activation of other enzymatic systems. In addition, ROS can stimulate the conversion of xanthine dehydrogenase (XDH) to XO by oxidation of the sulfhydryl residue. ROS produced by NOX can also cause mitochondrial DNA damage, oxidation of components of the membrane permeability transition pore and opening of the redox-sensitive mitochondrial ATP-sensitive K^+ channel (mitoKATP), all of which contribute to mitochondrial uncoupling and ROS production (Y. Zhang et al., 2020).

In spite of its well-characterised role in disease pathogenesis, clinical data from human studies on the role of cardiovascular oxidative stress in the clinical route, presentation, management and importantly prognosis of patients are sparse. Studies have linked myocardial oxidative stress with in-hospital development of atrial fibrillation, but its role in the prediction of long-term outcomes and mortality is yet to be elucidated. As a result, in this section I sought to investigate the prognostic potential of oxidative stress in atherosclerosis. In addition, I aimed to apply discovery network transcriptomics to internal mammary arteries (IMAs) obtained from patients undergoing cardiac surgery, in order to identify redox-related molecular pathways within the

vascular wall that can be treated therapeutically.

3.2 Methods

3.2.1 Study Participants

This chapter is split into different study arms; a comprehensive workflow diagram of each study arm design is presented in Figure 3.1. Study Arm 1 included 497 patients from the Oxford Heart, Vessels and Fat (Ox-HVF) cohort and aimed at exploring the prognostic role of vascular oxidative stress. Study Arm 2 included 205 patients from the Ox-HVF cohort and was used to construct transcriptomic signatures. Finally, Study Arm 3 included 258 patients from the Ox-HVF cohort with myocardial oxidative stress measurements.

3.2.2 In vivo clinical studies

Measurement of vascular and myocardial oxidative stress was performed as described in section 2.3.

3.2.3 Long-term clinical endpoints data collection

Long-term outcome data following surgery were collected through National Health Service (NHS) Digital, as described in section 2.2. Cardiovascular death was defined as any death due to proximate cardiac causes (e.g. myocardial infarction, low-output heart failure, fatal arrhythmia) or other non-cardiac vascular causes such as stroke or pulmonary embolism. Any death not covered by the previous definition, such as death caused by malignancy, accident, infection,

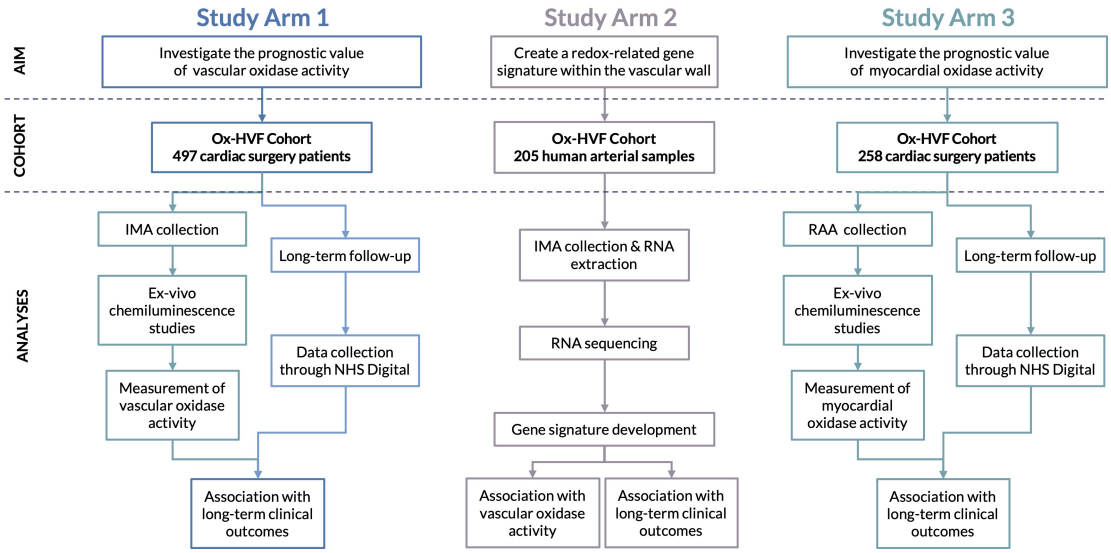


Figure 3.1: Chapter 3 Studies Workflow. Study Arm 1 included 497 patients undergoing cardiac surgery. Segments of the IMA were collected and used for NADPH oxidase activity measurements. Whole blood was also collected and used for DNA sequencing. Finally, the patients were followed-up for future cardiovascular events through NHS Digital records. Study Arm 2 consisted of 205 patients in whom segments of the IMA were collected and used for bulk RNA sequencing. Study Arm 3 included 258 patients undergoing cardiac surgery. Biospies of the RAA were collected and used for NADPH oxidase activity measurements. Finally, the patients were followed-up for future cardiovascular events through NHS Digital records. IMA: Internal mammary artery; RAA: Right atrial appendage.

sepsis, renal failure, or suicide was classified as non-cardiac.

3.2.4 Tissue Collection, RNA Isolation and Sequencing Data Analysis

All methods for human biopsies collection, RNA isolation, and sequencing can be found in sections 2.1.3.2, 2.4.1, and 2.4.4.

3.2.5 Transcriptomic Data Generation and Processing

RNAseq read pairs were split and only read 1 was used for alignment and quantification, appropriate for the library preparation protocol used. After initial poor mapping results with full-length 150bp reads, reads reduced to 75bp and trimmed for adapter and low-complexity sequence using fqtrim v0.9.515 were aligned to Homo sapiens reference genome, GRCh37 using Hisat2 version-2.0.4 (Kim et al., 2015). Gene annotation files were downloaded in GTF format from Ensembl, release 76 (Cunningham et al., 2015). Reads mapping to annotated exon features were quantified with featureCounts (Liao et al., 2014), part of subread-v1.5.0 (Liao et al., 2013), using default parameters and keeping all aligned reads including potential duplicates (due to the 3' protocol). Quality metrics for aligned reads were estimated using CollectRnaSeqMetrics, implemented in Picard tools v1.92 (*Web Page*, version at 10.01.2016). The raw count tables produced by featureCounts were imported in R Statistical Software for further processing and analysis using in-built functionality and relevant packages as detailed below. Differential gene expression analyses were performed using the edgeR package.

3.2.6 WGCNA analysis

Unsupervised identification of co-correlated genes was undertaken using the Weighted Gene Coexpression Network Analysis Bioconductor package in R (Langfelder & Horvath, 2008). Transcripts per million expression data were filtered using a threshold of at least 0.25 in at least 100 samples and a soft thresholding power was chosen based on the criterion of approximate scale-free topology. Gene networks were constructed, and modules identified from the resulting topological overlap matrix with a dissimilarity correlation threshold of 0.01 used to merge mod-

ule boundaries with a specified minimum module size of n=50. Modules were summarised as a network of modular eigengenes, which were then correlated with a matrix of clinical variables. Significance of correlation between a given clinical trait and a modular eigengene was assessed using linear regression with Bonferroni adjustment to correct for multiple testing. Hierarchical clustering was performed using a Pearson correlation distance metric and average linkage analysis performed using Genepattern.

3.2.7 Enrichment analyses

Enrichment analyses were performed using pathfindR (Bioconductor) with a significance threshold of 5% FDR.

3.2.8 Whole Genome Genotyping, Quality Checks and Imputation

Patients were genotyped with the genome-wide SNP array UK Biobank Axiom Array (Affymetrix). Details of genotyping and primary quality control of samples and SNPs described previously (Pott et al., 2017). In brief, sample quality control included analysis of Dish QC (DQC), call rate, heterozygosity, and sex mismatches. SNP quality control included call rate ($\leq$97%), violation of Hardy-Weinberg equilibrium (P$\geq 10^{-6}$) and plate associations (P$\geq 10^{-7}$). In total, 881 samples and 588,801 SNPs fulfilled all quality criteria for autosomal analysis. Genotypes were imputed using the Michigan Imputation Server (https://imputationserver.sph.umich.edu/index.html) using the version HRC r1.1, 2016, Eagle v2.3 for phasing and based on the European (EUR) Population. SNPs with Rsq>0.7 and minor allele frequency<0.01 were filtered. A total of 5,090,726 SNPs were considered for analysis.

3.2.9 Association Analyses

Of the 881 genotyped samples that passed QC checks, IMA NADPH superoxide levels were available for 437 patients. Association analysis was performed with the 1.9 version of the PLINK software (PLINK 1.9 (cog-genomics.org). Logarithmized IMA NADPH superoxide levels were adjusted for age, sex, smoking status, the first five principal components and an additive model of inheritance was assumed. A cut-off value of 1×10^{-5} was used as threshold for a suggestive significant. SNPs were comprehensively annotated with ANNOVAR (https://annovar.openbioinformatics.org).

3.2.10 Statistical analysis

Participant demographics are summarized as numbers (percentages) or median (25th to 75th percentile) for categorical and continuous variables, respectively. Between-group comparisons were performed using Pearson's chi-squared test for categorical variables, and Mann-Whitney's U test for continuous variables. Survival analyses were assessed in univariable Kaplan-Meier curves, and Cox regression models adjusted for age, sex, and cardiovascular risk factors (hypertension, dyslipidaemia, diabetes, smoking). Optimal cut points for survival analyses were identified by the value that maximized the log-rank statistic. Missing values within the datasets were imputed with predictive mean matching using the "mice" package in R. Statistical analyses were performed in the R environment (R version 3.6.0 and R Studio version 1.2.1335). All tests were two-sided and α was set at 0.05.

3.3 Results

3.3.1 Vascular NADPH oxidase activity is linked with mortality and MACE

Study Arm 1 included 497 patients undergoing cardiac surgery. Table 3.1 presents demographics of these patients. An alluvial plot presented in Figure 3.2 demonstrates the distribution of characteristics within patients that died during the study's follow-up period. In total, over a median follow-up period of 6.35 years [IQR: 3.97-8.38], 100 (20%) deaths were recorded, of which 50 (10%) were of cardiovascular aetiology. Also, 101 major adverse cardiac events occurred (MACE: Cardiovascular death or non-fatal acute myocardial infarction, non-fatal stroke, or first admission for heart failure).

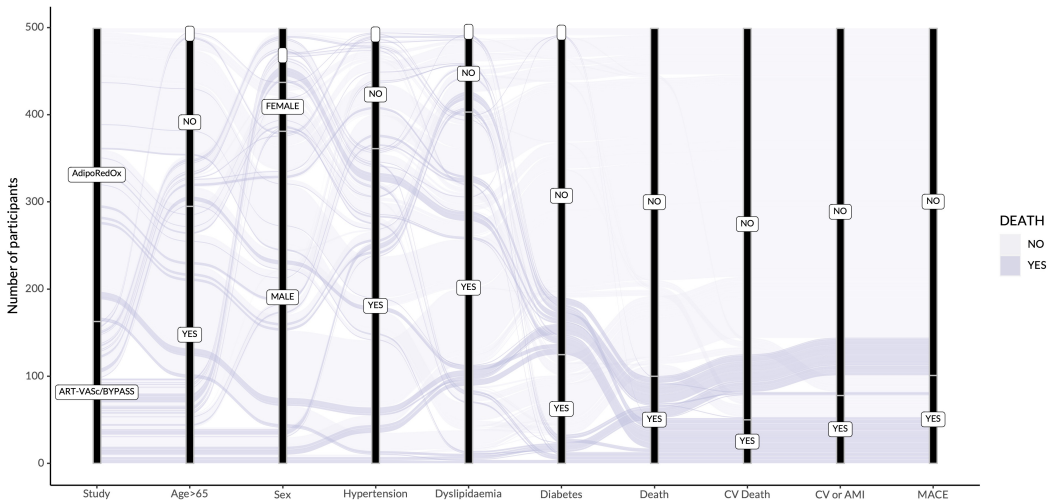


Figure 3.2: Study Arm 1 alluvial plot based on outcome. Dark purple lines represent participants that died during the study's follow up period. A large proportion of those experienced cardiovascular death, while almost half the patients experiencing a major adverse cardiovascular event originated from participants that did not die during follow up. Further, the majority of patients that died during follow up had hypertension and dyslipidaemia, as opposed to those with diabetes, which was less frequent amongst that subgroup.

Table 3.1: Study Arm 1 Population Characteristics

	Study Arm 1
n	497
MALE SEX (%)	381 (87.2)
HYPERTENSION (%)	361 (74.4)
DYSLIPIDAEMIA (%)	403 (82.1)
DIABETES (%)	125 (25.6)
SMOKING (%)	
Never	173 (36.4)
Past	251 (52.8)
Active	51 (10.7)
Follow-up (years)	6.35 [IQR: 3.97-8.38]
DEATH (%)	100 (20.0)
CV DEATH (%)	50 (10.0)
CARDIAC DEATH (%)	41 (8.2)
CVD/AMI (%)	78 (15.6)
CVD/AMI/STROKE (%)	96 (19.2)
MACE (%)	101 (20.2)

CV: Cardiovascular; AMI: non-fatal Acute Myocardial Infarction; STROKE: non-fatal stroke; MACE: Major adverse cardiac event (CVD or AMI or STROKE or first admission for heart failure)



Figure 3.3: IMA NADPH oxidase activity as a continuous variable and long-term outcomes: Univariate models. Hazard ratios (HR) and 95% confidence intervals derived from univariate Cox models for a range of long-term outcomes. The dotted line indicates HR=1. Numbers next to each outcome represent the number of events recorded.

In univariate Cox regression analysis (Figure 3.3), IMA NADPH oxidase activity was linked to a higher risk for all-cause mortality (HR [95% CI]: 1.42 [1.23-1.64] per 1 SD increase, P<0.0001), cardiovascular mortality (HR [95% CI]: 1.65 [1.39-1.97] per 1 SD increase, P<0.0001), and MACE (HR [95% CI]: 1.33 [1.13-1.55] per 1 SD increase, P=0.0003).

In multivariable Cox regression analysis (Figure 3.5) adjusted for age, sex, traditional cardiovascular risk factors, higher arterial oxidative stress reflected by IMA NADPH oxidase activity retained its prognostic value and was linked to a higher adjusted risk of all-cause mortality (HR [95% CI]: 1.44 [1.24-1.67] per 1 SD increase, P<0.0001), cardiovascular mortality (HR [95% CI]: 1.71 [1.42-2.05] per 1 SD increase, P<0.0001), and MACE (HR [95% CI]: 1.33 [1.13-1.56] per 1 SD increase, P=0.0004).

IMA resting oxidative stress and NADPH oxidase activity values measured by lucigenin chemiluminescence as relative light units (RLUs) per second, per milligram of tissue were left-skewed. This observation prompted survival optimal cut-off analysis, using the maximally selected rank statistic, for arterial oxidative stress as a predictor of all-cause mortality (Figure 3.4).

For an optimal cut-off point of 4.46 RLUs/sec/mg tissue patients with high resting IMA oxidative stress had a 1.9 times higher adjusted risk for all-cause mortality, and a 2.3 times higher adjusted risk of cardiovascular death. A similar seperation was observed for the MACE endpoint up until the 8th year of follow-up (Figure 3.6).

Similarly, and following multivariable adjustment for the aforementioned covariates, high NADPH oxidase activity was associated with a 2-fold increase in the adjusted risk for all-cause mortality, 3-fold increase in the adjusted risk for cardiovascular mortality, and 1.5-fold increase

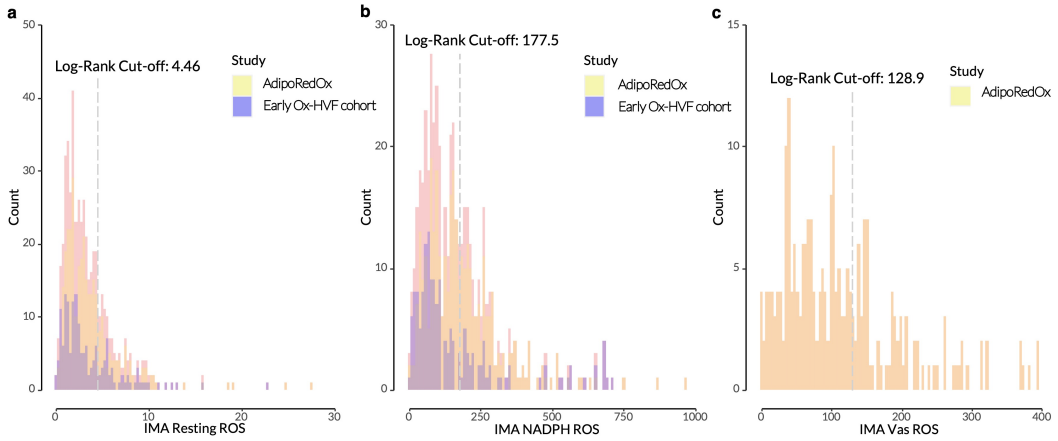


Figure 3.4: Computing cut-off points for vascular oxidative stress indices. Histograms present the distribution of IMA resting, NAPDH and Vas inhibitable ROS across the Ox-HVF cohort, labelled separately by colour for the more recent AdipoRedOx and the older cohorts. The dotted line indicates the value that maximises the log rank statistic. Values presented are in RLUs/sec/mg. RLU: relative light units; ROS: reactive oxygen species; IMA: internal mmammary artery.

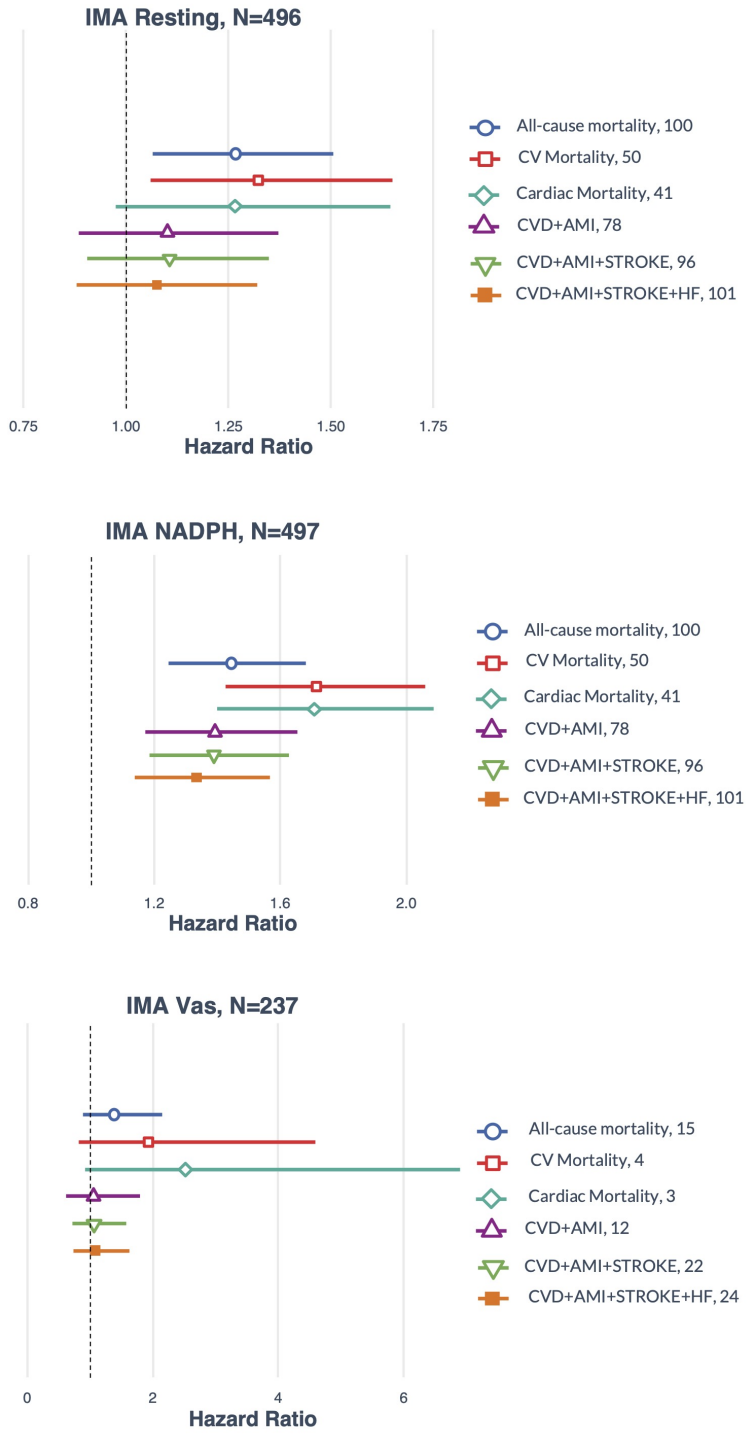


Figure 3.5: IMA NADPH oxidase activity as a continuous variable and long-term outcomes: Multivariable models. Hazard ratios (HR) and 95% confidence intervals derived from multivariable Cox models adjusted for age, sex, traditional cardiovascular risk factors for a range of long-term outcomes. The dotted line indicates HR=1. Numbers next to each outcome represent the number of events recorded.

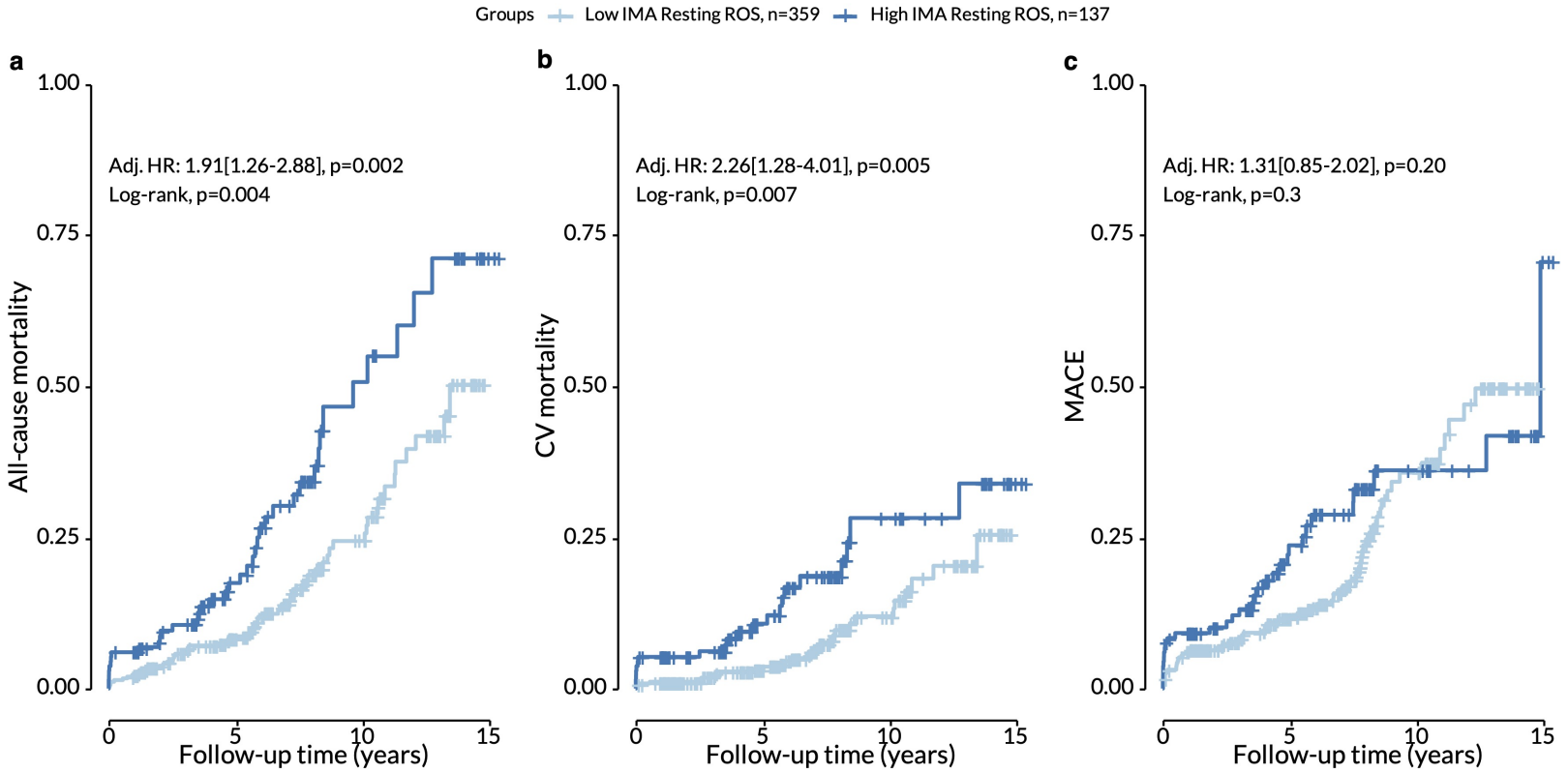


Figure 3.6: IMA resting oxidative stress Kaplan-Meier plots. Kaplan Meier curves and adjusted hazard ratios for three endpoints after dividing the Study Arm 1 population for an optimal IMA resting oxidative stress log-rank cut-off, and following multivariable adjustment for age, sex, and traditional cardiovascular risk factors.

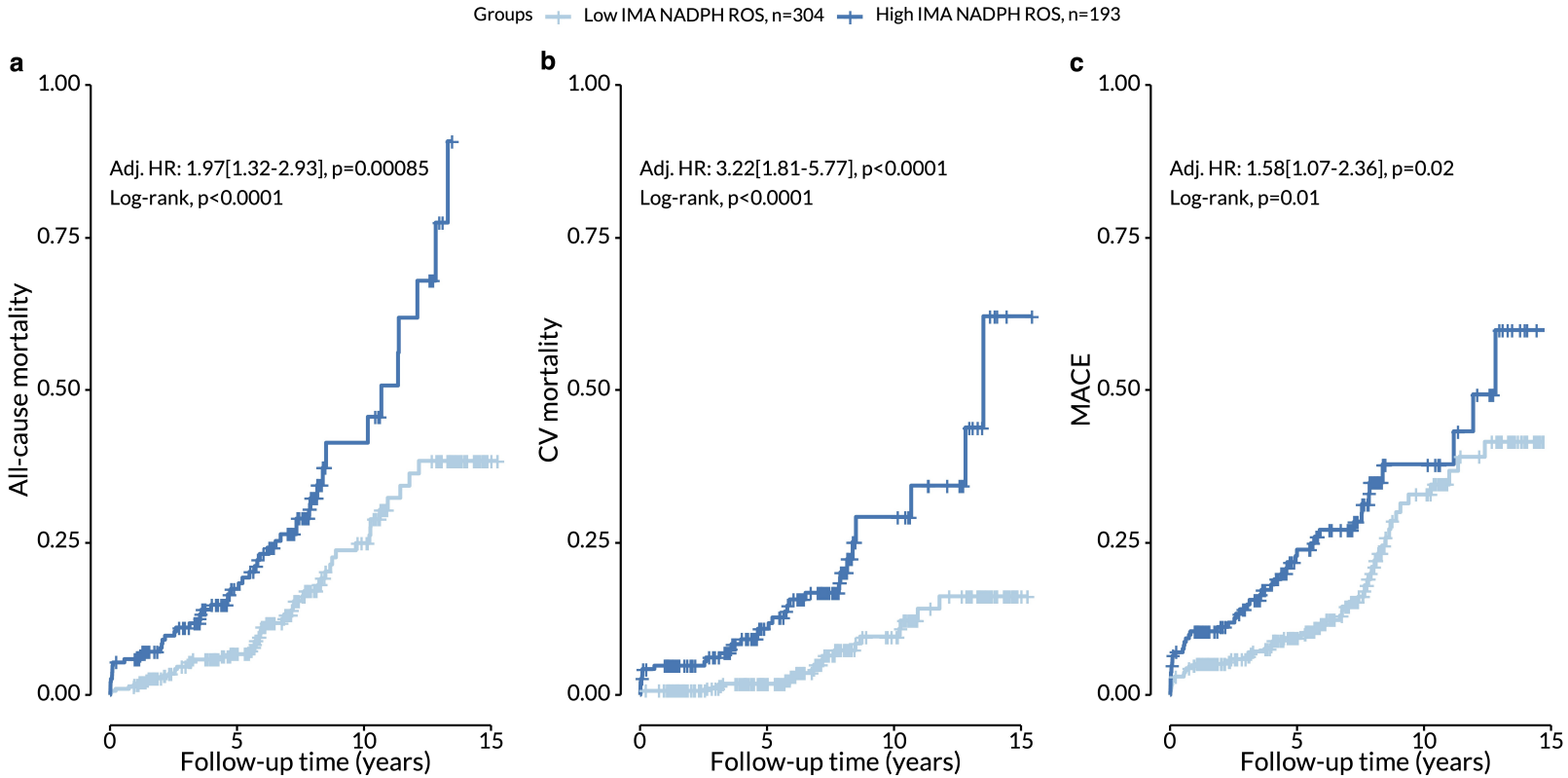


Figure 3.7: IMA NAPDH stimulated oxidative stress Kaplan-Meier plots. Kaplan Meier curves and adjusted hazard ratios for three endpoints after dividing the Study Arm 1 population for an optimal IMA NAPDH stimulated oxidative stress log-rank cut-off, and following multivariable adjustment for age, sex, and traditional cardiovascular risk factors.

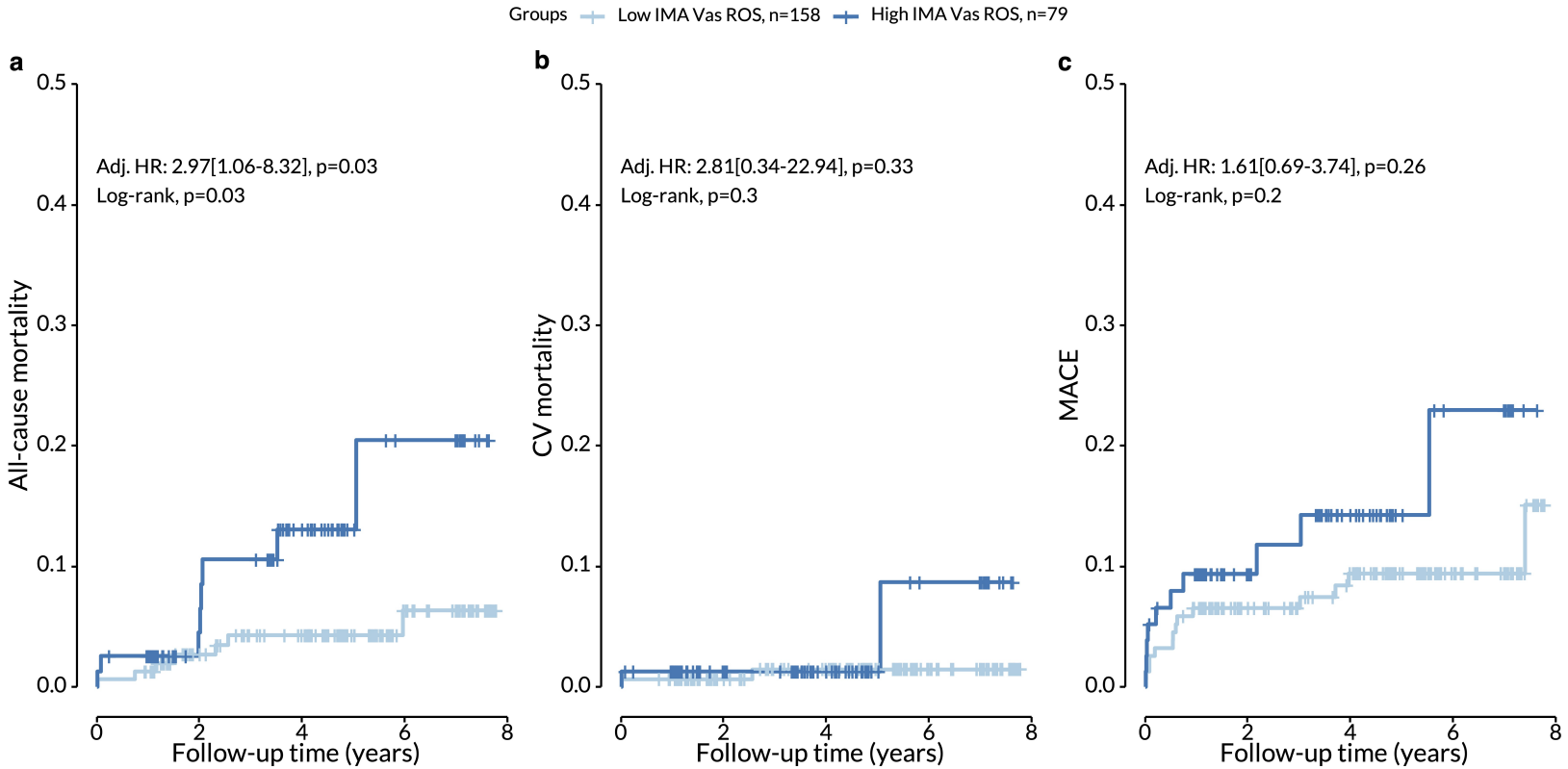


Figure 3.8: IMA Vas2870 inhibitable oxidative stress Kaplan-Meier plots. Kaplan Meier curves and adjusted hazard ratios for three endpoints after dividing the Study Arm 1 population for an optimal IMA Vas2870 inhibitable oxidative stress log-rank cut-off, and following multivariable adjustment for age, sex, and traditional cardiovascular risk factors.

in the adjusted risk for MACE (Figure 3.7).

Finally, the same approach was adapted for a subgroup of 237 patients in whom the Vas2870 inhibitable oxidative stress index was availablle. following multivariable adjustment for the aforementioned covariates, high Vas2870 inhibitable oxidase activity was associated with a 3-fold statistically significant, and a 1.6-fold (not statistically significant) increase in the adjusted risk for MACE (Figure 3.8). It is important to note that although these associations are not statistically significant, they still present the same separation as with the other oxidative stress indices, suggesting that non-significance is most likely driven by a small sample size or few outcome events. Indeed, as discussed above in this subgroup of 237 patients, only 4 cardiovascular deaths were recorded, while all cause mortality accounted for 6.32% (15 deaths).

Taken all together, these observations highlight for the first time that increased arterial oxidative stress is an independent predictor of long-term cardiac risk in patients with advanced atherosclerosis.

3.3.2 Exploring transcriptional changes in increased vascular oxidative stress

In order to better understand the biology behind these observations, I designed a large RNA sequencing experiment in the Study Arm 2 population. I arbitrarily split the cohort in tertiles of NADPH oxidase activity and used the highest and lowest tertiles to perform differential gene expression analysis. Figure 3.9 presents the distribution of NADPH oxidase activity in the Study Arm 2 population and the cut-offs used for determining tertiles.

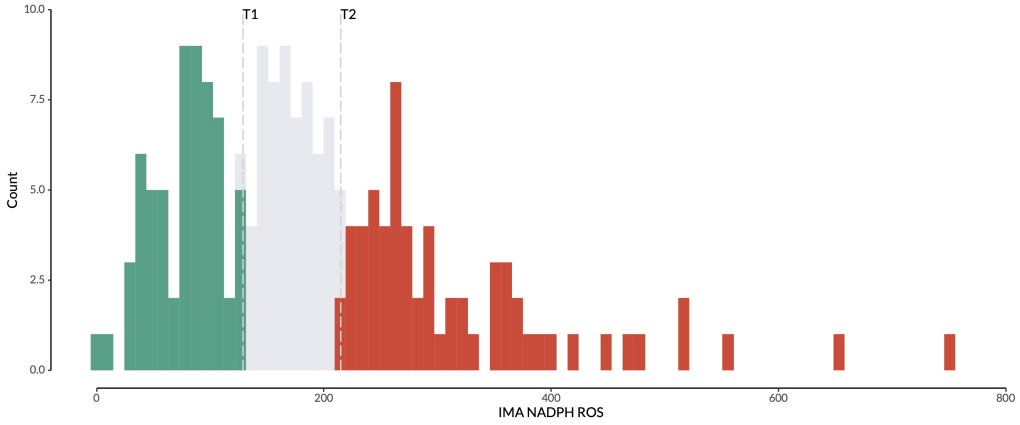


Figure 3.9: NADPH oxidase activity tertiles in the Study Arm 2 population. The two extreme groups were used in downstream differential gene expression analyses to investigate possible gene dysregulation in the vascular wall in the presence of increased oxidative stress.

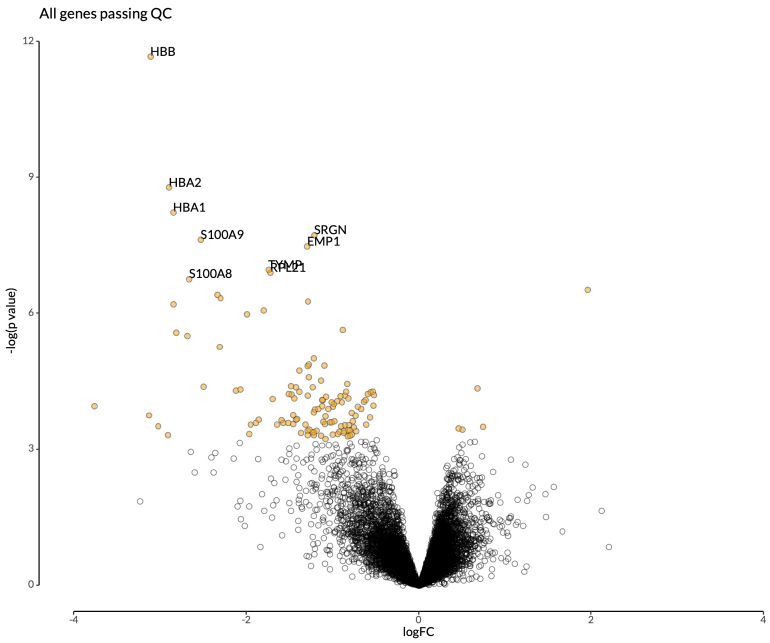


Figure 3.10: Volcano plot of differential gene expression for all genes sequenced.

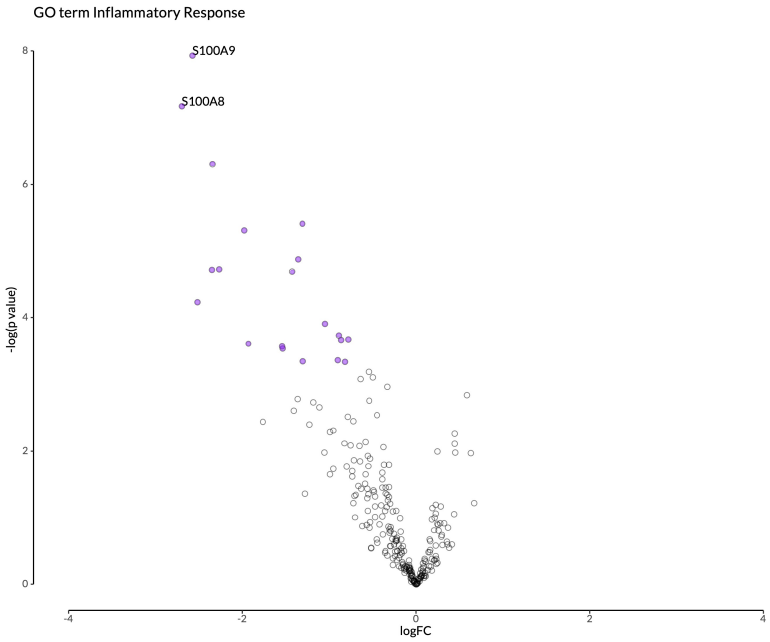


Figure 3.11: Volcano plot of differential gene expression for genes in the GO:Inflammatory Response.

A range of genes were found to pass the FDR corrected significance threshold of 0.05 in differential gene expression analyses (a list of FDR significant genes is available in Appendix C). Interestingly, most genes were found to be downregulated in the presence of oxidative stress (Figure 3.10). Because oxidative stress is linked with inflammation, I extracted genes annotated to the Gene Ontology term "Inflammatory Response" (Figure 3.11) in order to identify gene targets of relevance to both oxidative stress and vascular inflammation. This analysis revealed two candidate genes for downstream validation, S100A8 and S100A9.

These genes were found to be the most downregulated genes in the high NADPH oxidase activity group. I first aimed to validate this finding by conducting a cohort-wide qPCR of these genes in order to observe whether the gene expression levels will be negatively correlated with NADPH oxidase activity in the human internal mammary arteries. Indeed, the expression of the S100A8 gene in the cohort was significantly lower as oxidative stress increased as evidenced in Figure 3.12.

Having confirmed the direction of regulation, I designed an exploratory experiment to confirm whether exposure to ROS downregulates the S100A8 and S100A9 genes. I collected rings of the internal mammary artery and biopsies of the aortic wall (aortic buttons) from patients undergoing cardiac surgery. Control biopsies of each tissue type were incubated for 6 hours in KHB buffer. Intervention biopsies were incubated for 6 hours in KHB buffer and stimulated with NADPH at a supra-physiological concentration of 100μM every 2 hours during incubation so as to saturate NOXs and expose the tissue to the maximal possible amount of ROS. I next isolated total mRNA from all samples and looked into the expression pattern of S100A8 and S100A9 in the presence of NADPH stimulation as opposed to controls. A total of 20 samples were processed and analysed. More specifically, 10 paired biopsies of the internal mammary

artery taken from 5 patients, and 10 paired biopsies of the aortic arch taken from 5 patients.

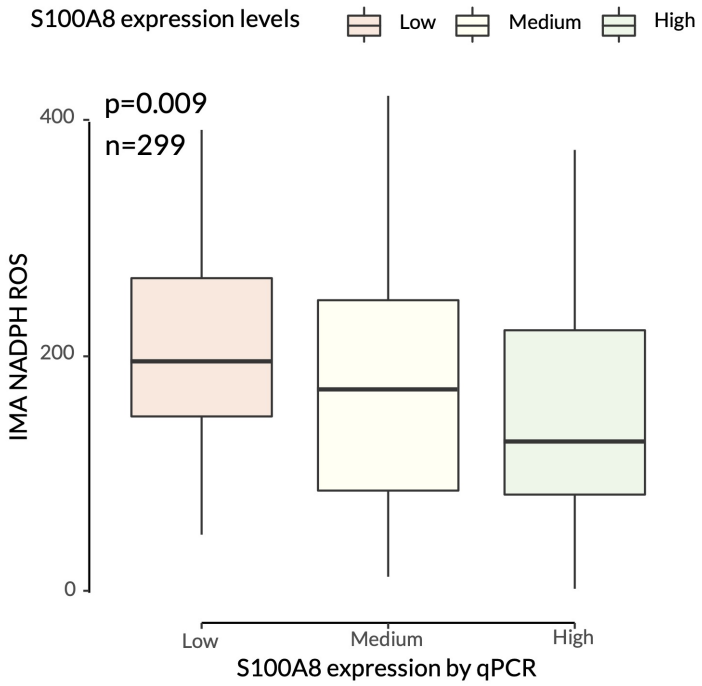


Figure 3.12: Validation qPCR for the S100A8 gene.

As shown in Figure 3.13 there was a clear trend for downregulation for both genes in both tissue types, which reached significance for S100A8 in the arterial tissue. This observation validates the findings from the sequencing and qPCR experiments, proposing S100A8 and S100A9 as possible gene targets, whose downregulation is implicated in oxidative stress in the vasculature. Further investigation of this finding was not feasible in the context of this thesis owing to laboratory closures and clinical studies disturbances because of the COVID-19 pandemic. As such, I next focused my research efforts in unveiling transcriptomic signatures within the vascular wall that relate to redox state and may have prognostic potential, as described in the next sections.

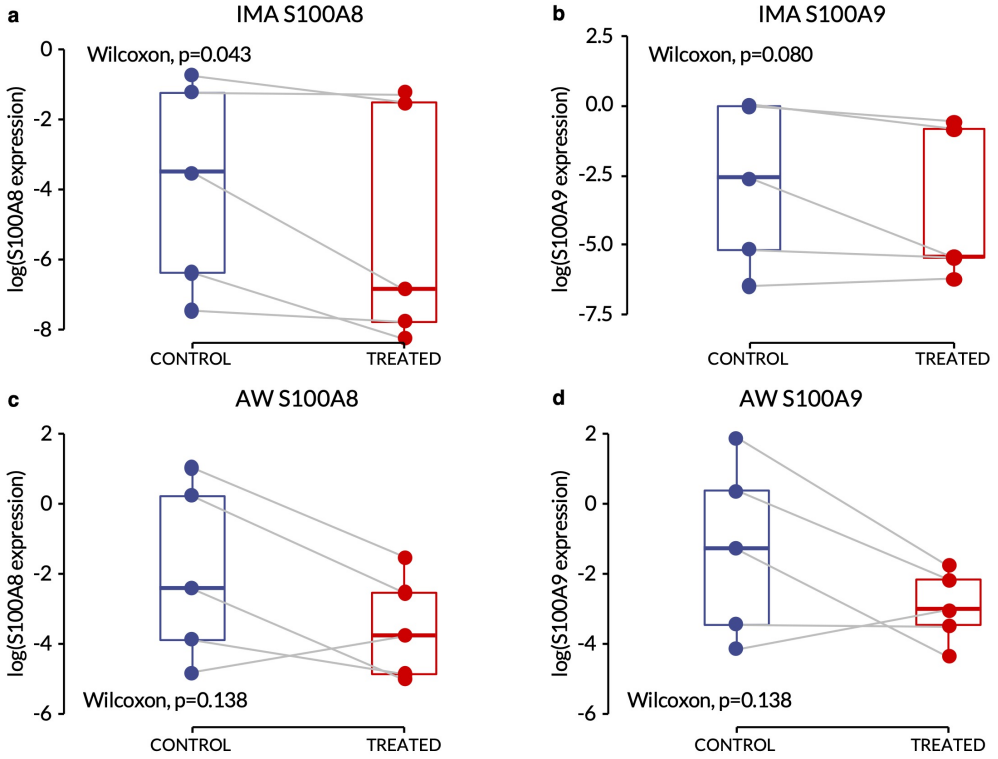


Figure 3.13: Exploratory experiments in IMA and aortic biopsies. (a-b) Stimulation of IMA rings with NADPH every 2 hours for 6 hours led to downregulation of the S100A8 (p=0.043) and S100A9 (p=0.080) genes. (c-d) Similarly, stimulation of AW biopsies with NADPH every 2 hours for 6 hours led to downregulation of the S100A8 (p=0.138) and S100A9 (p=0.138) genes. IMA: Internal mammary artery; AW: Aortic wall.

3.3.3 Constructing vascular wall transcriptomic signatures

Unsupervised analyses of high-throughput 'omic' data facilitate the discovery of previously unsuspected associations as they are, by definition, not founded on existing knowledge. I performed a large unsupervised transcriptomic analysis in order to explore the biological changes behind increased arterial oxidative stress. During an initial quality control phase to detect potential technical outliers per standard bioinformatics practice (You et al., 2019), I applied an unsupervised clustering algorithm in the entire cohort of patients with RNA sequencing data. Indeed, three outlier samples whose leaf node height was significantly higher than other sam-

ples and deviated from the main cluster obviously in the dendrogram were identified. To avoid effects on the subsequent analysis, a height cut at 25,000 was utilized to remove these samples automatically (Figure 3.14).

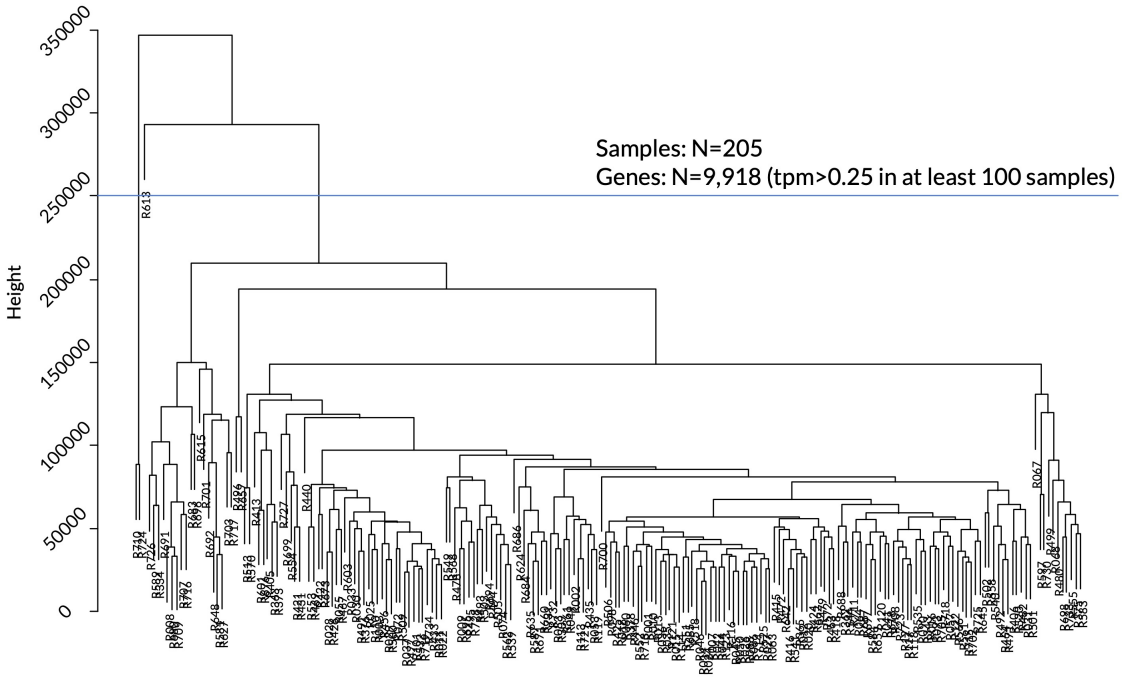


Figure 3.14: Quality check dendrogram. Unsupervised clustering of the entire RNASeq population revealed three patients as outliers. Final matrix for signature development consisted of 205 patients and 9,918 genes, following further filtering explained in text.

Study Arm 2 consisted of 205 patients and Table 3.2 presents baseline demographics and outcomes. Before applying weighted correlation network analysis a matrix consisting of transcripts per million values was computed for the entire Arm 2 population. In brief, Transcripts Per Million (TPM) is a normalization method for RNA-seq, and should be read as "for every 1,000,000 RNA molecules in the RNA-seq sample, X came from this gene/transcript":

1. For each transcript in the gene model, the number (raw count) of reads mapped is divided by the transcript's length, giving a normalized transcript-level expression.

Table 3.2: Study Arm 2 Population Characteristics

	Study Arm 2
n	205
MALE SEX (%)	175 (85.4)
HYPERTENSION (%)	152 (74.1)
DYSLIPIDAEMIA (%)	164 (80.0)
DIABETES (%)	44 (21.5)
SMOKING (%)	
Never	84 (41.0)
Past	97 (47.3)
Active	24 (11.7)
Follow-up (years)	4.12 [IQR: 2.11-7.61]
DEATH (%)	15 (7.3)
CV DEATH (%)	8 (3.9)
CARDIAC DEATH (%)	7 (3.4)
CVD/AMI (%)	14 (6.8)
CVD/AMI/STROKE (%)	19 (9.3)
MACE (%)	21 (10.2)

CV: Cardiovascular; AMI: non-fatal Acute Myocardial Infarction; STROKE: non-fatal stroke; MACE: Major adverse cardiac event (CVD or AMI or STROKE or first admission for heart failure)

2. The sum of all normalized transcript expression values is divided by 1,000,000, to create a scaling factor.

In order to filter out genes with very low tpm values or with tpm values other than zero in a subset of patients, the following filtering steps were applied:

1. tpm > 0.25
2. tpm > 0.25 in at least 100 samples

A tpm of 0.25 is used as it corresponds to a count of 10-15 for the library sizes in this data set. If the count is any smaller, it is considered to be very low, indicating that the associated gene is not expressed in that sample. A requirement for expression in at least 100 samples ensures that a gene will be retained only if it is expressed across a large subset of patients, as I

am looking to create a gene signature that is applicable, comprises of genes that are routinely expressed in IMAs, and reflects gene dysregulation.

Taken together all of the above filtering steps resulted in a final matrix consisting of 205 patients and 9,918 genes, which was fed into the WGCNA package. Weighted correlation network analysis revealed 10 modular coexpression signatures, labelled with individual colours (Figure 3.15).

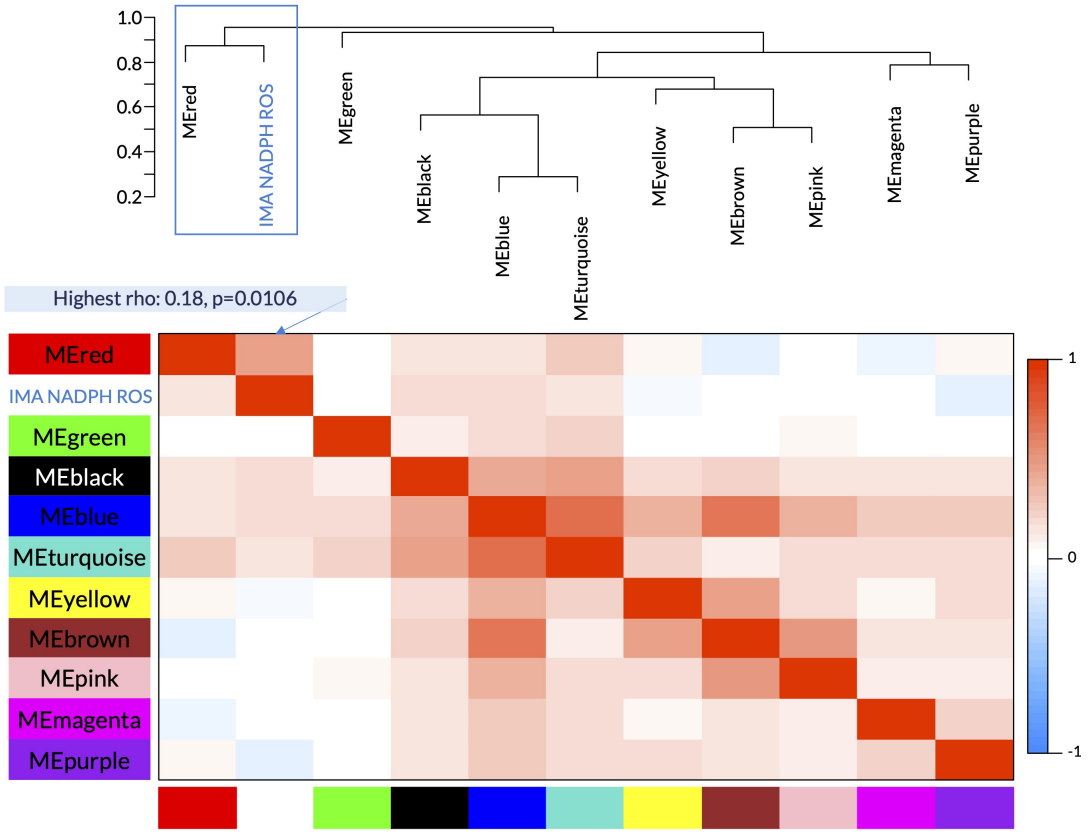


Figure 3.15: WGCNA modules. Weighted correlation network analysis revealed 10 modular coexpression signatures, labelled with the individual colours seen in the figure. For each signature a singular continuous numeric variable is created. The heatmap represents the correlation values between all modules/signatures. The red module or signature had the strongest correlation with arterial NADPH oxidase activity.

The red signature was revealed to cluster closer to with IMA NADPH oxidase activity, while in correlation analysis the red 'eigengenes' showed the strongest correlation. 'Eigen-

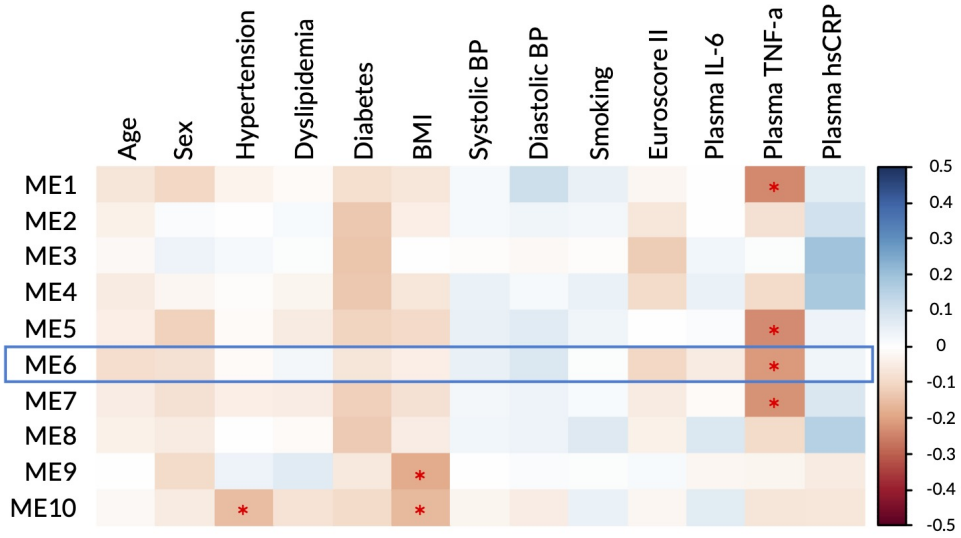


Figure 3.16: Correlation of gene modules with traditional risk factors. Most signatures did not show any particular correlation with background risk. Of note, the red signature (ME6) had a significant inverse correlation with plasma TNFa levels.

genes' summarising modular coexpression signatures were then correlated to baseline clinical data, revealing that most signatures are independent of background risk factors of cardiovascular disease (Figure 3.16). Since the red signature consisting of 277 genes showed the most promising association with IMA NADPH oxidase activity, we chose to investigate this further. Table 3.3 presents a list of all genes associated with the red gene signature.

Table 3.3: Genes in the 'red' signature

AA	Ensembl ID	Entrez Gene ID	External Gene Name
1	ENSG00000004142	26073	POLDIP2
2	ENSG00000006695	1352	Cox10
3	ENSG00000006757	8228	PNPLA4
4	ENSG00000008517	9235	IL32
5	ENSG00000008838	9862	MED24
6	ENSG00000010256	7384	UQCRC1
7	ENSG00000025039	58528	RRAGD
8	ENSG00000048140	26262	TSPAN17
9	ENSG00000051128	9454	HOMER3
10	ENSG00000054148	29085	PHPT1
11	ENSG00000058056	8975	USP13

12	ENSG00000062485	1431	CS
13	ENSG00000063241	79763	ISOC2
14	ENSG00000067225	5315	PKM
15	ENSG00000068903	22933	SIRT2
16	ENSG00000068976	5837	PYGM
17	ENSG00000069011	5307	PITX1
18	ENSG00000070182	6710	SPTB
19	ENSG00000070501	5423	POLB
20	ENSG00000072274	7037	TFRC
21	ENSG00000072954	79041	TMEM38A
22	ENSG00000075914	23016	EXOSC7
23	ENSG00000077009	27231	NMRK2
24	ENSG00000077522	88	ACTN2
25	ENSG00000078668	7419	VDAC3
26	ENSG00000079616	3835	KIF22
27	ENSG00000079739	5236	PGM1
28	ENSG00000084090	56910	STARD7
29	ENSG00000085662	231	AKR1B1
30	ENSG00000086015	23139	MAST2
31	ENSG00000090263	51650	MRPS33
32	ENSG00000091640	9552	SPAG7
33	ENSG00000095321	1384	CRAT
34	ENSG00000099204	3983	ABLIM1
35	ENSG00000099624	513	ATP5F1D
36	ENSG00000100116	23464	GCAT
37	ENSG00000100284	10043	TOM1
38	ENSG00000100347	25813	SAMM50
39	ENSG00000100577	2954	GSTZ1
40	ENSG00000100897	80344	DCAF11
41	ENSG00000101470	7125	TNNC2
42	ENSG00000101605	8736	MYOM1
43	ENSG00000102225	5127	CDK16
44	ENSG00000102878	3299	HSF4
45	ENSG00000103942	9455	HOMER2
46	ENSG00000103994	64397	ZNF106
47	ENSG00000104812	2997	GYS1
48	ENSG00000104823	1891	ECH1
49	ENSG00000105204	9149	DYRK1B
50	ENSG00000105379	2109	ETFB
51	ENSG00000105643	27106	ARRDC2

52	ENSG00000105711	6324	SCN1B
53	ENSG00000105953	4967	OGDH
54	ENSG00000107404	1855	DVL1
55	ENSG00000107537	5264	PHYH
56	ENSG00000108179	10105	PPIF
57	ENSG00000108515	2027	ENO3
58	ENSG00000108528	8402	SLC25A11
59	ENSG00000109063	4621	MYH3
60	ENSG00000109846	1410	CRYAB
61	ENSG00000110955	506	ATP5F1B
62	ENSG00000111669	7167	TPI1
63	ENSG00000112294	7915	ALDH5A1
64	ENSG00000112667	10591	DNPH1
65	ENSG00000114378	3373	HYAL1
66	ENSG00000114738	7867	MAPKAPK3
67	ENSG00000114770	10057	ABCC5
68	ENSG00000114854	7134	TNNC1
69	ENSG00000115286	374291	NDUFS7
70	ENSG00000116898	64960	MRPS15
71	ENSG00000117054	34	ACADM
72	ENSG00000117408	9670	IPO13
73	ENSG00000119013	4709	NDUFB3
74	ENSG00000120053	2805	GOT1
75	ENSG00000121577	64091	POPDC2
76	ENSG00000121769	2170	FABP3
77	ENSG00000122873	55847	CISD1
78	ENSG00000123178	57213	SPRYD7
79	ENSG00000123689	50486	G0S2
80	ENSG00000124596	221443	OARD1
81	ENSG00000124701	10930	APOBEC2
82	ENSG00000125166	2806	GOT2
83	ENSG00000125356	4694	NDUFA1
84	ENSG00000125744	6253	RTN2
85	ENSG00000126016	154796	AMOT
86	ENSG00000126267	1340	Cox6B1
87	ENSG00000126453	83596	BCL2L12
88	ENSG00000126778	6495	SIX1
89	ENSG00000127540	10975	UQCR11
90	ENSG00000127824	7277	TUBA4A
91	ENSG00000128311	7263	TST

92	ENSG00000128591	2318	FLNC
93	ENSG00000130005	2593	GAMT
94	ENSG00000130159	51295	ECSIT
95	ENSG00000130528	3270	HRC
96	ENSG00000130560	10422	UBAC1
97	ENSG00000130600	283120	H19
98	ENSG00000130600	102724852	H19
99	ENSG00000130770	93974	ATP5IF1
100	ENSG00000130821	6535	SLC6A8
101	ENSG00000131828	5160	PDHA1
102	ENSG00000132313	51318	MRPL35
103	ENSG00000132361	23277	CLUH
104	ENSG00000132688	10763	NES
105	ENSG00000132819	55544	RBM38
106	ENSG00000133878	78986	DUSP26
107	ENSG00000134253	80263	TRIM45
108	ENSG00000135447	5502	PPP1R1A
109	ENSG00000135469	93058	COQ10A
110	ENSG00000135617	84279	PRADC1
111	ENSG00000135723	29109	FHOD1
112	ENSG00000135940	1329	Cox5B
113	ENSG00000136270	9238	TBRG4
114	ENSG00000136383	57538	ALPK3
115	ENSG00000136463	51204	TACO1
116	ENSG00000136717	274	BIN1
117	ENSG00000137198	2766	GMPR
118	ENSG00000137288	84300	UQCC2
119	ENSG00000137309	3159	HMGA1
120	ENSG00000137547	29088	MRPL15
121	ENSG00000137700	2542	SLC37A4
122	ENSG00000138029	3032	HADHB
123	ENSG00000138073	10113	PREB
124	ENSG00000138615	8483	CILP
125	ENSG00000138629	84993	UBL7
126	ENSG00000139180	4704	NDUFA9
127	ENSG00000140403	55466	DNAJA4
128	ENSG00000140416	7168	TPM1
129	ENSG00000140990	4716	NDUFB10
130	ENSG00000141401	3613	IMPA2
131	ENSG00000141744	5409	PNMT

132	ENSG00000143028	284612	SYPL2
133	ENSG00000143164	55827	DCAF6
134	ENSG00000143434	10500	SEMA6C
135	ENSG00000143549	7170	TPM3
136	ENSG00000143632	58	ACTA1
137	ENSG00000143801	5664	PSEN2
138	ENSG00000143816	7483	WNT9A
139	ENSG00000146066	192286	HIGD2A
140	ENSG00000146701	4191	MDH2
141	ENSG00000147123	54539	NDUFB11
142	ENSG00000148187	92399	MRRF
143	ENSG00000148677	27063	ANKRD1
144	ENSG00000149016	64852	TUT1
145	ENSG00000149925	226	ALDOA
146	ENSG00000151632	1646	AKR1C2
147	ENSG00000151729	291	SLC25A4
148	ENSG00000152556	5213	PFKM
149	ENSG00000154153	54463	RETREG1
150	ENSG00000154518	518	ATP5MC3
151	ENSG00000154930	84532	ACSS1
152	ENSG00000156298	7102	TSPAN7
153	ENSG00000156381	122416	ANKRD9
154	ENSG00000158864	4720	NDUFS2
155	ENSG00000159199	516	ATP5MC1
156	ENSG00000159348	51706	CYB5R1
157	ENSG00000159423	8659	ALDH4A1
158	ENSG00000159713	51673	TPPP3
159	ENSG00000160097	252995	FNDC5
160	ENSG00000160194	4731	NDUFV3
161	ENSG00000160299	5116	PCNT
162	ENSG00000160392	126526	C19orf47
163	ENSG00000160539	84814	PLPP7
164	ENSG00000160972	84988	PPP1R16A
165	ENSG00000161281	1346	Cox7A1
166	ENSG00000162409	5563	PRKAA2
167	ENSG00000163050	56997	COQ8A
168	ENSG00000164405	27089	UQCRQ
169	ENSG00000164591	91977	MYOZ3
170	ENSG00000164896	10922	FASTK
171	ENSG00000164898	154791	FMC1

172	ENSG00000164967	138716	RPP25L
173	ENSG00000164976	57462	MYORG
174	ENSG00000165526	84881	RPUSD4
175	ENSG00000165795	57447	NDRG2
176	ENSG00000165886	80019	UBTD1
177	ENSG00000165912	29763	PACSIN3
178	ENSG00000166123	84706	GPT2
179	ENSG00000166289	79156	PLEKHF1
180	ENSG00000166348	159195	USP54
181	ENSG00000166619	10904	BLCAP
182	ENSG00000167508	4597	MVD
183	ENSG00000167549	84940	CORO6
184	ENSG00000167588	2819	GPD1
185	ENSG00000167676	729359	PLIN4
186	ENSG00000167693	64359	NXN
187	ENSG00000167700	113655	MFSD3
188	ENSG00000167705	83547	RILP
189	ENSG00000167792	4723	NDUFV1
190	ENSG00000167969	1632	ECI1
191	ENSG00000169021	7386	UQCRFS1
192	ENSG00000169252	154	ADRB2
193	ENSG00000169738	51181	DCXR
194	ENSG00000170681	347273	CAVIN4
195	ENSG00000170906	4696	NDUFA3
196	ENSG00000171055	9637	FEZ2
197	ENSG00000171161	79894	ZNF672
198	ENSG00000171813	170394	PWWP2B
199	ENSG00000171992	11346	SYNPO
200	ENSG00000172046	10869	USP19
201	ENSG00000172159	257019	FRMD3
202	ENSG00000172366	84331	MCRIP2
203	ENSG00000172456	55277	FGGY
204	ENSG00000172458	53342	IL17D
205	ENSG00000172508	57571	CARNS1
206	ENSG00000172663	80194	TMEM134
207	ENSG00000173641	27129	HSPB7
208	ENSG00000173991	8557	TCAP
209	ENSG00000174437	488	ATP2A2
210	ENSG00000175084	1674	DES
211	ENSG00000175445	4023	LPL

212	ENSG00000175606	54968	TMEM70
213	ENSG00000175826	23399	CTDNEP1
214	ENSG00000176087	113829	SLC35A4
215	ENSG00000176101	8636	SSNA1
216	ENSG00000176340	1351	Cox8A
217	ENSG00000176909	284358	MAMSTR
218	ENSG00000177791	58529	MYOZ1
219	ENSG00000178104	9659	PDE4DIP
220	ENSG00000178307	8834	TMEM11
221	ENSG00000178741	9377	Cox5A
222	ENSG00000178952	7284	TUFM
223	ENSG00000178982	27335	EIF3K
224	ENSG00000179091	1537	CYC1
225	ENSG00000179262	5886	RAD23A
226	ENSG00000179542	139065	SLITRK4
227	ENSG00000180209	29895	MYLPF
228	ENSG00000180992	64928	MRPL14
229	ENSG00000181817	84967	LSM10
230	ENSG00000181856	6517	SLC2A4
231	ENSG00000182054	3418	IDH2
232	ENSG00000182175	56963	RGMA
233	ENSG00000183386	2275	FHL3
234	ENSG00000183520	51118	UTP11
235	ENSG00000183628	8214	DGCR6
236	ENSG00000183828	256281	NUDT14
237	ENSG00000184076	29796	UQCR10
238	ENSG00000184207	283871	PGP
239	ENSG00000184343	26576	SRPK3
240	ENSG00000184489	11156	PTP4A3
241	ENSG00000185100	122622	ADSS1
242	ENSG00000185608	64976	MRPL40
243	ENSG00000185739	6345	SRL
244	ENSG00000187193	4501	MT1X
245	ENSG00000187486	3767	KCNJ11
246	ENSG00000188807	199953	TMEM201
247	ENSG00000189159	51155	JPT1
248	ENSG00000196465	140465	MYL6B
249	ENSG00000196923	9260	PDLIM7
250	ENSG00000198125	4151	MB
251	ENSG00000198720	124930	ANKRD13B

252	ENSG00000198892	149345	SHISA4
253	ENSG00000198925	79065	ATG9A
254	ENSG00000204564	221545	C6orf136
255	ENSG00000213619	4722	NDUFS3
256	ENSG00000214456	440503	PLIN5
257	ENSG00000224051	80772	CPTP
258	ENSG00000224165	729723	DNAJC27-AS1
259	ENSG00000235109	64288	ZSCAN31
260	ENSG00000239900	158	ADSL
261	ENSG00000241468	9551	ATP5MF
262	ENSG00000247516	100505738	MIR4458HG
263	ENSG00000247595	100506540	SPTY2D1OS
264	ENSG00000247596	11344	TWF2
265	ENSG00000249249	NA	AC010226.1
266	ENSG00000250479	400916	CHCHD10
267	ENSG00000253716	100507316	MINCR
268	ENSG00000255468	102724064	AP001107.9
269	ENSG00000259291	109729181	ZNF710-AS1
270	ENSG00000259494	26589	MRPL46
271	ENSG00000260401	NA	AP002761.4
272	ENSG00000264920	102724532	AC018521.5
273	ENSG00000265142	102723167	MIR133A1HG
274	ENSG00000267060	100885848	PTGES3L
275	ENSG00000269293	100129195	ZSCAN16-AS1
276	ENSG00000270039	NA	AC025165.5
277	ENSG00000272288	101929243	ILRUN-AS1

3.3.4 A vascular wall transcriptomic signature predicts long-term cardiovascular risk

Alluvial plots presented in Figure 3.17 demonstrate the distribution of characteristics within patients that died during the study arm's follow-up period. In total, over a median follow-up period of 4.12 years [IQR: 2.11-7.61], 15 (7.3%) deaths, 14 (6.8%) events of cardiovascular death or non-fatal acute myocardial infarction, 19 (9.3%) composite endpoints of cardiovascular death

or non-fatal acute myocardial infarction, non-fatal stroke, and 21 (10.2%) major adverse cardiac events were recorded (MACE: Cardiovascular death or non-fatal acute myocardial infarction, non-fatal stroke, or first admission for heart failure).

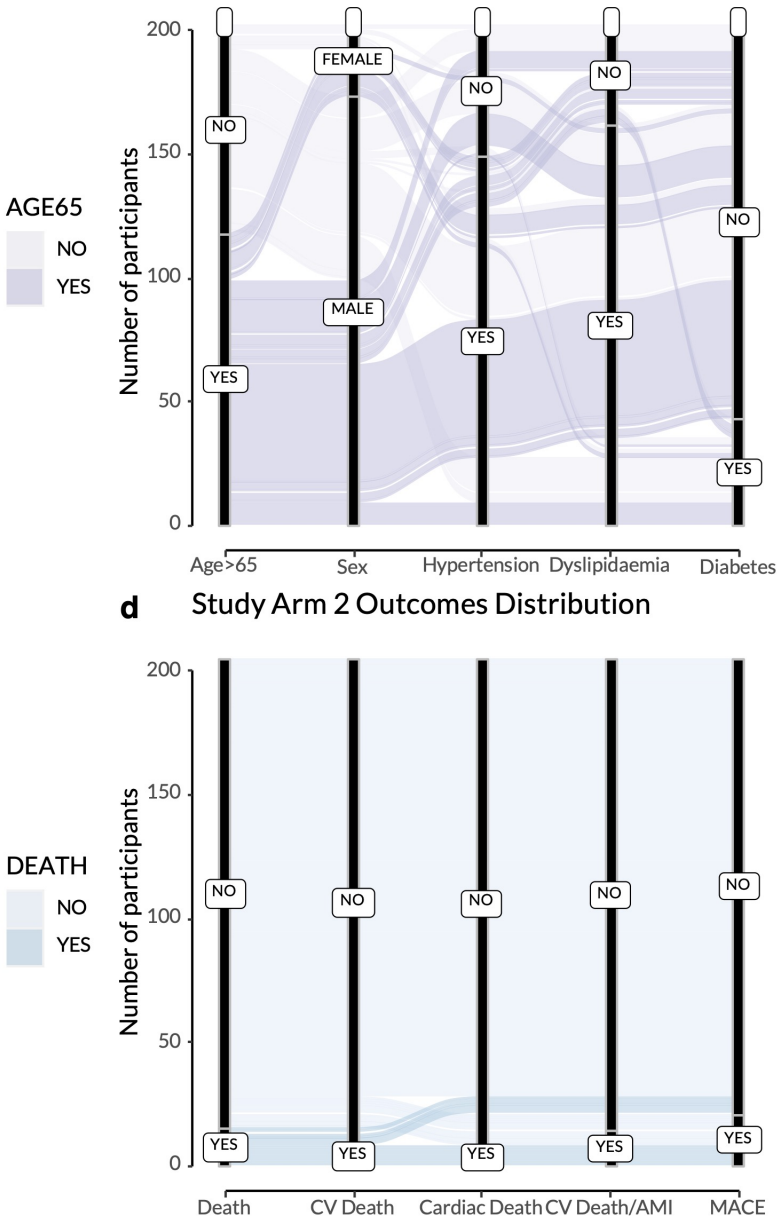


Figure 3.17: Study Arm 2 alluvial plot based on risk factors and long-term outcomes. (a) Dark purple lines represent participants aged over 65, with most of them having risk factors hypertension, dyslipidemia, and diabetes compared with younger participants. (b) Dark blue lines represent participants who died during follow up in Study Arm 2, most of which were of cardiovascular etiology.

Red signature eigengenes were left-skewed in the Study Arm 2 population and a log-rank threshold was computed. This was done to create a dichotomization in the cohort and avoid any potential effect of the data's skewed distribution on the Cox model outcome. Following multivariable adjustment for age, sex, and risk factors (hypertension, dyslipidaemia, diabetes, plasma TNFa), patients with high eigengenes for the red transcriptomic signature had a 3.4-fold higher adjusted risk for a composite endpoint of cardiovascular death or non-fatal acute myocardial infarction, non-fatal stroke, and a 3-fold increase in the adjusted risk for MACE (Figure 3.19).

I present here for the first time a novel human arterial transcriptomic signature reflecting changes in redox state, which identifies long-term cardiovascular risk.

In order to further explore the biological meaning of the discovered red signature that has striking prognostic value, I conducted pathway enrichment analyses. Enrichment analysis of genes within the red signature highlighted 'Oxidative phosphorylation', 'Glycolysis and Gluconeogenesis', and 'Hypoxia-Induced Factor-1 (HIF-1) signalling pathway' as the top enriched pathways (Figure 3.18). Interestingly, the most significant pathway was that of NAFLD which is a compelling finding that needs to be further explored for potential causality links in the future.

An intersection plot reveals that many genes are shared between enriched pathways, while others are more intrinsic to particular pathways enriched, such as the transferrin receptor gene (TFRC) in the HIF-1 signalling pathway, the Cytochrome C Oxidase Assembly Protein (Cox-10) gene in the thermogenesis and oxidative phosphorylation pathways, or the Adrenoceptor Beta 2 (ADRB2) gene found in the Adrenergic signalling in cardiomyocytes and cGMP-PKG signalling pathways (Figure 3.20).

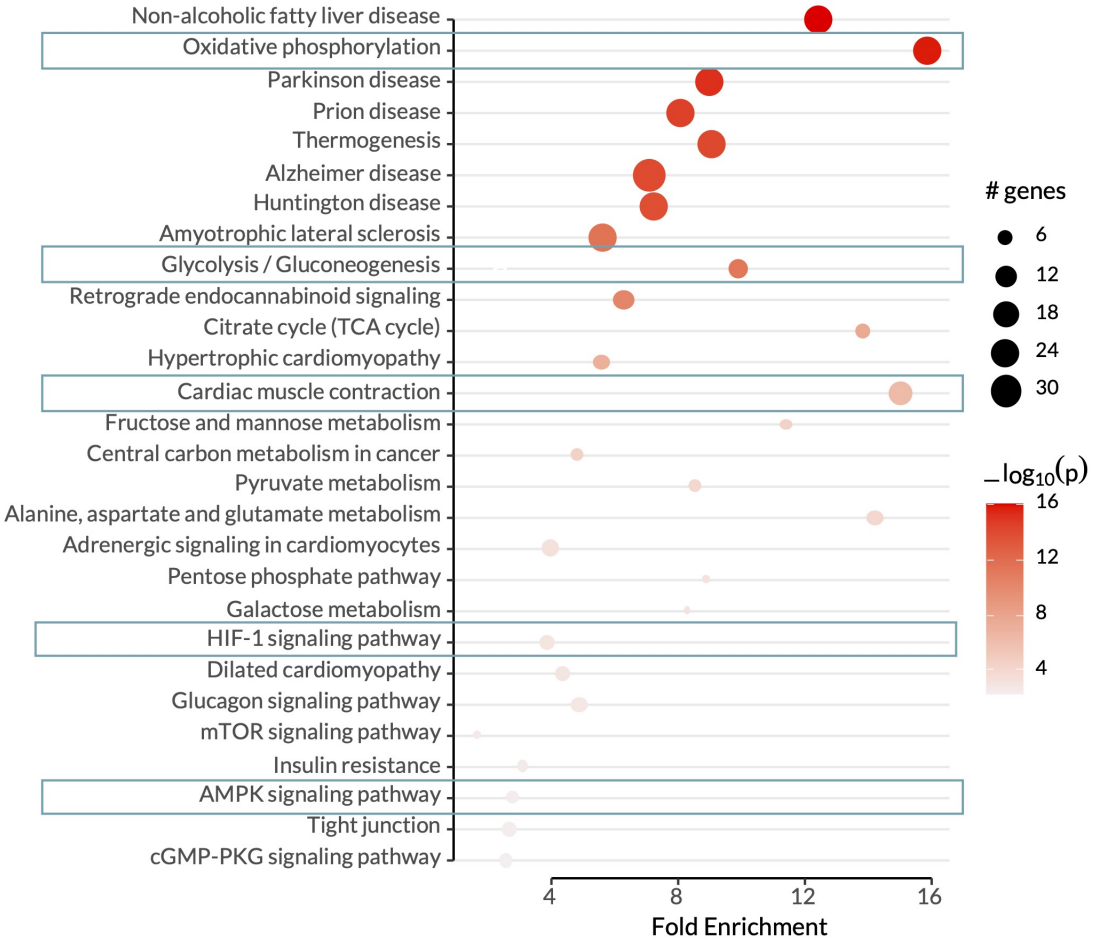


Figure 3.18: Pathway enrichment analysis for the red signature. Pathway enrichment analysis for genes in the red signature. Enrichment analysis of genes within the red signature highlighted 'Oxidative phosphorylation', 'Glycolysis and Gluconeogenesis', and 'Hypoxia-Induced Factor-1 (HIF-1) signalling pathway' as the top enriched pathways. FDR corrected p values are indicated by red colour's intensity as seen in right hand side lower panel.

In addition, to provide further insight into the nature of the red signature I also performed gene ontology analyses based on the list of 277 genes comprising the signature. Figure 3.21 presents the top gene ontology terms enriched within the 'Biological Process' domain. 'Mitochondrial respiratory chain' processes were the top processes enriched with metabolic processes, such as 'gluconeogenesis', and 'canonical glycolysis' following. As expected, these pathways mirror the results of the pathway enrichment analysis. Figure 3.22 showcases the top terms en-

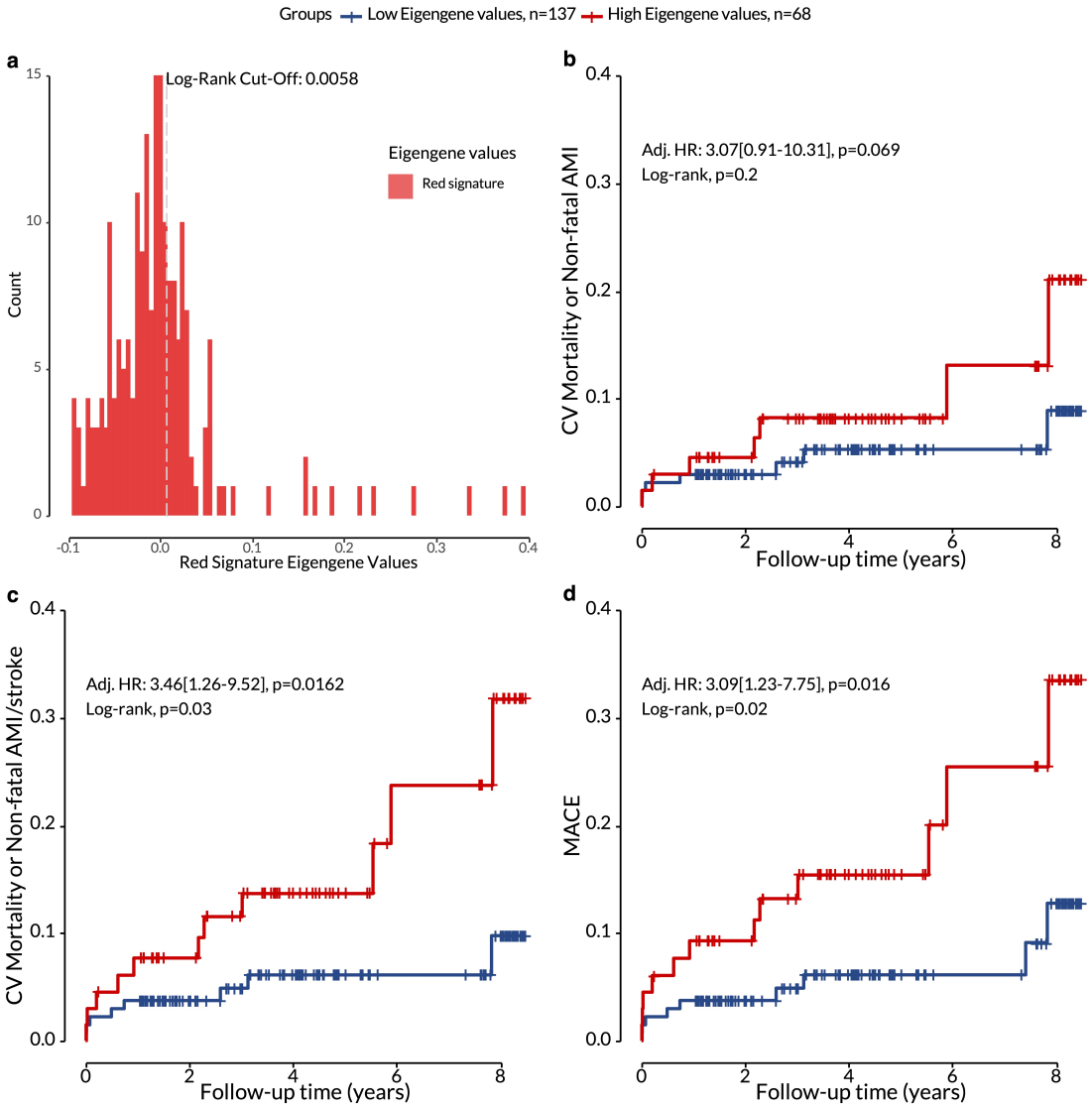


Figure 3.19: Prognostic value of the red transcriptomic signature. (a) Red signature eigengenes were left-skewed in the Study Arm 2 population and a log-rank threshold was computed. (b-d) Kaplan Meier curves and adjusted hazard ratios for three endpoints after dividing the Study Arm 2 population for an optimal red signature eigengenes log-rank cut-off, and following multivariable adjustment for age, sex, and risk factors (hypertension, dyslipidaemia, diabetes, plasma TNFa).

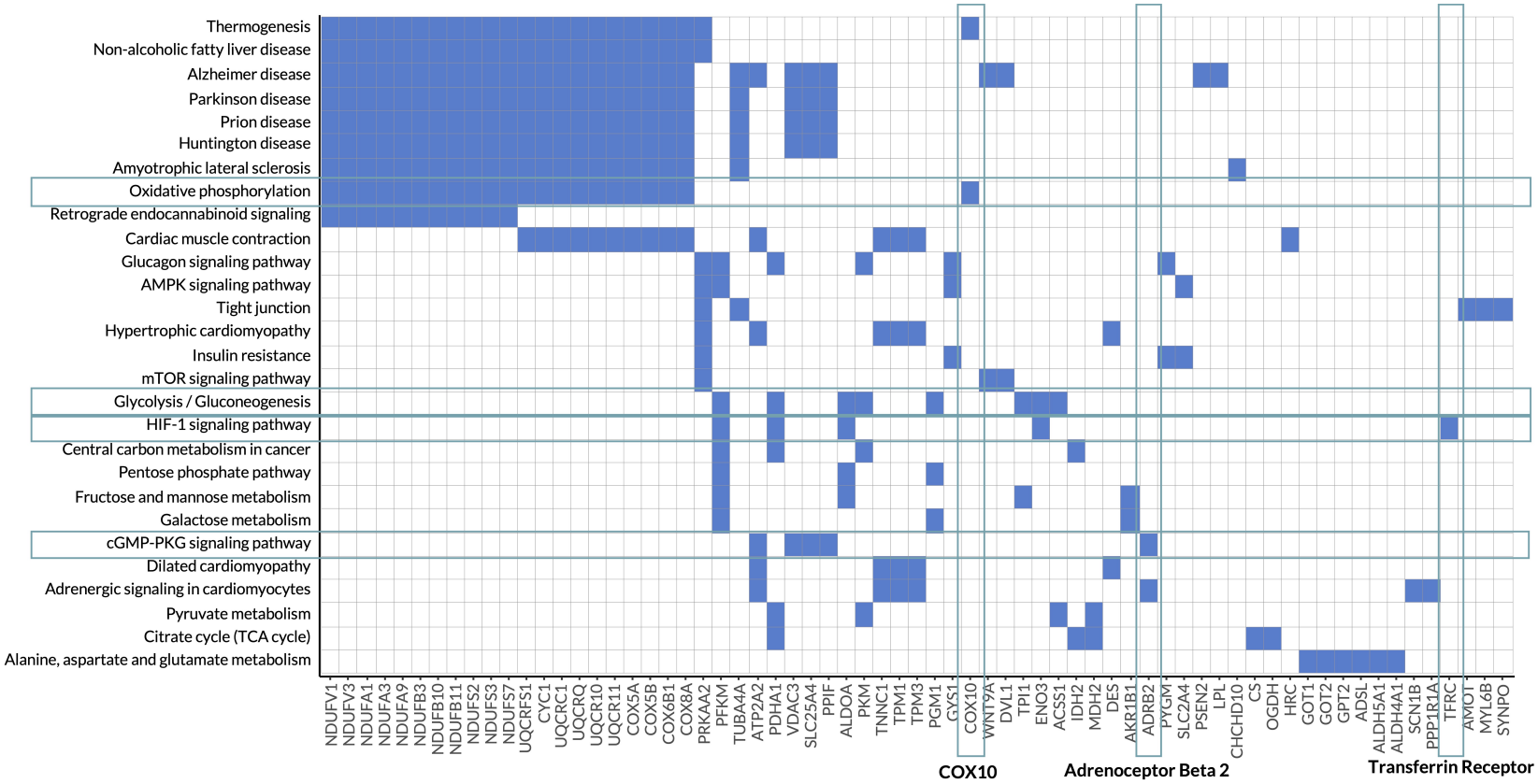


Figure 3.20: Intersection plot for pathways in the red signature.

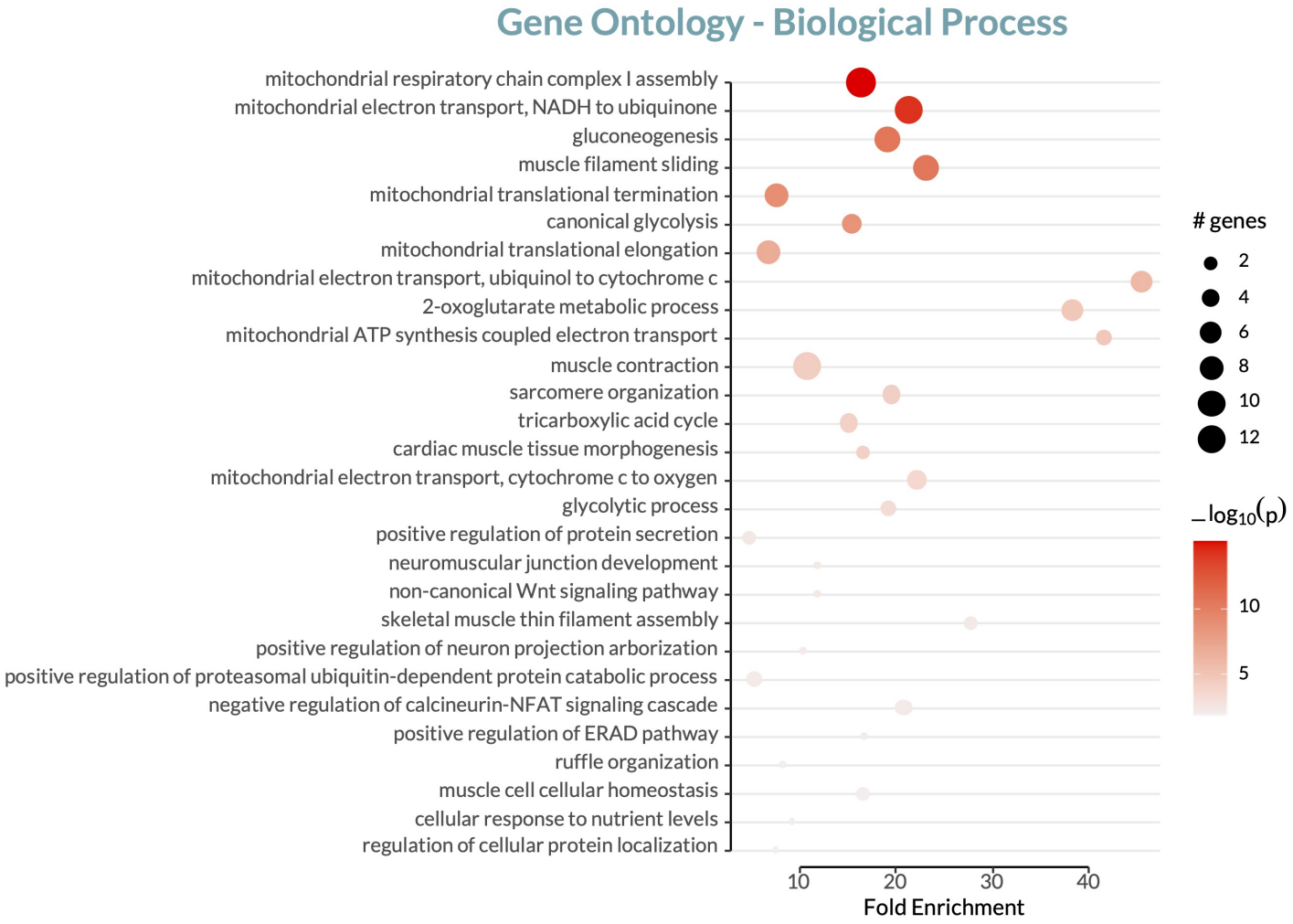


Figure 3.21: Gene Ontology analysis of the red signature: Biological Process. FDR corrected p values are indicated by red colour's intensity as seen in right hand side lower panel.

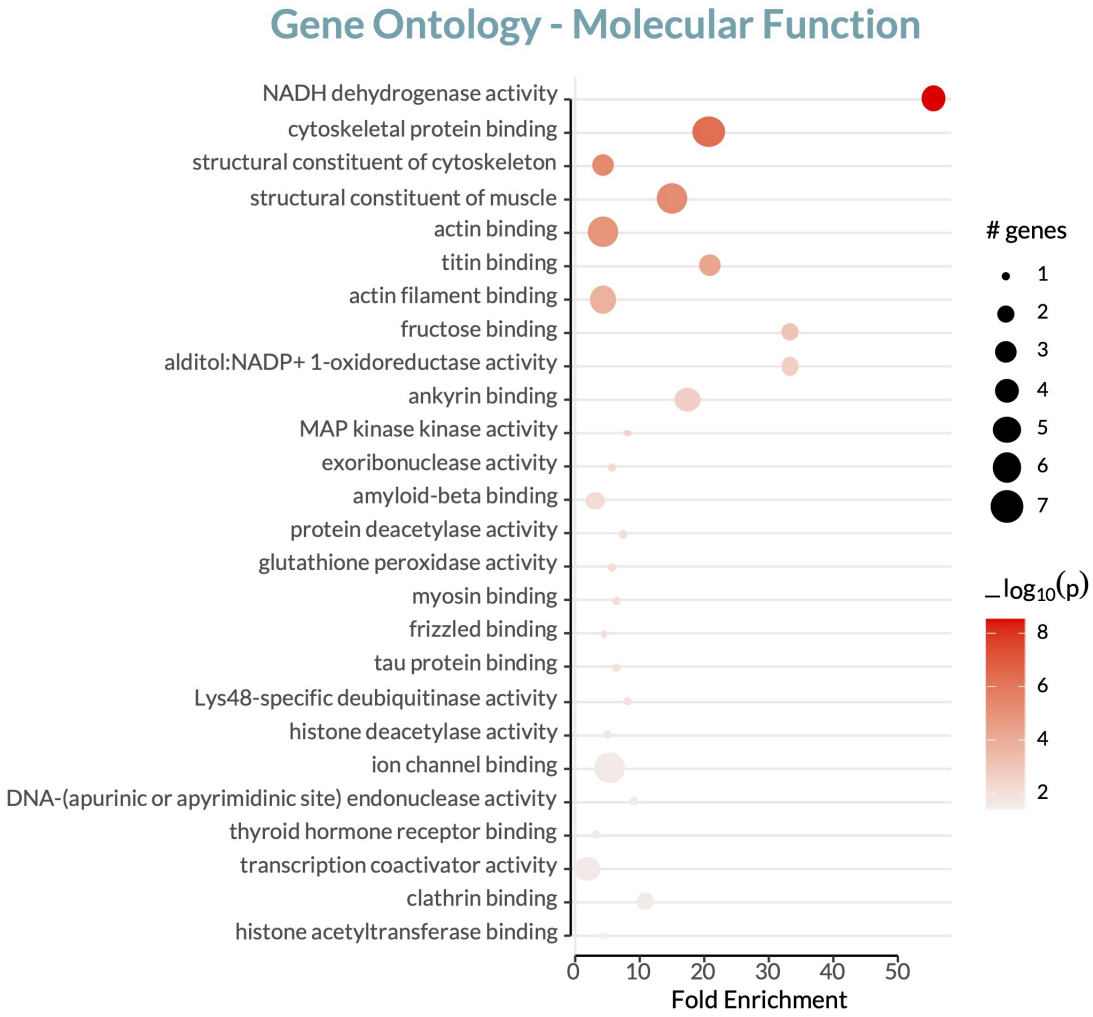


Figure 3.22: Gene Ontology analysis of the red signature: Molecular Function. FDR corrected p values are indicated by red colour's intensity as seen in right hand side lower panel.

riched within the 'Molecular Function' domain of gene ontology, with 'NADH dehydrogenase activity', 'cytoskeletal protein binding', and 'structural constituent of cytoskeleton' being the top three terms. This information highlight the importance of these pathways in determining risk associated with increases arterial oxidative stress and may inform the discovery of novel therapeutic targets to improve long-term outcomes in patients with atherosclerosis.

Studying these gene interactions would have the potential to reveal pathways or individual genes as novel candidates that may lead to the development of novel therapeutics in cardiovascular disease.

3.3.5 Combining transcriptomic and genomic data reveals OGDH, SRL, and USP13 genes as top genetic candidates of vascular oxidative stress

Finally, to test potential causality, I looked into data from an exploratory genome wide association study with IMA NADPH oxidase activity in the Study Arm 1 population and sought to identify genes that would be highlighted in genomic analysis and simultaneously form part of my newly developed arterial transcriptomic signature. Indeed, using a soft GWAS threshold of p=0.0001, three genes -OGDH, SRL, and USP13- were identified, genetic variations of which were found to correlate with IMA NADPH oxidase activity, while at the same time their expression levels were found to be upregulated in the vascular wall in a manner that is linked with oxidative stress and long-term risk of cardiovascular events (Figure 3.23).

Oxoglutarate Dehydrogenase, a Krebs cycle enzyme, was the top gene with SNP rs148449548, being the only one that attained genome-wide significance. Interestingly, high OGDH expres-

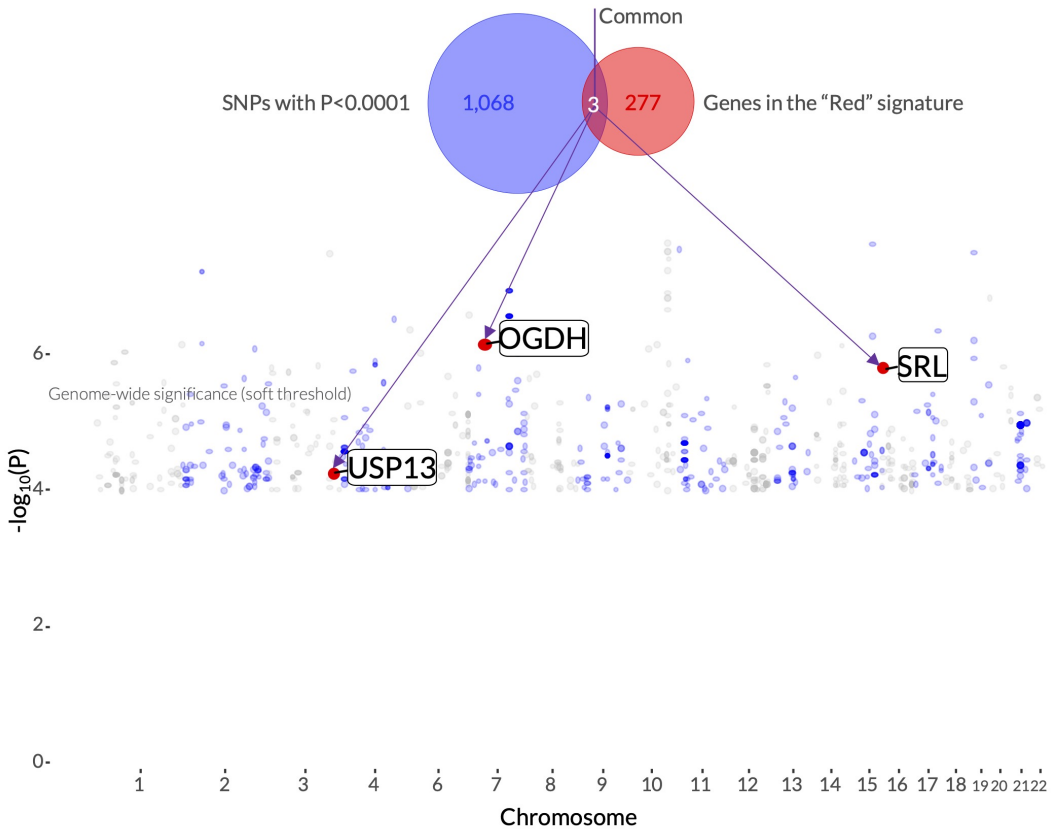


Figure 3.23: Genes in the red signature identified in GWAS in association with IMA NADPH oxidase activity. Applying a soft GWAS threshold of p=0.0001, three genes -OGDH, SRL, and USP13- were identified, genetic variations of which were found to correlate with IMA NADPH oxidase activity, while at the same their expression levels were annotated in the red signature. (Genes with p values above 0.0001 are not presented). OGDH:Oxoglutarate Dehydrogenase; SRL:Sarcalumenin; USP13:Ubiquitin carboxyl-terminal hydrolase 13.

sion in internal mammary arteries was associated with a 3.3-fold higher adjusted risk for the composite endpoint of CV mortality, non-fatal Acute Myocardial Infarction or non-fatal stroke and a 3.9-fold higher adjusted risk of MACE (Figure 3.24).

This approach reveals the significant potential of combining clinical, follow-up, transcriptomic and genomic data from patients in order to identify top candidate genes and pathways that may improve our understanding of cardiovascular disease pathogenesis and lead to new therapies.

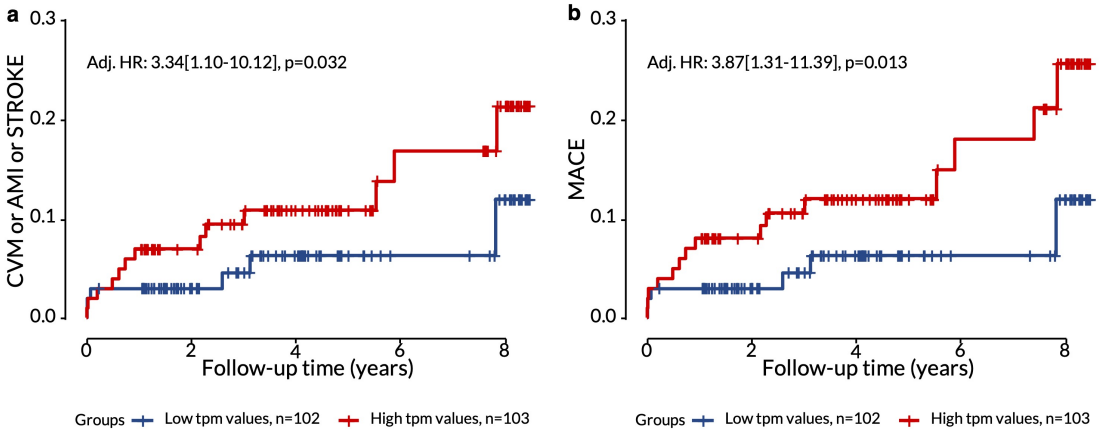


Figure 3.24: High OGDH expression in internal mammary arteries is associated with cardiac risk. Kaplan Meier curves and adjusted hazard ratios for two endpoints (a: cardiovascular death or non-fatal myocardial infarction or non-fatal stroke, b: cardiovascular death or non-fatal myocardial infarction or non-fatal stroke or first admission for heart failure) after dividing the Study Arm 2 population for an optimal IMA OGDH tpm value log-rank cut-off, and following multivariable adjustment for age, sex, and risk factors (hypertension, dyslipidaemia, diabetes, plasma TNFα). OGDH:Oxoglutarate Dehydrogenase; tpm: transcripts per million.

3.3.6 Myocardial oxidative stress and long-term outcomes

Study Arm 3 included 258 patients undergoing cardiac surgery. Table 3.4 presents demographics of these patients. Alluvial plots presented in Figure 3.25 demonstrates the distribution of characteristics within patients that died during the study's follow-up period. In total, over a median follow-up period of 5.45 years [IQR: 4.28-6.83], 22 (8.5%) deaths were recorded, of which 10 (3.9%) were of cardiovascular aetiology. Also, 28 major adverse cardiac events occurred (MACE: Cardiovascular death or non-fatal acute myocardial infarction, non-fatal stroke, or first admission for heart failure).

In univariate Cox regression analysis (Figure 3.27), myocardial NADPH oxidase activity (right atrial appendage (RAA) NADPH) was linked to a higher risk for all-cause mortality (HR [95% CI]: 1.38 [1.11-1.72] per 1 SD increase, P=0.0037), cardiovascular mortality (HR [95%

Table 3.4: Study Arm 3 Population Characteristics

	Study Arm 3
n	258
MALE SEX (%)	220 (85.3)
HYPERTENSION = YES (%)	186 (72.1)
DYSLIPIDAEMIA = YES (%)	204 (79.1)
DIABETES = YES (%)	47 (18.2)
SMOKING (%)	
Never	99 (38.4)
Past	134 (51.9)
Active	25 (9.7)
Follow-up (years)	5.45 [IQR: 4.28-6.83]
DEATH (%)	22 (8.5)
CV DEATH (%)	10 (3.9)
CARDIAC DEATH (%)	7 2.7)
CVD/AMI (%)	19 (7.4)
CVD/AMI/STROKE (%)	27 (10.5)
MACE (%)	28 (10.9)

CV: Cardiovascular; AMI: non-fatal Acute Myocardial Infarction; STROKE: non-fatal stroke; MACE: Major adverse cardiac event (CVD or AMI or STROKE or first admission for heart failure)

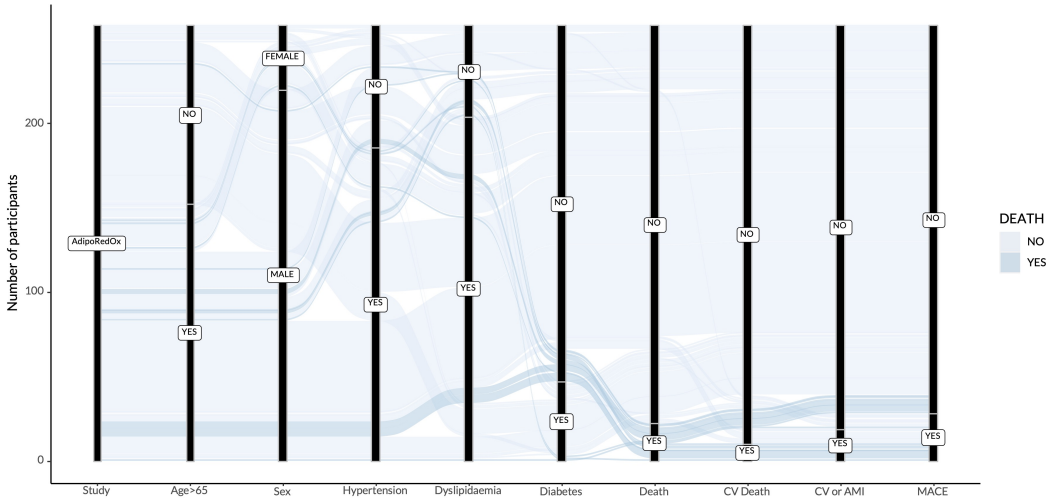


Figure 3.25: Study Arm 3 alluvial plot based on outcome. Dark blue lines represent participants that died during the study's follow up period. Almost half of those experienced cardiovascular death. Further, the majority of patients that died during follow up were males aged above 65, had hypertension and dyslipidaemia, as opposed to those with diabetes, which was a less frequently observed risk factor amongst that subgroup.

CI]: 1.48 [1.11-1.99] per 1 SD increase, P=0.008), and MACE (HR [95% CI]: 1.36 [1.09-1.70] per 1 SD increase, P=0.005). Equally, myocardial Vas2870 inhibitable oxidative stress (RAA Vas) was linked to a higher risk for all-cause mortality (HR [95% CI]: 1.47 [1.18-1.83] per 1 SD increase, P=0.0005), cardiovascular mortality (HR [95% CI]: 1.67 [1.25-2.23] per 1 SD increase, P=0.0004), and MACE (HR [95% CI]: 1.43 [1.14-1.79] per 1 SD increase, P=0.001).

In multivariable Cox regression analysis (Figure 3.27) adjusted for age, sex, traditional cardiovascular risk factors, higher myocardial oxidative stress reflected by RAA NADPH oxidase activity retained its prognostic value and was linked to a higher adjusted risk of all-cause mortality (HR [95% CI]: 1.49 [1.12-1.97] per 1 SD increase, P=0.005), cardiovascular mortality (HR [95% CI]: 1.76 [1.14-2.71] per 1 SD increase, P=0.009), and MACE (HR [95% CI]: 1.39 [1.06-1.83] per 1 SD increase, P=0.01). Equally, myocardial Vas2870 inhibitable oxidative stress (RAA Vas) was linked to a higher adjusted risk of all-cause mortality (HR [95% CI]: 1.59 [1.21-2.08] per 1 SD increase, P=0.0006), cardiovascular mortality (HR [95% CI]: 1.96 [1.33-2.88] per 1 SD increase, P=0.0005), and MACE (HR [95% CI]: 1.46 [1.12-1.90] per 1 SD increase, P=0.004).

RAA resting oxidative stress and NADPH oxidase activity values measured by lucigenin chemiluminescence as relative light units (RLUs) per second, per tissue protein content were left-skewed. This observation prompted survival optimal cut-off analysis, using the maximally selected rank statistic, for myocardial oxidative stress as a predictor of all-cause mortality (Figure 3.26).

For an optimal cut-off point of 24,590 RLUs/sec/mg tissue protein patients with high RAA NADPH stimulated oxidative stress had a 14.9 times higher adjusted risk for cardiovascular

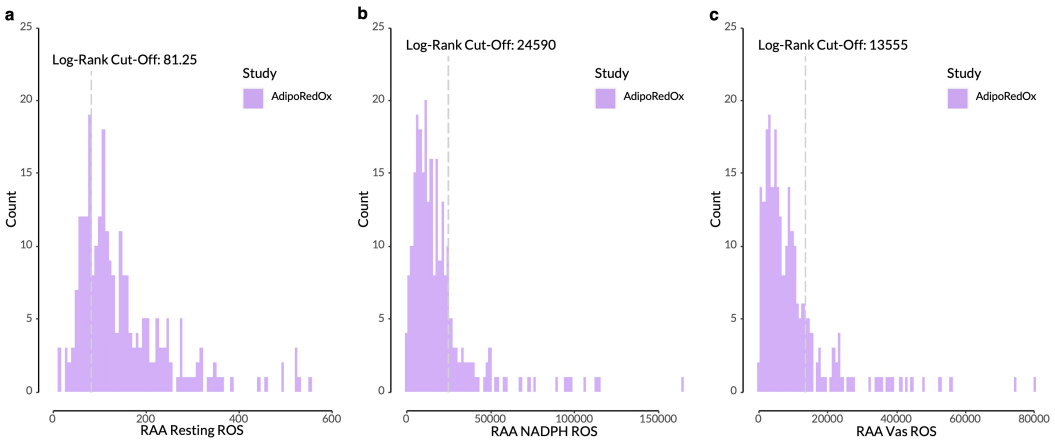


Figure 3.26: Computing cut-off points for myocardial oxidative stress indices. Histograms present the distribution of myocardial right atrial appendage resting, NAPDH and Vas inhibitable ROS across the Ox-HVF cohort. The dotted line indicates the value that maximises the log rank statistic. Values presented are in RLUs/sec/mg. RLU: relative light units; ROS: reactive oxygen species.

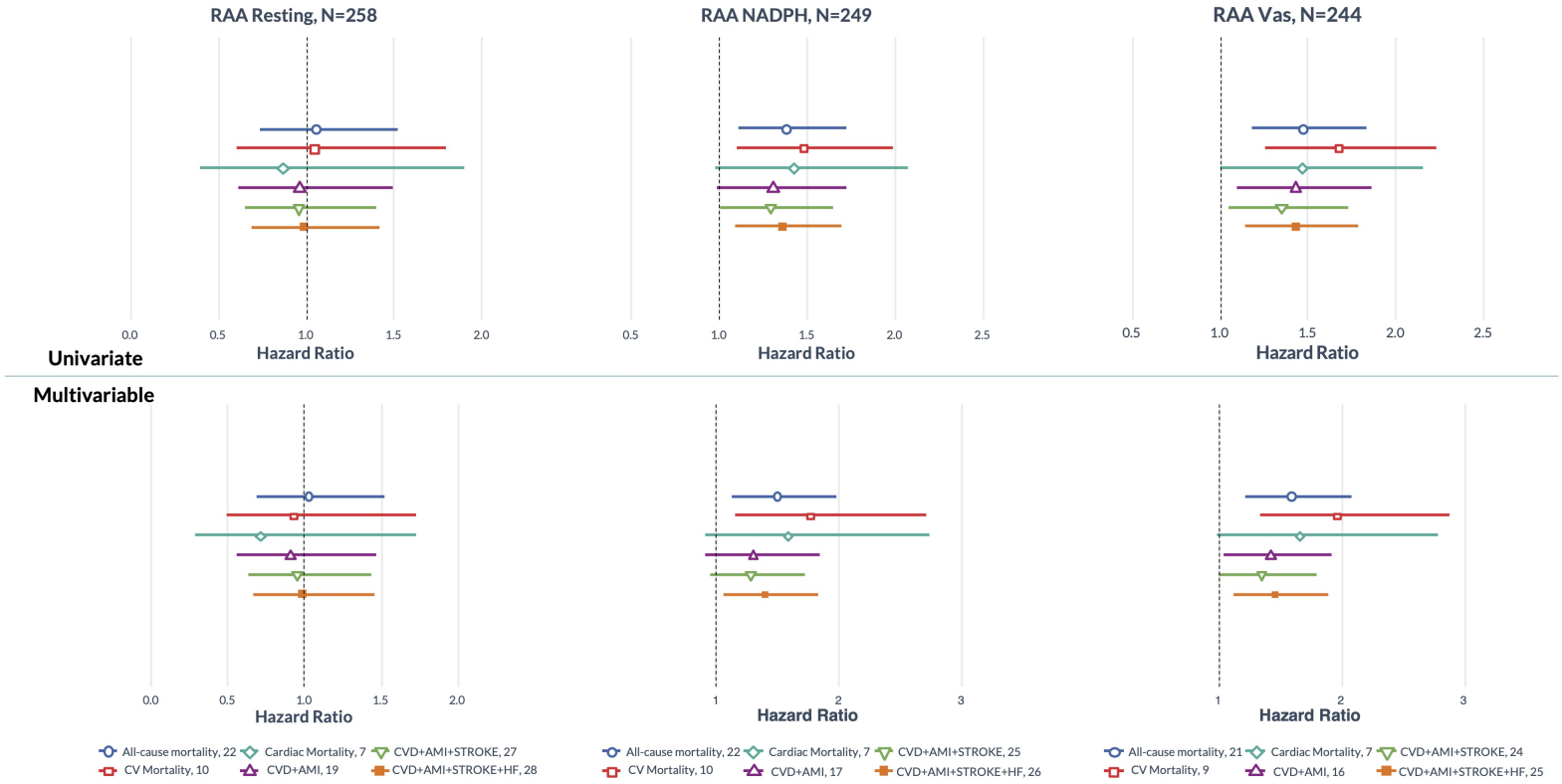


Figure 3.27: RAA oxidative stress as a continuous variable and long-term outcomes. Hazard ratios derived from univariate and multivariable Cox models. Numbers next to each outcome represent the number of events recorded.

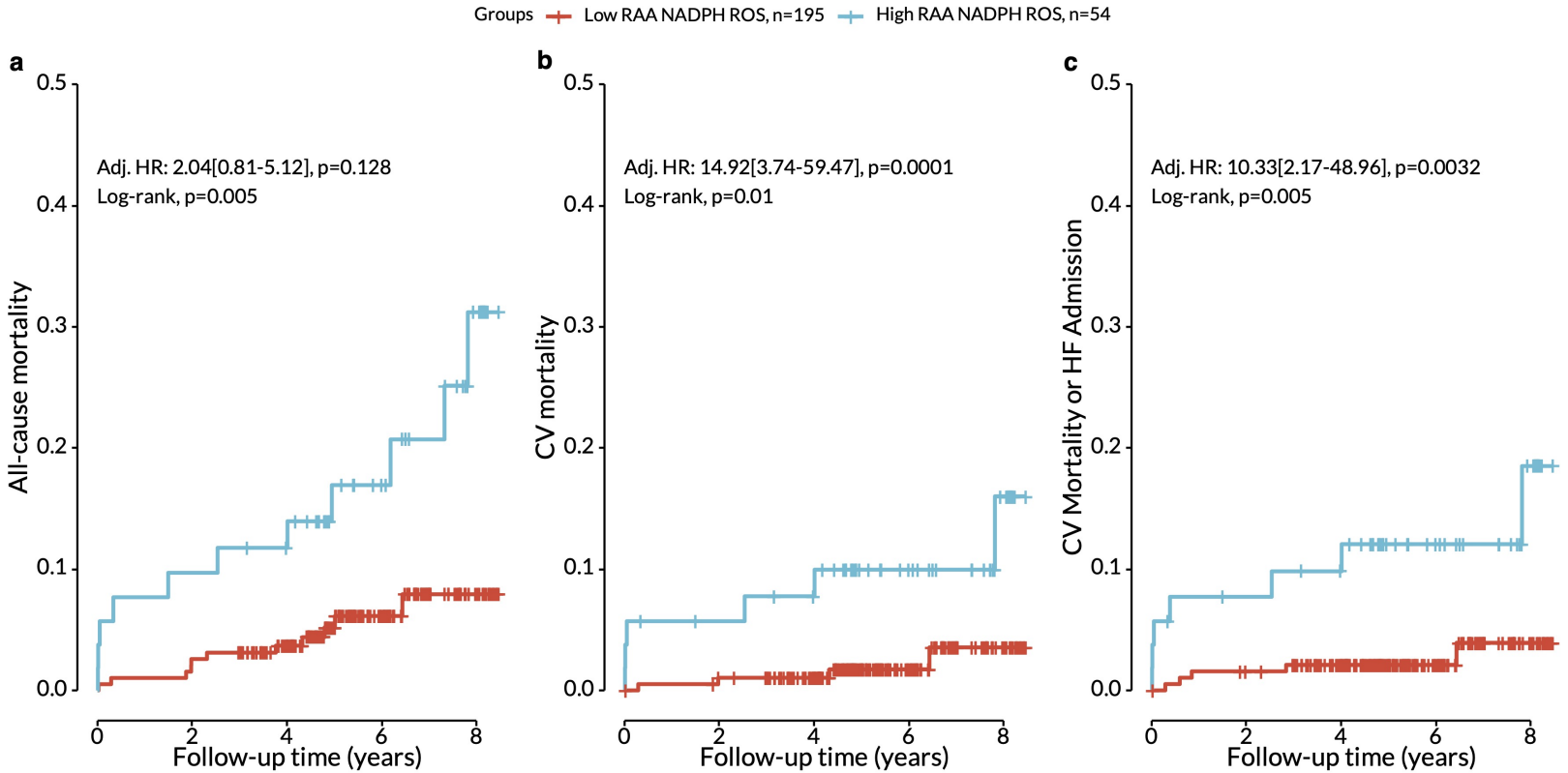


Figure 3.28: RAA NADPH stimulated oxidative stress Kaplan-Meier plots. Kaplan Meier curves and adjusted hazard ratios for three endpoints after dividing the Study Arm 3 population for an optimal RAA NADPH stimulated oxidative stress log-rank cut-off, and following multivariable adjustment for age, sex, and traditional cardiovascular risk factors.

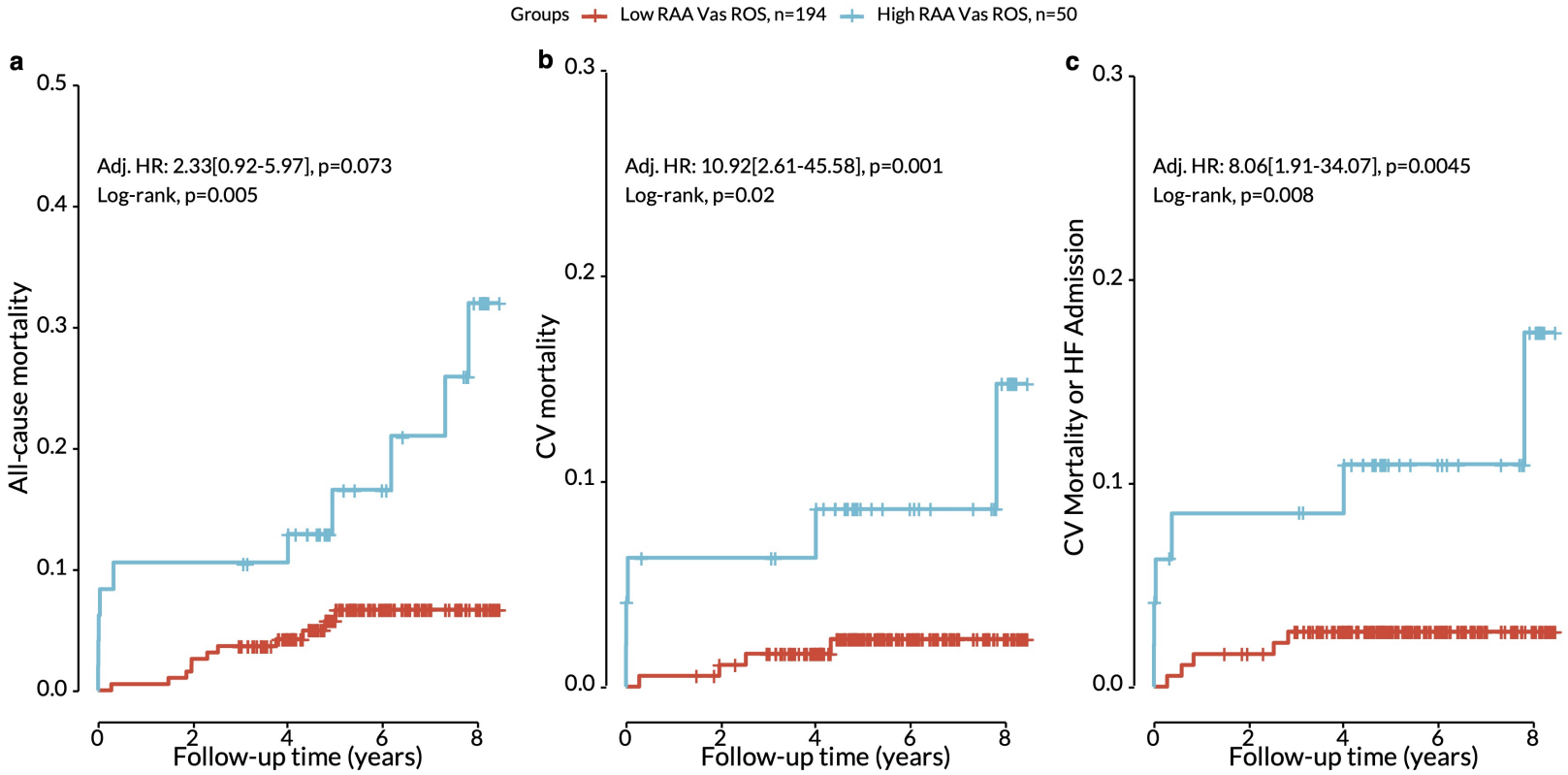


Figure 3.29: RAA Vas2870 inhibitable oxidative stress Kaplan-Meier plots. Kaplan Meier curves and adjusted hazard ratios for three endpoints after dividing the Study Arm 3 population for an optimal RAA Vas2870 inhibitable oxidative stress log-rank cut-off, and following multivariable adjustment for age, sex, and traditional cardiovascular risk factors.

death (P=0.0001), and a 10.3 times higher adjusted risk of a composite endpoint of cardiovascular mortality and first admission for heart failure (Figure 3.28).

Similarly, the same approach was adapted for myocardial Vas2870 inhibitable oxidative stress. Following multivariable adjustment for the aforementioned covariates, high Vas2870 inhibitable oxidase activity was associated with a 10.9-fold increase in the adjusted risk for cardiovascular death (Figure 4.1), and an eight times higher adjusted risk of a composite endpoint of cardiovascular mortality and first admission for heart failure.

In addition, I looked into Intensive Care Unit (ICU) admissions for the Study Arm 3 population, and observed that patients that had an unplanned ICU admission had significantly higher myocardial oxidative stress (Figure 3.30).

Taken all together, these observations highlight for the first time that increased myocardial oxidative stress is an independent predictor of long-term cardiac risk in patients with advanced atherosclerosis.

3.4 Discussion

In this chapter, I demonstrate that arterial oxidative stress leads to high risk of all-cause mortality, cardiovascular mortality and MACE in patients with advanced atherosclerosis. In addition, I unveil S100A8 and S100A9 as genes within the inflammatory pathways that are the most dysregulated in the presence of oxidative stress in the arterial wall. I also present for the first time a novel human arterial transcriptomic signature reflecting changes in redox state, which identifies long-term cardiovascular risk. I reveal pathways related with oxidative stress, or glucose metabolism or Hypoxia-Inducible Factor-1 in the human arterial wall, as potential rational

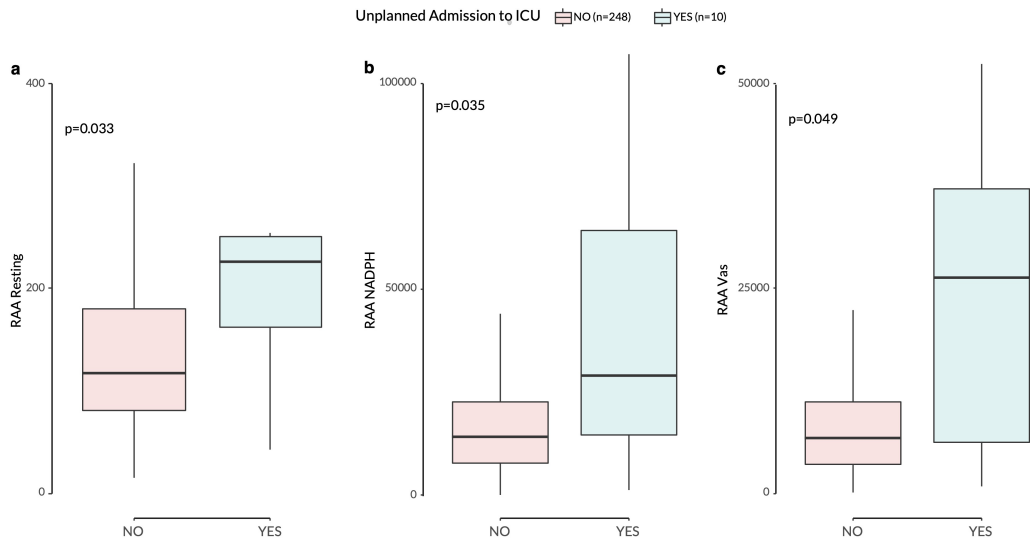


Figure 3.30: Myocardial oxidative stress and ICU admission. Patients with an unplanned ICU admission occurring during a future hospital admission (not within their cardiac surgery admission) had significantly higher myocardial oxidative stress.

therapeutic targets to reduce cardiovascular risk in secondary prevention. Furthermore, after combining genomic and transcriptomic data, I reveal genes that may form suitable candidates for future study as therapeutic targets, such as Oxoglutarate Dehydrogenase. Finally, I show for the first time the long-term prognostic potential of myocardial oxidative stress in cardiovascular mortality and for unplanned admission to the intensive care unit.

3.4.1 Oxidative stress in atherosclerosis

Oxidative stress is a key component of the inflammatory cascade, which has been linked with cardiovascular disease pathogenesis. Many studies have shown an increase in oxidized lipids and other oxidative stress markers in atherosclerotic lesions (Glavind, Hartmann, Clemmesen, Jessen, & Dam, 1952). Oxidative stress is responsible for the conversion of LDL cholesterol into the atherogenic form of oxidized-LDL (OxLDL), which has a crucial role in initiating and promoting the inflammatory response and recruitment of leukocytes in the lesion site, and

contributes to the development of atherosclerosis through activation of smooth muscle cells and reduced ˙NO bioavailability (X. Yang et al., 2017). In addition, lipid peroxidation product HNE-modified low-density lipoprotein (LDL) have been found to be elevated by 50% in plasma of patients with atherosclerosis compared with healthy volunteers (Salomon et al., 2000).

3.4.2 The "antioxidant paradox"

Despite the fact that ROS are involved in several human diseases, large doses of dietary antioxidant supplementation have failed to exert a therapeutic effect. A large meta-analysis showed that antioxidant supplements have no benefit or even increase mortality (Bjelakovic, Nikolova, Gluud, Simonetti, & Gluud, 2007). This observation is called the "antioxidant paradox" and can be attributed to a number of factors. First the antioxidant regime, route of administration, dose or duration may not be appropriate or sufficient. Second, the site of production for ROS that need targeting may not be accessible to the antioxidant, particularly for instance if ROS are generated in intracellular compartments and organelles. Also, the target population is of importance, as the individuals included in studies so far may be too heterogenous. It is possible that antioxidant supplements are beneficial only in particular individuals with specific phenotypes. For example, Vitamin E supplementation reduced cardiovascular events in a subgroup type 2 diabetes patients with the haptoglobin 2-2 genotype (Milman et al., 2008). However a large meta-analysis on vitamin use was negative (Ye & Song, 2008). Finally, a range of antioxidant strategies, such as dismutase mimics, NOX inhibitors, and GPX mimics, have shown promising results in cell lines and non-human animal models. It is clear therefore that the "antioxidant paradox" does not disprove the central role of oxidative stress in cardiovascular disease. It rather highlights the need for better informed, targeted antioxidant therapeutic strategies.

3.4.3 Vascular oxidative stress as a predictor of long-term clinical outcomes

Vascular oxidative stress has been linked with diabetes and obesity. In particular, insulin has been shown to lead to increased production of superoxide in the vascular wall (Akoumianakis et al., 2020). However, the fashion in which prolonged oxidative stress in the human vasculature affects survival has never been studied. In this chapter, I elucidate for the first time the relationship of vascular oxidative stress with long-term outcomes in humans.

To that end I used three metrics of oxidative stress, measured by lucigenin chemiluminescence, in fresh human biopsies of the internal mammary artery collected from patients undergoing cardiac surgery. Those include: a) the resting signal, which reflects the amount of ROS present in the tissue at the equilibrium state, b) the NADPH stimulated signal, which is produced after stimulating the tissue with a supra-physiological concentration of NADPH so as to saturate all oxidase systems that use it as a substrate, and reflects the capacity of the tissue to produce superoxide and experience maximal oxidative stress, and c) the Vas2870 inhibitable signal, which is given after blocking all NOXs with the pan-NOX inhibitor Vas2870, and captures a more specific signal directly relevant to NADPH oxidases. The internal mammary artery is a model used regularly in translational cardiovascular research mainly for its ability to evade atherosclerosis. Therefore, its use even in patients with advanced disease requiring surgical intervention is warranted because the lack of plaque formation along the vessel's path means its biology is reflective of systemic or regional signals that are independent of focal lesions, and are therefore easily generalisable. As already mentioned, I utilised a large cohort of patients, who are very well phenotyped. I was able to collect long-term clinical and mortality outcomes on

these patients to correlate with vascular oxidative stress.

Resting and NADPH stimulated signals showed a striking significant association with all-cause and cardiovascular mortality. Patients with high oxidative stress had 2-times and 3-times higher adjusted risk for all-cause and cardiovascular death respectively. The Vas2870 signal showed similar trends although reaching significance only for all-cause mortality, an observation attributed mainly to the fact that this metric was available in a subgroup of most recent patients within the cohort, with few outcomes, and therefore limited statistical power. Furthermore, NADPH stimulated signal showed a striking correlation with composite endpoints constructed by combinations of cardiovascular death, and/or non-fatal myocardial infarction, and/or non-fatal stroke, and/or first admission for heart failure. All these observations remained significant after correcting for cardiovascular risk factor, suggesting that the risk identified is not captured by any of the existing clinical models or clinical biomarkers, and therefore, cardiovascular redox state could be used as a direct biomarker for personalized risk stratification in cardiac surgery.

I have shown for the first time that superoxide production in the vascular wall is predictive of survival in patients with atherosclerosis, independent of current risk assessment factors. This observation highlights yet again the importance of vascular redox state in the natural history of atherosclerosis, and brings anti-oxidant strategies back on the spotlight of atherosclerosis management.

3.4.4 Revealing S100A8 and S100A9 as gene targets dysregulated by oxidative stress

In order to elucidate the biology behind these observations and in an effort to reveal tangible therapeutic targets, I designed a large sequencing experiment with RNA from internal mammary arteries of the patients in my original dataset. Since the NADPH stimulated signal was the strongest predictor in survival analyses, I used it to trichotomize the cohort and perform differential gene expression analysis between the groups of patients with high and low values. S100A8 and S100A9 were amongst the most dysregulated genes. Filtering based on inflammatory pathways, which are the most involved in oxidative stress, I observed that both these genes were the top dysregulated targets. More specifically, in patients with high NADPH oxidase activity these genes were significantly downregulated. I went on to validate this finding by performing qPCR in the entire cohort. Following these observations, I performed an exploratory experiment where I exposed biopsies of human internal mammary arteries and aortas to increased oxidative stress. I found the expression of both genes to be decreased, validating externally my findings from the data science investigations.

S100A8 and S100A9 (also known as MRP8 and MRP14, respectively) are Ca_2^+ binding proteins belonging to the S100 family, that have been reported as players in the pathogenesis of many diseases, often with contradicting roles (Averill, Kerkhoff, & Bornfeldt, 2012). In metabolic inflammatory diseases, such as gout, diabetes, and obesity, S100A8/A9 are secreted and distributed in a disease-specific manner, and elevated levels of S100A8/A9 have been detected in sera and inflammatory sites (Gebhardt, Nemeth, Angel, & Hess, 2006). In addition, upregulation of S100A8/A9 occurs in multiple immune system dysfunction diseases (J. Yang et

al., 2018). At the same time, S100A8/A9 have been suggested to inhibit oxidative metabolism of polymorphonuclear leukocytes (PMNs) in vitro and scavenge released ROS, ameliorating oxidative damage in lungs and livers of LPS-treated mice. non-covalent and high-affinity binding of S100A8/A9 with pro-inflammatory IL-1β, IL-6, and TNF-α suggests the capacity of S100A8/A9 to trap cytokines. S100A8 and S100A9 have further been shown to reduce generation of hypochlorite-oxidized proteins in endothelial cells, suggesting a protective role for these proteins in the vasculature (Gomes et al., 2013). Consequently, my findings support the hypothesis that in cardiovascular disease S100A8/9 exert mainly a protective, anti-oxidant role. Abolition of their presence through downregulation in the human vascular wall exacerbates oxidative stress, leading to increased risk for long-term mortality. Targeting normalisation of S100A8/9 expression in the vasculature may be a sound therapeutic strategy in advanced atherosclerosis.

Despite the fact that I was unable to explore these gene targets further due to extenuating circumstances imposed by the COVID-19 pandemic, the readers and future researchers can be informed by my findings on the significance on S100A8 and S100A9 in vascular redox state and their potential contribution as prognostic or therapeutic targets.

3.4.5 A transcriptomic signature related with oxidative stress and clinical outcomes

The transcriptomic profile of the human vascular wall is implicated in a range of pathologies. RNA sequencing technologies allow for interrogation of gene expression patterns that are associated with clinical outcomes and can guide future research and drug development.

I applied discovery network transcriptomics to internal mammary arteries (IMAs) ob-

tained from patients undergoing cardiac surgery, to unveil ten unsupervised gene modules or signatures within the dataset. Eigengene values characterising each module showed no particular correlation with traditional cardiovascular risk factors, suggesting that the transcriptomic patterns within the arterial vascular wall are either independent of any systemic signals, or reflect factors that we have not captured in our prognostic calculations. Indeed, I identified one signature (namely the "red" module or signature) that was weakly yet significantly correlated with vascular redox state. In survival analysis, eigengene values for this gene signature showed significant association with long-term cardiovascular risk - both for MACE and for a composite endpoint of cardiovascular mortality and non-fatal myocardial infarction and non-fatal stroke - independent of traditional risk factors, suggesting that gene networks annotated within may describe molecular processes not identifiable with current methods that carry prognostic information.

To explore this finding further in terms of its translatability, I conducted pathway enrichment analysis within the 277 genes comprising the red signature. This revealed a plethora of pathways; amongst the top enriched were pathways relevant to oxidative phosphorylation, glucose metabolism, and the hypoxia-inducible factor 1. A group of diseases were picked up at the top, such as Parkinson's, prion disease, Alzheimer's, Huntington's, but intersection analysis showed that these diseases share the exact same genes found in the oxidative phosphorylation pathway, therefore their presence in the enrichment list is of little significance. Performing gene ontology analysis revealed biological processes relevant to the pathways enriched, with mitochondrial respiratory chain complex I assembly, mitochondrial electron transport, and gluconeogenesis coming at the top.

All these findings highlight the importance of mitochondria and glucose metabolism in

maintaining increased levels of oxidative stress in the human vessels, and underlined their significance as therapeutic targets. As already discussed, OP2113 is a drug that is safe for use in humans, which inhibits complex I and does not interfere with ATP production. Recently, in a rat model of ischemia/reperfusion injury OP2113 reduced mitochondrial ROS generation and led to significantly lower myocardial infarct size (W. Dai et al., 2021). Currently, no clinical trial on the use of OP2113 in atherosclerosis is underway. Perhaps my findings will inform the future clinicians and prompt researchers to look into the potential use of mitochondrial ROS inhibition in improving survival in patients with atherosclerosis.

3.4.6 Combining transcriptomic with genomic data to reveal redox state-related gene targets

In an effort to explore potential causality, and identify gene polymorphisms related with redox-state-induced arterial transcription and long-term outcomes, I perused data from a genome wide association study (GWAS) performed in the Ox-HVF cohort. I used the list of genes with SNPs that reach a soft GWAS threshold for association with vascular oxidative stress to overlap with the list of genes within the red vascular transcriptomic signature. I revealed 3 common genes, oxoglutarate dehydrogenase (OGDH), sarcalumenin (SRL), and ubiquitin carboxyl-terminal hydrolase 13 (USP13). Of these, high OGDH expression in internal mammary arteries was associated with higher adjusted risk of MACE. This approach allowed me to identify SNP rs148449548 within the OGDH gene, highlighting it as a locus with both genetic polymorphisms and arterial transcriptional alterations linked with oxidative stress and long-term clinical endpoints. Specific inhibition of OGDH by succinyl phosphonate (SP) has been studied in cancer research, where it was shown to reduce viability of cancer cells in a cell-specific

metabolism-dependent manner (Bunik et al., 2016). In addition, OGDH inhibitor (S)-2-[(2,6-dichlorobenzoyl) amino] succinic acid (AA6) reduced metastasis formation in an orthotopic mouse model of breast cancer (Atlante et al., 2018). Future research is needed to elucidate OGDH inhibition in the context of cardiovascular disease.

3.4.7 Myocardial oxidative stress as a predictor of long-term clinical outcomes

Myocardial oxidative stress has been linked with cardiac hypertrophy and remodelling leading to atrial fibrillation (Shah, Bhullar, Elimban, & Dhalla, 2021). Its prognostic role has only been tested in short-term follow-up and shown to be linked with in-hospital new onset atrial fibrillation post cardiac surgery (Antoniades et al., 2012). In this chapter I have shown that increased myocardial oxidative stress predicts a striking increase of 5-year cardiac mortality and development of new heart failure in patients undergoing cardiac surgery. The risk identified is not captured by any of the existing clinical models or clinical biomarkers. Myocardial redox state could be used as a direct biomarker for personalised risk stratification in cardiac surgery (Figure 3.31). Targeting sources of oxidative stress such as NADPH oxidases in the human heart, appears to be a rational therapeutic approach to improve long-term outcomes in advanced atherosclerosis.

3.4.8 Conclusion

I present for the first time vascular and myocardial oxidative stress as an independent prognostic marker of mortality and long-term clinical outcomes post cardiac surgery in patients with

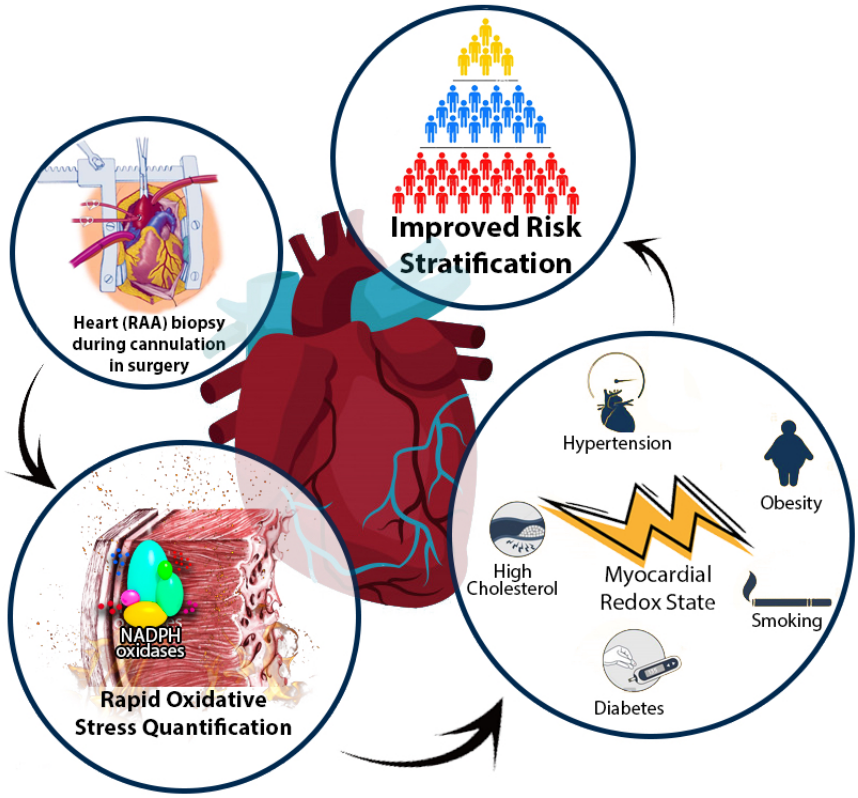


Figure 3.31: Utilising myocardial oxidative stress as a cardiac risk stratification tool in cardiac surgery.

advanced atherosclerosis. I further present for the first time a novel human arterial transcriptomic signature reflecting changes in redox state, which identifies long-term cardiovascular risk. Targeting pathways in the vasculature related with oxidative stress, or mitochondrial electron transport chain, or glucose metabolism or HIF-1 in the human arterial wall may lead to the development of novel therapeutics in cardiovascular disease.

4 | Perivascular Adipose Tissue: Radiotranscriptomic Prognostic Signatures

4.1 Introduction

Cardiovascular complications have emerged as a key feature of COVID-19 pathogenesis and drive adverse outcomes (Teuwen, Geldhof, Pasut, & Carmeliet, 2020; Ackermann et al., 2020; Gupta et al., 2020; Varga et al., 2020; Rauch et al., 2020). Inflammation-induced injury of the vascular endothelium (through direct viral entry, and cytokine-mediated) plays a fundamental role in COVID-19 pathogenesis by altering the integrity of vessel barrier and promoting a pro-coagulant state, contributing to multi-organ failure (Varga et al., 2020; Group, 2020).

Perivascular adipose tissue (PVAT) is a distinct, dynamic fat depot which has a wide range of bi-directional interactions with the vascular wall (Aghamohammadzadeh et al., 2012). Recent evidence suggests that PVAT "senses" inflammatory signals coming from the arterial wall, activates perivascular lipolysis and supresses adipogenesis, resulting in accumulation of small and fat-free adipocytes in PVAT surrounding inflamed arteries (Antonopoulos et al., 2017). This is also accompanied by perivascular oedema, due to the increased permeability of the inflamed perivascular arterioles (Kotanidis & Antoniades, 2020b), which results in significant changes in the texture of PVAT around inflamed arteries. Different types of vascular inflammation in-

duce different types of changes in PVAT texture, which may involve additional development of perivascular microvessels and fibrous tissue, further to the local lipolysis and the variable degree of perivascular oedema (Oikonomou & Antoniades, 2019; Oikonomou et al., 2019). PVAT texture can, therefore, be used to build "molecular fingerprints" that reflect the type and degree of vascular inflammation. A non-invasive method that could visualise and quantify these changes in the texture and composition of PVAT, could revolutionise cardiovascular diagnostics by allowing direct assessment of the type and the degree of vascular inflammation. These new insights, gained early in the acute phase of COVID-19, have the potential for more effective therapeutic stratification of patients, before current clinical indicators of deterioration. Furthermore, direct evaluation of vascular inflammation will contribute to understanding the pathogenesis of acute COVID-19, pave the way for more efficient trials of new treatments, and identify patients who may be at risk of long-term complications. We have recently described a method that uses radiomic analysis of computed tomography (CT) images to characterize the changes in the texture of PVAT driven by inflammatory signals coming from the adjacent arterial wall.12 By applying quantitative radiotranscriptomics we can develop radiomic signatures of PVAT, trained against the tissue transcriptomic profile (Oikonomou et al., 2019).

I have now used quantitative radiotranscriptomics to train a radiomic signature in the PVAT around the internal mammary arteries visualised in CTA, to reflect the degree of arterial inflammation, as defined by activation of the respective molecular pathways mapped by RNA sequencing in biopsies of these arteries. The ability of this new radiotranscriptomic signature to quantify the degree of vascular inflammation in COVID-19 has been evaluated together with its prognostic value in detecting the patients at risk for poor in-hospital outcomes.

4.2 Methods

4.2.1 Study Participants

A comprehensive workflow diagram of each study design is presented in Figure 4.1. The reader should note that the term "Study Arm" is used in this chapter to indicate independent cohorts that were assembled to address separate research questions that work synergistically to achieve the overarching aim of development, testing and validation of the radiotranscriptomic signature C19-RS.

Study Arm 1 (Design of the novel radiotranscriptomic imaging signature, C19-RS)

This study arm included 55 patients from the Oxford Heart, Vessels and Fat (Ox-HVF), undergoing cardiac surgery. Segments of Internal Mammary arteries (IMAs) were collected for transcriptomic analysis, and the RNA sequencing data were linked with coronary CT angiograms (CCTA) and used as ground truth in machine learning, to train a radiotranscriptomic signature of cytokine-driven inflammation (C19-RS)- see below. This study was approved by the local Research Ethics Committee (Oxford REC C: 11/SC/0140).

Study Arm 2 (Testing C19-RS changes post-COVID-19)]

This study arm included 44 patients from Oxford University Hospitals who had CCTAs before the pandemic, and then underwent repeat CCTA either within 6 months post COVID-19 infection (n=22) or as part of research follow-up performed also before the pandemic (n=22 controls with pre-pandemic paired scans, matched for age, sex and BMI), as described in the Online Appendix. This was a sub-study of the Oxford Risk Factors and non-invasive Imaging

(ORFAN) study (NCT05169333), that received National Flagship Status by the National Institute of Health Research and the British Heart Foundation, (The UK COVID-19 Cardiovascular Research Consortium -UK C19-CRC).

Study Arm 3 (Validation of the ability of C19RS to predict in-hospital mortality in COVID-19, and its interaction with anti-inflammatory treatments)

This study arm included 418 patients from the Oxford University Hospitals NHS Trust undergoing CT pulmonary angiography (CTPA), hospitalised between March 2020 - January 2021 during the first and second pandemic waves. This included 284 individuals who were verified as COVID-19 positive, based on either positive PCR on a pharyngeal swab or the presence of clinico-radiological features on CT imaging. The rest served as controls and were patients admitted to hospital for other reasons and had a clinically indicated CTPA (n=100). This study arm population was identified during the first UK wave (March to June 2020) (n=269), before the introduction of routine dexamethasone treatment that could confound the study results, This population was split randomly in a 20% exploratory subpopulation and an 80% validation subpopulation. The exploratory subpopulation was used for radiomic feature filtering as outlined below. The remaining 80% validation subpopulation pooled together with the rest of the Study Arm 3 population (n=254) was used to test C19-RS. Viral whole-genome sequencing was performed in Study Arm 3 patients to determine lineage. RNA sequencing from whole blood was obtained for 23 patients from Study Arm 3, who were also part of the COMBAT study (Ahern et al., 2021), a multi-omic blood study of COVID patients (South Central Oxford C Research Ethics Committee (REC) in England (Sepsis Immunomics REC reference 19/SC/0296; ISARIC WHO Clinical Characterisation Protocol for Severe Emerging Infections REC reference 13/SC/0149)).

Study Arm 4 (Further external validation of the prognostic value of C19-RS in geographically different populations)

This study arm included 134 patients from University Hospitals of Leicester NHS Trust and Royal United Hospitals Bath NHS Trust verified as COVID-19 positive and they all had a CTPA during their hospital stay, of whom 104 were included in the external validation analysis. In-hospital short-term outcomes were collected from local hospital Electronic Patient Records. They also belonged to the UK C19-CRC sub-study of the ORFAN cohort.

4.2.2 Tissue Collection, RNA Isolation and Sequencing Data Analysis

In Study Arm 1, IMA specimens were collected during surgery and stored at -80^{o}C until thawed for RNA isolation. RNA sequencing was done using the QuantSeq 3' mRNA (Lexogen) library preparation kit. All samples were sequenced as part of a large multiplex pool on an Illumina NovaSeq 6000 system producing 150bp paired-end reads (details in Online Methods). In Study Arm 3 COMBAT participants' total RNA was extracted from whole blood samples collected in Tempus Tubes, and libraries prepared using NEBNext Ultra II Directional RNA Library Prep Kit for Illumina after rRNA and globin depletion. Pooled libraries were sequenced on the NovaSeq 6000, with a target of 50M 100bp read pairs per sample, and gene expression was quantified using STAR v2.7.314 and featureCounts v1.6.415.

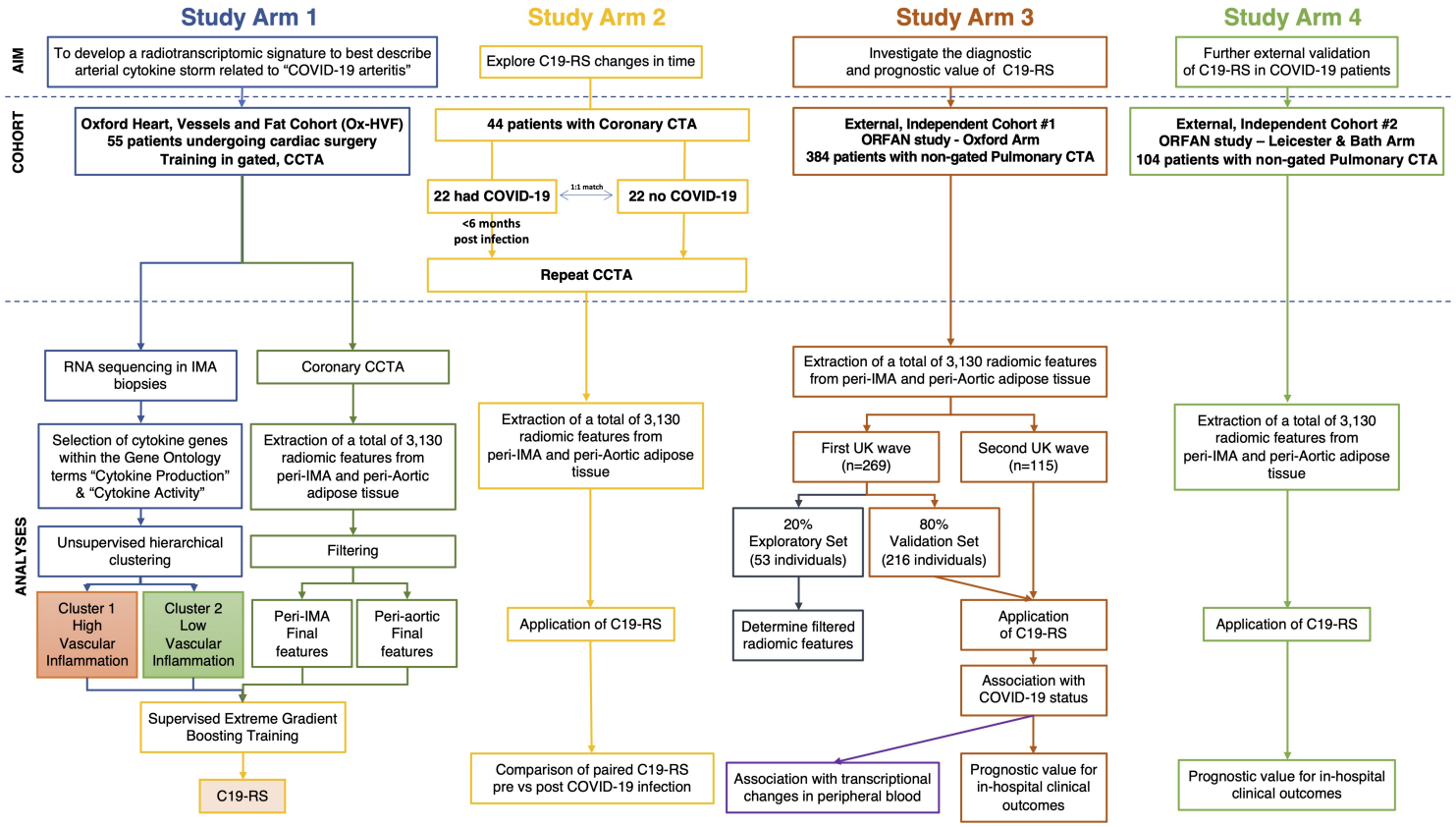


Figure 4.1: Chapter 4 Workflow Diagram. Study Arm 1 utilised 55 patients from the Oxford Heart Vessels and Fat (Ox-HVF) Cohort that underwent cardiac surgery and CCTA imaging in order to develop the radiomic signature C19-RS based on high vascular inflammation. Study Arm 2 included 88 paired CCTA scans. Study Arm 3 included 384 participants with CTPA imaging and was used for radiomic feature filtering and to validate C19-RS for COVID-19 discrimination and in-hospital outcome correlation. Study Arm 4 served as an external, independent validation cohort of COVID-19 patients testing the prognostic value of C19-RS for in-hospital outcomes.

4.2.3 Defining Inflammatory-related Genes

In order to stratify the cohort of patients in Study Arm 1 by upregulation of inflammatory pathways within the vasculature, relevant to the "cytokine storm" described in COVID-19, we composed a list of genes relevant to inflammation annotated in the Gene Ontology (GO) terms "Cytokine Production" (GO:0001816) from the GO main domain "Biological Process" and "Cytokine Activity" (GO:005125) from the GO main domain "Molecular Function". That included a range of genes to best represent the inflammatory burst, including C-C motif chemokine ligands, interferons, interleukins, and TNF family genes. The full list of 145 genes selected is available in Table 4.1.

Table 4.1: List of genes chosen for unsupervised clustering in Study Arm 1

CCL1	CXCL13	IFNL4	IL1RL2	IL6R
CCL11	CXCL14	IFNW1	IL1RN	IL6ST
CCL13	CXCL16	IL10	IL2	IL7
CCL14	CXCL17	IL11	IL20	IL9
CCL15	CXCL2	IL12A	IL20RB	TNF
CCL16	CXCL3	IL12B	IL21	TNFAIP3
CCL17	CXCL5	IL12RB1	IL22	TNFRSF11B
CCL18	CXCL6	IL12RB2	IL23A	TNFRSF13C
CCL19	CXCL8	IL13	IL23R	TNFRSF14
CCL2	CXCL9	IL15	IL24	TNFRSF1B
CCL20	IFNA1	IL16	IL25	TNFRSF21
CCL21	IFNA10	IL17A	IL26	TNFRSF4

CCL22	IFNA14	IL17B	IL27	TNFRSF8
CCL23	IFNA16	IL17C	IL27RA	TNFRSF9
CCL24	IFNA17	IL17D	IL3	TNFSF10
CCL25	IFNA2	IL17F	IL31	TNFSF11
CCL26	IFNA21	IL17RA	IL31RA	TNFSF12
CCL27	IFNA4	IL17RB	IL32	TNFSF13
CCL28	IFNA5	IL17RC	IL33	TNFSF13B
CCL3	IFNA6	IL18	IL34	TNFSF14
CCL4	IFNA7	IL18R1	IL36A	TNFSF15
CCL5	IFNA8	IL18RAP	IL36B	TNFSF18
CCL7	IFNB1	IL19	IL36G	TNFSF4
CCL8	IFNE	IL1A	IL36RN	TNFSF8
CX3CL1	IFNG	IL1B	IL37	TNFSF9
CX3CR1	IFNGR1	IL1F10	IL4	
CXCL1	IFNK	IL1R1	IL4R	
CXCL10	IFNL1	IL1R2	IL5	
CXCL11	IFNL2	IL1RAP	IL5RA	
CXCL12	IFNL3	IL1RL1	IL6	

4.2.4 Clustering and Differential Expression Analysis

The set of inflammatory genes was extracted from the count table and filtered to exclude those with low expression levels: counts per million (CPM) values were generated using the edgeR

package (Robinson, McCarthy, & Smyth, 2010) and 51 genes with CPM > 1 in at least 10 out of 55 patients were retained. Unsupervised hierarchical clustering was performed on this set of genes with the Minkowksi distance metric (p=10) and ward.D clustering method (heatmap.2 function in the gplots package) and visualised as a heatmap with dendrogram. The clusters produced were used as the "ground truth" in a machine learning exercise to build a CT-radiomic signature from PVAT, to detect noninvasively this type of cytokine-induced arterial inflammation (Figure 4.2).

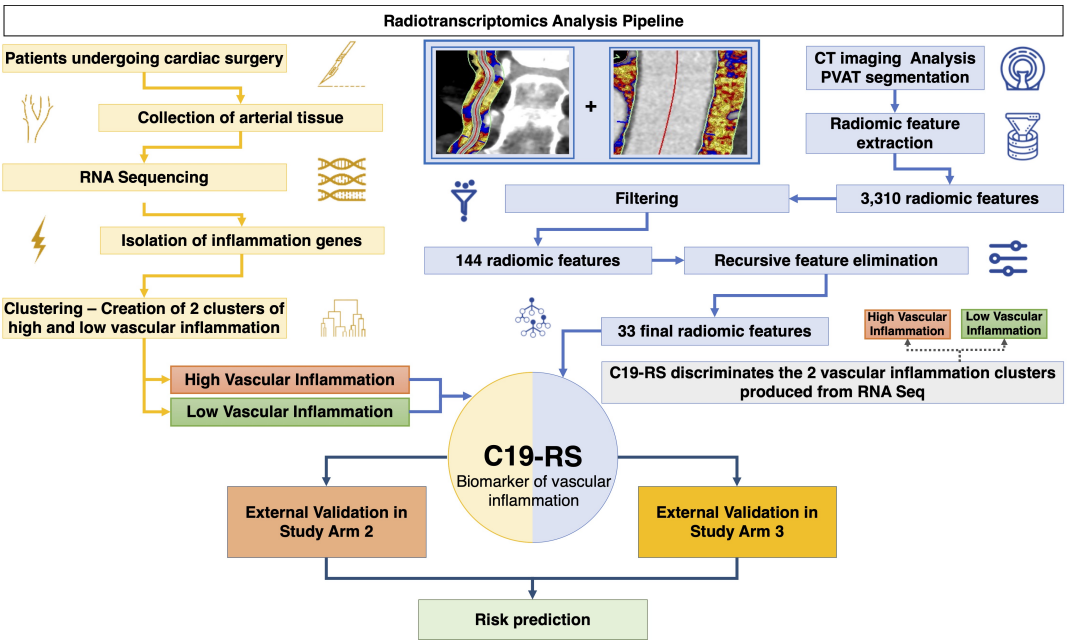


Figure 4.2: Building C19-RS: A radiotranscriptomics analysis. Workflow depicting the multiple steps taken in order to train and develop the radiomic signature C19-RS. To limit our analysis to radiomic features that could be of value as imaging biomarkers, we performed a series of filtering steps, so as to exclude features that are not stable in test-retest analyses, features that are highly correlated with each other, features that are significantly correlated with BMI or intrathoracic adipose tissue volume, and retain only features that predict the outcome variable with the same direction within the Study Arm 1 and 20% exploratory Study Arm 3 sub-population. Finally, recursive feature elimination with a random forest algorithm and repeated five-fold cross-validation showed a plateau in the accuracy of the trained model with a selection of 33 final features. Those features were next used within the Study Arm 1 population to train an XGBoost algorithm using decisions trees in order to discriminate patients with activated inflammatory pathways within their arterial vasculature. The raw product of the algorithm was named C19-RS.

The 2 clusters of samples identified based on the inflammatory expression profile were then assessed for differential expression (edgeR package) on the full set of expressed genes in the RNA-Seq dataset. This generated a list of 132 genes identified as differentially upregulated (logFC $>$ 1 and p $<$ 0.05) between the 2 clusters of patients. In order to validate our clusters for activation of inflammation within the vasculature we conducted pathway enrichment analysis in ConsensusPathDB-human with the up-regulated differentially expressed genes (DEGs); the input for pathway analysis was the set of 132 genes with logFC $>$ 1 and p $<$ 0.05.

In the COMBAT dataset, 77 of the inflammatory genes had been retained post-filtering on the full dataset. The scaled expression of these genes across the range of C19-RS were visualised as a heatmap using the pheatmap R package, and unsupervised clustering was performed as above. Differential expression analysis was performed on protein-coding genes using one sample per patient (closest timepoint to CT scan) and the limma package, comparing high (above median) and low (below median) C19-RS scores and adjusting for age and sex. Multiple testing correction was performed using the Benjamini-Hochberg method.

Weighted Gene Co-expression Network Analysis (WGCNA) was applied through the "cornet" pipeline to identify modules of correlated genes in the complete COMBAT dataset (143 samples from 123 patients) (https://github.com/sansomlab/cornet.git). In brief, this uses a stepwise approach of correlation network construction and module detection. Using the soft thresholding power of 4, a signed-hybrid network was built, with the biweight midcorrelation as the adjacency function. The adjacency matrix was transformed into a topological overlap matrix to calculate the dissimilarity, and a dissimilarity threshold of 0.3 was used to merge modules with very similar expression profiles. Module eigengene values (module first principal component) were used to summarise modules and perform module-C19-RS correla-

tion analysis (Pearson correlation). Pathway enrichment analysis was performed using the hypergeometric test with the default settings of the "cornet" pipeline (https://github.com/sansomlab/cornet.git).

4.2.5 Coronary and Pulmonary Computed Tomography Angiography Acquisition Protocols

In Study Arm 1 participants underwent coronary CTA (CCTA) using a 64-slice scanner (LightSpeed Ultra or Revolution GSI, General Electric) as previously described8. Heart rate was optimised using intravenous injection of beta-blockers and sublingual glyceryl-trinitrate (800ug) was also administered to achieve maximum coronary vasodilatation. CCTA was performed following intravenous injection of 95ml of iodine-based contrast medium (Niopam 370, BRACCO) at a flow rate of 6mL/sec (tube energy of 120 or 100 kVp, axial slice thickness of 0.625 mm, rotation time of 0.35 sec, detector coverage of 40 mm). Prospective image acquisition was used by ECG-gating at 75% of cardiac cycle (with 100 msec padding for optimal imaging of the right coronary artery if required). In Study Arm 2, CCTA scans were performed on a 320 slice scanner (Aquilion One, Canon Medical Systems, Tochigi, Japan) In patients with heart rate > 65 beats/minute, 5 mg of intravenous metoprolol (with incremental 5 mg doses up to a maximum dose of 40 mg) Patients also received 0.8 mg of nitroglycerin sublingually immediately before CCTA and iodinated contrast (Iomeron 350, Bracco UK Ltd) was administered at flow rate of 5-6 ml/s. In Study Arm 3, participants underwent pulmonary CTA (CTPA) performed on the GE Revolution HD CT scanner. During the initial phase of the pandemic, suspected cases of COVID-19 pneumonia had standard CTPA or dual energy CTPA (DECTPA) (Lang et al., 2020). The single energy CTPA were perform using 80-120kV and contrast 70-100mL at 4 mL/s de-

pendent on body size. DECTPA were performed using rapid kV switching to optimise contrast and thrombus visualisation. These scans were all non-ECG gated. In Study Arm 4, scans from University Hospitals of Leicester were performed on a Siemens Somatom Definition Flash CT scanner, using a FLASH protocol with the following scan parameters: dose modulation on, quality reference kVp 100, ref mAs 100, pitch: 2.1, rotation time 0.28s, detector configuration 128x0.6mm, suspended respiration scan from lung apices to lung bases, using a pre monitoring slice at the level of the pulmonary artery for optimal contrast enhancement of the pulmonary arteries, contrast agent: omnipaque 350, 50mls at 4ml/sec plus 50mls saline flush. Scans from the Royal United Hospitals Bath were performed on either Siemens Somatom Definition Edge scanner with the following scan parameters: dose modulation on, quality reference kVp 120, ref mAs 145, pitch 1.2, rotation time 0.5s, detector configuration 128x0.6mm, suspended respiration scan from lung apices to lung bases, using a bolus-tracking method with threshold of 100 HU in an ROI in a slice at the level of the main pulmonary artery and a 4 second delay after triggering, contrast agent: omnipaque 350, 60mls at 5ml/s plus 50mls 0.9% saline flush at 5ml/sec or Siemens Somatom Drive scanner with the following scan parameters: dose modulation on, dual source dual energy 80 kVp / ref mAs 141 and Sn-filter 140 kVp / ref mAs 60, pitch 1.2, rotation time 0.5s, detector configuration 128x0.6mm, suspended respiration scan from lung apices to lung bases, using a bolus-tracking method with threshold of 100 HU in an ROI in a slice at the level of the main pulmonary artery and a 9 second delay after triggering, contrast agent: omnipaque 350, 75mls at 5ml/s plus 25mls 50:50 mix omnipaque 350 / 0.9% saline flush at 5ml/sec.

4.2.6 Adipose Tissue Segmentation and Radiomic Characterization

Perivascular adipose tissue segmentation was performed manually around the right IMA from the level of the aortic arch to 120mm caudally. Perivascular space was defined as the space within a radial distance from the outer vessel wall equal to the diameter of the respective vessel, as previously described (Oikonomou et al., 2018). Perivascular adipose tissue segmentation around the descending thoracic aorta was performed manually from the level of the pulmonary artery bifurcation to 67.5mm caudally, as previously described (Schlett et al., 2009). Perivascular space was defined as the space within a cylindrical layer that is expanded beyond the vessel borders by a distance equal to 10mm. In order to avoid lung tissue and any COVID-19 related lesions peri-aortic adipose tissue directly adjacent to the left lateral side of the descending thoracic aorta that is in close proximity to. All analyses were performed using the standard operating procedures of the Oxford Academic Cardiovascular CT (OXACCT) core lab and for C19-RS measurements inter-observer agreement amongst two independent operators was excellent [ICC: 0.914 (95% CI: 0.769-0.968), p<0.001]. All segmentations were performed using 3D Slicer (v.4.10.2) (Fedorov et al., 2012). Given the heterogeneity of tube voltage and effective energies used in the various imaging protocols in Studies 1 and 2, we rescaled all images using 100kVp as reference. Conversion factors (Table 2.4) for tube voltage 120kVp and effective energies 55, 58, and 70 keVs were calculated from data previously validated (Okayama et al., 2012). Image processing and extraction of radiomic features was performed using the CaRi-Research toolbox (Caristo Diagnostics, Oxford UK) and pyradiomics (Knuuti et al., 2020). A total of 1,655 radiomic features were extracted from each segmented PVAT volume.

4.2.7 Radiomic Characterization Details

A total of 1,655 radiomic features were extracted from each segmented PVAT volume. Briefly, the radiomic features obtained were based on shape-based analysis, first order statistics, grey level co-occurrence matrix (glcm), grey level run length matrix (glrlm), grey level size zone matrix (glszm), grey level dependence matrix (gldm), neighbouring grey tone difference matrix (ngtdm). All these features were calculated on the original images and after applying transformations on the images. The transformations included Laplacian of Gaussian (log) with various sigma (1, 2, 3, 4, 5 mm), wavelet-LLH , wavelet-LHL, wavelet-LHH, wavelet-HLL, wavelet-HLH, wavelet-HHL, square, square root, logarithm and exponential. The bin width was kept at 25.

4.2.8 Radiomic feature filtering and selection

Firstly, I performed a stability assessment of all 3,310 different radiomic features. For this purpose I used 24 Lung CT scans (12 paired scans, performed 15 minutes apart) from the RIDER dataset ("RIDER. The Reference Image Database to Evaluate Therapy Response", 2013) to assess the scan-rescan ICC of each radiomic feature. Only radiomic features with ICC$\geq$0.90 (n=2,177) were included in further analyses (Figure 4.3).

I next filtered out redundant radiomic features with Spearman's rho coefficient lower than an absolute value of 0.9, using the "findCorrelation" function of the "caret" package in R (n=497). For further filtering of radiomic features I removed features significantly correlated with BMI and total intrathoracic adipose tissue, using a threshold of 0.05 in the Spearman's rho correlation p value (n=333). Next, I isolated a randomly split 20% exploratory subset from

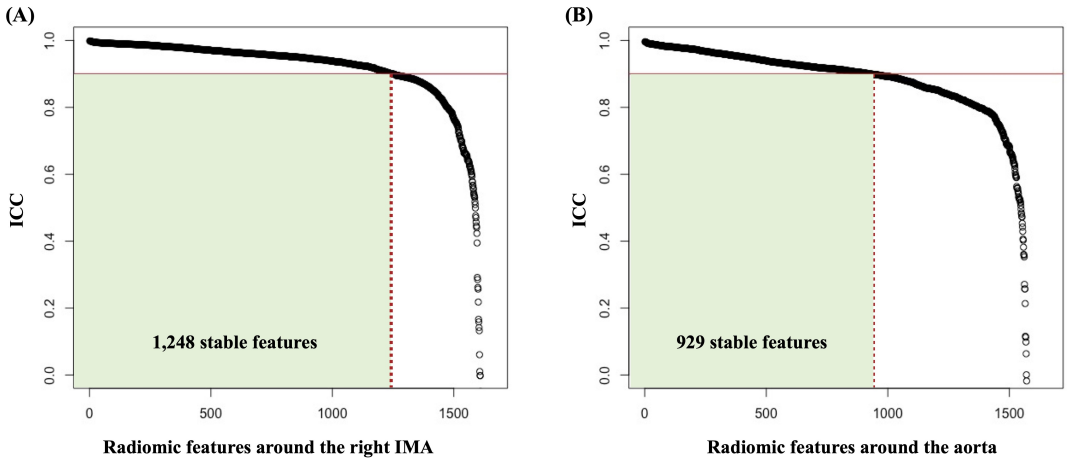


Figure 4.3: Reproducibility analysis of perivascular adipose tissue features. Plot of the test-retest intraclass correlation coefficient (ICC) in the RIDER dataset of all 1,655 radiomic features measured around the right IMA (A) and descending aorta (B). Radiomic features are ranked on descending order based on their ICC value. A total of 1,248 and 929 radiomic features respectively were found to have an ICC equal to or greater than 0.90.

the Study Arm 3 population, applied a univariate ROC analysis for outcome prediction in that subset (outcome: COVID-19 positive status) as well as in Study Arm 1 (outcome: high vascular inflammation), and filtered in only those radiomic features that predicted the outcome in both datasets in the same direction (n=144). Finally, recursive feature elimination with a random forest algorithm and repeated five-fold cross-validation showed a plateau in the accuracy of the trained model with a selection of 33 final features (Figure 4.4).

4.2.9 Viral Genome Sequencing

Samples were sequenced using a multiplex PCR based approach with the ARTIC LoCost protocol (Quick, 2020) and v3 primers1using R9.4.1 flow cells (Oxford Nanopore Technologies, Oxford, UK). Consensus sequences were generated using ARTIC field bioinformatics v1.2.1. (Loman, 2021) All sequences underwent quality control, requiring >90% consensus genome

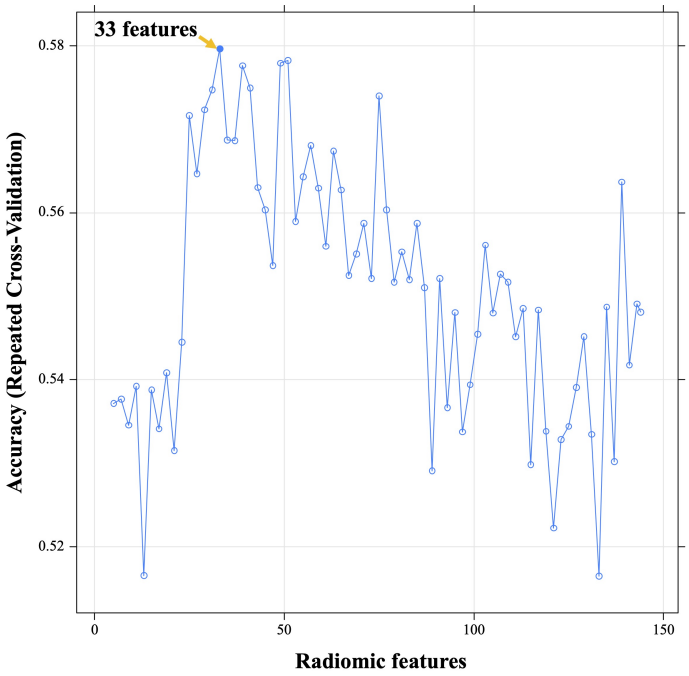


Figure 4.4: Recursive feature elimination. Recursive feature elimination with a random forest algorithm and repeated five-fold cross-validation showed a plateau in the accuracy of the trained model with a maximal number of 33 selected features.

coverage at ≥20 depth. Lineages were assigned with Pangolin ("Pangolin software package", n.d.).

4.2.10 Statistical analysis

Participant demographics are summarized as numbers (percentages) or median (25th to 75th percentile) for categorical and continuous variables, respectively. Between-group comparisons were performed using Pearson's chi-squared test for categorical variables, and Mann-Whitney's U test for continuous variables. In Study Arm 1, hierarchical clustering was performed using Ward's method and Minkowski distance with p set to 10. Radiomic features that were retained after filtering, were scaled and fit in an extreme gradient boosting algorithm. The method chosen was decision trees, with eta set to 0.5, number of rounds 100, and maximum tree depth 50.

In Study Arm 3, following radiomic extraction, we applied the algorithm developed in Study Arm 1; the final product of the XGBoost algorithm (namely the raw logit values) was defined as C19-RS. Its prognostic value for in-hospital death and a composite endpoint of in-hospital death and intensive care unit (ICU) admission was then assessed in univariable Kaplan-Meier curves, logistic and Cox regression models adjusted for age above 65, sex, cardiovascular risk factors (hypertension, hyperlipidaemia, diabetes, BMI, presence of coronary artery disease), C-reactive protein plasma levels, white blood cell count, plasma troponin, history of chronic obstructive pulmonary disease and CT tube voltage. Optimal cut-off points for logistic regression analyses were determined by the Youden's statistic method, while optimal cut points for survival analyses were identified by the value that maximized the log-rank statistic for death in hospital. Missing values within the datasets were imputed with predictive mean matching using the "mice" package in R. Missingness in the total Study Arm 3 population was 29.7% for BMI, 10.4% for CRP, 54.4% for Troponin and below 10% for the rest of the variables. Missingness in the total Study Arm 4 population was 45.2% for BMI, 75% for Troponin, and below 10% for the rest of the variables. In the COMBAT total RNAseq data, differential gene expression analysis was performed using the limma R package, co-expressed gene modules identified using WGCNA, and pathway enrichment assessed used GOBP annotations and hypergeometric test as previously described (ref COMBAT paper). Correlation with the C19-RS signature was quantified by Pearson's r. Statistical analyses were performed in the R environment (R version 3.6.0 and R Studio version 1.2.1335; COMBAT whole blood: R version 3.6.2, RStudio 1.2.5042 running on the BMRC compute cluster). All tests were two-sided and Î$\pm wassetat 0.05$.

4.3 Results

4.3.1 Designing a platform for developing radiotranscriptomic imaging biomarkers

I developed a platform for rapid development of novel imaging biomarkers of vascular inflammation, by applying quantitative radiotranscriptomics to images from standard Computed Tomography Angiography (CTA). We used this platform to train a radiotranscriptomic signature (C19-RS) from the perivascular space around the aorta and the internal mammary artery, visualized in routine chest CTAs, to best describe cytokine-driven vascular inflammation, defined using transcriptomic profiles from RNA sequencing data from human arterial biopsies. A detailed workflow of the steps involved in the radiotranscriptomic platform is presented in Figure 4.2.

4.3.2 Clustering of inflammatory genes expression within human internal mammary arteries to stratify vascular inflammation

Using unsupervised hierarchical clustering, I identified two clusters of patients of high and low inflammatory cytokine activation within the arterial wall (Figure 4.5). Key demographic and clinical characteristics for the two clusters are presented in Table 4.2.

Pathway enrichment analysis with the top differentially upregulated genes between the two clusters revealed pathways directly related to the immune system and cytokine signalling (Figure 4.6). We have previously shown that inflammation in the IMA is an excellent surrogate

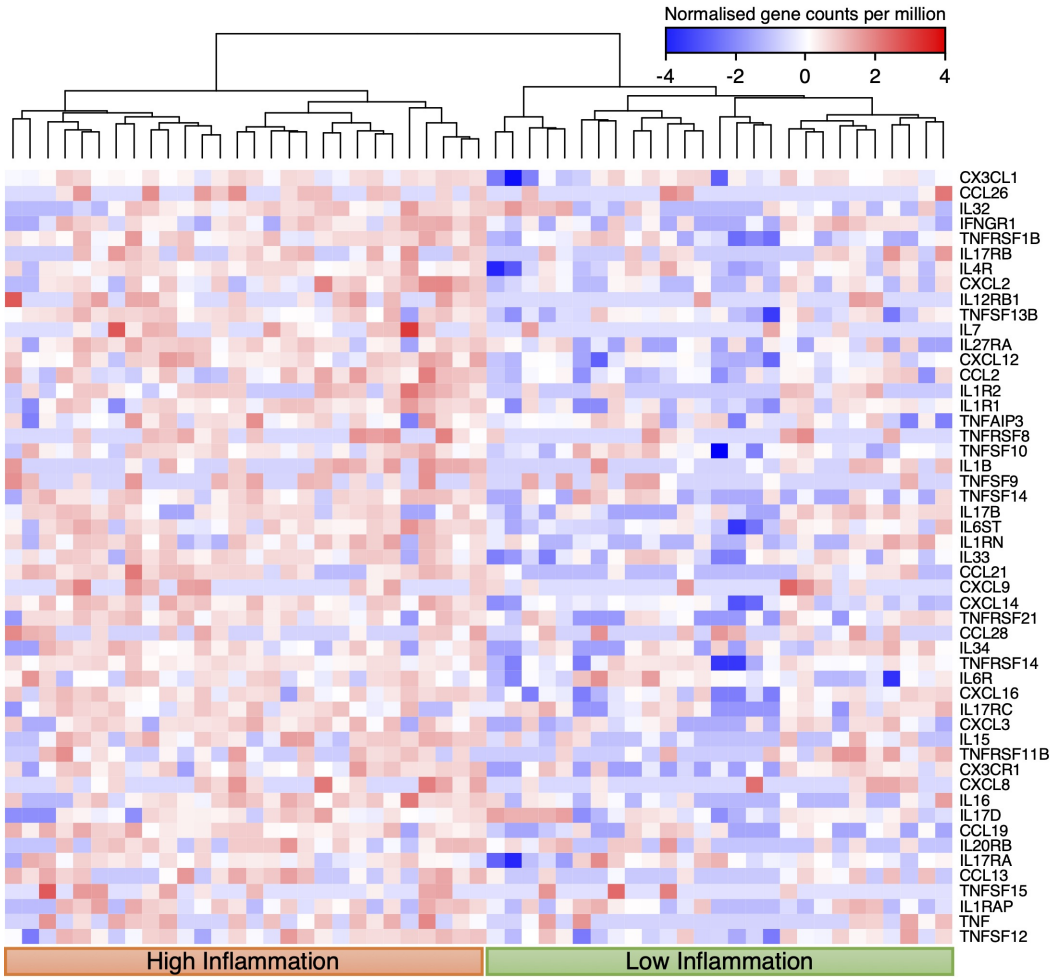


Figure 4.5: Unsupervised hierarchical clustering of cytokine production genes. Unsupervised hierarchical clustering of the list of genes relevant to inflammation annotated in the Gene Ontology (GO) terms "Cytokine Production" (GO:0001816) from the GO main domain "Biological Process" and "Cytokine Activity" (GO:005125) from the GO main domain "Molecular Function".

Table 4.2: Demographic characteristics of the Study Arm 1 population

	Study Arm 1 population			
	All	**Cluster 1**	**Cluster 2**	**P value**
Total (n)	55	28	27	-
Age (years)	67.94±9.24	67.07±10.01	68.88±8.43	0.476
Sex (male, %)	85.5	85.7	85.2	0.564
Risk factors (%)				
Hypertension	70.9	60.7	81.5	0.087
Dyslipidaemia	80.0	75.0	85.2	0.263
Diabetes mellitus	16.4	14.3	18.5	0.524
Smoking	56.4	57.2	55.5	0.928
Systolic blood pressure (mmHg)	130.02±17.92	129.19±19.48	130.92±16.42	0.731
Body Mass Index (BMI, kg/m^2)	27.82±4.21	27.14±4.63	28.52±3.68	0.236
Medication (%)				
Statins	87.3	85.7	88.9	0.913
ACEi	63.6	57.1	70.4	0.360
b-blockers	72.7	75.0	70.4	0.924
Nitrates	54.5	60.7	48.1	0.597
CT Scanning data				
Scan type	CCTA	CCTA	CCTA	
Tube Voltage (kVp) n (%)				
100	2	1	1	1
120	53	27	26	1

ACEi:angiotensin converting enzyme inhibitors; continuous variables reported as means±SEM or median [IQR], as appropriate.
CCTA: Gated coronary computed tomography angiography.

for the inflammatory status of the entire vasculature as it is reflecting a non-atheroma-driven response (Otsuka, Yahagi, Sakakura, & Virmani, 2013a), and ex-vivo models using segments of IMA have been extensively used in the literature for studying arterial biology (Akoumianakis et al., 2019; Margaritis et al., 2013).

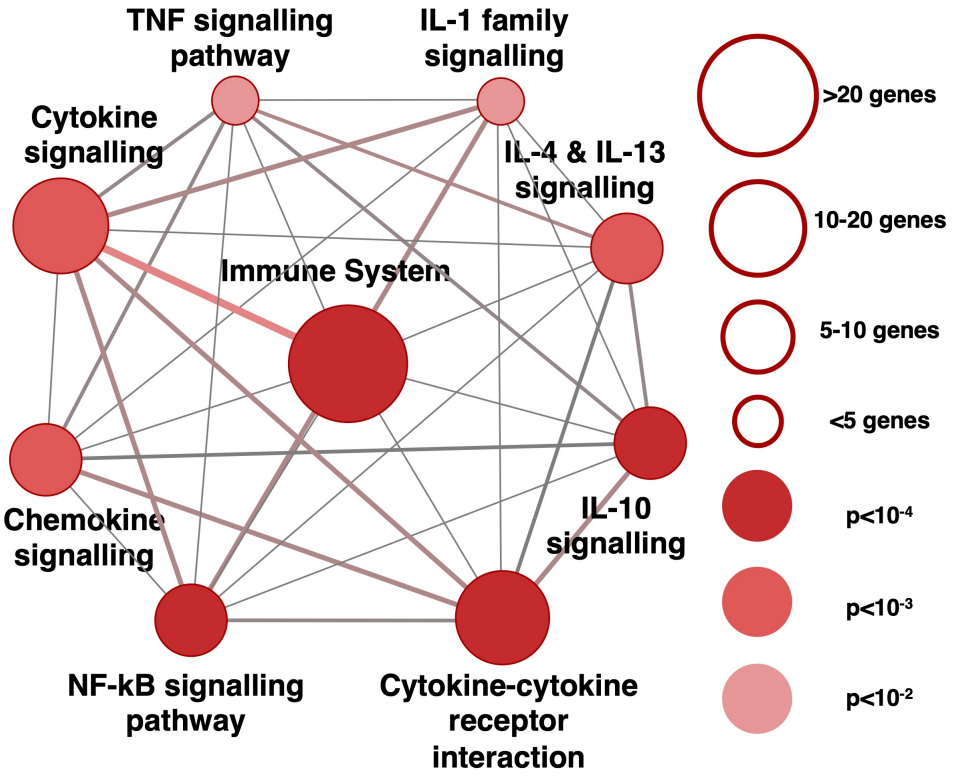


Figure 4.6: Validation pathway enrichment analysis. Enriched signalling pathways of DEGs between the two clusters of vascular inflammation identified through ConsensusPathDB.

4.3.3 Training of C19-RS

In the above inflammatory cytokine clustering was used as the "ground truth" in a machine learning exercise to build a CT-radiomic signature from PVAT, to detect noninvasively this type of cytokine-induced arterial inflammation. Following multiple filtering steps (described in the Methods section and Figure 4.2), a final set of 33 radiomic features was used to train an XGBoost

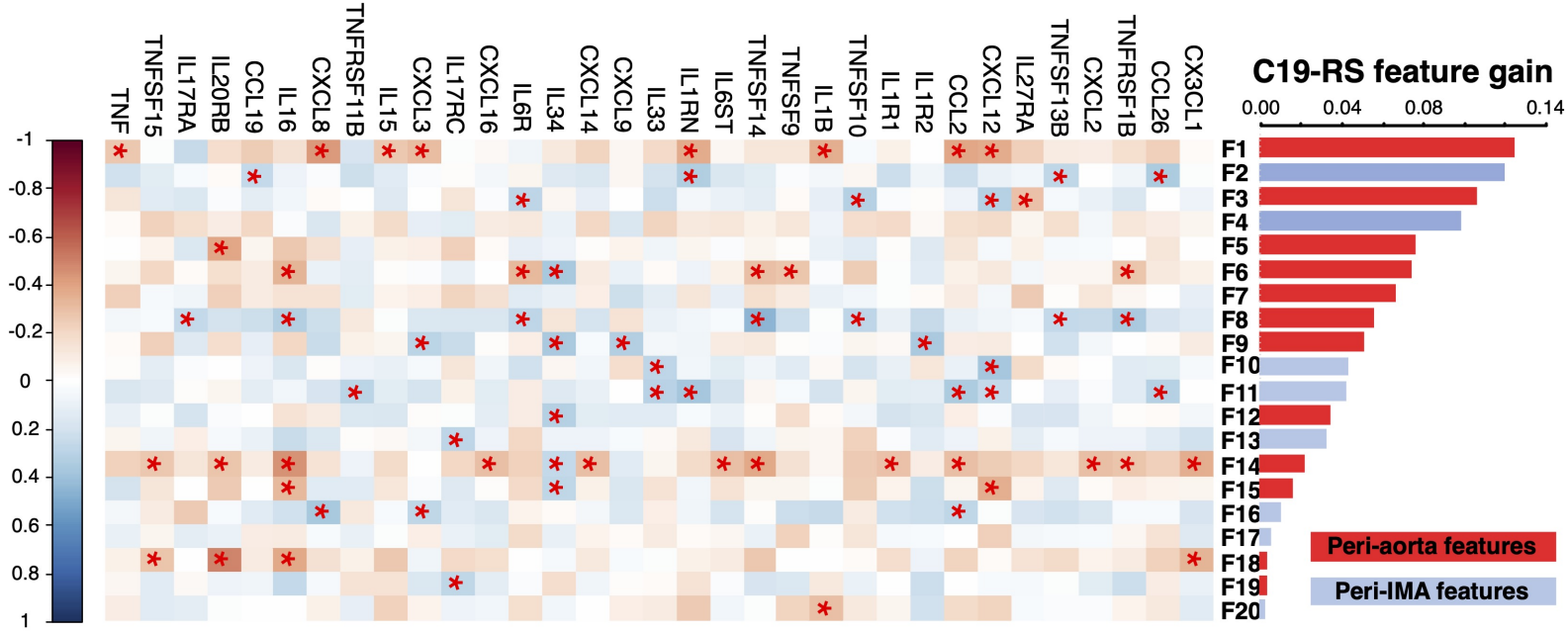


Figure 4.7: C19-RS. Feature importance of the top 20 radiomic features comprising C19-RS (F1: Wavelet LHH glcm Informational Measure of Correlation 2; F2: log.sigma.4.0.mm.3D glszm Gray Level Non-Uniformity Normalized; F3: Wavelet LHH glcm Correlation; F4: Wavelet LLL glcm Joint Average; F5: log.sigma.1.0.mm.3D ngtdm Strength; F6: Wavelet LLL glcm Difference Variance; F7: log.sigma.2.0.mm.3D glcm Correlation; F8: log.sigma.1.0.mm.3D first order Skewness; F9: log.sigma.1.0.mm.3D glszm Size Zone Non-Uniformity; F10: Logarithm glcm Informational Measure of Correlation 2; F11: Wavelet LLL glszm Gray Level Non-Uniformity Normalized; F12: log.sigma.5.0.mm.3D glrlm Run Length Non-Uniformity Normalized; F13: Wavelet HLH first order Maximum; F14: log.sigma.5.0.mm.3D glszm Small Area High Gray Level Emphasis; F15: Wavelet LHL first order Median; F16: log.sigma.3.0.mm.3D first order Maximum; F17: log.sigma.1.0.mm.3D glcm Inverse Variance; F18: Wavelet LHL first order Range; F19: log.sigma.4.0.mm.3D first order Median; F20: Wavelet HHH glcm Cluster Tendency) and their correlation with cpm (count per million) values with key inflammatory genes in the Study Arm 1 population (*denotes significance, $p<0.05$ by the Spearman's rho correlation coefficient).

machine learning algorithm to quantify cytokine-related arterial inflammation. The product of the algorithm was named C19-RS and retained 25 features (Figure 4.4). To understand the biological interpretation of C19-RS, we tested the relation of each chosen radiomic feature with key inflammatory genes in the arterial wall. Most C19-RS features were differentially associated with multiple genes relevant to cytokine production within the arterial wall (Figure 4.7).

4.3.4 Exploring the ability of C19-RS to track COVID-19-induced vascular inflammation

First, 22 patients who had a CCTA before the pandemic underwent repeat CCTA <6 months post COVID-19 infection. 22 controls (matched for age, gender, and BMI) who had paired CCTA scans before the pandemic were also identified, and C19-RS was determined in all 88 paired scans (Figure 4.8a). Demographics available in Table 4.3. We observed that C19-RS was increased only in the COVID-19 group (Figure 4.8b) but not in the control group (Figure 4.8c). Indeed, the delta(C19-RS) was strikingly different in the COVID-19 vs the control patients (Figure 4.8d). Although the two populations had similar C19-RS at baseline (Figure 4.8e), patients with COVID-19 have significantly higher C19-RS post infection (Figure 4.8f). In multivariable logistic regression for differentiating patients who had COVID-19 from controls (adjusting for age, sex, hypertension, diabetes mellitus, BMI and time between scans), delta C19-RS was significantly predictive Adj. OR: 1.65 (1.15 to 2.74), p=0.02.

In Study Arm 3 (Table 4.4) I validated externally the clinical value of C19-RS as a non-invasive imaging biomarker of arterial inflammation in patients with COVID-19. C19-RS was significantly higher in the COVID-19 positive compared to COVID-19 negative patients (Figure

Table 4.3: Demographic characteristics of the Study Arm 2 population

	COVID	**Controls**	**P value**
Total (n)	22	22	-
Age (years)	56.27+/-11.45	55.50+/-8.20	0.798
Sex (male, %)	72.7	72.7	1
Risk factors (%)			
Hypertension	50.0	50.0	1
Diabetes mellitus	18.2	31.8	0.486
Body Mass Index (kg/m^2)	32.47+/-7.69	32.25+/-4.74	0.911
C19-RS Baseline	6.55 [3.99, 7.69]	5.09 [4.62, 6.82]	0.453
C19-RS Follow-up	7.74 [6.93, 8.37]	4.64 [3.71, 6.60]	<0.001
Delta C19-RS	1.74 [-0.07, 3.19]	-0.31 [-1.79, 0.96]	0.005
Time between scans (years)	2.2 [1.8, 4.1]	1552.5 [1500.0, 1616.8]	0.002

Continuous variables reported as means+/-SEM or median [IQR], as appropriate.

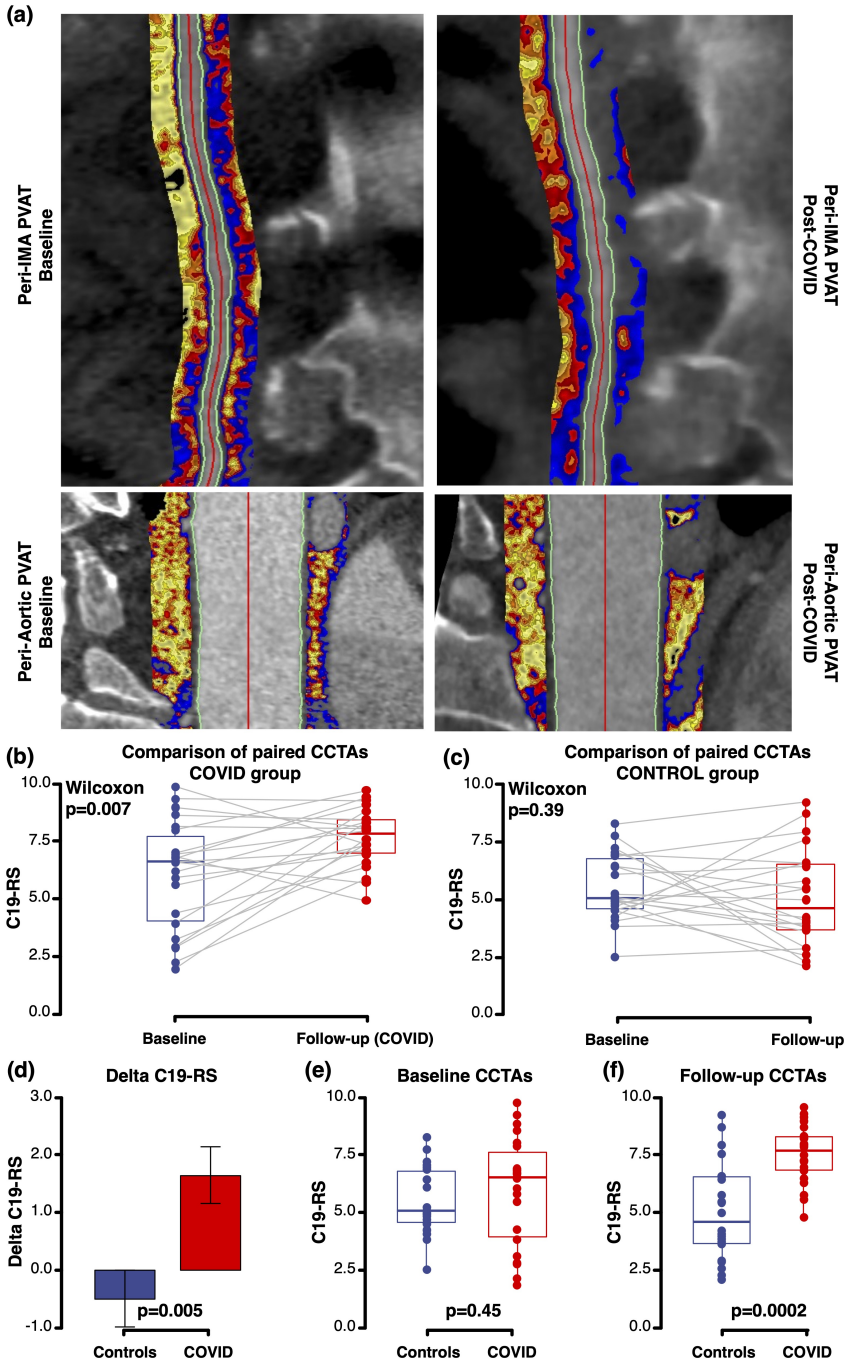


Figure 4.8: C19-RS for COVID-19 detection. (a) Illustration of PVAT mapping in CCTA in a patient 3 years before and during COVID-19 infection. (b) C19-RS was significantly higher in patients who acquired COVID-19 compared to baseline scans. (c) In matched paired controls C19-RS showed no significant change over time. (d) Comparison of the deltas in C19-RS between baseline and follow-up (e) Baseline scans in both groups had similar C19-RS values. (f) Equally, in follow-up scans, C19-RS was significantly higher in patients with COVID-19.

4.9). An optimal cut-off point for the detection of COVID-19 positive patients was determined by the Youden's index (C19-RS= 4.21, Figure 4.10): Patients with C19-RS above that cut-off (n=237) had an odds ratio of 2.97 (Adj. OR=2.97 [95%CI:1.43-6.27], p=0.004) of being COVID-19 positive compared to patients with low C19-RS values (n=94), after adjusting for age above 65, sex, cardiovascular risk factors (hypertension, hyperlipidaemia, diabetes, BMI, presence of coronary artery disease), plasma C-reactive protein plasma concentrations, white blood cell count, plasma troponin concentrations, history of chronic obstructive pulmonary disease, and CT scan tube voltage. Top third (n=8) comprising C19-RS significantly improved the discrimination of a baseline model consisting of the aforementioned covariates for COVID-19 diagnosis (Figure 4.11). This confirms that C19-RS can indeed capture the type of cytokine-induced vascular inflammation observed in COVID-19.

4.3.5 C19-RS is higher in patients infected with the B.1.1.7 SARS-CoV-2 variant

I used data on viral whole-genome sequencing to determine infecting lineages. In Study Arm 3, 115 patients underwent viral whole-genome sequencing with 71 of them found to be B.1.1.7. C19-RS had significantly higher values in COVID-19 patients with the B.1.1.7 variant compared with those infected by non-B.1.1.7 variants (Figure 4.12). C19-RS was able to distinguish B.1.1.7 patients from individuals with non-B.1.1.7 variants even after adjusting for age, sex, presence of coronary artery disease, history of chronic obstructive pulmonary disease white blood cell count, plasma C-reactive protein plasma concentrations, white blood cell count, plasma troponin concentrations (Adj. OR= 1.89 [95%CI:1.17-3.20] per SD, p=0.01), suggesting a higher vascular assault in these patients that is not captured by risk factors or circulating

Table 4.4: Demographic characteristics of the Study Arm 3 population

	First UK Wave		**Second UK Wave**
	Exploratory (20%)	**Validation (80%)**	**Validation (100%)**
	N=53	N=216	N=115
Age (years)	64.3±16.4	58.1±18.4	62.9 ±14.8
Sex (male, %)	26 (49.1)	95 (44.0)	72 (62.6)
Risk factors, n (%)			
Hypertension	23 (43.4)	69 (31.9)	26 (22.6)
Dyslipidaemia	6 (11.3)	31 (14.4)	16 (13.9)
Diabetes mellitus	13 (24.5)	37 (17.1)	25 (21.7)
COPD	2 (3.8)	12 (5.6)	9 (7.8)
CAD	5 (9.4)	16 (7.4)	15 (13.0)
SBP (mmHg)	130.9±27.3	132.5±22.0	129.7±18.6
BMI (kg/m^2)	30.0±9.6	27.7±6.3	30.6±7.6
Medication, n (%)			
Statins	13 (24.5)	59 (27.3)	18 (15.7)
ACEi	7 (13.2)	27 (12.5)	10 (8.7)
Beta blockers	5 (9.4)	23 (10.6)	9 (7.8)
Biochemical measurements			
CRP (mg/L)	82.9[33.0-180.0]	75.6[18.0-156.3]	98.8 [54.9, 141.4]
WBC (x10^3)	8.3 [6.4-12.0]	8.6 [6.1-12.3]	7.1 [5.3, 9.5]
Troponin (ng/L)	5.0 [2.0-62.5]	5.0 [2.0-20.0]	6.0 [4.0, 17.5]
Scan parameters			
Tube Voltage (kVp) or Effective Energy (keV), n (%)			
100 kVp	35 (66.0)	142 (65.7)	98 (85.2)
110 kVp	0 (0)	0 (0)	13 (11.3)
120 kVp	8 (15.1)	27 (12.5)	4 (3.5)
55 keV	1 (1.9)	3 (1.4)	0 (0)
58 keV	9 (17.0)	40 (18.5)	0 (0)
70 keV	0 (0.0)	4 (1.9)	0 (0)
Outcomes			
Days in hospital	7.0[0.0-18.0]	4.0[0.0-13.0]	8.0 [5.0, 14.0]
Death in-hospital, n(%)	12 (22.6)	21 (9.7)	19 (16.5)
Composite endpoint, n(%)	19 (35.8)	59 (27.3)	30 (26.1)

COPD=Chronic Obstructive pulmonary disease; CAD: Coronary Artery Disease; SBP: Systolic blood pressure; ACEi=angiotensin converting enzyme inhibitors; BMI=Body Mass Index; WBC=White Blood Cells count; ICU=Intensive care unit; Composite endpoint includes death in-hospital and/or admission to intensive care unit; continuous variables are expressed as mean±SD or median[range] as appropriate.

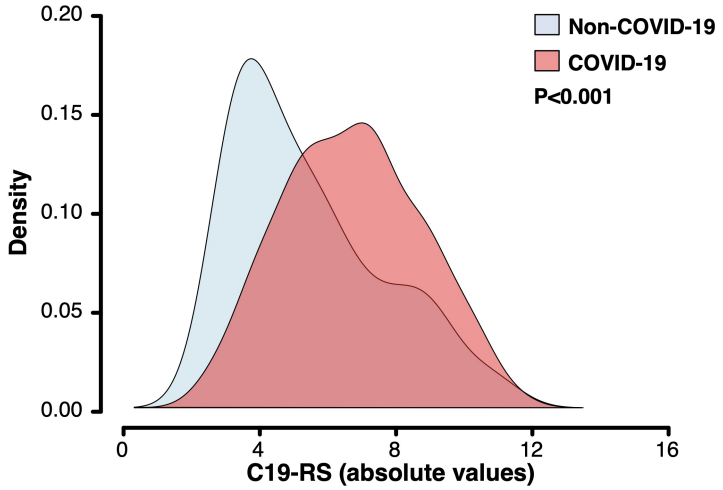


Figure 4.9: C19-RS is higher in COVID-19. C19-RS values were higher in the COVID-19 positive patients with an area under the curve for COVID-19 detection of 0.66 [95%CI: 0.59-0.74], p<0.001.

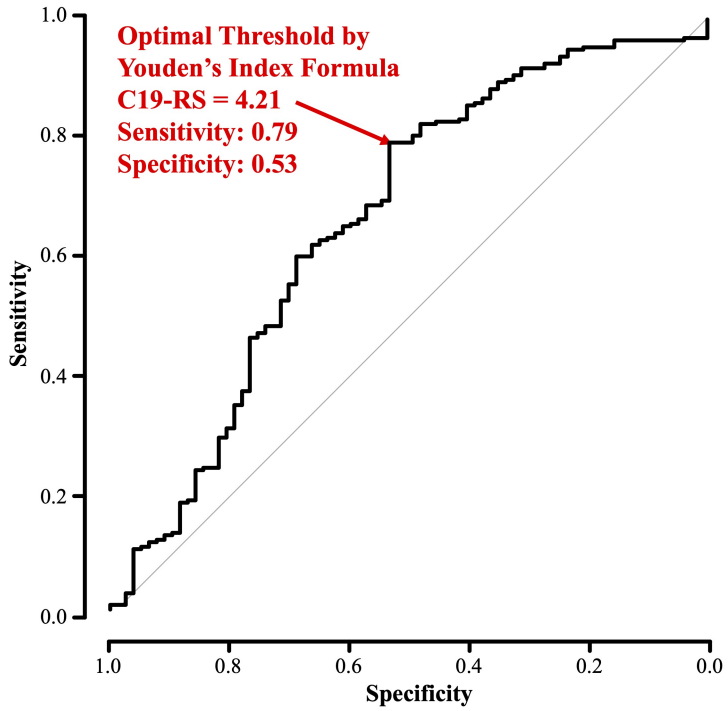


Figure 4.10: Optimal C19-RS cut-off for COVID-19 detection. Area under the curve (0.65 [95%CI: 0.57-0.73], p<0.001) and optimal cut-off point for COVID-19 detection in Study Arm 3 population.

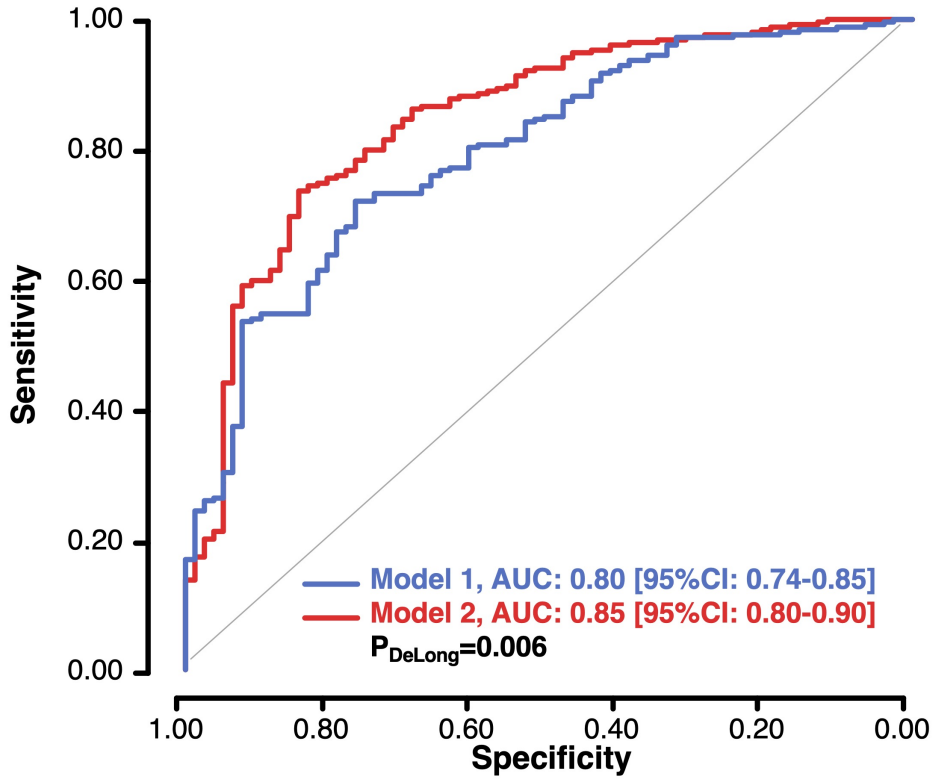


Figure 4.11: Incremental value of C19-RS radiomic features in COVID-19 detection. The combination of the top third (n=8) radiomic features comprising C19-RS significantly improved the discrimination of a baseline model consisting of age, sex, cardiovascular risk factors (hypertension, hyperlipidaemia, diabetes, BMI, presence of coronary artery disease), C-reactive protein plasma levels, white blood cell count, plasma troponin, and history of chronic obstructive pulmonary disease for COVID-19 detection.

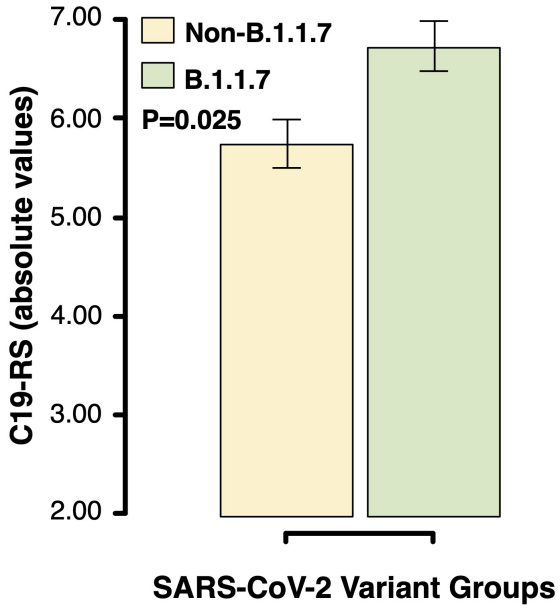


Figure 4.12: C19-RS is higher in patients with the B.1.1.7 variant. Patients with the B.1.1.7 variant after viral genome sequencing had significantly higher C19-RS values, suggesting higher degrees of vascular inflammation (values are presented as mean±standard error).

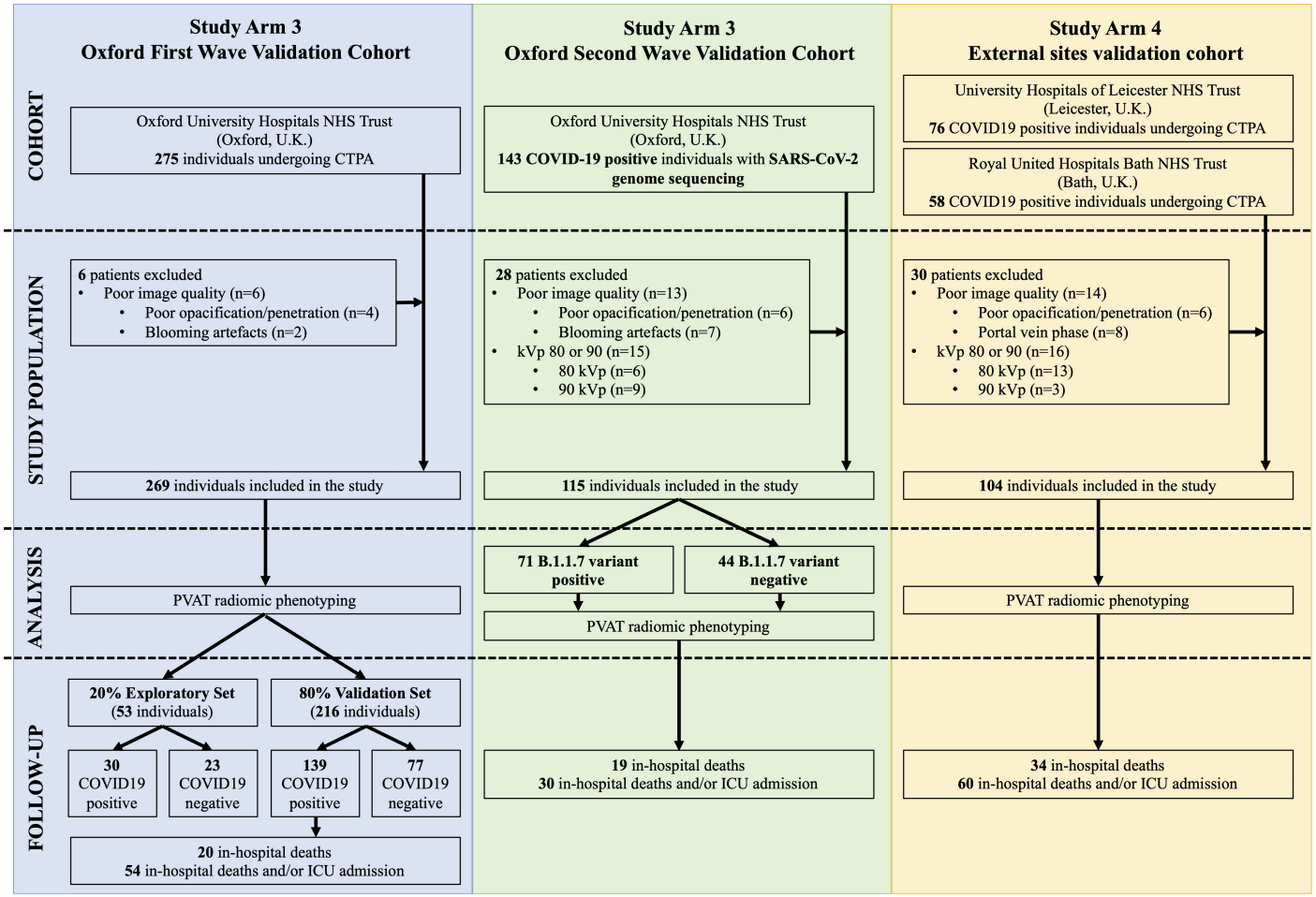


Figure 4.13: Image analysis and in-hospital outcomes collection diagram for Study Arms 3 4. ICU: Intensive care unit.

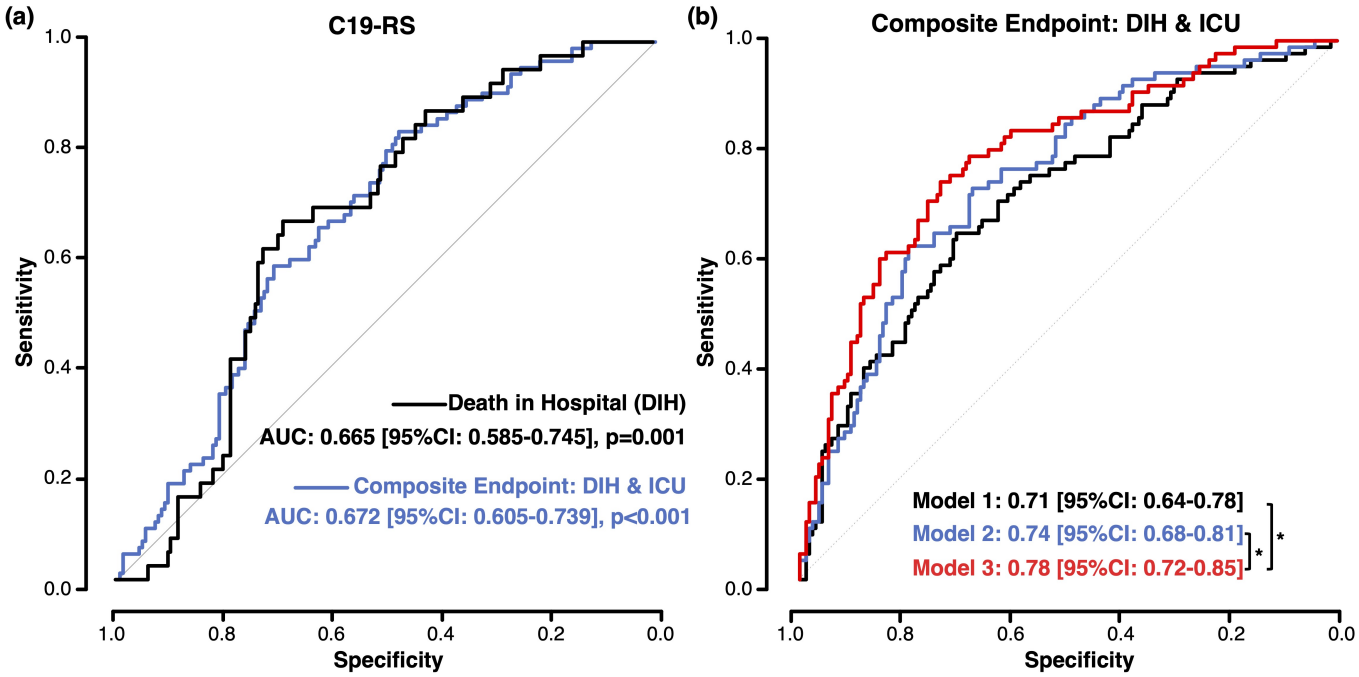


Figure 4.14: Prognostic value of C19-RS. (a) Univariate ROC analysis for the ability of C19-RS to predict death in-hospital (DIH) and a composite endpoint of DIH and/or intensive care unit (ICU) admission. (b) Comparison of receiver operator curves derived from logistic regression models showcasing the additive value of C19-RS. Model 1 consists of demographic variables age, sex, hypertension (HTN), hyperlipidaemia (HLD), diabetes mellitus (DM), body mass index (BMI), presence of coronary artery disease (CAD), history of chronic obstructive pulmonary disease (COPD), and tube voltage. Model 2 includes biochemistry biomarkers white blood cell count (WBC), C-reactive protein (CRP), and plasma troponin (Tn). Model 3 includes all parameters in model 2 plus C19-RS.

inflammatory markers.

4.3.6 Exploring the prognostic value of C19-RS in COVID-19

Thirty-nine COVID-19 positive patients in Study Arm 3 died in hospital, and 84 had a composite endpoint of either death in hospital or admission to the intensive care unit (Figure 4.13). C19-RS was able to predict both death in hospital and the composite endpoint with AUC of 66.5% and 67.2% respectively, even when it was used as a single variable (Figure 4.14). C19-RS could predict death in hospital with a hazard ratio of 1.91 ([95% CI: 1.23-2.96], p=0.004) per standard deviation increase, adjusted for clinical, biochemical risk factors and technical characteristics. Using an optimal cut-off point (C19-RS=6.99, Figure 4.15), patients with high C19-RS values had a 3.3-fold higher risk of in-hospital death compared to patients with low C19-RS (Figure 4.16). The addition of C19-RS to a comprehensive baseline model consisting of clinical and biochemical risk factors as well as technical characteristics (see Online Methods) significantly improved the model's accuracy (deltaAUC=0.04, PDeLong=0.046, Panova<0.001) for predicting the composite endpoint in COVID-19 positive patients (Figure 4.14). As expected, C19-RS was significantly correlated with plasma C-reactive protein concentrations (rho=0.18, p=0.003), and length of hospital stay (rho=0.20, p=0.002).

The inclusion of patients from the second UK wave in Study Arm 3 (October 2020 to January 2021) provided the unique opportunity to perform subgroup analyses based on treatment strategies deployed while the pandemic is still unfolding. Dexamethasone was not part of standard treatment during the first months of the pandemic; however it became an essential element of COVID-19 management in the second wave. We, therefore, performed a sensitivity analysis with patients receiving dexamethasone and observed that the prognostic value of C19-RS was

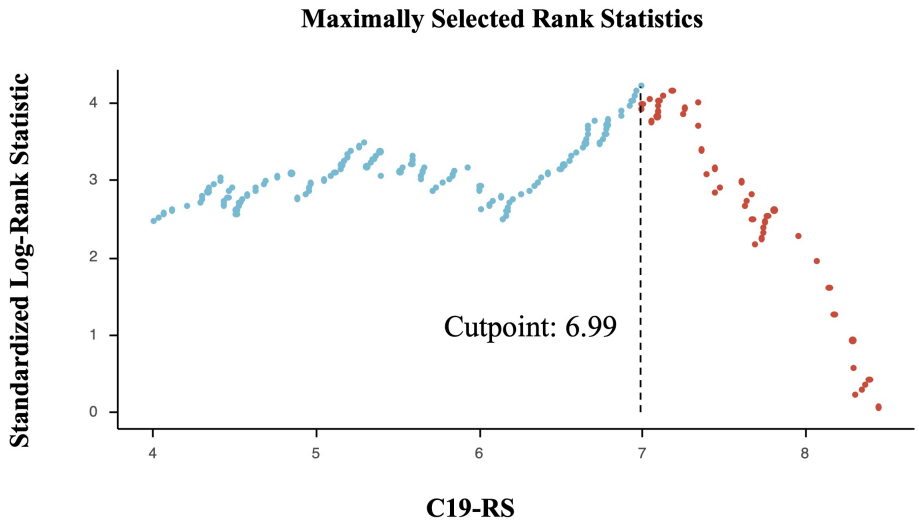


Figure 4.15: Identifying the optimal C19-RS cut-off for in-hospital death prediction. Plot of the standardized log-rank statistic for prediction of death in-hospital versus different cut-off points for C19-RS, showing optimal discrimination for a cut-off point of 6.99, in the Study Arm 3 population.

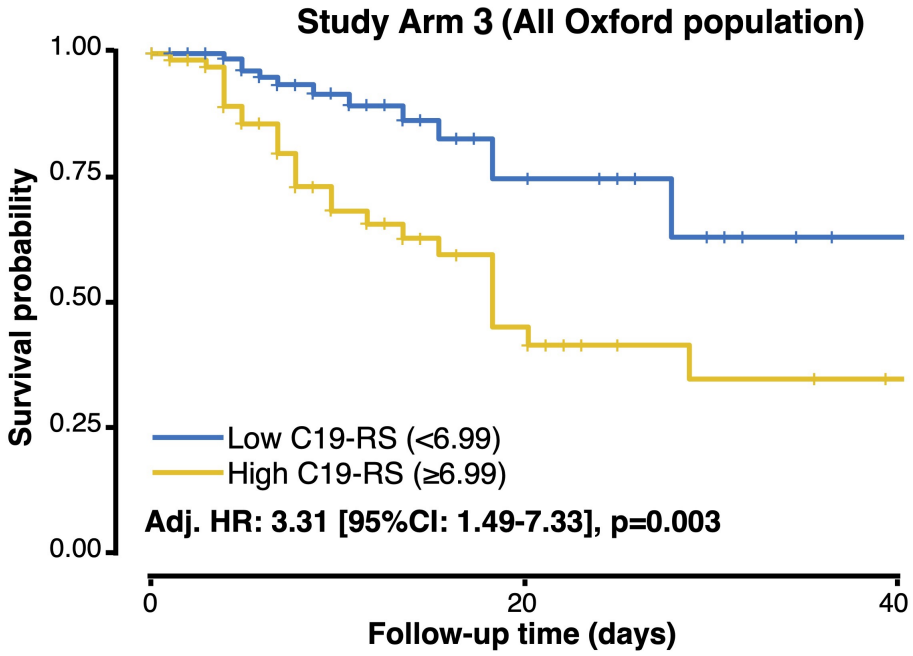


Figure 4.16: Kaplan-Meier plots of C19-RS for in-hospital death. Kaplan-Meier curve, and adjusted hazard ratio (HR) for in-hospital death for high versus low C19-RS groups in the Study Arm 3 population (n=254 with 39 deaths). HR is adjusted for age above 65, sex, cardiovascular risk factors (hypertension, hyperlipidaemia, diabetes, BMI, presence of coronary artery disease), C-reactive protein plasma levels, white blood cell count, plasma troponin, history of chronic obstructive pulmonary disease, tube voltage, and dexamethasone treatment.

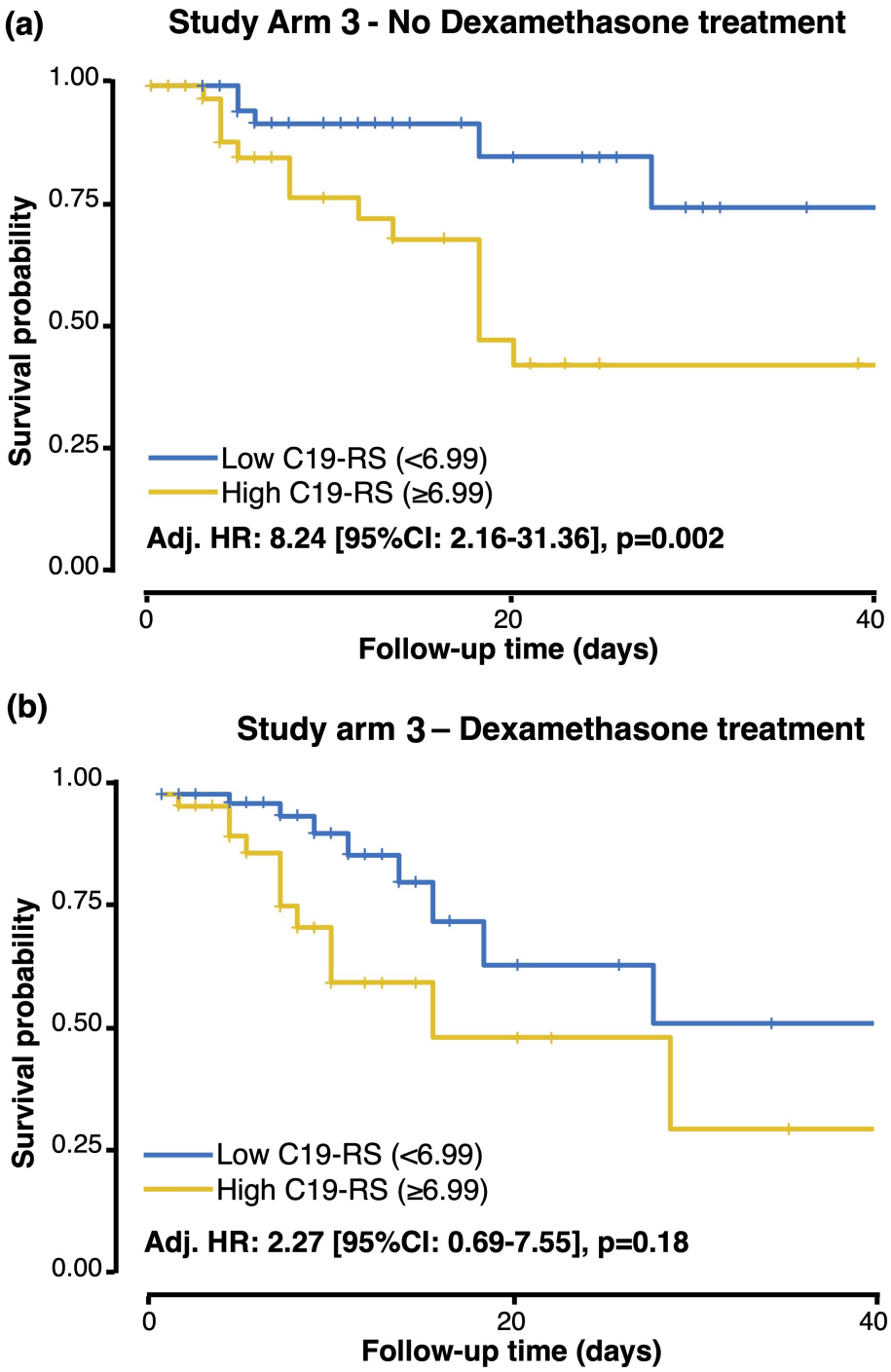


Figure 4.17: Kaplan-Meier plots of C19-RS for in-hospital death stratified based on dexamethasone treatment. Kaplan-Meier curves, and adjusted hazard ratios (HR) for in-hospital death for high versus low C19-RS groups in the Study Arm 3 population subgrouped by dexamethasone treatment (n=144 with 19 deaths for panel (a) and n=110 with 20 deaths for panel (b). HRs are adjusted for age above 65, sex, cardiovascular risk factors (hypertension, hyperlipidaemia, diabetes, BMI), C-reactive protein plasma levels, white blood cell count, history of chronic obstructive pulmonary disease, and tube voltage.

significantly blunted in this group (Figure 4.17).

Since generalisability is a limitation of machine learning models, we next evaluated the robustness of C19-RS as a prognostic imaging biomarker of arterial inflammation in COVID-19 in a fourth independent study arm (Study Arm 4), comprising 104 consecutive COVID-19 positive patients from different geographical areas with different local demographics from Bath and Leicester (Table 4.5).

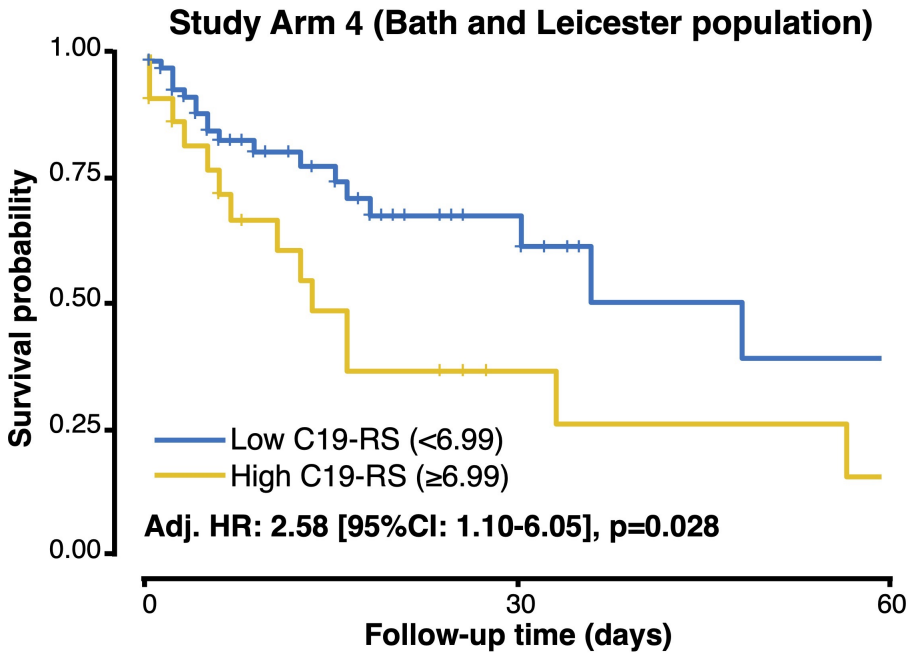


Figure 4.18: Kaplan-Meier plots of C19-RS for in-hospital death in the external validation cohort. Kaplan-Meier curve, and adjusted hazard ratio (HR) for in-hospital death for high versus low C19-RS groups in the External Validation Study Arm 4 population (n=104 with 34 deaths). HR is adjusted for age above 65, sex, cardiovascular risk factors (hypertension, hyperlipidaemia, diabetes, BMI, presence of coronary artery disease), C-reactive protein plasma levels, white blood cell count, plasma troponin, history of chronic obstructive pulmonary disease, and tube voltage.

A total of 34 in-hospital deaths were recorded, while 60 patients had the composite endpoint. C19-RS was associated with mortality, even after adjusting for clinical, biochemical

risk factors and technical characteristics (Adj.HR: 1.61 [96%CI: 1.08-2.40], per SD increase, p=0.02). Using the optimal cut-off point calculated in Study Arm 3 (C19-RS=6.99), patients with high C19-RS values had a 2.6-fold higher risk of in-hospital death compared to patients with low C19-RS after aforementioned adjustments (Figure 4.18). Patients with high C19-RS values also had 4.9 times higher risk of meeting the composite endpoint (Adj. OR: 4.92 [96%CI: 1.54-18.02, p=0.01). This provides a second external validation of C19-RS using different scanners, hospital settings in patients from different geographical locations than those in Study Arm 3.

Table 4.5: Demographic characteristics of the Study Arm 4 population

	Study Arm 4 population
Total (n)	104
Recruitment centre/region	
Leicester	56
Bath	48
Age (years)	63.9±14.1
Male sex, n (%)	63 (60.6)
Risk factors, n (%)	
Hypertension	30 (28.8)
Dyslipidaemia	13 (12.5)
Diabetes mellitus	28 (26.9)
CAD	3 (2.9)
COPD	17 (16.3)
Systolic blood pressure (mmHg)	128.2±22.4
Body Mass Index (kg/m2)	29.7±5.8
Biochemical measurements	
C-reactive protein (mg/L)	62.5 [28.0, 148.5]
Troponin	9.5 [6.0, 23.3]
White blood cell count ($x10^3$)	9.4 [6.5, 12.0]
Lymphocytes cell count ($x10^3$)	1.0 [0.7, 1.6]
Monocytes cell count ($x10^3$)	0.5 [0.3, 0.8]
Tube Voltage (kVp)	
100 (kVp, n, %)	55 (52.9)
110 (kVp, n, %)	3 (2.9)
120 (kVp, n, %)	39 (37.5)
140 (kVp, n, %)	7 (6.7)

COPD=Chronic Obstructive pulmonary disease; CAD: Coronary Artery Disease; continuous variables reported as means+/-SD or median[range] as appropriate.

4.3.7 C19-RS shows strong correlation with coagulation gene module

To further explore the cause of vascular inflammation linked to C19-RS, I examined the gene expression profile of whole blood from 23 patients provided by the COMBAT consortium. We first examined the expression of the inflammatory gene set (77 inflammatory genes expressed in whole blood). No relationship was found between the expression profile of these genes and the C19-RS score for the patients (Figure 4.19a), nor were any genes significantly differentially expressed (FDR<0.05) between patients with a high or low C19-RS score in a global analysis, suggesting that C19-RS is a vessel-centric inflammatory signature, not captured by measurements of systemic inflammation. However, analysing the correlation of C19-RS with eigengenes summarising gene co-expression modules derived using weighted Gene Correlation Network Analysis (WGCNA) on the full COMBAT dataset (Figure 4.19b), we found a striking correlation between C19-RS and the MEgreen eigengene module (r=0.61, p=0.00031; Figure 4.19c), which is highly enriched with coagulation pathways (Figure 4.19d).

The links between C19RS and coagulation (but not with inflammatory signatures in peripheral blood) implies that vascular inflammation may be the trigger of thrombosis, responsible for the multi-organ failure in COVID-19. This provides an important mechanistic insight into COVID-19 pathogenesis.

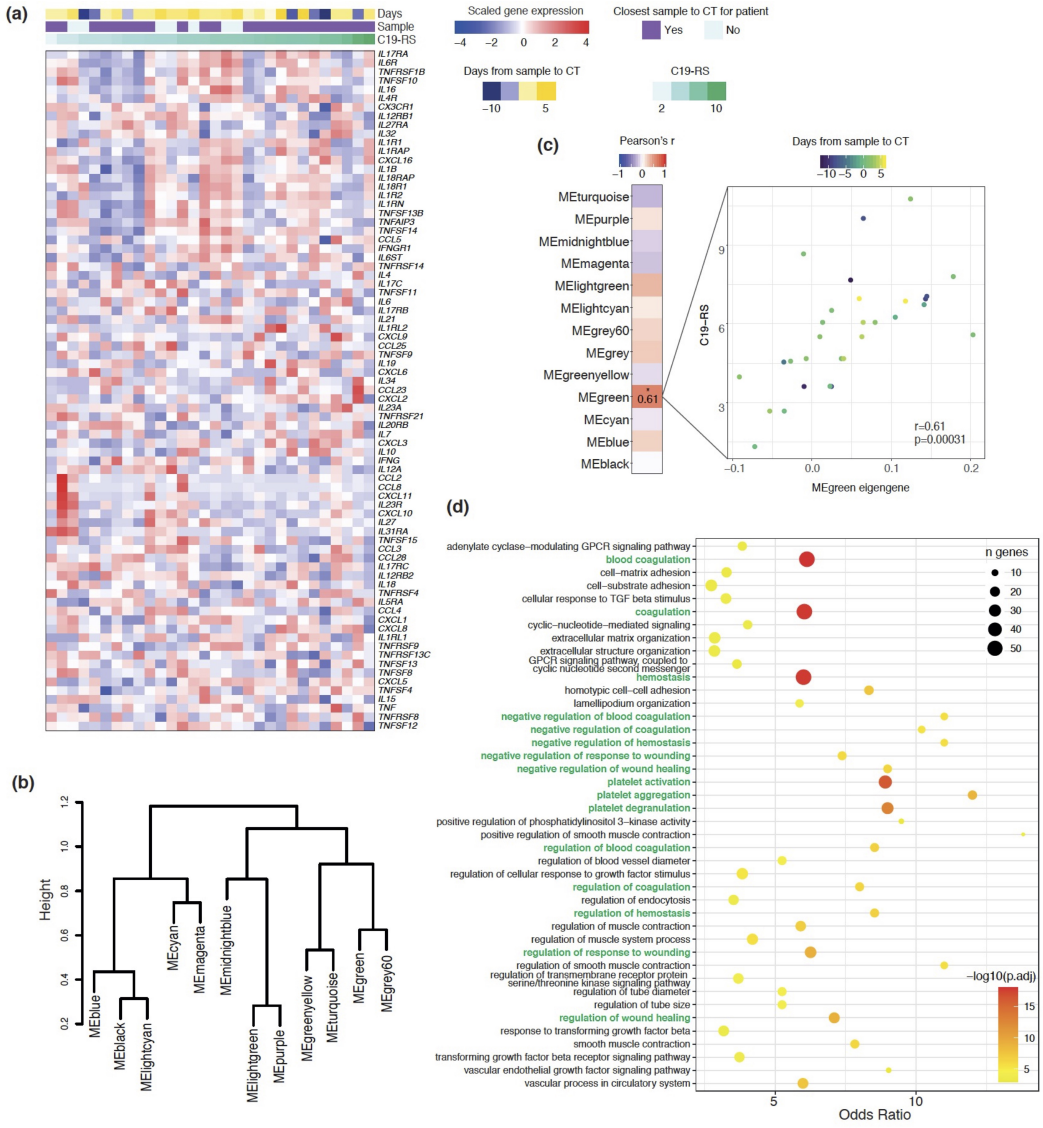


Figure 4.19: Whole blood gene expression profiles and C19-RS. (a) Expression of the inflammation-related gene set in the COMBAT whole blood RNAseq dataset (30 samples from 23 COVID-19 patients with CT scans, 77 genes detected). Samples are ordered by C19-RS, genes are clustered using Ward's method and Minkowski distance. Colour bar indicates sample timing and C19-RS. (b) Weighted Gene Correlation Network Analysis (WGCNA) on the full COMBAT dataset defined gene expression modules13. Unassigned genes were categorised as MEgrey. (c) Correlation between C19-RS and the MEgreen eigengene. (d) GOBP pathway enrichment analysis for MEgreen module member genes using hypergeometric test (terms with adjusted p-value <0.001 shown, full results Online Table 7). X axis (odds ratio) indicates strength of association between pathway and module memberships, size of point (n genes) indicates number of genes with overlapping membership, colour of points (adjusted p value) indicates significance of association (Figure generated by Dr Katie Burnham).

4.4 Discussion

4.4.1 Presenting a custom-made radiotranscriptomic signature

The radiotranscriptomic signature of vascular inflammation, the C19-RS, was developed using radiomic analysis of the perivascular space around the mammary arteries and the aorta. C19-RS was trained against the RNA-sequencing transcriptomic fingerprint of vascular inflammation of internal mammary arteries biopsies that may mimic the type of vascular inflammation that drives complications in COVID-19. In external validation, C19-RS measured in routine pulmonary artery CT angiograms of patients with acute COVID-19 was greater than in patients without COVID-19. Vascular inflammation measured by this method had a significant prognostic value for in-hospital mortality, confirming that vascular inflammation is a key feature of the disease pathogenesis. Indeed, C19-RS showed a significant but very weak correlation with C-reactive protein, suggesting that measures of systemic inflammation provide limited information on the inflammatory burden of the arterial wall. These findings have important clinical implications for understanding acute COVID-19 pathogenesis. Early identification of patients with high vascular inflammation has great potential for early stratification of patients with COVID-19 and could potentially guide treatments with steroids and anti-cytokine therapies, before clinical deterioration or increased oxygen requirements are evident. Furthermore, systematic radiotranscriptomic evaluation of COVID-19 related vascular inflammation has the potential to identify new targetable pathways, and to provide new insights into the pathogenesis of the long-term consequences of COVID-19 (Figure 4.20).

Another important finding of this study was that C19-RS was shown to have higher values

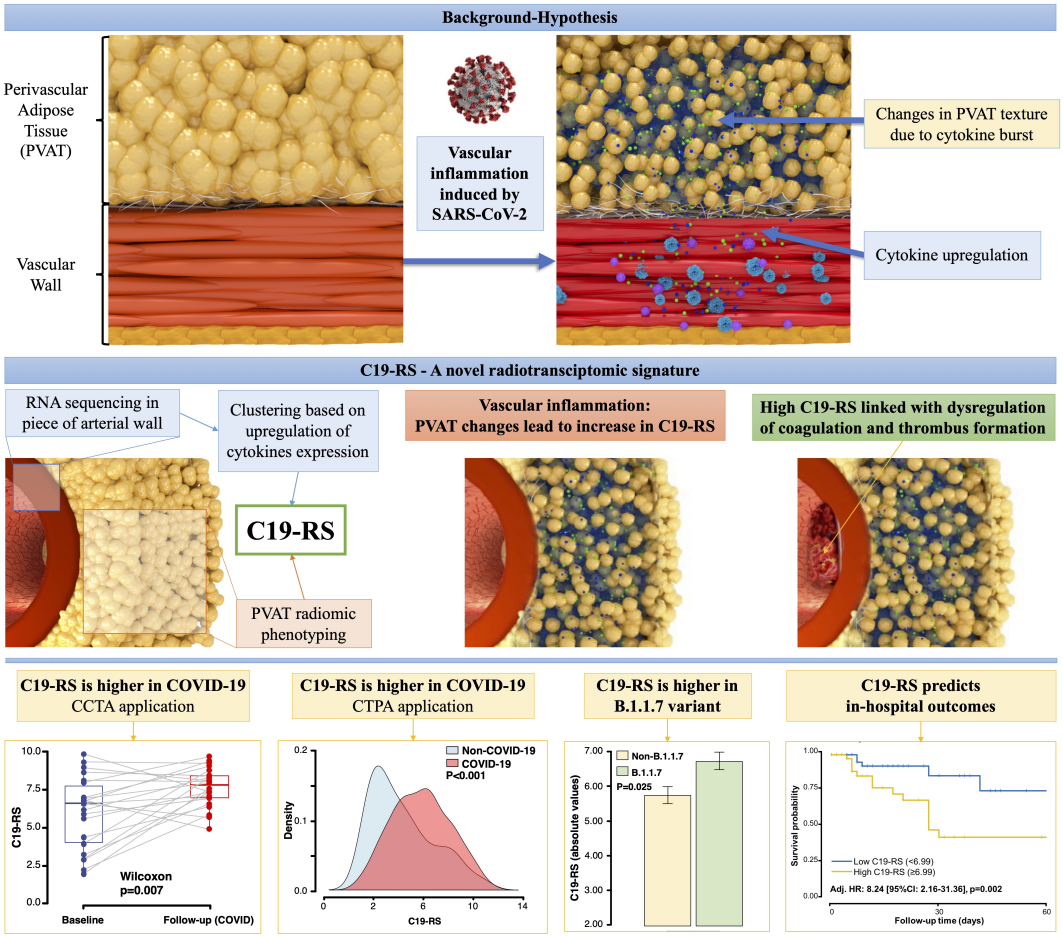


Figure 4.20: The proposed imaging biomarker C19-RS. Vascular inflammation induced by the SARS-CoV-2 virus causes structural changes to perivascular adipose tissue. Utilising RNA sequencing data, a novel imaging biomarker -namely C19-RS- was trained to reflect upregulation of cytokine related genes in the arterial wall. C19-RS was higher in COVID-19 positive patients, particularly in those with the B.1.1.7 variant, and had significant prognostic value for in-hospital death prediction.

in patients infected with the B.1.1.7 variant, suggesting a higher degree of vascular involvement in these patients. This information may be of significant use for the management of such patients both during the acute phase and at the post pandemic era, alerting the clinical care team to potential short- or long-term vascular complications.

4.4.2 C19-RS to guide selection of dexamethasone

In subgroup analyses based on dexamethasone treatment prognostic strength of C19-RS was shown to have a significant spike in the study patients that did not receive dexamethasone as part of their hospital admission, with the hazard ratio climbing to an 8-fold higher risk of in-hospital death. On the contrary, in the patients who were treated with dexamethasone, the prognostic potential of C19-RS dropped to two and lost its significance. This confirms the importance of dexamethasone treatment in attenuating COVID-19's assault to the vasculature, but at the same time highlights the importance of selecting patients for steroid treatment based on disease severity. A recent systematic review has identified the "unholy trinity" of diabetes, corticosteroids, and COVID-19 which appears to increase mucormycosis, a rare fungal infection with a 30.7% mortality rate (Singh, Singh, Joshi, & Misra, 2021). C19-RS can be used to screen patients with the highest vascular assault and guide dexamethasone treatment towards those patients who really need it (i.e. the ones with vascular inflammation who will respond well to antinflmmatory treatments), rather than treating everyone with steroids and exposing them to increased risk of a fatal fungal infection.

Although the leading cause of mortality in patients with COVID-19 is hypoxic respiratory failure from acute respiratory distress syndrome (ARDS) (Wu & McGoogan, 2020), it is now believed pulmonary micro-thrombosis caused by acute cytokine-driven inflammation of the pulmonary circulation is another key contributor to disease severity (Guzik et al., 2020). Corresponding inflammation in other vascular territories is believed to be the main driver of cardiac, renal and multi-organ injury in COVID-19 (T. Wang et al., 2020). High vascular inflammation appears closely linked with genes involved in platelet activation and degranulation in the pe-

ripheral blood, which has the potential to lead to micro-thrombi formation and may account for extrapulmonary COVID-19 manifestations or even long-COVID symptoms.

4.4.3 Identifying the degree of vascular inflammation in COVID-19

Acute vascular inflammation in COVID-19 can be caused by multiple mechanisms. SARS-CoV-2 binds to the ACE2 receptor, expressed in the vasculature of most organs in the human body (Hoffmann et al., 2020). This triggers a "cytokine storm" within the vascular wall, leading to inflammation of the small and large arteries (Varga et al., 2020). Cytokines IL-1β and TNF activate glucuronidases, that degrade the glycocalyx and upregulate hyaluronic acid synthase 2, leading to increased deposition of hyaluronic acid in the extracellular matrix promoting fluid retention (Teuwen et al., 2020). These mechanisms, together, lead to increased vascular permeability and can cause alterations in perivascular structures including PVAT. Quantifying cytokine-induced vascular inflammation in patients with COVID-19 is an unmet need for risk stratification of hospitalised patients to optimise management and allocation of resources, but also for guiding deployment of preventive measures post-hospital discharge, as viral infections have been known to increase the risk for future cardiovascular events (Chow et al., 2020). The long-term consequences of increased vascular inflammation induced by COVID-19, require urgent further investigation, particularly those with so-called "long-COVID".

As discussed previously (Investigators, 2018), vessel-derived cytokines diffuse into the perivascular space and cause characteristic rapid changes in the texture of the perivascular space, which can be captured and quantified in clinical CT angiography by using texture radiomics (Kotanidis & Antoniades, 2020c). By using a radiotranscriptomic approach, we constructed a novel imaging signature, the C19-RS, which can be extracted from any CT angiogram that visu-

alises the internal mammary arteries, and provides a quantitative measure of cytokine-induced vascular inflammation in patients with acute COVID-19 infection. Indeed, high vascular inflammation measured using this method, was associated with higher risk for in-hospital death in COVID-19 patients, independently from clinical risk factors or blood biomarkers (e.g. CRP, troponin, or WBC count). This technology provides significant incremental prognostic value above the current state of the art used for risk stratification in COVID-19, and calls for urgent clinical trials to evaluate its ability to guide deployment of anti-inflammatory treatments during the acute phase or after hospital discharge.

The power of this radiotranscriptomic approach is highlighted by the fact that the C19-RS was trained by analysis of the perivascular space around the mammary arteries and the aorta using coronary CT angiograms from non-COVID-19 patients and was then tested in CT angiograms of the pulmonary artery, in COVID-19 patients from 3 different geographical areas in England, with striking prognostic value. This signature is therefore easily generalisable and overcomes some of the major limitations of machine learning when applied to clinical practice. Since this is a generic signature of cytokine-driven vascular inflammation, it is expected to be applicable in many other diseases, beyond COVID-19. This proof of principle study demonstrates that platforms using quantitative radiotranscriptomics can offer unique opportunities for rapid development of radiotranscriptomic biomarkers to capture different types of vascular inflammation using post-processing of CT images performed in routine clinical care and will have widespread diagnostic applications across multiple medical specialties in the near future.

4.4.4 Limitations

While our results describe significant observations, there are a number of challenges that need to be taken into account. The findings about the impact of dexamethasone treatment on the prognostic value of C19-RS do not come from a randomised clinical trial, and they should be considered as hypothesis generating. Moreover, the calculation of C19-RS relies on CT angiograms, which are not routinely performed in acute COVID-19 infection in many centres; this inevitably limited my findings to those with a rather severe COVID-19 infection, but it still underscored the principle that vascular inflammation is triggered by COVID-19 in a clinically meaningful way. The subanalysis for correlation between C19-RS and gene expression profile of whole blood were performed in a relatively small number of patients (n=23), and the sampling time point for bulk RNA sequencing is not absolutely contemporaneous, ranging between 12 days before and 6 days after the C19-RS measurement.

Moreover, the internal mammary artery is known to not develop atherosclerotic plaques, which may limit its use in studying vascular inflammation. This can be attributed to a number of factors: the IMA endothelium shows fewer fenestrations and lower intercellular junction permeability, while inducible nitric oxide synthase (iNOS) and intercellular adhesion molecule-1 (ICAM-1) are only moderately expressed on the luminal surface and vasa vasorum of IMAs removed from patients with acute coronary syndrome or chronic stable angina (Foglieni et al., 2008). Moreover, IMA endothelial cells are rich in heparin sulfate and endothelial nitric oxide synthase, and release a larger amount of NO, which contributes to the vessel's antithrombotic and anti-atherosclerotic properties (Otsuka, Yahagi, Sakakura, & Virmani, 2013b). Nevertheless, in COVID-19, we are more interested in identifying a surrogate metric of global, acute,

cytokine-driven vascular inflammation, and the internal mammary artery may offer an advantage, exactly because it does not develop atherosclerotic plaques, which makes it ideally suited to provide a systemic metric of acute vascular inflammation, independent of local atherosclerotic disease. Indeed, it has previously been shown that inflammation in the IMA is an excellent surrogate for the inflammatory status of the entire vasculature as it reflects a non-atheroma-driven response (Otsuka et al., 2013b), and ex-vivo models using segments of IMA have been extensively used in for studying arterial biology (Akoumianakis et al., 2020, 2019). Moreover, the IMA also offers a unique arterial conduit for radiotranscriptomic analysis, given its accessibility during cardiac surgery and the ability to obtain tissue samples for subsequent analysis, and the fact that the IMA has homogenous PVAT along its length, enabling reliable radiomic features extraction from its perivascular spaceon the CCTA/CTPA images.

4.4.5 Translational Perspective

Vascular inflammation measured by applying quantitative radiotranscriptomics of perivascular fat on computed tomography angiography images, has striking prognostic value in patients with COVID-19, and identifies those who are most likely to benefit from anti-inflammatory treatments. A novel radiotranscriptomic signature of perivascular adipose tissue, the C19-RS, can quantify the degree of cytokine-driven vascular inflammation in COVID-19 patients and predicts in-hospital death independently of clinical factors and biochemical biomarkers of inflammation and myocardial injury. Anti-inflammatory treatment with dexamethasone reverses the detrimental effect of vascular inflammation on in-hospital mortality. High vascular inflammation is linked with coagulation activation in the periphery and triggers thrombotic disease in COVID-19.

4.4.6 Conclusions

In summary, I constructed and validated an imaging radiotranscriptomic signature, C19-RS, that detects cytokine-driven vascular inflammation. This technology applied in COVID-19 quantifies vascular inflammation, tracks patients who will develop arterial thrombosis, predicts in hospital outcomes of COVID 19 patients, and identifies responders to anti-inflammatory treatments. Introducing C19-RS into clinical practice may impact rapidly on patient management by helping streamline resource allocation, and providing a scalable tool to improve handling of any further COVID-19 waves, or even future pandemics. Given the role of acute vascular inflammation in destabilizing atherosclerotic plaques and triggering acute vascular syndromes, the technology presented in this study calls for large-scale outcomes studies to evaluate the ability of COVID-19-induced vascular inflammation to trigger acute vascular events in the months or even years after the infection. Such a finding would enable deployment of aggressive long-term preventive measures to those who experience high vascular inflammation during the acute phase of the infection.

5 | Summary, Limitations, and Future Directions

5.1 Summary of findings

Chapter 1 introduced the need for novel cardiovascular disease biomarkers, summarised findings around the role of oxidative stress in CVD in literature so far, explored the potential of using the field of radiomics to develop imaging biomarkers with biological significance, and in general provided the background foundation for the body of research work presented in this thesis. Chapter 2 summarised the methods used and developed for this thesis, which concentrated on human biopsies ex-vivo experiments, nucleic acid assays, sequencing, bioinformatics, image analysis methodology, data science, and statistics.

5.1.1 Oxidative stress in cardiovascular disease

The link between oxidative stress and cardiovascular disease pathogenesis is well established, particularly through basic science and animal model studies. Data from human trials have highlighted the role of increased ROS production in hypertension, atherosclerosis, myocardial infarction, and heart failure. However, whether oxidative stress contributes to the perseverance of cardiovascular disease and therefore may be a prognostic marker of disease outcome or even a therapeutic target, remains under heated debate. Antioxidants focused on ROS scavenging have so far failed to demonstrate a therapeutic benefit. Recently, new drugs targeting specific

enzymes involved in ROS generation across many intracellular organelles have been developed and showed to have promising results in non-human models. Nevertheless, the lack of clear evidence on the extent to which oxidative stress is involved in progression and severity of disease hinders their application in human clinical trials.

In Chapter 3 observed strong correlations of vascular and myocardial oxidative stress with mortality and long-term clinical outcomes. For the first time, increased oxidative stress was shown to, not only contribute to disease progression, but also to exert deleterious effects on survival. In order to elucidate the biology behind these observations and in an effort to reveal tangible therapeutic targets, I performed a large sequencing experiment with RNA from human internal mammary. Differential gene expression analysis between patients with high and low vascular oxidative stress revealed S100A8 and S100A9 amongst the most dysregulated genes. More specifically, in patients with high vascular NADPH oxidase activity these genes were significantly downregulated. I went on to validate this finding, thus highlighting these two genes as possible targets in the amelioration of vascular oxidative stress. In addition, I applied discovery network transcriptomics to internal mammary arteries to reveal a novel redox-sensitive transcriptomic signature that predicted long-term events. I revealed biological processes and pathways, such as oxidative phosphorylation, glucose metabolism, hypoxia-inducible factor 1 pathway, mitochondrial respiratory chain complex I assembly, mitochondrial electron transport, and gluconeogenesis, that are dysregulated in the vascular wall with high oxidative stress and can form therapeutic targets. Finally, after combining transcriptomic with genomic data, I identified oxoglutarate dehydrogenase as a target enzyme within the pathways enriched as a locus with both genetic polymorphisms and arterial transcriptional alterations linked with oxidative stress and long-term clinical endpoints.

5.1.2 Perivascular adipose tissue derived radiotranscriptomic signatures: an application in COVID-19

In Chapter 4 I present a new technology that uses quantitative radiotranscriptomics, to quantify the degree of cytokine-induced vascular inflammation by analysing images from CT angiograms of the coronary or the pulmonary arteries. The radiotranscriptomic signature of vascular inflammation, the C19-RS, was developed using radiomic analysis of the perivascular space around the mammary arteries and the aorta. C19-RS was trained against the RNA-sequencing transcriptomic fingerprint of vascular inflammation of internal mammary arteries biopsies, that may mimic the type of vascular inflammation that drives complications in COVID-19. In external validation, C19-RS measured in routine pulmonary artery CT angiograms of patients with acute COVID-19 was greater than in patients without COVID-19. Vascular inflammation measured by this method, had a significant prognostic value for in-hospital mortality, confirming that vascular inflammation is a key feature of the disease pathogenesis. Indeed, C19-RS showed a significant but very weak correlation with C-reactive protein, suggesting that measures of systemic inflammation provide limited information on the inflammatory burden of the arterial wall. These findings have important clinical implications for understanding acute COVID-19 pathogenesis. Early identification of patients with high vascular inflammation has great potential for early stratification of patients with COVID-19 and could potentially guide treatments with steroids and anti-cytokine therapies, before clinical deterioration or increased oxygen requirements are evident. Furthermore, systematic radiotranscriptomic evaluation of COVID-19 related vascular inflammation has the potential to identify new targetable pathways, and to provide new insights in to the pathogenesis of the long term consequences of COVID-19.

Although the leading cause of mortality in patients with COVID-19 is hypoxic respiratory failure from acute respiratory distress syndrome (ARDS) (Wu & McGoogan, 2020), it is now believed that this is driven by pulmonary micro-thrombosis caused by acute cytokine-driven inflammation of the pulmonary circulation (Guzik et al., 2020). Corresponding inflammation in other vascular territories is believed to be the main driver of cardiac, renal and multi-organ injury in COVID-19 (T. Wang et al., 2020). Acute vascular inflammation in COVID-19 can be caused by multiple mechanisms. SARS-CoV-2 binds to the ACE2 receptor, expressed in the vasculature of most organs in the human body (Hoffmann et al., 2020). This triggers a "cytokine storm" within the vascular wall, leading to inflammation of the small and large arteries (Varga et al., 2020). Cytokines IL-1β and TNF activate glucuronidases, that degrade the glycocalyx and up-regulate hyaluronic acid synthase 2, leading to increased deposition of hyaluronic acid in the extracellular matrix promoting fluid retention (Teuwen et al., 2020). These mechanisms, together, lead to increased vascular permeability and can cause alterations in perivascular structures including PVAT. Quantifying cytokine-induced vascular inflammation in patients with COVID-19 is an unmet need for risk stratification of hospitalised patients to optimise management and allocation of resources, but also for guiding deployment of preventive measures post-hospital discharge, as viral infections have been known to increase the risk for future cardiovascular events (Chow et al., 2020). The long-term consequences of increased vascular inflammation induced by COVID-19, require urgent further investigation, particularly those with so-called "long-COVID".

As discussed previously, (Oikonomou et al., 2019), vessel-derived cytokines diffuse into the perivascular space and cause characteristic rapid changes in the texture of the perivascular space, which can be captured and quantified in clinical CT angiography by using texture ra-

diomics. By using a radiotranscriptomic approach, we constructed a novel imaging signature, the C19-RS, which can be extracted from any CT angiogram that visualises the internal mammary arteries, and provides a quantitative measure of cytokine-induced vascular inflammation in patients with acute COVID-19 infection. Indeed, high vascular inflammation measured using this method, was associated with a 5-11 times higher risk for in-hospital death in COVID-19 patients, independently from clinical risk factors or blood biomarkers (e.g. CRP, troponin, or WBC count). This technology provides significant incremental prognostic value above the current state of the art used for risk stratification in COVID-19, and calls for urgent clinical trials to evaluate its ability to guide deployment of anti-inflammatory treatments during the acute phase or after hospital discharge.

The power of this radiotranscriptomic approach is highlighted by the fact that the C19-RS was trained by analysis of the perivascular space around the mammary arteries and the aorta using coronary CT angiograms from non-COVID-19 patients and was then tested in CT angiograms of the pulmonary artery, in COVID-19 patients from 3 different geographical areas in England, with striking prognostic value. This signature is therefore easily generalisable and overcomes some of the major limitations of machine learning when applied to clinical practice. Since this is a generic signature of cytokine-driven vascular inflammation, it is expected to be applicable in many other diseases, beyond COVID-19. This proof of principle study demonstrates that platforms using quantitative radiotranscriptomics can offer unique opportunities for rapid development of radiotranscriptomic biomarkers to capture different types of vascular inflammation using post-processing of CT images performed in routine clinical care and will have widespread diagnostic applications across multiple medical specialties in the near future.

Chapter 4 demonstrated the role of vascular inflammation in clinical outcomes of patients

with COVID-19. Introducing C19-RS into clinical practice may impact rapidly on patient management by helping healthcare systems to streamline resource allocation during the pandemic. Clinical trials are needed to test whether knowing the degree of vascular inflammation in patients with COVID-19, can help guide the timely use of anti-inflammatory treatments to those who need them.

5.2 Limitations

While my results describe significant observations, there are a number of challenges that need to be taken into account. In Chapter 3 the population used included exclusively patients with advanced atherosclerosis undergoing cardiac surgery. This may complicate the generalisation of certain conclusions of this thesis to a broader context of health and disease. The uniqueness of my work is largely based on the fact that I have used one of the most extensively phenotyped cohorts of vascular disease in the world, and this allows for an invaluable link between clinical parameters and biological readouts in these patients. Therefore, many of the clinical associations presented in this thesis involve biological readout variables such as vascular gene expression studies, and vascular $O_2^{\bullet -}$ measurements. Although the associations observed may help identify novel translational hypotheses, they are at the same time difficult to replicate in disease-free human cohorts due to lack of such biological material availability. Indeed, recruitment of CABG patients is virtually the only efficient and consistent way to gain access to human vascular tissue for the purposes of this thesis. Consequently, most of my findings are directly applicable to patients with atherosclerosis, but possibly not as readily generalisable in other study populations. However, this does not comprise a major limitation since the primary target subjects for this

work were patients with atherosclerosis to start with.

For the purposes of this thesis, I used IMA segments as models to study human vascular biology and vascular disease mechanisms, with a focus on atherosclerosis. This vessel is traditionally believed not to develop atherosclerosis, and this is precisely why it is the gold standard vascular graft choice. However, the IMA is still exposed to the main systemic atherosclerosis risk factors (i.e., smoking, diabetes, hyperlipidaemia, hypertension, high fat diet, systemic oxidative stress etc), and therefore can be assumed to reflect vascular biology across the whole vasculature. Besides, upon exposure to high pressure turbulent flow (i.e., after being grafted to the coronary circulation following CABG), IMA may develop atherosclerosis, which suggests that these vessels do share certain pathophysiological responses to certain pro-atherogenic stimuli with other vessels that frequently develop atherosclerosis such as the coronaries.

On the other hand, I believe that studying human vessels, even ones without atherosclerosis, is more important than the alternative which comprises studying diseased arteries of atherosclerosis animal models. This is because of the often-striking discrepancy amongst species regarding vascular biology; study of human vascular biology patterns in thus necessary if we hope to understand human vascular disease. Ideally, hypotheses should be tested in models of human vessels to assure relevance to human disease, then tested in animal models to confirm in vivo links with vascular disease. In the context of this thesis, certain experiments were replicated in mouse aortae which served as controls or in vivo replications of the hypotheses tested, to further increase the relevance of the proposed mechanisms to vascular disease in vivo.

In Chapter 4 the findings about the impact of dexamethasone treatment on the prognostic value of C19-RS do not come from a randomised clinical trial, and they should be considered as

hypothesis generating. Moreover, the calculation of C19-RS relies on CT angiograms, which are not routinely performed in acute COVID-19 infection in many centres; this inevitably limited my findings to those with a rather severe COVID-19 infection, but it still highlighted the principle that vascular inflammation is triggered by COVID-19 in a clinically meaningful way.

5.3 Future directions

My work has provided novel insights in the concept of vascular oxidative stress and perivascular adipose tissue phenotyping, introducing new unanswered questions and hypotheses.

5.3.1 Time to revisit antioxidant strategies in atherosclerosis

My observations on the independent prognostic role of vascular oxidative stress in survival estimates for patients with advances atherosclerosis, brings the field of antioxidant treatments back on the spotlight. Firstly, oxidative stress markers can be used for risk re-stratification in cardiac surgery. Currently, all prognostic models rely on clinical or biochemical information that is not vessel or myocardium specific. Development of rapid ROS quantification assays in vascular and myocardial tissue traditionally discarded during bypass cardiac surgery can inform the clinician on tissue specific redox state. Indeed, this prospect of making the most out of harvested tissues in cardiac surgery may form an interesting approach to individualising long-term risk management for the patient, through addition of a tissue-derived prognostic marker to the traditional reservoir of risk factors that determine medical care.

As mentioned already antioxidant strategies have been on pause lately owing mainly to the lack of definite evidence on the role of vascular oxidative stress in long-term outcomes, and

to the failure of ROS scavenging agents. My work highlights the importance of revisiting the antioxidant paradox through novel targets. To that end, I have unveiled a series of targets that may form the focus of study for future research, particularly clinical trials. Firstly, I have unveiled S100A8 and S100A9 to be downregulated in the presence of increased vascular oxidative stress. As discussed previously in this thesis (section 3.4.4), these proteins have been shown to have many contradicting properties. However, my observations favour previous reports about their ROS scavenging role and may form the basis of future research looking into reinstating the expression levels of these genes in the vasculature, thus restoring a natural defence mechanism, and reducing oxidative stress. Secondly, I have revealed oxidative phosphorylation, glucose metabolism, and mitochondrial respiratory chain assembly pathways as dysregulated gene networks under redox state conditions that favour oxidants. Targeting these pathways with drugs readily available (section 3.4.5) in clinical trials may provide the future clinician with another class of drugs to tackle CVD. Finally, I have unveiled SNP rs148449548 in the oxoglutarate dehydrogenase (OGDH) gene as a locus related with vascular oxidative stress in a gene that is transcriptionally affected by ROS. Use of this SNP as a screening tool in patients that may warrant more intensive management plans in medical care is yet to be studied, as well as inhibition of the OGDH enzyme in humans, following promising observations in animal studies (section 3.4.6).

5.3.2 Is radiotranscriptomics the future of cardiac imaging?

I have developed a platform for creating custom-made radiotranscriptomic signatures in perivascular adipose tissue. PVAT has been known for a while to undergo molecular, and macroscopic structural changes that reflect the inflammatory state of the adjacent vessel. By combining tran-

scriptomic and radiomic data I have introduced a concept that will allow future researchers to develop imaging biomarkers through isolation of biologically relevant propertied of images. In the context of this thesis, I have tested this principal in COVID-19, and showed that this approach can yield a promising tool (C19-RS) that captures vascular inflammation and predicts systemic thrombosis, and in-hospital death (section 4.4.1). Application of this technology in the future may inform better about the subgroup of patients that may benefit the most from particular drugs. This can be achieved by utilising data readily available, such as the RECOVERY trial, which randomises COVID-19 patients to different treatment interventions. Furthermore, testing the variability of the C19-RS biomarker months or years after a COVID-19 infection, may inform regarding the degree of remaining vascular inflammation. Inspecting the behaviour of C19-RS over time constitutes a valid future direction for the researchers who would like to investigate the role of vascular protective drugs, such as statins for example in the medical care of patients presenting with long-COVID.

In addition, the radiotranscriptomic concept may be further finetuned by looking into transcriptional data from PVAT itself and how they correlate with transcriptional data from the vessels and with radiomic data from images. Towards that end, I have already created an RNA sequencing library of 308 PVAT samples from the Ox-HVF cohort that can benefit future research attempts in understanding better the interactions between the vascular wall and perivascular space, while at the same time providing a unique opportunity of isolating radiomic patterns directly inherent to specific gene alterations. Taken all together, these proof-of-concept approaches have the trajectory to produce many exciting new hypotheses and tools for future research.

5.3.3 Ox-HVF: What does the future hold?

The body of research of work presented in this thesis is largely based on the Ox-HVF cohort, one of the most well phenotyped cohorts of human cardiac and vascular tissue. The Oxford Heart, Vessels Fat cohort consists of a cluster of clinical studies (namely ART Vascular, Bypass Grafts, AdipoRedOx, and ORFAN), which provide synergistic results allowing the deployment of a multi-level strategy to understand the mechanisms of cardiovascular diseases. As each one of the individual studies approaches the issue of cardiovascular disease pathogenesis from a different angle, the Ox-HVF cohort provides a unique and powerful platform. The strength of the cohort is the direct access to human tissue (vessels, myocardial and fat biopsies, DNA, plasma and others), in combination with extensive non-invasive cardiovascular phenotyping that includes cardiovascular computed tomography angiography, ultrasound and others (taken from oxhvf.com, drafted by myself).

During my days as a DPhil student, I have worked towards expanding this cohort, being responsible for tissue collection, DNA and RNA extractions, ex vivo functional assay implementation and archiving of all the biological material and data. I further contributed to image analysis creating the first radiomics library for the cohort. In addition, I set up a 3-year data sharing agreement with NHS Digital, which will continue to enrich the long-term outcome data, either mortality or hospital episodes, on existing and future participants across the country. This agreement benefits the whole cohort which involves other than the AdipoRedOx study which includes cardiac surgery patients, the ORFAN study, which includes control subjects. A plethora of projects arising from the Ox-HVF cohort is currently underway. The roles of micro-RNA-92a produced by epicardial adipose tissue and circulating ceramides originating

from lipid metabolism, in myocardial redox state is actively studied. Further, the interaction patterns of transcription between vascular and perivascular fat tissue are being studied by the bioinformatics core of the Oxford Translational Cardiovascular Research Group. The ORFAN study finally promises large-scale validation studies for novel imaging biomarkers in the context of atherosclerosis, COVID-19 vascular inflammation, atrial fibrillation, radiation induced inflammation in cancer, diabetes and many others.

Bibliography

Abazid, R. M., Smettei, O. A., Kattea, M. O., Sayed, S., Saqqah, H., Widyan, A. M., & Opolski, M. P. (2017). Relation Between Epicardial Fat and Subclinical Atherosclerosis in Asymptomatic Individuals. *J Thorac Imaging*, *32*(6), 378-382.

Ackermann, M., Verleden, S. E., Kuehnel, M., Haverich, A., Welte, T., Laenger, F., Vanstapel, A., Werlein, C., Stark, H., Tzankov, A., Li, W. W., Li, V. W., Mentzer, S. J., & Jonigk, D. (2020). Pulmonary Vascular Endothelialitis, Thrombosis, and Angiogenesis in Covid-19. *N Engl J Med*, *383*(2), 120-128.

Aerts, H. J., Velazquez, E. R., Leijenaar, R. T., Parmar, C., Grossmann, P., Carvalho, S., Bussink, J., Monshouwer, R., Haibe-Kains, B., & Rietveld, D. (2014). Decoding tumour phenotype by noninvasive imaging using a quantitative radiomics approach. *Nature communications*, *5*, 4006.

Aghamohammadzadeh, R., Withers, S., Lynch, F., Greenstein, A., Malik, R., & Heagerty, A. (2012). Perivascular adipose tissue from human systemic and coronary vessels: the emergence of a new pharmacotherapeutic target. *Br J Pharmacol*, *165*(3), 670-82.

Ahern, D. J., Ai, Z., Ainsworth, M., Allan, C., Allcock, A., Ansari, A., Arancibia-Carcamo, C. V., Aschenbrenner, D., Attar, M., Baillie, J. K., Barnes, E., Bashford-Rogers, R., Bashyal, A., Beer, S., Berridge, G., Beveridge, A., Bibi,

S., Bicanic, T., Blackwell, L., Bowness, P., Brent, A., Brown, A., Broxholme, J., Buck, D., Burnham, K. L., Byrne, H., Camara, S., Candido Ferreira, I., Charles, P., Chen, W., Chen, Y.-L., Chong, A., Clutterbuck, E., Coles, M., Conlon, C. P., Cornall, R., Cribbs, A. P., Curion, F., Davenport, E. E., Davidson, N., Davis, S., Dendrou, C., Dequaire, J., Dib, L., Docker, J., Dold, C., Dong, T., Downes, D., Drakesmith, A., Dunachie, S. J., Duncan, D. A., Eijsbouts, C., Esnouf, R., Espinosa, A., Etherington, R., Fairfax, B., Fairhead, R., Fang, H., Fassih, S., Felle, S., Fernandez Mendoza, M., Ferreira, R., Fischer, R., Foord, T., Forrow, A., Frater, J., Fries, A., Gallardo Sanchez, V., Garner, L., Geeves, C., Georgiou, D., Godfrey, L., Golubchik, T., Gomez Vazquez, M., Green, A., Harper, H., Harrington, H. A., Heilig, R., Hester, S., Hill, J., Hinds, C., Hird, C., Ho, L.-P., Hoekzema, R., Hollis, B., Hughes, J., Hutton, P., Jackson, M., Jainarayanan, A., James-Bott, A., Jansen, K., Jeffery, K., Jones, E., Jostins, L., Kerr, G., Kim, D., Klenerman, P., Knight, J. C., Kumar, V., Kumar Sharma, P., et al. (2021). A blood atlas of COVID-19 defines hallmarks of disease severity and specificity. *medRxiv*, 2021.05.11.21256877.

Akoumianakis, I. (2019). *Regulation of human vascular redox state in obesity and insulin resistance* (Thesis).

Akoumianakis, I., & Antoniades, C. (2017). The interplay between adipose tissue and the cardiovascular system: is fat always bad? *Cardiovasc Res*, *113*(9), 999-1008.

Akoumianakis, I., Badi, I., Douglas, G., Chuaiphichai, S., Herdman, L., Akawi, N., Margaritis, M., Antonopoulos, A. S., Oikonomou, E. K., Psarros, C., Galiat-

satos, N., Tousoulis, D., Kardos, A., Sayeed, R., Krasopoulos, G., Petrou, M., Schwahn, U., Wohlfart, P., Tennagels, N., Channon, K. M., & Antoniades, C. (2020). Insulin-induced vascular redox dysregulation in human atherosclerosis is ameliorated by dipeptidyl peptidase 4 inhibition. *Sci Transl Med*, *12*(541).

Akoumianakis, I., Sanna, F., Margaritis, M., Badi, I., Akawi, N., Herdman, L., Coutinho, P., Fagan, H., Antonopoulos, A. S., Oikonomou, E. K., Thomas, S., Chiu, A. P., Chuaiphichai, S., Kotanidis, C. P., Christodoulides, C., Petrou, M., Krasopoulos, G., Sayeed, R., Lv, L., Hale, A., Naeimi Kararoudi, M., McNeill, E., Douglas, G., George, S., Tousoulis, D., Channon, K. M., & Antoniades, C. (2019). Adipose tissue-derived WNT5A regulates vascular redox signaling in obesity via USP17/RAC1-mediated activation of NADPH oxidases. *Sci Transl Med*, *11*(510), eaav5055.

Altenhofer, S., Kleikers, P. W., Radermacher, K. A., Scheurer, P., Rob Hermans, J. J., Schiffers, P., Ho, H., Wingler, K., & Schmidt, H. H. (2012). The NOX toolbox: validating the role of NADPH oxidases in physiology and disease. *Cell Mol Life Sci*, *69*(14), 2327-43.

Altenhofer, S., Radermacher, K. A., Kleikers, P. W., Wingler, K., & Schmidt, H. H. (2015). Evolution of NADPH Oxidase Inhibitors: Selectivity and Mechanisms for Target Engagement. *Antioxid Redox Signal*, *23*(5), 406-27.

Anderson, C. M., Sonis, S. T., Lee, C. M., Adkins, D., Allen, B. G., Sun, W., Agarwala, S. S., Venigalla, M. L., Chen, Y., Zhen, W., Mould, D. R., Holmlund, J. T., Brill, J. M., & Buatti, J. M. (2018). Phase 1b/2a Trial of the Superoxide Dismutase

Mimetic GC4419 to Reduce Chemoradiotherapy-Induced Oral Mucositis in Patients With Oral Cavity or Oropharyngeal Carcinoma. *Int J Radiat Oncol Biol Phys*, *100*(2), 427-435.

Anderson, E. J., Lustig, M. E., Boyle, K. E., Woodlief, T. L., Kane, D. A., Lin, C.-T., Price, J. W., Kang, L., Rabinovitch, P. S., & Szeto, H. H. (2009). Mitochondrial H 2 O 2 emission and cellular redox state link excess fat intake to insulin resistance in both rodents and humans. *The Journal of clinical investigation*, *119*(3), 573-581.

Anderson, M. E., Powrie, F., Puri, R. N., & Meister, A. (1985). Glutathione monoethyl ester: preparation, uptake by tissues, and conversion to glutathione. *Arch Biochem Biophys*, *239*(2), 538-48.

Antoniades, C., Bakogiannis, C., Tousoulis, D., Antonopoulos, A. S., & Stefanadis, C. (2009). The CD40/CD40 ligand system: linking inflammation with atherothrombosis. *J Am Coll Cardiol*, *54*(8), 669-77.

Antoniades, C., Demosthenous, M., Reilly, S., Margaritis, M., Zhang, M. H., Antonopoulos, A., Marinou, K., Nahar, K., Jayaram, R., Tousoulis, D., Bakogiannis, C., Sayeed, R., Triantafyllou, C., Koumallos, N., Psarros, C., Miliou, A., Stefanadis, C., Channon, K. M., & Casadei, B. (2012). Myocardial redox state predicts in-hospital clinical outcome after cardiac surgery effects of short-term pre-operative statin treatment. *J Am Coll Cardiol*, *59*(1), 60-70.

Antoniades, C., Kotanidis, C. P., & Berman, D. S. (2019). State-of-the-art review article. Atherosclerosis affecting fat: What can we learn by imaging perivascular

adipose tissue? *J Cardiovasc Comput Tomogr*, *13*(5), 288-296.

Antoniades, C., Shirodaria, C., Warrick, N., Cai, S., de Bono, J., Lee, J., Leeson, P., Neubauer, S., Ratnatunga, C., Pillai, R., Refsum, H., & Channon, K. M. (2006). 5-methyltetrahydrofolate rapidly improves endothelial function and decreases superoxide production in human vessels: effects on vascular tetrahydrobiopterin availability and endothelial nitric oxide synthase coupling. *Circulation*, *114*(11), 1193-201.

Antonopoulos, A. S., & Antoniades, C. (2017). The role of epicardial adipose tissue in cardiac biology: classic concepts and emerging roles. *J Physiol*, *595*(12), 3907-3917.

Antonopoulos, A. S., Margaritis, M., Coutinho, P., Digby, J., Patel, R., Psarros, C., Ntusi, N., Karamitsos, T. D., Lee, R., De Silva, R., Petrou, M., Sayeed, R., Demosthenous, M., Bakogiannis, C., Wordsworth, P. B., Tousoulis, D., Neubauer, S., Channon, K. M., & Antoniades, C. (2014). Reciprocal effects of systemic inflammation and brain natriuretic peptide on adiponectin biosynthesis in adipose tissue of patients with ischemic heart disease. *Arterioscler Thromb Vasc Biol*, *34*(9), 2151-9.

Antonopoulos, A. S., Margaritis, M., Coutinho, P., Shirodaria, C., Psarros, C., Herdman, L., Sanna, F., De Silva, R., Petrou, M., Sayeed, R., Krasopoulos, G., Lee, R., Digby, J., Reilly, S., Bakogiannis, C., Tousoulis, D., Kessler, B., Casadei, B., Channon, K. M., & Antoniades, C. (2015). Adiponectin as a link between type 2 diabetes and vascular NADPH oxidase activity in the human arterial wall: the

regulatory role of perivascular adipose tissue. *Diabetes*, *64*(6), 2207-19.

Antonopoulos, A. S., Margaritis, M., Lee, R., Channon, K., & Antoniades, C. (2012). Statins as anti-inflammatory agents in atherogenesis: molecular mechanisms and lessons from the recent clinical trials. *Curr Pharm Des*, *18*(11), 1519-30.

Antonopoulos, A. S., Sanna, F., Sabharwal, N., Thomas, S., Oikonomou, E. K., Herdman, L., Margaritis, M., Shirodaria, C., Kampoli, A. M., Akoumianakis, I., Petrou, M., Sayeed, R., Krasopoulos, G., Psarros, C., Ciccone, P., Brophy, C. M., Digby, J., Kelion, A., Uberoi, R., Anthony, S., Alexopoulos, N., Tousoulis, D., Achenbach, S., Neubauer, S., Channon, K. M., & Antoniades, C. (2017). Detecting human coronary inflammation by imaging perivascular fat. *Sci Transl Med*, *9*(398), eaal2658.

Antonopoulos, A. S., & Tousoulis, D. (2017). The molecular mechanisms of obesity paradox. *Cardiovasc Res*, *113*(9), 1074-1086.

Anvari, E., Wikstrom, P., Walum, E., & Welsh, N. (2015). The novel NADPH oxidase 4 inhibitor GLX351322 counteracts glucose intolerance in high-fat diet-treated C57BL/6 mice. *Free radical research*, *49*(11), 1308-1318.

Aston, K., Rath, N., Naik, A., Slomczynska, U., Schall, O. F., & Riley, D. P. (2001). Computer-aided design (CAD) of Mn(II) complexes: superoxide dismutase mimetics with catalytic activity exceeding the native enzyme. *Inorg Chem*, *40*(8), 1779-89.

Atlante, S., Visintin, A., Marini, E., Savoia, M., Dianzani, C., Giorgis, M., Surun, D., Maione, F., Schnutgen, F., Farsetti, A., Zeiher, A. M., Bertinaria, M., Giraudo,

E., Spallotta, F., Cencioni, C., & Gaetano, C. (2018). alpha-ketoglutarate dehydrogenase inhibition counteracts breast cancer-associated lung metastasis. *Cell Death Dis*, *9*(7), 756.

Aune, D., Sen, A., Prasad, M., Norat, T., Janszky, I., Tonstad, S., Romundstad, P., & Vatten, L. J. (2016). BMI and all cause mortality: systematic review and non-linear dose-response meta-analysis of 230 cohort studies with 3.74 million deaths among 30.3 million participants. *BMJ*, *353*, i2156.

Averill, M. M., Kerkhoff, C., & Bornfeldt, K. E. (2012). S100A8 and S100A9 in cardiovascular biology and disease. *Arterioscler Thromb Vasc Biol*, *32*(2), 223-9.

Aviram, M., Rosenblat, M., Etzioni, A., & Levy, R. (1996). Activation of NADPH oxidase is required for macrophage-mediated oxidation of low-density lipoprotein. *Metabolism*, *45*(9), 1069-1079.

Ayala-Lopez, N., Thompson, J. M., & Watts, S. W. (2017). Perivascular Adipose Tissue's Impact on Norepinephrine-Induced Contraction of Mesenteric Resistance Arteries. *Front Physiol*, *8*, 37.

Baker, A. R., Silva, N. F., Quinn, D. W., Harte, A. L., Pagano, D., Bonser, R. S., Kumar, S., & McTernan, P. G. (2006). Human epicardial adipose tissue expresses a pathogenic profile of adipocytokines in patients with cardiovascular disease. *Cardiovasc Diabetol*, *5*(1), 1.

Ballinger, S. W., Patterson, C., Knight-Lozano, C. A., Burow, D. L., Conklin, C. A., Hu, Z., Reuf, J., Horaist, C., Lebovitz, R., Hunter, G. C., McIntyre, K., & Runge,

M. S. (2002). Mitochondrial integrity and function in atherogenesis. *Circulation*, *106*(5), 544-9.

Banfi, B., Malgrange, B., Knisz, J., Steger, K., Dubois-Dauphin, M., & Krause, K.-H. (2004). NOX3, a superoxide-generating NADPH oxidase of the inner ear. *Journal of Biological Chemistry*, *279*(44), 46065-46072.

Banfi, B., Tirone, F., Durussel, I., Knisz, J., Moskwa, P., Molnar, G. Z., Krause, K. H., & Cox, J. A. (2004). Mechanism of Ca2+ activation of the NADPH oxidase 5 (NOX5). *J Biol Chem*, *279*(18), 18583-91.

Barry-Lane, P. A., Patterson, C., Van Der Merwe, M., Hu, Z., Holland, S. M., Yeh, E. T., & Runge, M. S. (2001). p47phox is required for atherosclerotic lesion progression in ApoEâ/âmice. *The Journal of clinical investigation*, *108*(10), 1513-1522.

Batinic-Haberle, I., Spasojevic, I., Hubert, M. T., Tovmasyan, A., Rajic, Z., Clair, D. K. S., Vujaskovic, Z., Dewhirst, M. W., & Piganelli, J. D. (2012). Design of Mn porphyrins for treating oxidative stress injuries and their redox-based regulation of cellular transcriptional activities. *Amino acids*, *42*(1), 95-113.

Batinic-Haberle, I., Tovmasyan, A., & Spasojevic, I. (2015). An educational overview of the chemistry, biochemistry and therapeutic aspects of Mn porphyrinsâfrom superoxide dismutation to H2O2-driven pathways. *Redox biology*, *5*, 43-65.

Bedard, K., & Krause, K. H. (2007a). The NOX family of ROS-generating NADPH oxidases: physiology and pathophysiology. *Physiol Rev*, *87*(1), 245-313.

Bedard, K., & Krause, K.-H. (2007b). The NOX family of ROS-generating NADPH oxidases: physiology and pathophysiology. *Physiological reviews*, *87*(1), 245-

313.

BelAiba, R. S., Djordjevic, T., Petry, A., Diemer, K., Bonello, S., Banfi, B., Hess, J., Pogrebniak, A., Bickel, C., & Gorlach, A. (2007). NOX5 variants are functionally active in endothelial cells. *Free Radic Biol Med*, *42*(4), 446-59.

Bjelakovic, G., Nikolova, D., Gluud, L. L., Simonetti, R. G., & Gluud, C. (2007). Mortality in randomized trials of antioxidant supplements for primary and secondary prevention: systematic review and meta-analysis. *JAMA*, *297*(8), 842-57.

Blum, S., Asaf, R., Guetta, J., Miller-Lotan, R., Asleh, R., Kremer, R., Levy, N. S., Berger, F. G., Aronson, D., Fu, X., Zhang, R., Hazen, S. L., & Levy, A. P. (2007). Haptoglobin genotype determines myocardial infarct size in diabetic mice. *J Am Coll Cardiol*, *49*(1), 82-7.

Borghi, C., Omboni, S., Reggiardo, G., Bacchelli, S., Esposti, D. D., Ambrosioni, E., & Project, S. W. (2018). Effects of the concomitant administration of xanthine oxidase inhibitors with zofenopril or other ACE-inhibitors in post-myocardial infarction patients: a meta-analysis of individual data of four randomized, double-blind, prospective studies. *BMC Cardiovasc Disord*, *18*(1), 112.

Bos, D., Shahzad, R., van Walsum, T., van Vliet, L. J., Franco, O. H., Hofman, A., Niessen, W. J., Vernooij, M. W., & van der Lugt, A. (2015). Epicardial fat volume is related to atherosclerotic calcification in multiple vessel beds. *Eur Heart J Cardiovasc Imaging*, *16*(11), 1264-9.

Boveris, A., Cadenas, E., & Stoppani, A. O. (1976). Role of ubiquinone in the mitochondrial generation of hydrogen peroxide. *Biochem J*, *156*(2), 435-44.

Brand, M. (2010). Mitochondrial proton and electron leaks essays in biochemistry. *Essays Biochem*, *47*, 53-67.

Brandes, R. P., Weissmann, N., & Schroder, K. (2014). Nox family NADPH oxidases: Molecular mechanisms of activation. *Free Radic Biol Med*, *76*, 208-26.

Brown, D. I., & Griendling, K. K. (2015). Regulation of signal transduction by reactive oxygen species in the cardiovascular system. *Circ Res*, *116*(3), 531-49.

Brownlee, M. (2005). The pathobiology of diabetic complications: a unifying mechanism. *Diabetes*, *54*(6), 1615-25.

Bunik, V. I., Mkrtchyan, G., Grabarska, A., Oppermann, H., Daloso, D., Araujo, W. L., Juszczak, M., Rzeski, W., Bettendorff, L., Fernie, A. R., Meixensberger, J., Stepulak, A., & Gaunitz, F. (2016). Inhibition of mitochondrial 2-oxoglutarate dehydrogenase impairs viability of cancer cells in a cell-specific metabolism-dependent manner. *Oncotarget*, *7*(18), 26400-21.

Cai, H., & Harrison, D. G. (2000). Endothelial dysfunction in cardiovascular diseases: the role of oxidant stress. *Circ Res*, *87*(10), 840-4.

Ceylan-Isik, A. F., Guo, K. K., Carlson, E. C., Privratsky, J. R., Liao, S.-J., Cai, L., Chen, A. F., & Ren, J. (2009). Metallothionein abrogates GTP cyclohydrolase I inhibitionâinduced cardiac contractile and morphological defects: role of mitochondrial biogenesis. *Hypertension*, *53*(6), 1023-1031.

Chadderdon, S. M., Belcik, J. T., Bader, L., Kirigiti, M. A., Peters, D. M., Kievit, P., Grove, K. L., & Lindner, J. R. (2014). Proinflammatory endothelial activation detected by molecular imaging in obese nonhuman primates coincides with onset of

insulin resistance and progressively increases with duration of insulin resistance. *Circulation*, *129*(4), 471-8.

Chalupsky, K., & Cai, H. (2005a). Endothelial dihydrofolate reductase: critical for nitric oxide bioavailability and role in angiotensin II uncoupling of endothelial nitric oxide synthase. *Proc Natl Acad Sci U S A*, *102*(25), 9056-61.

Chalupsky, K., & Cai, H. (2005b). Endothelial dihydrofolate reductase: critical for nitric oxide bioavailability and role in angiotensin II uncoupling of endothelial nitric oxide synthase. *Proceedings of the National Academy of Sciences*, *102*(25), 9056-9061.

Chance, B., Sies, H., & Boveris, A. (1979). Hydroperoxide metabolism in mammalian organs. *Physiol Rev*, *59*(3), 527-605.

Chang, L., Xiong, W., Zhao, X., Fan, Y., Guo, Y., Garcia-Barrio, M., Zhang, J., Jiang, Z., Lin, J. D., & Chen, Y. E. (2018). Bmal1 in perivascular adipose tissue regulates resting-phase blood pressure through transcriptional regulation of angiotensinogen. *Circulation*, *138*(1), 67-79.

Chechi, K., Voisine, P., Mathieu, P., Laplante, M., Bonnet, S., Picard, F., Joubert, P., & Richard, D. (2017). Functional characterization of the Ucp1-associated oxidative phenotype of human epicardial adipose tissue. *Sci Rep*, *7*(1), 15566.

Chen, C. A., Wang, T. Y., Varadharaj, S., Reyes, L. A., Hemann, C., Talukder, M. A., Chen, Y. R., Druhan, L. J., & Zweier, J. L. (2010). S-glutathionylation uncouples eNOS and regulates its cellular and vascular function. *Nature*, *468*(7327), 1115-8.

Chen, F., Li, X., Aquadro, E., Haigh, S., Zhou, J., Stepp, D. W., Weintraub, N. L., Barman, S. A., & Fulton, D. J. (2016). Inhibition of histone deacetylase reduces transcription of NADPH oxidases and ROS production and ameliorates pulmonary arterial hypertension. *Free Radical Biology and Medicine*, *99*, 167-178.

Chen, F., Wang, Y., Barman, S., & Fulton, D. J. (2015). Enzymatic regulation and functional relevance of NOX5. *Curr Pharm Des*, *21*(41), 5999-6008.

Chen, F., Yin, C., Dimitropoulou, C., & Fulton, D. J. (2016). Cloning, Characteristics, and Functional Analysis of Rabbit NADPH Oxidase 5. *Front Physiol*, *7*, 284.

Chow, E. J., Rolfes, M. A., O'Halloran, A., Anderson, E. J., Bennett, N. M., Billing, L., Chai, S., Dufort, E., Herlihy, R., Kim, S., Lynfield, R., McMullen, C., Monroe, M. L., Schaffner, W., Spencer, M., Talbot, H. K., Thomas, A., Yousey-Hindes, K., Reed, C., & Garg, S. (2020). Acute Cardiovascular Events Associated With Influenza in Hospitalized Adults : A Cross-sectional Study. *Ann Intern Med*, *173*(8), 605-613.

[Computer Program]. (2013).

Conrad, C., Lymp, J., Thompson, V., Dunn, C., Davies, Z., Chatfield, B., Nichols, D., Clancy, J., Vender, R., & Egan, M. (2015). Long-term treatment with oral N-acetylcysteine: affects lung function but not sputum inflammation in cystic fibrosis subjects. A phase II randomized placebo-controlled trial. *Journal of Cystic Fibrosis*, *14*(2), 219-227.

Crabtree, M. J., & Channon, K. M. (2011). Synthesis and recycling of tetrahydro-

biopterin in endothelial function and vascular disease. *Nitric Oxide*, *25*(2), 81-8.

Crewe, C., An, Y. A., & Scherer, P. E. (2017). The ominous triad of adipose tissue dysfunction: inflammation, fibrosis, and impaired angiogenesis. *J Clin Invest*, *127*(1), 74-82.

Cunningham, F., Amode, M. R., Barrell, D., Beal, K., Billis, K., Brent, S., Carvalho-Silva, D., Clapham, P., Coates, G., Fitzgerald, S., Gil, L., Giron, C. G., Gordon, L., Hourlier, T., Hunt, S. E., Janacek, S. H., Johnson, N., Juettemann, T., Kahari, A. K., Keenan, S., Martin, F. J., Maurel, T., McLaren, W., Murphy, D. N., Nag, R., Overduin, B., Parker, A., Patricio, M., Perry, E., Pignatelli, M., Riat, H. S., Sheppard, D., Taylor, K., Thormann, A., Vullo, A., Wilder, S. P., Zadissa, A., Aken, B. L., Birney, E., Harrow, J., Kinsella, R., Muffato, M., Ruffier, M., Searle, S. M., Spudich, G., Trevanion, S. J., Yates, A., Zerbino, D. R., & Flicek, P. (2015). Ensembl 2015. *Nucleic Acids Res*, *43*(Database issue), D662-9.

Dai, D. F., Chen, T., Szeto, H., Nieves-Cintron, M., Kutyavin, V., Santana, L. F., & Rabinovitch, P. S. (2011). Mitochondrial targeted antioxidant Peptide ameliorates hypertensive cardiomyopathy. *J Am Coll Cardiol*, *58*(1), 73-82.

Dai, D. F., Johnson, S. C., Villarin, J. J., Chin, M. T., Nieves-Cintron, M., Chen, T., Marcinek, D. J., Dorn, n., G. W., Kang, Y. J., Prolla, T. A., Santana, L. F., & Rabinovitch, P. S. (2011). Mitochondrial oxidative stress mediates angiotensin II-induced cardiac hypertrophy and Galphaq overexpression-induced heart failure. *Circ Res*, *108*(7), 837-46.

Dai, W., Amoedo, N. D., Perry, J., Le Grand, B., Boucard, A., Carreno, J., Zhao, L.,

Brown, D. A., Rossignol, R., & Kloner, R. A. (2021). Effects of Op2113 on Myocardial Infarct Size and No Reflow in a Rat Myocardial Ischemia/reperfusion Model. *Cardiovascular Drugs and Therapy*, 1-11.

Davidovich, D., Gastaldelli, A., & Sicari, R. (2013). Imaging cardiac fat. *Eur Heart J Cardiovasc Imaging*, *14*(7), 625-30.

Day, B. J. (2009). Catalase and glutathione peroxidase mimics. *Biochem Pharmacol*, *77*(3), 285-96.

Detaille, D., Pasdois, P., Semont, A., Dos Santos, P., & Diolez, P. (2019). An old medicine as a new drug to prevent mitochondrial complex I from producing oxygen radicals. *PloS one*, *14*(5), e0216385.

Dey, D., & Commandeur, F. (2017). Radiomics to Identify High-Risk Atherosclerotic Plaque From Computed Tomography: The Power of Quantification. *Circ Cardiovasc Imaging*, *10*(12).

Dey, S., DeMazumder, D., Sidor, A., Foster, D. B., & O'Rourke, B. (2018). Mitochondrial ROS Drive Sudden Cardiac Death and Chronic Proteome Remodeling in Heart Failure. *Circ Res*, *123*(3), 356-371.

Dikalova, A. E., Bikineyeva, A. T., Budzyn, K., Nazarewicz, R. R., McCann, L., Lewis, W., Harrison, D. G., & Dikalov, S. I. (2010). Therapeutic targeting of mitochondrial superoxide in hypertension. *Circulation research*, *107*(1), 106-116.

Dorotea, D., Kwon, G., Lee, J. H., Saunders, E., Bae, Y. S., Moon, S. H., Lee, S. J., Cha, D. R., & Ha, H. (2018). A pan-NADPH oxidase inhibitor ameliorates kidney injury in type 1 diabetic rats. *Pharmacology*, *102*(3-4), 180-189.

Doughan, A. K., Harrison, D. G., & Dikalov, S. I. (2008a). Molecular mechanisms of angiotensin II-mediated mitochondrial dysfunction: linking mitochondrial oxidative damage and vascular endothelial dysfunction. *Circ Res*, *102*(4), 488-96.

Doughan, A. K., Harrison, D. G., & Dikalov, S. I. (2008b). Molecular mechanisms of angiotensin IIâmediated mitochondrial dysfunction: linking mitochondrial oxidative damage and vascular endothelial dysfunction. *Circulation research*, *102*(4), 488-496.

Douglas, G., Bendall, J. K., Crabtree, M. J., Tatham, A. L., Carter, E. E., Hale, A. B., & Channon, K. M. (2012). Endothelial-specific Nox2 overexpression increases vascular superoxide and macrophage recruitment in ApoEâ/â mice. *Cardiovascular research*, *94*(1), 20-29.

Drummond, G. R., Selemidis, S., Griendling, K. K., & Sobey, C. G. (2011). Combating oxidative stress in vascular disease: NADPH oxidases as therapeutic targets. *Nature reviews Drug discovery*, *10*(6), 453-471.

Dunbar, S. B., Khavjou, O. A., Bakas, T., Hunt, G., Kirch, R. A., Leib, A. R., Morrison, R. S., Poehler, D. C., Roger, V. L., Whitsel, L. P., & American Heart, A. (2018). Projected Costs of Informal Caregiving for Cardiovascular Disease: 2015 to 2035: A Policy Statement From the American Heart Association. *Circulation*, *137*(19), e558-e577.

Durham, A. L., Speer, M. Y., Scatena, M., Giachelli, C. M., & Shanahan, C. M. (2018). Role of smooth muscle cells in vascular calcification: implications in atherosclerosis and arterial stiffness. *Cardiovasc Res*, *114*(4), 590-600.

Elbim, C. (2005). Phagocyte NADPH oxidase: a multicomponent enzyme essential for host defenses. *Arch Immunol Ther Exp*, *53*, 199-206.

Engberding, N., Spiekermann, S., Schaefer, A., Heineke, A., Wiencke, A., Muller, M., Fuchs, M., Hilfiker-Kleiner, D., Hornig, B., Drexler, H., & Landmesser, U. (2004). Allopurinol attenuates left ventricular remodeling and dysfunction after experimental myocardial infarction: a new action for an old drug? *Circulation*, *110*(15), 2175-9.

Escobedo, N., Proulx, S. T., Karaman, S., Dillard, M. E., Johnson, N., Detmar, M., & Oliver, G. (2016). Restoration of lymphatic function rescues obesity in Prox1-haploinsufficient mice. *JCI Insight*, *1*(2).

Escribano-Lopez, I., Diaz-Morales, N., Rovira-Llopis, S., de Maranon, A. M., Orden, S., Alvarez, A., Banuls, C., Rocha, M., Murphy, M. P., Hernandez-Mijares, A., & Victor, V. M. (2016). The mitochondria-targeted antioxidant MitoQ modulates oxidative stress, inflammation and leukocyte-endothelium interactions in leukocytes isolated from type 2 diabetic patients. *Redox Biol*, *10*, 200-205.

Faria, A. M., Papadimitriou, A., Silva, K. C., de Faria, J. M. L., & de Faria, J. B. L. (2012). Uncoupling endothelial nitric oxide synthase is ameliorated by green tea in experimental diabetes by re-establishing tetrahydrobiopterin levels. *Diabetes*, *61*(7), 1838-1847.

Fedorov, A., Beichel, R., Kalpathy-Cramer, J., Finet, J., Fillion-Robin, J.-C., Pujol, S., Bauer, C., Jennings, D., Fennessy, F., & Sonka, M. (2012). 3D Slicer as an image computing platform for the Quantitative Imaging Network. *Magnetic resonance*

imaging, *30*(9), 1323-1341.

Ferrari, R., & Catapano, A. L. (2016). Residual cardiovascular risk. *Eur Heart J Suppl*, *18*(Suppl C), C1.

Fischer, C., Seki, T., Lim, S., Nakamura, M., Andersson, P., Yang, Y., Honek, J., Wang, Y., Gao, Y., Chen, F., Samani, N. J., Zhang, J., Miyake, M., Oyadomari, S., Yasue, A., Li, X., Zhang, Y., Liu, Y., & Cao, Y. (2017). A miR-327-FGF10-FGFR2-mediated autocrine signaling mechanism controls white fat browning. *Nat Commun*, *8*(1), 2079.

Flegal, K. M., Kit, B. K., Orpana, H., & Graubard, B. I. (2013). Association of all-cause mortality with overweight and obesity using standard body mass index categories: a systematic review and meta-analysis. *JAMA*, *309*(1), 71-82.

Foglieni, C., Maisano, F., Dreas, L., Giazzon, A., Ruotolo, G., Ferrero, E., Li Volsi, L., Coli, S., Sinagra, G., & Zingone, B. (2008). Mild inflammatory activation of mammary arteries in patients with acute coronary syndromes. *American Journal of Physiology-Heart and Circulatory Physiology*, *294*(6), H2831-H2837.

Fontayne, A., Dang, P. M.-C., Gougerot-Pocidalo, M.-A., & El Benna, J. (2002). Phosphorylation of p47phox Sites by PKCa, bÎÎ, d, and z: Effect on Binding to p22phox and on NADPH Oxidase Activation. *Biochemistry*, *41*(24), 7743-7750.

Forman, H. J., & Zhang, H. (2021). Targeting oxidative stress in disease: Promise and limitations of antioxidant therapy. *Nature Reviews Drug Discovery*, 1-21.

Forstermann, U., & Munzel, T. (2006). Endothelial nitric oxide synthase in vascular disease: from marvel to menace. *Circulation*, *113*(13), 1708-1714.

Franssens, B. T., Hoogduin, H., Leiner, T., van der Graaf, Y., & Visseren, F. L. (2017). Relation between brown adipose tissue and measures of obesity and metabolic dysfunction in patients with cardiovascular disease. *Journal of Magnetic Resonance Imaging*, *46*(2), 497-504.

Franssens, B. T., Nathoe, H. M., Leiner, T., van der Graaf, Y., Visseren, F. L., & group, S. s. (2017). Relation between cardiovascular disease risk factors and epicardial adipose tissue density on cardiac computed tomography in patients at high risk of cardiovascular events. *Eur J Prev Cardiol*, *24*(6), 660-670.

Fujisaka, S., Usui, I., Bukhari, A., Ikutani, M., Oya, T., Kanatani, Y., Tsuneyama, K., Nagai, Y., Takatsu, K., Urakaze, M., Kobayashi, M., & Tobe, K. (2009). Regulatory mechanisms for adipose tissue M1 and M2 macrophages in diet-induced obese mice. *Diabetes*, *58*(11), 2574-82.

Fuster, J. J., Ouchi, N., Gokce, N., & Walsh, K. (2016). Obesity-induced changes in adipose tissue microenvironment and their impact on cardiovascular disease. *Circulation research*, *118*(11), 1786-1807.

Ganesh, D., Kumarathasan, P., Thomson, E. M., St-Germain, C., Blais, E., Crapo, J., & Vincent, R. (2016). Impact of Superoxide Dismutase Mimetic AEOL 10150 on the Endothelin System of Fischer 344 Rats. *PLoS One*, *11*(3), e0151810.

Garland, M., Hryckowian, A. J., Tholen, M., Bender, K. O., Van Treuren, W. W., Loscher, S., Sonnenburg, J. L., & Bogyo, M. (2020). The Clinical Drug Ebselen Attenuates Inflammation and Promotes Microbiome Recovery in Mice after Antibiotic Treatment for CDI. *Cell Rep Med*, *1*(1), 100005.

Gebhardt, C., Nemeth, J., Angel, P., & Hess, J. (2006). S100A8 and S100A9 in inflammation and cancer. *Biochem Pharmacol*, *72*(11), 1622-31.

Gillies, R. J., Kinahan, P. E., & Hricak, H. (2015). Radiomics: images are more than pictures, they are data. *Radiology*, *278*(2), 563-577.

Gimenez, M., Schickling, B. M., Lopes, L. R., & Miller, J., F. J. (2016). Nox1 in cardiovascular diseases: regulation and pathophysiology. *Clin Sci (Lond)*, *130*(3), 151-65.

Gimenez, M., Schickling, B. M., Lopes, L. R., & Miller Jr, F. J. (2016). Nox1 in cardiovascular diseases: regulation and pathophysiology. *Clinical science*, *130*(3), 151-165.

Gladden, J. D., Zelickson, B. R., Wei, C.-C., Ulasova, E., Zheng, J., Ahmed, M. I., Chen, Y., Bamman, M., Ballinger, S., & Darley-Usmar, V. (2011). Novel insights into interactions between mitochondria and xanthine oxidase in acute cardiac volume overload. *Free Radical Biology and Medicine*, *51*(11), 1975-1984.

Glavind, J., Hartmann, S., Clemmesen, J., Jessen, K. E., & Dam, H. (1952). Studies on the role of lipoperoxides in human pathology. II. The presence of peroxidized lipids in the atherosclerotic aorta. *Acta Pathol Microbiol Scand*, *30*(1), 1-6.

Gomes, L. H., Raftery, M. J., Yan, W. X., Goyette, J. D., Thomas, P. S., & Geczy, C. L. (2013). S100A8 and S100A9-oxidant scavengers in inflammation. *Free Radic Biol Med*, *58*, 170-86.

Graham, D., Huynh, N. N., Hamilton, C. A., Beattie, E., Smith, R. A., Cocheme, H. M., Murphy, M. P., & Dominiczak, A. F. (2009). Mitochondria-targeted antioxidant

MitoQ10 improves endothelial function and attenuates cardiac hypertrophy. *Hypertension*, *54*(2), 322-8.

Graham, D. B., Jasso, G. J., Mok, A., Goel, G., Ng, A. C. Y., Kolde, R., Varma, M., Doench, J. G., Root, D. E., Clish, C. B., Carr, S. A., & Xavier, R. J. (2018). Nitric Oxide Engages an Anti-inflammatory Feedback Loop Mediated by Peroxiredoxin 5 in Phagocytes. *Cell Rep*, *24*(4), 838-850.

Gray, S. P., Di Marco, E., Kennedy, K., Chew, P., Okabe, J., El-Osta, A., Calkin, A. C., Biessen, E. A., Touyz, R. M., & Cooper, M. E. (2016). Reactive oxygen species can provide atheroprotection via NOX4-dependent inhibition of inflammation and vascular remodeling. *Arteriosclerosis, thrombosis, and vascular biology*, *36*(2), 295-307.

Gray, S. P., Di Marco, E., Okabe, J., Szyndralewiez, C., Heitz, F., Montezano, A. C., de Haan, J. B., Koulis, C., El-Osta, A., Andrews, K. L., Chin-Dusting, J. P., Touyz, R. M., Wingler, K., Cooper, M. E., Schmidt, H. H., & Jandeleit-Dahm, K. A. (2013). NADPH oxidase 1 plays a key role in diabetes mellitus-accelerated atherosclerosis. *Circulation*, *127*(18), 1888-902.

Groemping, Y., Lapouge, K., Smerdon, S. J., & Rittinger, K. (2003). Molecular basis of phosphorylation-induced activation of the NADPH oxidase. *Cell*, *113*(3), 343-55.

Group, R. C. (2020). Dexamethasone in hospitalized patients with Covid-19âpreliminary report. *New England Journal of Medicine*.

Gupta, A., Madhavan, M. V., Sehgal, K., Nair, N., Mahajan, S., Sehrawat, T. S., Bikdeli,

B., Ahluwalia, N., Ausiello, J. C., Wan, E. Y., Freedberg, D. E., Kirtane, A. J., Parikh, S. A., Maurer, M. S., Nordvig, A. S., Accili, D., Bathon, J. M., Mohan, S., Bauer, K. A., Leon, M. B., Krumholz, H. M., Uriel, N., Mehra, M. R., Elkind, M. S. V., Stone, G. W., Schwartz, A., Ho, D. D., Bilezikian, J. P., & Landry, D. W. (2020). Extrapulmonary manifestations of COVID-19. *Nat Med*, *26*(7), 1017-1032.

Guzik, T. J., & Channon, K. M. (2005). Measurement of vascular reactive oxygen species production by chemiluminescence. In *Hypertension* (p. 73-89). Springer.

Guzik, T. J., Chen, W., Gongora, M. C., Guzik, B., Lob, H. E., Mangalat, D., Hoch, N., Dikalov, S., Rudzinski, P., Kapelak, B., Sadowski, J., & Harrison, D. G. (2008). Calcium-dependent NOX5 nicotinamide adenine dinucleotide phosphate oxidase contributes to vascular oxidative stress in human coronary artery disease. *J Am Coll Cardiol*, *52*(22), 1803-9.

Guzik, T. J., Mohiddin, S. A., Dimarco, A., Patel, V., Savvatis, K., Marelli-Berg, F. M., Madhur, M. S., Tomaszewski, M., Maffia, P., D'Acquisto, F., Nicklin, S. A., Marian, A. J., Nosalski, R., Murray, E. C., Guzik, B., Berry, C., Touyz, R. M., Kreutz, R., Wang, D. W., Bhella, D., Sagliocco, O., Crea, F., Thomson, E. C., & McInnes, I. B. (2020). COVID-19 and the cardiovascular system: implications for risk assessment, diagnosis, and treatment options. *Cardiovasc Res*, *116*(10), 1666-1687.

Guzik, T. J., Sadowski, J., Kapelak, B., Jopek, A., Rudzinski, P., Pillai, R., Korbut, R., & Channon, K. M. (2004). Systemic regulation of vascular NAD(P)H oxidase

activity and nox isoform expression in human arteries and veins. *Arterioscler Thromb Vasc Biol*, *24*(9), 1614-20.

Han, J., Meng, Q., Shen, L., & Wu, G. (2018). Interleukin-6 induces fat loss in cancer cachexia by promoting white adipose tissue lipolysis and browning. *Lipids Health Dis*, *17*(1), 14.

Hare, J. M., Mangal, B., Brown, J., Fisher, J., C., Freudenberger, R., Colucci, W. S., Mann, D. L., Liu, P., Givertz, M. M., Schwarz, R. P., & Investigators, O.-C. (2008). Impact of oxypurinol in patients with symptomatic heart failure. Results of the OPT-CHF study. *J Am Coll Cardiol*, *51*(24), 2301-9.

Harrington, R. A. (2017). Targeting Inflammation in Coronary Artery Disease. *N Engl J Med*, *377*(12), 1197-1198.

Harvey, A. P., Montezano, A. C., Hood, K. Y., Lopes, R. A., Rios, F., Ceravolo, G., Graham, D., & Touyz, R. M. (2017). Vascular dysfunction and fibrosis in stroke-prone spontaneously hypertensive rats: the aldosterone-mineralocorticoid receptor-Nox1 axis. *Life sciences*, *179*, 110-119.

Hell, M. M., Ding, X., Rubeaux, M., Slomka, P., Gransar, H., Terzopoulos, D., Hayes, S., Marwan, M., Achenbach, S., Berman, D. S., & Dey, D. (2016). Epicardial adipose tissue volume but not density is an independent predictor for myocardial ischemia. *J Cardiovasc Comput Tomogr*, *10*(2), 141-9.

Hoffmann, M., Kleine-Weber, H., Schroeder, S., KrÃ¼ger, N., Herrler, T., Erichsen, S., Schiergens, T. S., Herrler, G., Wu, N.-H., & Nitsche, A. (2020). SARS-CoV-2 cell entry depends on ACE2 and TMPRSS2 and is blocked by a clinically proven

protease inhibitor. *Cell*.

Iacobellis, G. (2015). Local and systemic effects of the multifaceted epicardial adipose tissue depot. *Nat Rev Endocrinol*, *11*(6), 363-71.

Iacobellis, G., Ribaudo, M. C., Assael, F., Vecci, E., Tiberti, C., Zappaterreno, A., Di Mario, U., & Leonetti, F. (2003). Echocardiographic epicardial adipose tissue is related to anthropometric and clinical parameters of metabolic syndrome: a new indicator of cardiovascular risk. *The Journal of Clinical Endocrinology Metabolism*, *88*(11), 5163-5168.

Ide, T., Tsutsui, H., Kinugawa, S., Suematsu, N., Hayashidani, S., Ichikawa, K., Utsumi, H., Machida, Y., Egashira, K., & Takeshita, A. (2000). Direct evidence for increased hydroxyl radicals originating from superoxide in the failing myocardium. *Circ Res*, *86*(2), 152-7.

Investigators, S.-H. (2018). Coronary CT angiography and 5-year risk of myocardial infarction. *New England Journal of Medicine*, *379*(10), 924-933.

Ito, T., Suzuki, Y., Ehara, M., Matsuo, H., Teramoto, T., Terashima, M., Nasu, K., Kinoshita, Y., Tsuchikane, E., Suzuki, T., & Kimura, G. (2013). Impact of epicardial fat volume on coronary artery disease in symptomatic patients with a zero calcium score. *Int J Cardiol*, *167*(6), 2852-8.

Jay, D. B., Papaharalambus, C. A., Seidel-Rogol, B., Dikalova, A. E., Lassegue, B., & Griendling, K. K. (2008). Nox5 mediates PDGF-induced proliferation in human aortic smooth muscle cells. *Free Radic Biol Med*, *45*(3), 329-35.

Jha, J. C., Watson, A. M. D., Mathew, G., de Vos, L. C., & Jandeleit-Dahm, K. (2017).

The emerging role of NADPH oxidase NOX5 in vascular disease. *Clin Sci (Lond)*, *131*(10), 981-990.

Judkins, C. P., Diep, H., Broughton, B. R., Mast, A. E., Hooker, E. U., Miller, A. A., Selemidis, S., Dusting, G. J., Sobey, C. G., & Drummond, G. R. (2010). Direct evidence of a role for Nox2 in superoxide production, reduced nitric oxide bioavailability, and early atherosclerotic plaque formation in ApoEâ/â mice. *American Journal of Physiology-Heart and Circulatory Physiology*, *298*(1), H24-H32.

Kadiyala, A., & Kumar, A. (2018). Applications of python to evaluate the performance of decision treeâbased boosting algorithms. *Environmental Progress Sustainable Energy*, *37*(2), 618-623.

Kalbacher, D., Waldeyer, C., Blankenberg, S., & Westermann, D. (2018). Beyond conventional secondary prevention in coronary artery disease-what to choose in the era of CANTOS, COMPASS, FOURIER, ODYSSEY and PEGASUS-TIMI 54? A review on contemporary literature. *Ann Transl Med*, *6*(16), 323.

Kaul, S., Rothney, M. P., Peters, D. M., Wacker, W. K., Davis, C. E., Shapiro, M. D., & Ergun, D. L. (2012). Dual-energy X-ray absorptiometry for quantification of visceral fat. *Obesity (Silver Spring)*, *20*(6), 1313-8.

Kaushal, G. P., Chandrashekar, K., & Juncos, L. A. (2019). Molecular interactions between reactive oxygen species and autophagy in kidney disease. *International journal of molecular sciences*, *20*(15), 3791.

Ketelhuth, D. F. J., Lutgens, E., Back, M., Binder, C. J., Van den Bossche, J., Daniel, C., Dumitriu, I. E., Hoefer, I., Libby, P., O'Neill, L., Weber, C., & Evans, P. C.

(2019). Immunometabolism and atherosclerosis: perspectives and clinical significance: a position paper from the Working Group on Atherosclerosis and Vascular Biology of the European Society of Cardiology. *Cardiovasc Res*, *115*(9), 1385-1392.

Kim, D., Langmead, B., & Salzberg, S. L. (2015). HISAT: a fast spliced aligner with low memory requirements. *Nat Methods*, *12*(4), 357-60.

Kimura, S., Zhang, G. X., Nishiyama, A., Shokoji, T., Yao, L., Fan, Y. Y., Rahman, M., & Abe, Y. (2005a). Mitochondria-derived reactive oxygen species and vascular MAP kinases: comparison of angiotensin II and diazoxide. *Hypertension*, *45*(3), 438-44.

Kimura, S., Zhang, G.-X., Nishiyama, A., Shokoji, T., Yao, L., Fan, Y.-Y., Rahman, M., & Abe, Y. (2005b). Mitochondria-derived reactive oxygen species and vascular MAP kinases: comparison of angiotensin II and diazoxide. *Hypertension*, *45*(3), 438-444.

King, A. L., Polhemus, D. J., Bhushan, S., Otsuka, H., Kondo, K., Nicholson, C. K., Bradley, J. M., Islam, K. N., Calvert, J. W., & Tao, Y.-X. (2014). Hydrogen sulfide cytoprotective signaling is endothelial nitric oxide synthase-nitric oxide dependent. *Proceedings of the National Academy of Sciences*, *111*(8), 3182-3187.

Kitada, M., Koya, D., Sugimoto, T., Isono, M., Araki, S.-i., Kashiwagi, A., & Haneda, M. (2003). Translocation of glomerular p47phox and p67phox by protein kinase C-b activation is required for oxidative stress in diabetic nephropathy. *Diabetes*,

52(10), 2603-2614.

Kleniewska, P., Piechota, A., Skibska, B., & GorÄca, A. (2012). The NADPH oxidase family and its inhibitors. *Archivum immunologiae et therapiae experimentalis*, *60*(4), 277-294.

Knuuti, J., Wijns, W., Saraste, A., Capodanno, D., Barbato, E., Funck-Brentano, C., Prescott, E., Storey, R. F., Deaton, C., Cuisset, T., Agewall, S., Dickstein, K., Edvardsen, T., Escaned, J., Gersh, B. J., Svitil, P., Gilard, M., Hasdai, D., Hatala, R., Mahfoud, F., Masip, J., Muneretto, C., Valgimigli, M., Achenbach, S., Bax, J. J., & Group, E. S. C. S. D. (2020). 2019 ESC Guidelines for the diagnosis and management of chronic coronary syndromes. *Eur Heart J*, *41*(3), 407-477.

Kolossvary, M., Karady, J., Szilveszter, B., Kitslaar, P., Hoffmann, U., Merkely, B., & Maurovich-Horvat, P. (2017). Radiomic Features Are Superior to Conventional Quantitative Computed Tomographic Metrics to Identify Coronary Plaques With Napkin-Ring Sign. *Circ Cardiovasc Imaging*, *10*(12), e006843.

Konior, A., Schramm, A., Czesnikiewicz-Guzik, M., & Guzik, T. J. (2014). NADPH oxidases in vascular pathology. *Antioxid Redox Signal*, *20*(17), 2794-814.

Koppenol, W. H. (1993). The centennial of the Fenton reaction. *Free Radic Biol Med*, *15*(6), 645-51.

Kotanidis, C. P., & Antoniades, C. (2020a). Perivascular Adipose Tissue and Atherosclerosis. In G. Iacobellis (Ed.), *Epicardial Adipose Tissue* (p. 91-115). Cham: Springer International Publishing. Retrieved from https://doi.org/10.1007/978-3-030-40570-0_9 doi: 10.1007/978-3-030

-40570-0_9

Kotanidis, C. P., & Antoniades, C. (2020b). Perivascular Fat Imaging by Computed Tomography: A Virtual Guide. *British Journal of Pharmacology*.

Kotanidis, C. P., & Antoniades, C. (2020c). Selfies in cardiovascular medicine: welcome to a new era of medical diagnostics. *Eur Heart J*, *41*(46), 4412-4414.

Kotanidis, C. P., & Antoniades, C. (2021). Perivascular fat imaging by computed tomography (CT): a virtual guide. *Br J Pharmacol*.

Krotkiewski, M., Bjorntorp, P., Sjostrom, L., & Smith, U. (1983). Impact of obesity on metabolism in men and women. Importance of regional adipose tissue distribution. *J Clin Invest*, *72*(3), 1150-62.

Krumm, P., Mangold, S., Gatidis, S., Nikolaou, K., Nensa, F., Bamberg, F., & la Fougere, C. (2018). Clinical use of cardiac PET/MRI: current state-of-the-art and potential future applications. *Jpn J Radiol*, *36*(5), 313-323.

Kuroda, J., Ago, T., Matsushima, S., Zhai, P., Schneider, M. D., & Sadoshima, J. (2010). NADPH oxidase 4 (Nox4) is a major source of oxidative stress in the failing heart. *Proceedings of the National Academy of Sciences*, *107*(35), 15565-15570.

Kwiecinski, J., Dey, D., Cadet, S., Lee, S.-E., Otaki, Y., Huynh, P. T., Doris, M. K., Eisenberg, E., Yun, M., & Jansen, M. A. (2019). Peri-coronary adipose tissue density is associated with 18F-sodium fluoride coronary uptake in stable patients with high-risk plaques. *JACC: Cardiovascular Imaging*, *12*(10), 2000-2010.

Kwok, J. M., Ma, C. C.-H., & Ma, S. (2013). Recent development in the effects of statins on cardiovascular disease through Rac1 and NADPH oxidase. *Vascular*

pharmacology, *58*(1-2), 21-30.

Lambeth, J. D. (2004). NOX enzymes and the biology of reactive oxygen. *Nat Rev Immunol*, *4*(3), 181-9.

Lambeth, J. D., Kawahara, T., & Diebold, B. (2007). Regulation of Nox and Duox enzymatic activity and expression. *Free Radic Biol Med*, *43*(3), 319-31.

Lang, M., Som, A., Mendoza, D. P., Flores, E. J., Reid, N., Carey, D., Li, M. D., Witkin, A., Rodriguez-Lopez, J. M., Shepard, J. O., & Little, B. P. (2020). Hypoxaemia related to COVID-19: vascular and perfusion abnormalities on dual-energy CT. *Lancet Infect Dis*, *20*(12), 1365-1366.

Langbein, H., Brunssen, C., Hofmann, A., Cimalla, P., Brux, M., Bornstein, S. R., Deussen, A., Koch, E., & Morawietz, H. (2016). NADPH oxidase 4 protects against development of endothelial dysfunction and atherosclerosis in LDL receptor deficient mice. *Eur Heart J*, *37*(22), 1753-61.

Langfelder, P., & Horvath, S. (2008). WGCNA: an R package for weighted correlation network analysis. *BMC Bioinformatics*, *9*(1), 559.

Lassegue, B., & Griendling, K. K. (2010). NADPH oxidases: functions and pathologies in the vasculature. *Arteriosclerosis, thrombosis, and vascular biology*, *30*(4), 653-661.

Lausen, B., & Schumacher, M. (1992). Maximally selected rank statistics. *Biometrics*, 73-85.

Lee, C.-H., Chan, R. S., Wan, H. Y., Woo, Y.-C., Cheung, C. Y., Fong, C. H., Cheung, B. M., Lam, T.-H., Janus, E., & Woo, J. (2018). Dietary intake of anti-oxidant vi-

tamins A, C, and E Is inversely associated with adverse cardiovascular outcomes in ChineseâA 22-years population-based prospective study. *Nutrients*, *10*(11), 1664.

Lee, Y. C., Chang, H. H., Chiang, C. L., Liu, C. H., Yeh, J. I., Chen, M. F., Chen, P. Y., Kuo, J. S., & Lee, T. J. (2011). Role of perivascular adipose tissue-derived methyl palmitate in vascular tone regulation and pathogenesis of hypertension. *Circulation*, *124*(10), 1160-71.

Leipsic, J., Abbara, S., Achenbach, S., Cury, R., Earls, J. P., Mancini, G. J., Nieman, K., Pontone, G., & Raff, G. L. (2014). SCCT guidelines for the interpretation and reporting of coronary CT angiography: a report of the Society of Cardiovascular Computed Tomography Guidelines Committee. *J Cardiovasc Comput Tomogr*, *8*(5), 342-58.

Levy, E. J., Anderson, M. E., & Meister, A. (1993). Transport of glutathione diethyl ester into human cells. *Proceedings of the National Academy of Sciences*, *90*(19), 9171-9175.

Li, G. R., & Ferrier, G. R. (1992). Effects of allopurinol on reperfusion arrhythmias in isolated ventricles. *Am J Physiol*, *263*(2 Pt 2), H341-8.

Li, H., Li, Q., Zhang, Y., Liu, W., Gu, B., Narumi, T., Siu, K. L., Youn, J. Y., Liu, P., & Yang, X. (2019). Novel treatment of hypertension by specifically targeting E2F for restoration of endothelial dihydrofolate reductase and eNOS function under oxidative stress. *Hypertension*, *73*(1), 179-189.

Li, Q., Youn, J. Y., Siu, K. L., Murugesan, P., Zhang, Y., & Cai, H. (2019). Knockout

of dihydrofolate reductase in mice induces hypertension and abdominal aortic aneurysm via mitochondrial dysfunction. *Redox Biol*, *24*, 101185.

Liao, Y., Smyth, G. K., & Shi, W. (2013). The Subread aligner: fast, accurate and scalable read mapping by seed-and-vote. *Nucleic Acids Res*, *41*(10), e108.

Liao, Y., Smyth, G. K., & Shi, W. (2014). featureCounts: an efficient general purpose program for assigning sequence reads to genomic features. *Bioinformatics*, *30*(7), 923-30.

Libby, P., Ridker, P. M., Hansson, G. K., & Leducq Transatlantic Network on, A. (2009). Inflammation in atherosclerosis: from pathophysiology to practice. *J Am Coll Cardiol*, *54*(23), 2129-38.

Loman, N. (2021). Artic-network field bioinformatics: 1.2.1.

Looi, Y. H., Grieve, D. J., Siva, A., Walker, S. J., Anilkumar, N., Cave, A. C., Marber, M., Monaghan, M. J., & Shah, A. M. (2008). Involvement of Nox2 NADPH oxidase in adverse cardiac remodeling after myocardial infarction. *Hypertension*, *51*(2), 319-25.

Lumeng, C. N., Bodzin, J. L., & Saltiel, A. R. (2007). Obesity induces a phenotypic switch in adipose tissue macrophage polarization. *J Clin Invest*, *117*(1), 175-84.

Mackensen, G. B., Patel, M., Sheng, H., Calvi, C. L., Batinic-Haberle, I., Day, B. J., Liang, L. P., Fridovich, I., Crapo, J. D., Pearlstein, R. D., & Warner, D. S. (2001). Neuroprotection from delayed postischemic administration of a metalloporphyrin catalytic antioxidant. *J Neurosci*, *21*(13), 4582-92.

Madamanchi, N. R., & Runge, M. S. (2007). Mitochondrial dysfunction in atheroscle-

rosis. *Circ Res*, *100*(4), 460-73.

Maejima, Y., Kuroda, J., Matsushima, S., Ago, T., & Sadoshima, J. (2011). Regulation of myocardial growth and death by NADPH oxidase. *J Mol Cell Cardiol*, *50*(3), 408-16.

Magnani, F., Nenci, S., Millana Fananas, E., Ceccon, M., Romero, E., Fraaije, M. W., & Mattevi, A. (2017). Crystal structures and atomic model of NADPH oxidase. *Proc Natl Acad Sci U S A*, *114*(26), 6764-6769.

Mahabadi, A. A., Balcer, B., Dykun, I., Forsting, M., Schlosser, T., Heusch, G., & Rassaf, T. (2017). Cardiac computed tomography-derived epicardial fat volume and attenuation independently distinguish patients with and without myocardial infarction. *PLoS One*, *12*(8), e0183514.

Mahabadi, A. A., Lehmann, N., Kalsch, H., Robens, T., Bauer, M., Dykun, I., Budde, T., Moebus, S., Jockel, K. H., Erbel, R., & Mohlenkamp, S. (2014). Association of epicardial adipose tissue with progression of coronary artery calcification is more pronounced in the early phase of atherosclerosis: results from the Heinz Nixdorf recall study. *JACC Cardiovasc Imaging*, *7*(9), 909-16.

Maiellaro, K., & Taylor, W. R. (2007). The role of the adventitia in vascular inflammation. *Cardiovasc Res*, *75*(4), 640-8.

Mancio, J., Oikonomou, E. K., & Antoniades, C. (2018). Perivascular adipose tissue and coronary atherosclerosis. *Heart*, *104*(20), 1654-1662.

Manea, S.-A., Antonescu, M.-L., Fenyo, I. M., Raicu, M., Simionescu, M., & Manea, A. (2018). Epigenetic regulation of vascular NADPH oxidase expression and re-

active oxygen species production by histone deacetylase-dependent mechanisms in experimental diabetes. *Redox biology*, *16*, 332-343.

Margaritis, M., Antonopoulos, A. S., Digby, J., Lee, R., Reilly, S., Coutinho, P., Shirodaria, C., Sayeed, R., Petrou, M., De Silva, R., Jalilzadeh, S., Demosthenous, M., Bakogiannis, C., Tousoulis, D., Stefanadis, C., Choudhury, R. P., Casadei, B., Channon, K. M., & Antoniades, C. (2013). Interactions between vascular wall and perivascular adipose tissue reveal novel roles for adiponectin in the regulation of endothelial nitric oxide synthase function in human vessels. *Circulation*, *127*(22), 2209-21.

Margaritis, M., Sanna, F., Lazaros, G., Akoumianakis, I., Patel, S., Antonopoulos, A. S., Duke, C., Herdman, L., Psarros, C., Oikonomou, E. K., Shirodaria, C., Petrou, M., Sayeed, R., Krasopoulos, G., Lee, R., Tousoulis, D., Channon, K. M., & Antoniades, C. (2017). Predictive value of telomere length on outcome following acute myocardial infarction: evidence for contrasting effects of vascular vs. blood oxidative stress. *Eur Heart J*, *38*(41), 3094-3104.

Masini, E., Cuzzocrea, S., Mazzon, E., Marzocca, C., Mannaioni, P. F., & Salvemini, D. (2002). Protective effects of M40403, a selective superoxide dismutase mimetic, in myocardial ischaemia and reperfusion injury in vivo. *Br J Pharmacol*, *136*(6), 905-17.

Matsushima, S., Kuroda, J., Ago, T., Zhai, P., Park, J. Y., Xie, L. H., Tian, B., & Sadoshima, J. (2013). Increased oxidative stress in the nucleus caused by Nox4 mediates oxidation of HDAC4 and cardiac hypertrophy. *Circ Res*, *112*(4), 651-

63.

Mazurek, T., Kobylecka, M., Zielenkiewicz, M., Kurek, A., Kochman, J., Filipiak, K. J., Mazurek, K., Huczek, Z., Krolicki, L., & Opolski, G. (2017). PET/CT evaluation of (18)F-FDG uptake in pericoronary adipose tissue in patients with stable coronary artery disease: Independent predictor of atherosclerotic lesions' formation? *J Nucl Cardiol*, *24*(3), 1075-1084.

Meyer, A. J., & Dick, T. P. (2010). Fluorescent protein-based redox probes. *Antioxid Redox Signal*, *13*(5), 621-50.

Milman, U., Blum, S., Shapira, C., Aronson, D., Miller-Lotan, R., Anbinder, Y., Alshiek, J., Bennett, L., Kostenko, M., & Landau, M. (2008). Vitamin E supplementation reduces cardiovascular events in a subgroup of middle-aged individuals with both type 2 diabetes mellitus and the haptoglobin 2-2 genotype: a prospective double-blinded clinical trial. *Arteriosclerosis, thrombosis, and vascular biology*, *28*(2), 341-347.

Mittal, M., Siddiqui, M. R., Tran, K., Reddy, S. P., & Malik, A. B. (2014). Reactive oxygen species in inflammation and tissue injury. *Antioxid Redox Signal*, *20*(7), 1126-67.

Moens, A. L., Champion, H. C., Claeys, M. J., Tavazzi, B., Kaminski, P. M., Wolin, M. S., Borgonjon, D. J., Van Nassauw, L., Haile, A., Zviman, M., Bedja, D., Wuyts, F. L., Elsaesser, R. S., Cos, P., Gabrielson, K. L., Lazzarino, G., Paolocci, N., Timmermans, J. P., Vrints, C. J., & Kass, D. A. (2008). High-dose folic acid pretreatment blunts cardiac dysfunction during ischemia coupled to mainte-

nance of high-energy phosphates and reduces postreperfusion injury. *Circulation*, *117*(14), 1810-9.

Moens, A. L., Ketner, E. A., Takimoto, E., Schmidt, T. S., O'Neill, C. A., Wolin, M. S., Alp, N. J., Channon, K. M., & Kass, D. A. (2011). Bi-modal dose-dependent cardiac response to tetrahydrobiopterin in pressure-overload induced hypertrophy and heart failure. *J Mol Cell Cardiol*, *51*(4), 564-9.

Montezano, A. C., Tsiropoulou, S., Dulak-Lis, M., Harvey, A., Camargo Lde, L., & Touyz, R. M. (2015). Redox signaling, Nox5 and vascular remodeling in hypertension. *Curr Opin Nephrol Hypertens*, *24*(5), 425-33.

Morand, S., Ueyama, T., Tsujibe, S., Saito, N., Korzeniowska, A., & Leto, T. L. (2009). Duox maturation factors form cell surface complexes with Duox affecting the specificity of reactive oxygen species generation. *The FASEB Journal*, *23*(4), 1205-1218.

Munzel, T. (2002). Afanas' ev IB, Kleschyov AL, and Harrison DG. *Detection of superoxide in vascular tissue. Arterioscler Thromb Vasc Biol*, *22*, 1761-1768.

Nakamura, Y., Feng, Q., Kumagai, T., Torikai, K., Ohigashi, H., Osawa, T., Noguchi, N., Niki, E., & Uchida, K. (2002). Ebselen, a glutathione peroxidase mimetic seleno-organic compound, as a multifunctional antioxidant: implication for inflammation-associated carcinogenesis. *Journal of Biological Chemistry*, *277*(4), 2687-2694.

Nakazono, K., Watanabe, N., Matsuno, K., Sasaki, J., Sato, T., & Inoue, M. (1991). Does superoxide underlie the pathogenesis of hypertension? *Proceedings of the*

National Academy of Sciences, *88*(22), 10045-10048.

Nelson, A. J., Worthley, M. I., Psaltis, P. J., Carbone, A., Dundon, B. K., Duncan, R. F., Piantadosi, C., Lau, D. H., Sanders, P., Wittert, G. A., & Worthley, S. G. (2009). Validation of cardiovascular magnetic resonance assessment of pericardial adipose tissue volume. *J Cardiovasc Magn Reson*, *11*(1), 15.

Neves, K. B., Lobato, N. S., Lopes, R. A., Filgueira, F. P., Zanotto, C. Z., Oliveira, A. M., & Tostes, R. C. (2014). Chemerin reduces vascular nitric oxide/cGMP signalling in rat aorta: a link to vascular dysfunction in obesity? *Clin Sci (Lond)*, *127*(2), 111-22.

Nidorf, S. M., Fiolet, A. T., Mosterd, A., Eikelboom, J. W., Schut, A., Opstal, T. S., The, S. H., Xu, X.-F., Ireland, M. A., & Lenderink, T. (2020). Colchicine in patients with chronic coronary disease. *New England journal of medicine*, *383*(19), 1838-1847.

Nishikawa, T., Edelstein, D., Du, X. L., Yamagishi, S., Matsumura, T., Kaneda, Y., Yorek, M. A., Beebe, D., Oates, P. J., Hammes, H. P., Giardino, I., & Brownlee, M. (2000). Normalizing mitochondrial superoxide production blocks three pathways of hyperglycaemic damage. *Nature*, *404*(6779), 787-90.

Nolfi-Donegan, D., Braganza, A., & Shiva, S. (2020). Mitochondrial electron transport chain: Oxidative phosphorylation, oxidant production, and methods of measurement. *Redox Biol*, *37*, 101674.

Oak, J. H., & Cai, H. (2007a). Attenuation of angiotensin II signaling recouples eNOS and inhibits nonendothelial NOX activity in diabetic mice. *Diabetes*, *56*(1), 118-

26.

Oak, J.-H., & Cai, H. (2007b). Attenuation of angiotensin II signaling recouples eNOS and inhibits nonendothelial NOX activity in diabetic mice. *Diabetes*, *56*(1), 118-126.

Oda, T., Hashimoto, H., Kuwabara, N., Akashi, S., Hayashi, K., Kojima, C., Wong, H. L., Kawasaki, T., Shimamoto, K., Sato, M., & Shimizu, T. (2010). Structure of the N-terminal regulatory domain of a plant NADPH oxidase and its functional implications. *J Biol Chem*, *285*(2), 1435-45.

Ogawa, A., Yoshimoto, T., Kikuchi, H., Sano, K., Saito, I., Yamaguchi, T., & Yasuhara, H. (1999). Ebselen in acute middle cerebral artery occlusion: a placebo-controlled, double-blind clinical trial. *Cerebrovasc Dis*, *9*(2), 112-8.

Ohyama, K., Matsumoto, Y., Amamizu, H., Uzuka, H., Nishimiya, K., Morosawa, S., Hirano, M., Watabe, H., Funaki, Y., Miyata, S., Takahashi, J., Ito, K., & Shimokawa, H. (2017). Association of Coronary Perivascular Adipose Tissue Inflammation and Drug-Eluting Stent-Induced Coronary Hyperconstricting Responses in Pigs: (18)F-Fluorodeoxyglucose Positron Emission Tomography Imaging Study. *Arterioscler Thromb Vasc Biol*, *37*(9), 1757-1764.

Oikonomou, E. K., & Antoniades, C. (2018). Immunometabolic Regulation of Vascular Redox State: The Role of Adipose Tissue. *Antioxid Redox Signal*, *29*(3), 313-336.

Oikonomou, E. K., & Antoniades, C. (2019). The role of adipose tissue in cardiovascular health and disease. *Nat Rev Cardiol*, *16*(2), 83-99.

Oikonomou, E. K., Antonopoulos, A. S., Schottlander, D., Marwan, M., Mathers, C., Tomlins, P., Siddique, M., KlÃ¼ner, L. V., Shirodaria, C., Mavrogiannis, M. C., Thomas, S., Fava, A., Deanfield, J., Channon, K. M., Neubauer, S., Desai, M. Y., Achenbach, S., & Antoniades, C. (2021). Standardized measurement of coronary inflammation using cardiovascular computed tomography: integration in clinical care as a prognostic medical device. *Cardiovascular Research*, *117*(13), 2677-2690.

Oikonomou, E. K., Marwan, M., Desai, M. Y., Mancio, J., Alashi, A., Hutt Centeno, E., Thomas, S., Herdman, L., Kotanidis, C. P., Thomas, K. E., Griffin, B. P., Flamm, S. D., Antonopoulos, A. S., Shirodaria, C., Sabharwal, N., Deanfield, J., Neubauer, S., Hopewell, J. C., Channon, K. M., Achenbach, S., & Antoniades, C. (2018). Non-invasive detection of coronary inflammation using computed tomography and prediction of residual cardiovascular risk (the CRISP CT study): a post-hoc analysis of prospective outcome data. *Lancet*, *392*(10151), 929-939.

Oikonomou, E. K., Siddique, M., & Antoniades, C. (2020). Artificial intelligence in medical imaging: A radiomic guide to precision phenotyping of cardiovascular disease. *Cardiovasc Res*, *116*(13), 2040-2054.

Oikonomou, E. K., Williams, M. C., Kotanidis, C. P., Desai, M. Y., Marwan, M., Antonopoulos, A. S., Thomas, K. E., Thomas, S., Akoumianakis, I., Fan, L. M., Kesavan, S., Herdman, L., Alashi, A., Centeno, E. H., Lyasheva, M., Griffin, B. P., Flamm, S. D., Shirodaria, C., Sabharwal, N., Kelion, A., Dweck, M. R., Van Beek, E. J. R., Deanfield, J., Hopewell, J. C., Neubauer, S., Channon, K. M.,

Achenbach, S., Newby, D. E., & Antoniades, C. (2019). A novel machine learning-derived radiotranscriptomic signature of perivascular fat improves cardiac risk prediction using coronary CT angiography. *Eur Heart J*, *40*(43), 3529-3543.

Okayama, S., Soeda, T., Takami, Y., Kawakami, R., Somekawa, S., Uemura, S., & Saito, Y. (2012). The influence of effective energy on computed tomography number depends on tissue characteristics in monoenergetic cardiac imaging. *Radiol Res Pract*, *2012*, 150980.

Oldenburg, O., Cohen, M. V., Yellon, D. M., & Downey, J. M. (2002). Mitochondrial KATP channels: role in cardioprotection. *Cardiovascular research*, *55*(3), 429-437.

Onogi, Y., Wada, T., Kamiya, C., Inata, K., Matsuzawa, T., Inaba, Y., Kimura, K., Inoue, H., Yamamoto, S., Ishii, Y., Koya, D., Tsuneki, H., Sasahara, M., & Sasaoka, T. (2017). PDGFRbeta Regulates Adipose Tissue Expansion and Glucose Metabolism via Vascular Remodeling in Diet-Induced Obesity. *Diabetes*, *66*(4), 1008-1021.

Otsuka, F., Yahagi, K., Sakakura, K., & Virmani, R. (2013a). Why is the mammary artery so special and what protects it from atherosclerosis? *Annals of cardiothoracic surgery*, *2*(4), 519.

Otsuka, F., Yahagi, K., Sakakura, K., & Virmani, R. (2013b). Why is the mammary artery so special and what protects it from atherosclerosis? *Annals of cardiothoracic surgery*, *2*(4), 519.

Ozaki, M., Kawashima, S., Yamashita, T., Hirase, T., Namiki, M., Inoue, N., Hirata, K., Yasui, H., Sakurai, H., Yoshida, Y., Masada, M., & Yokoyama, M. (2002). Overexpression of endothelial nitric oxide synthase accelerates atherosclerotic lesion formation in apoE-deficient mice. *J Clin Invest*, *110*(3), 331-40.

Panday, A., Sahoo, M. K., Osorio, D., & Batra, S. (2015). NADPH oxidases: an overview from structure to innate immunity-associated pathologies. *Cell Mol Immunol*, *12*(1), 5-23.

Pandey, D., & Fulton, D. J. (2011). Molecular regulation of NADPH oxidase 5 via the MAPK pathway. *Am J Physiol Heart Circ Physiol*, *300*(4), H1336-44.

Pandey, D., Gratton, J. P., Rafikov, R., Black, S. M., & Fulton, D. J. (2011). Calcium/calmodulin-dependent kinase II mediates the phosphorylation and activation of NADPH oxidase 5. *Mol Pharmacol*, *80*(3), 407-15.

Pangolin software package. (n.d.).

Parajuli, N., Patel, V. B., Wang, W., Basu, R., & Oudit, G. Y. (2014). Loss of NOX2 (gp91 phox) prevents oxidative stress and progression to advanced heart failure. *Clinical science*, *127*(5), 331-340.

Pasarica, M., Sereda, O. R., Redman, L. M., Albarado, D. C., Hymel, D. T., Roan, L. E., Rood, J. C., Burk, D. H., & Smith, S. R. (2009). Reduced adipose tissue oxygenation in human obesity: evidence for rarefaction, macrophage chemotaxis, and inflammation without an angiogenic response. *Diabetes*, *58*(3), 718-725.

Passacquale, G., Di Giosia, P., & Ferro, A. (2016). The role of inflammatory biomarkers in developing targeted cardiovascular therapies: lessons from the cardiovascular

inflammation reduction trials. *Cardiovasc Res*, *109*(1), 9-23.

Pattison, D. I., Davies, M. J., & Hawkins, C. L. (2012). Reactions and reactivity of myeloperoxidase-derived oxidants: differential biological effects of hypochlorous and hypothiocyanous acids. *Free Radic Res*, *46*(8), 975-95.

Pavon, N., Correa, F., Buelna-Chontal, M., Hernandez-Esquivel, L., & Chavez, E. (2015). Ebselen induces mitochondrial permeability transition because of its interaction with adenine nucleotide translocase. *Life sciences*, *139*, 108-113.

Pertea, G. (2015). fqtrim: v0. 9.4 release.

Pierdomenico, S. D., Pierdomenico, A. M., Cuccurullo, F., & Iacobellis, G. (2013). Meta-analysis of the relation of echocardiographic epicardial adipose tissue thickness and the metabolic syndrome. *Am J Cardiol*, *111*(1), 73-8.

Piganelli, J. D., Flores, S. C., Cruz, C., Koepp, J., Batinic-Haberle, I., Crapo, J., Day, B., Kachadourian, R., Young, R., Bradley, B., & Haskins, K. (2002). A metalloporphyrin-based superoxide dismutase mimic inhibits adoptive transfer of autoimmune diabetes by a diabetogenic T-cell clone. *Diabetes*, *51*(2), 347-55.

Pott, J., Burkhardt, R., Beutner, F., Horn, K., Teren, A., Kirsten, H., Holdt, L. M., Schuler, G., Teupser, D., Loeffler, M., Thiery, J., & Scholz, M. (2017). Genome-wide meta-analysis identifies novel loci of plaque burden in carotid artery. *Atherosclerosis*, *259*, 32-40.

Queliconi, B. B., Wojtovich, A. P., Nadtochiy, S. M., Kowaltowski, A. J., & Brookes, P. S. (2011). Redox regulation of the mitochondrial KATP channel in cardioprotection. *Biochimica et Biophysica Acta (BBA)-Molecular Cell Research*, *1813*(7),

1309-1315.

Quick, J. (2020). nCoV-2019 sequencing protocol v3 (LoCost).

Raftos, J. E., Whillier, S., Chapman, B. E., & Kuchel, P. W. (2007). Kinetics of uptake and deacetylation of N-acetylcysteine by human erythrocytes. *Int J Biochem Cell Biol*, *39*(9), 1698-706.

Rauch, A., Dupont, A., Goutay, J., Caplan, M., Staessens, S., Moussa, M., Jeanpierre, E., Corseaux, D., Lefevre, G., & Lassalle, F. (2020). Endotheliopathy is induced by plasma from critically ill patients and associated with organ failure in severe COVID-19. *Circulation*, *142*(19), 1881-1884.

RIDER. The Reference Image Database to Evaluate Therapy Response. (2013).

Ridker, P. M. (2007). C-reactive protein and the prediction of cardiovascular events among those at intermediate risk: moving an inflammatory hypothesis toward consensus. *J Am Coll Cardiol*, *49*(21), 2129-38.

Ridker, P. M., Danielson, E., Fonseca, F. A., Genest, J., Gotto, J., A. M., Kastelein, J. J., Koenig, W., Libby, P., Lorenzatti, A. J., MacFadyen, J. G., Nordestgaard, B. G., Shepherd, J., Willerson, J. T., Glynn, R. J., & Group, J. S. (2008). Rosuvastatin to prevent vascular events in men and women with elevated C-reactive protein. *N Engl J Med*, *359*(21), 2195-207.

Ridker, P. M., Everett, B. M., Pradhan, A., MacFadyen, J. G., Solomon, D. H., Zaharris, E., Mam, V., Hasan, A., Rosenberg, Y., Iturriaga, E., Gupta, M., Tsigoulis, M., Verma, S., Clearfield, M., Libby, P., Goldhaber, S. Z., Seagle, R., Ofori, C., Saklayen, M., Butman, S., Singh, N., Le May, M., Bertrand, O., Johnston, J.,

Paynter, N. P., Glynn, R. J., & Investigators, C. (2019). Low-Dose Methotrexate for the Prevention of Atherosclerotic Events. *N Engl J Med*, *380*(8), 752-762.

Ridker, P. M., Everett, B. M., Thuren, T., MacFadyen, J. G., Chang, W. H., Ballantyne, C., Fonseca, F., Nicolau, J., Koenig, W., Anker, S. D., Kastelein, J. J. P., Cornel, J. H., Pais, P., Pella, D., Genest, J., Cifkova, R., Lorenzatti, A., Forster, T., Kobalava, Z., Vida-Simiti, L., Flather, M., Shimokawa, H., Ogawa, H., Dellborg, M., Rossi, P. R. F., Troquay, R. P. T., Libby, P., Glynn, R. J., & Group, C. T. (2017). Antiinflammatory Therapy with Canakinumab for Atherosclerotic Disease. *N Engl J Med*, *377*(12), 1119-1131.

Ridker, P. M., MacFadyen, J. G., Thuren, T., & Libby, P. (2019). Residual inflammatory risk associated with interleukin-18 and interleukin-6 after successful interleukin-1Î²^{2}$inhibitionwithcanakinumab$: $furtherrationaleforthedevelopmentoftargetedanti$ $-$ $cytokinetherapiesforthetreatmentofatherothrombosis.$***European Heart Journal.***

Robinson, M. D., McCarthy, D. J., & Smyth, G. K. (2010). edgeR: a Bioconductor package for differential expression analysis of digital gene expression data. *Bioinformatics*, *26*(1), 139-40.

Roger, A. J., Munoz-Gomez, S. A., & Kamikawa, R. (2017). The Origin and Diversification of Mitochondria. *Curr Biol*, *27*(21), R1177-R1192.

Rubbo, H., Radi, R., Trujillo, M., Telleri, R., Kalyanaraman, B., Barnes, S., Kirk, M., & Freeman, B. A. (1994). Nitric oxide regulation of superoxide and peroxynitrite-dependent lipid peroxidation. Formation of novel nitrogen-containing oxidized

lipid derivatives. *Journal of Biological Chemistry*, *269*(42), 26066-26075.

Rushworth, G. F., & Megson, I. L. (2014). Existing and potential therapeutic uses for N-acetylcysteine: the need for conversion to intracellular glutathione for antioxidant benefits. *Pharmacol Ther*, *141*(2), 150-9.

Rutkowski, J. M., Stern, J. H., & Scherer, P. E. (2015). The cell biology of fat expansion. *J Cell Biol*, *208*(5), 501-12.

Sahoo, S., Meijles, D. N., & Pagano, P. J. (2016). NADPH oxidases: key modulators in aging and age-related cardiovascular diseases? *Clin Sci (Lond)*, *130*(5), 317-35.

Salomon, R. G., Kaur, K., Podrez, E., Hoff, H. F., Krushinsky, A. V., & Sayre, L. M. (2000). HNE-derived 2-pentylpyrroles are generated during oxidation of LDL, are more prevalent in blood plasma from patients with renal disease or atherosclerosis, and are present in atherosclerotic plaques. *Chem Res Toxicol*, *13*(7), 557-64.

Salvemini, D., Mazzon, E., Dugo, L., Riley, D. P., Serraino, I., Caputi, A. P., & Cuzzocrea, S. (2001). Pharmacological manipulation of the inflammatory cascade by the superoxide dismutase mimetic, M40403. *Br J Pharmacol*, *132*(4), 815-27.

Salvemini, D., Mazzon, E., Dugo, L., Serraino, I., De Sarro, A., Caputi, A. P., & Cuzzocrea, S. (2001). Amelioration of joint disease in a rat model of collagen-induced arthritis by M40403, a superoxide dismutase mimetic. *Arthritis Rheum*, *44*(12), 2909-21.

Sarin, S., Wenger, C., Marwaha, A., Qureshi, A., Go, B. D., Woomert, C. A., Clark, K., Nassef, L. A., & Shirani, J. (2008). Clinical significance of epicardial fat

measured using cardiac multislice computed tomography. *Am J Cardiol*, *102*(6), 767-71.

Schlett, C. L., Massaro, J. M., Lehman, S. J., Bamberg, F., O'Donnell, C. J., Fox, C. S., & Hoffmann, U. (2009). Novel measurements of periaortic adipose tissue in comparison to anthropometric measures of obesity, and abdominal adipose tissue. *Int J Obes (Lond)*, *33*(2), 226-32.

Schmidt, A. F., Pearce, L. S., Wilkins, J. T., Overington, J. P., Hingorani, A. D., & Casas, J. P. (2017). PCSK9 monoclonal antibodies for the primary and secondary prevention of cardiovascular disease. *Cochrane Database Syst Rev*, *4*, CD011748.

Schuhmacher, S., Oelze, M., Bollmann, F., Kleinert, H., Otto, C., Heeren, T., Steven, S., Hausding, M., Knorr, M., & Pautz, A. (2011). Vascular dysfunction in experimental diabetes is improved by pentaerithrityl tetranitrate but not isosorbide-5-mononitrate therapy. *Diabetes*, *60*(10), 2608-2616.

Schulz, E., Wenzel, P., Munzel, T., & Daiber, A. (2014a). Mitochondrial redox signaling: Interaction of mitochondrial reactive oxygen species with other sources of oxidative stress. *Antioxid Redox Signal*, *20*(2), 308-24.

Schulz, E., Wenzel, P., Munzel, T., & Daiber, A. (2014b). Mitochondrial redox signaling: interaction of mitochondrial reactive oxygen species with other sources of oxidative stress. *Antioxidants redox signaling*, *20*(2), 308-324.

Schurmann, C., Rezende, F., Kruse, C., Yasar, Y., LÃ¶we, O., Fork, C., Van De Sluis, B., Bremer, R., Weissmann, N., & Shah, A. M. (2015). The NADPH oxidase

Nox4 has anti-atherosclerotic functions. *European heart journal*, *36*(48), 3447-3456.

Sehested, T. S. G., Bjerre, J., Ku, S., Chang, A., Jahansouz, A., Owens, D. K., Hlatky, M. A., & Goldhaber-Fiebert, J. D. (2019). Cost-effectiveness of Canakinumab for Prevention of Recurrent Cardiovascular Events. *JAMA Cardiol*, *4*(2), 128-135.

Seshiah, P. N., Weber, D. S., Rocic, P., Valppu, L., Taniyama, Y., & Griendling, K. K. (2002). Angiotensin II stimulation of NAD(P)H oxidase activity: upstream mediators. *Circ Res*, *91*(5), 406-13.

Shah, A. K., Bhullar, S. K., Elimban, V., & Dhalla, N. S. (2021). Oxidative Stress as A Mechanism for Functional Alterations in Cardiac Hypertrophy and Heart Failure. *Antioxidants*, *10*(6), 931.

Sies, H. (2015). Oxidative stress: a concept in redox biology and medicine. *Redox Biol*, *4*, 180-3.

Simons, J. M., A't Hart, B., Ching, T. R. I. V., Van Dijk, H., & Labadie, R. P. (1990). Metabolic activation of natural phenols into selective oxidative burst agonists by activated human neutrophils. *Free Radical Biology and Medicine*, *8*(3), 251-258.

Singh, A. K., Singh, R., Joshi, S. R., & Misra, A. (2021). Mucormycosis in COVID-19: A systematic review of cases reported worldwide and in India. *Diabetes Metab Syndr*, *15*(4), 102146.

Siu, K. L., Li, Q., Zhang, Y., Guo, J., Youn, J. Y., Du, J., & Cai, H. (2017). NOX isoforms in the development of abdominal aortic aneurysm. *Redox Biol*, *11*, 118-125.

Siu, K. L., Lotz, C., Ping, P., & Cai, H. (2015). Netrin-1 abrogates ischemia/reperfusion-induced cardiac mitochondrial dysfunction via nitric oxide-dependent attenuation of NOX4 activation and recoupling of NOS. *Journal of molecular and cellular cardiology*, *78*, 174-185.

Siu, K. L., Miao, X. N., & Cai, H. (2014a). Recoupling of eNOS with folic acid prevents abdominal aortic aneurysm formation in angiotensin II-infused apolipoprotein E null mice. *PLoS One*, *9*(2), e88899.

Siu, K. L., Miao, X. N., & Cai, H. (2014b). Recoupling of eNOS with folic acid prevents abdominal aortic aneurysm formation in angiotensin II-infused apolipoprotein E null mice. *PloS one*, *9*(2), e88899.

Smilkstein, M. J., Knapp, G. L., Kulig, K. W., & Rumack, B. H. (1988). Efficacy of oral N-acetylcysteine in the treatment of acetaminophen overdose. Analysis of the national multicenter study (1976 to 1985). *N Engl J Med*, *319*(24), 1557-62.

Souilhol, C., Serbanovic-Canic, J., Fragiadaki, M., Chico, T. J., Ridger, V., Roddie, H., & Evans, P. C. (2020). Endothelial responses to shear stress in atherosclerosis: a novel role for developmental genes. *Nat Rev Cardiol*, *17*(1), 52-63.

Streeter, J., Thiel, W., Brieger, K., & Miller, F. J., Jr. (2013). Opportunity nox: the future of NADPH oxidases as therapeutic targets in cardiovascular disease. *Cardiovascular therapeutics*, *31*(3), 125-137.

Suzuki, H., DeLano, F. A., Parks, D. A., Jamshidi, N., Granger, D. N., Ishii, H., Suematsu, M., Zweifach, B. W., & Schmid-Schonbein, G. W. (1998). Xanthine oxidase activity associated with arterial blood pressure in spontaneously hyper-

tensive rats. *Proc Natl Acad Sci U S A*, *95*(8), 4754-9.

Suzuki, Y., Wang, W., Vu, T. H., & Raffin, T. A. (1992). Effect of NADPH oxidase inhibition on endothelial cell ELAM-1 mRNA expression. *Biochem Biophys Res Commun*, *184*(3), 1339-43.

Szasz, T., & Webb, R. C. (2012). Perivascular adipose tissue: more than just structural support. *Clinical science*, *122*(1), 1-12.

Takaoka, M., Suzuki, H., Shioda, S., Sekikawa, K., Saito, Y., Nagai, R., & Sata, M. (2010). Endovascular injury induces rapid phenotypic changes in perivascular adipose tissue. *Arterioscler Thromb Vasc Biol*, *30*(8), 1576-82.

Takaya, T., Hirata, K., Yamashita, T., Shinohara, M., Sasaki, N., Inoue, N., Yada, T., Goto, M., Fukatsu, A., Hayashi, T., Alp, N. J., Channon, K. M., Yokoyama, M., & Kawashima, S. (2007). A specific role for eNOS-derived reactive oxygen species in atherosclerosis progression. *Arterioscler Thromb Vasc Biol*, *27*(7), 1632-7.

Takimoto, E., & Kass, D. A. (2007). Role of oxidative stress in cardiac hypertrophy and remodeling. *Hypertension*, *49*(2), 241-8.

Tanami, Y., Jinzaki, M., Kishi, S., Matheson, M., Vavere, A. L., Rochitte, C. E., Dewey, M., Chen, M. Y., Clouse, M. E., Cox, C., Kuribayashi, S., Lima, J. A., & Arbab-Zadeh, A. (2015). Lack of association between epicardial fat volume and extent of coronary artery calcification, severity of coronary artery disease, or presence of myocardial perfusion abnormalities in a diverse, symptomatic patient population: results from the CORE320 multicenter study. *Circ Cardiovasc Imaging*, *8*(3), e002676.

Tardif, J.-C., Kouz, S., Waters, D. D., Bertrand, O. F., Diaz, R., Maggioni, A. P., Pinto, F. J., Ibrahim, R., Gamra, H., & Kiwan, G. S. (2019). Efficacy and safety of low-dose colchicine after myocardial infarction. *New England journal of medicine*, *381*(26), 2497-2505.

Taube, A., Schlich, R., Sell, H., Eckardt, K., & Eckel, J. (2012). Inflammation and metabolic dysfunction: links to cardiovascular diseases. *Am J Physiol Heart Circ Physiol*, *302*(11), H2148-65.

Teuwen, L.-A., Geldhof, V., Pasut, A., & Carmeliet, P. (2020). COVID-19: the vasculature unleashed. *Nature Reviews Immunology*, 1-3.

Thony, B., Auerbach, G., & Blau, N. (2000). Tetrahydrobiopterin biosynthesis, regeneration and functions. *Biochem J*, *347 Pt 1*(1), 1-16.

Tisdale, M. J. (2002). Cachexia in cancer patients. *Nat Rev Cancer*, *2*(11), 862-71.

Tousoulis, D., Psarros, C., Demosthenous, M., Patel, R., Antoniades, C., & Stefanadis, C. (2014). Innate and adaptive inflammation as a therapeutic target in vascular disease: the emerging role of statins. *J Am Coll Cardiol*, *63*(23), 2491-2502.

Valko, M., Leibfritz, D., Moncol, J., Cronin, M. T., Mazur, M., & Telser, J. (2007). Free radicals and antioxidants in normal physiological functions and human disease. *Int J Biochem Cell Biol*, *39*(1), 44-84.

Van Buul, J. D., Fernandez-Borja, M., Anthony, E. C., & Hordijk, P. L. (2005). Expression and localization of NOX2 and NOX4 in primary human endothelial cells. *Antioxid Redox Signal*, *7*(3-4), 308-17.

van Griethuysen, J. J. M., Fedorov, A., Parmar, C., Hosny, A., Aucoin, N., Narayan, V.,

Beets-Tan, R. G. H., Fillion-Robin, J. C., Pieper, S., & Aerts, H. (2017). Computational Radiomics System to Decode the Radiographic Phenotype. *Cancer Res*, *77*(21), e104-e107.

Varga, Z., Flammer, A. J., Steiger, P., Haberecker, M., Andermatt, R., Zinkernagel, A. S., Mehra, M. R., Schuepbach, R. A., Ruschitzka, F., & Moch, H. (2020). Endothelial cell infection and endotheliitis in COVID-19. *Lancet*, *395*(10234), 1417-1418.

Vasquez-Vivar, J. (1996). Hogg N, Pritchard KA Jr, Martasek P, and Kalyanaraman B. *Superoxide anion formation from lucigenin: an electron spin resonance spin-trapping study. FEBS Lett*, *403*, 127-130.

Vergeade, A., Mulder, P., Vendeville, C., Ventura-Clapier, R., Thuillez, C., & Monteil, C. (2012). Xanthine oxidase contributes to mitochondrial ROS generation in an experimental model of cocaine-induced diastolic dysfunction. *Journal of cardiovascular pharmacology*, *60*(6), 538-543.

Versteylen, M. O., Takx, R. A., Joosen, I. A., Nelemans, P. J., Das, M., Crijns, H. J., Hofstra, L., & Leiner, T. (2012). Epicardial adipose tissue volume as a predictor for coronary artery disease in diabetic, impaired fasting glucose, and non-diabetic patients presenting with chest pain. *Eur Heart J Cardiovasc Imaging*, *13*(6), 517-23.

Villarroya, F., Cereijo, R., Villarroya, J., & Giralt, M. (2017). Brown adipose tissue as a secretory organ. *Nature Reviews Endocrinology*, *13*(1), 26.

Wallach, T. M., & Segal, A. W. (1997). Analysis of glycosylation sites on gp91phox,

the flavocytochrome of the NADPH oxidase, by site-directed mutagenesis and translation in vitro. *Biochemical Journal*, *321*(3), 583-585.

Wang, H. D., Xu, S., Johns, D. G., Du, Y., Quinn, M. T., Cayatte, A. J., & Cohen, R. A. (2001). Role of NADPH oxidase in the vascular hypertrophic and oxidative stress response to angiotensin II in mice. *Circ Res*, *88*(9), 947-53.

Wang, T., Du, Z., Zhu, F., Cao, Z., An, Y., Gao, Y., & Jiang, B. (2020). Comorbidities and multi-organ injuries in the treatment of COVID-19. *Lancet*, *395*(10228), e52.

Wang, X., Elksnis, A., Wikstrom, P., Walum, E., Welsh, N., & Carlsson, P.-O. (2018). The novel NADPH oxidase 4 selective inhibitor GLX7013114 counteracts human islet cell death in vitro. *PLoS One*, *13*(9), e0204271.

Wartenberg, M., Hoffmann, E., Schwindt, H., Grunheck, F., Petros, J., Arnold, J. R., Hescheler, J., & Sauer, H. (2005). Reactive oxygen species-linked regulation of the multidrug resistance transporter P-glycoprotein in Nox-1 overexpressing prostate tumor spheroids. *FEBS Lett*, *579*(20), 4541-4549.

Watts, G., Playford, D., Croft, K., Ward, N., Mori, T., & Burke, V. (2002). Coenzyme Q10 improves endothelial dysfunction of the brachial artery in Type II diabetes mellitus. *Diabetologia*, *45*(3), 420-426.

(Vol. 2020) [Web Page]. (version at 10.01.2016). Retrieved from https://broadinstitute.github.io/picard/ doi: https://broadinstitute.github.io/picard/,(versionat10.01.2016)

Wendel, A., & Cikryt, P. (1980). The level and half-life of glutathione in human plasma. *FEBS Lett*, *120*(2), 209-11.

WHO | Disease burden and mortality estimates. (2018). *WHO*.

Williams, H. C., & Griendling, K. K. (2007). NADPH oxidase inhibitors: new antihypertensive agents? *J Cardiovasc Pharmacol*, *50*(1), 9-16.

Wu, Z., & McGoogan, J. M. (2020). Characteristics of and important lessons from the coronavirus disease 2019 (COVID-19) outbreak in China: summary of a report of 72 314 cases from the Chinese Center for Disease Control and Prevention. *Jama*, *323*(13), 1239-1242.

Xie, Z., Wang, X., Liu, X., Du, H., Sun, C., Shao, X., Tian, J., Gu, X., Wang, H., Tian, J., & Yu, B. (2018). Adipose-Derived Exosomes Exert Proatherogenic Effects by Regulating Macrophage Foam Cell Formation and Polarization. *J Am Heart Assoc*, *7*(5), e007442.

Yamaguchi, T., Sano, K., Takakura, K., Saito, I., Shinohara, Y., Asano, T., & Yasuhara, H. (1998). Ebselen in acute ischemic stroke: a placebo-controlled, double-blind clinical trial. Ebselen Study Group. *Stroke*, *29*(1), 12-7.

Yang, J., Anholts, J., Kolbe, U., Stegehuis-Kamp, J. A., Claas, F. H., & Eikmans, M. (2018). Calcium-binding proteins S100A8 and S100A9: investigation of their immune regulatory effect in myeloid cells. *International journal of molecular sciences*, *19*(7), 1833.

Yang, X., Li, Y., Li, Y., Ren, X., Zhang, X., Hu, D., Gao, Y., Xing, Y., & Shang, H. (2017). Oxidative Stress-Mediated Atherosclerosis: Mechanisms and Therapies. *Front Physiol*, *8*, 600.

Ye, Z., & Song, H. (2008). Antioxidant vitamins intake and the risk of coronary

heart disease: meta-analysis of cohort studies. *European Journal of Preventive Cardiology*, *15*(1), 26-34.

You, L., Wang, J., Zhang, F., Zhang, J., Tao, H., Zheng, X., & Hu, Y. (2019). Potential fourâmiRNA signature associated with T stage and prognosis of patients with pancreatic ductal adenocarcinoma identified by coâexpression analysis. *Molecular Medicine Reports*, *19*(1), 441-451.

Youn, J., Gao, L., & Cai, H. (2012). The p47phox-and NADPH oxidase organiser 1 (NOXO1)-dependent activation of NADPH oxidase 1 (NOX1) mediates endothelial nitric oxide synthase (eNOS) uncoupling and endothelial dysfunction in a streptozotocin-induced murine model of diabetes. *Diabetologia*, *55*(7), 2069-2079.

Youn, J. Y., Siu, K. L., Lob, H. E., Itani, H., Harrison, D. G., & Cai, H. (2014). Role of vascular oxidative stress in obesity and metabolic syndrome. *Diabetes*, *63*(7), 2344-55.

Youn, J. Y., Wang, T., Blair, J., Laude, K. M., Oak, J.-H., McCann, L. A., Harrison, D. G., & Cai, H. (2012). Endothelium-specific sepiapterin reductase deficiency in DOCA-salt hypertension. *American Journal of Physiology-Heart and Circulatory Physiology*, *302*(11), H2243-H2249.

Yu, L., Yang, G., Zhang, X., Wang, P., Weng, X., Yang, Y., Li, Z., Fang, M., Xu, Y., & Sun, A. (2018). Megakaryocytic leukemia 1 bridges epigenetic activation of NADPH oxidase in macrophages to cardiac ischemia-reperfusion injury. *Circulation*, *138*(24), 2820-2836.

Yudkin, J. S., Eringa, E., & Stehouwer, C. D. (2005). "Vasocrine" signalling from perivascular fat: a mechanism linking insulin resistance to vascular disease. *Lancet*, *365*(9473), 1817-20.

Zang, M., Xu, S., Maitland-Toolan, K. A., Zuccollo, A., Hou, X., Jiang, B., Wierzbicki, M., Verbeuren, T. J., & Cohen, R. A. (2006). Polyphenols stimulate AMP-activated protein kinase, lower lipids, and inhibit accelerated atherosclerosis in diabetic LDL receptor-deficient mice. *Diabetes*, *55*(8), 2180-91.

Zhang, M., Brewer, A. C., Schroder, K., Santos, C. X., Grieve, D. J., Wang, M., Anilkumar, N., Yu, B., Dong, X., Walker, S. J., Brandes, R. P., & Shah, A. M. (2010). NADPH oxidase-4 mediates protection against chronic load-induced stress in mouse hearts by enhancing angiogenesis. *Proc Natl Acad Sci U S A*, *107*(42), 18121-6.

Zhang, Y., Murugesan, P., Huang, K., & Cai, H. (2020). NADPH oxidases and oxidase crosstalk in cardiovascular diseases: novel therapeutic targets. *Nat Rev Cardiol*, *17*(3), 170-194.

Zhao, Q. D., Viswanadhapalli, S., Williams, P., Shi, Q., Tan, C., Yi, X., Bhandari, B., & Abboud, H. E. (2015). NADPH oxidase 4 induces cardiac fibrosis and hypertrophy through activating Akt/mTOR and NFÎºB signaling pathways. *Circulation*, *131*(7), 643-655.

Zou, M. H., Shi, C., & Cohen, R. A. (2002). Oxidation of the zinc-thiolate complex and uncoupling of endothelial nitric oxide synthase by peroxynitrite. *J Clin Invest*, *109*(6), 817-26.

Appendices

A | Variables in outcomes dataset

Admitted Patient Care Dataset Variables

ENCRYPTED_STUDY_ID
ADMIDATE
ADMIMETH
ADMISORC
AEKEY
BEDYEAR
CAUSE
CLASSPAT
DIAG_01
DIAG_02
DIAG_03
DIAG_04
DIAG_05
DIAG_06
DIAG_07
DIAG_08
DIAG_09
DIAG_10
DIAG_11
DIAG_12
DIAG_13
DIAG_14
DIAG_15
DIAG_16
DIAG_17
DIAG_18
DIAG_19
DIAG_20
DISDATE
DISDEST
DISMETH
DISREADYDATE
DOMPROC
ELECDATE
EPIDUR
EPIEND
EPIKEY
EPIORDER
EPISTART
EPISTAT
EPITYPE
FIRSTREG
GPPRAC
INTMANIG
MAINSPEF
MATCH_RANK

NHSNOIND
OPDATE_01
OPDATE_02
OPDATE_03
OPDATE_04
OPDATE_05
OPDATE_06
OPDATE_07
OPDATE_08
OPDATE_09
OPDATE_10
OPDATE_11
OPDATE_12
OPDATE_13
OPDATE_14
OPDATE_15
OPDATE_16
OPDATE_17
OPDATE_18
OPDATE_19
OPDATE_20
OPDATE_21
OPDATE_22
OPDATE_23
OPDATE_24
OPERSTAT
OPERTN_01
OPERTN_02
OPERTN_03
OPERTN_04
OPERTN_05
OPERTN_06
OPERTN_07
OPERTN_08
OPERTN_09
OPERTN_10
OPERTN_11
OPERTN_12
OPERTN_13
OPERTN_14
OPERTN_15
OPERTN_16
OPERTN_17
OPERTN_18
OPERTN_19
OPERTN_20
OPERTN_21
OPERTN_22

OPERTN_23
OPERTN_24
POSOPDUR
PREOPDUR
SPELBGIN
SPELDUR
SPELEND
STARTAGE
SUSRECID
TRETSPEF
STUDY_ID

B | Radiomic features

List of radiomic features

Image
Label
Mask
diagnostics_Versions_PyRadiomics
diagnostics_Versions_Numpy
diagnostics_Versions_SimpleITK
diagnostics_Versions_PyWavelet
diagnostics_Versions_Python
diagnostics_Configuration_Settings
diagnostics_Configuration_EnabledImageTypes
diagnostics_Image-original_Hash
diagnostics_Image-original_Dimensionality
diagnostics_Image-original_Spacing
diagnostics_Image-original_Size
diagnostics_Image-original_Mean
diagnostics_Image-original_Minimum
diagnostics_Image-original_Maximum
diagnostics_Mask-original_Hash
diagnostics_Mask-original_Spacing
diagnostics_Mask-original_Size
diagnostics_Mask-original_BoundingBox
diagnostics_Mask-original_VoxelNum
diagnostics_Mask-original_VolumeNum
diagnostics_Mask-original_CenterOfMassIndex
diagnostics_Mask-original_CenterOfMass
diagnostics_Image-interpolated_Spacing
diagnostics_Image-interpolated_Size
diagnostics_Image-interpolated_Mean
diagnostics_Image-interpolated_Minimum
diagnostics_Image-interpolated_Maximum
diagnostics_Mask-interpolated_Spacing
diagnostics_Mask-interpolated_Size
diagnostics_Mask-interpolated_BoundingBox
diagnostics_Mask-interpolated_VoxelNum
diagnostics_Mask-interpolated_VolumeNum
diagnostics_Mask-interpolated_CenterOfMassIndex
diagnostics_Mask-interpolated_CenterOfMass
diagnostics_Mask-interpolated_Mean
diagnostics_Mask-interpolated_Minimum
diagnostics_Mask-interpolated_Maximum
diagnostics_Mask-resegmented_Spacing
diagnostics_Mask-resegmented_Size
diagnostics_Mask-resegmented_BoundingBox

diagnostics_Mask-resegmented_VoxelNum
diagnostics_Mask-resegmented_VolumeNum
diagnostics_Mask-resegmented_CenterOfMassIndex
diagnostics_Mask-resegmented_CenterOfMass
diagnostics_Mask-resegmented_Mean
diagnostics_Mask-resegmented_Minimum
diagnostics_Mask-resegmented_Maximum
original_shape_VoxelVolume
original_shape_MeshVolume
original_shape_SurfaceArea
original_shape_SurfaceVolumeRatio
original_shape_Compactness1
original_shape_Compactness2
original_shape_Sphericity
original_shape_SphericalDisproportion
original_shape_Maximum3DDiameter
original_shape_Maximum2DDiameterSlice
original_shape_Maximum2DDiameterColumn
original_shape_Maximum2DDiameterRow
original_shape_MajorAxisLength
original_shape_MinorAxisLength
original_shape_LeastAxisLength
original_shape_Elongation
original_shape_Flatness
original_firstorder_10Percentile
original_firstorder_90Percentile
original_firstorder_Energy
original_firstorder_Entropy
original_firstorder_InterquartileRange
original_firstorder_Kurtosis
original_firstorder_Maximum
original_firstorder_MeanAbsoluteDeviation
original_firstorder_Mean
original_firstorder_Median
original_firstorder_Minimum
original_firstorder_Range
original_firstorder_RobustMeanAbsoluteDeviation
original_firstorder_RootMeanSquared
original_firstorder_Skewness
original_firstorder_TotalEnergy
original_firstorder_Uniformity
original_firstorder_Variance
original_glcm_Autocorrelation
original_glcm_JointAverage
original_glcm_ClusterProminence

original_glcm_ClusterShade
original_glcm_ClusterTendency
original_glcm_Contrast
original_glcm_Correlation
original_glcm_DifferenceAverage
original_glcm_DifferenceEntropy
original_glcm_DifferenceVariance
original_glcm_JointEnergy
original_glcm_JointEntropy
original_glcm_Imc1
original_glcm_Imc2
original_glcm_Idm
original_glcm_Idmn
original_glcm_Id
original_glcm_Idn
original_glcm_InverseVariance
original_glcm_MaximumProbability
original_glcm_SumEntropy
original_glcm_SumSquares
original_glrlm_GrayLevelNonUniformity
original_glrlm_GrayLevelNonUniformityNormalized
original_glrlm_GrayLevelVariance
original_glrlm_HighGrayLevelRunEmphasis
original_glrlm_LongRunEmphasis
original_glrlm_LongRunHighGrayLevelEmphasis
original_glrlm_LongRunLowGrayLevelEmphasis
original_glrlm_LowGrayLevelRunEmphasis
original_glrlm_RunEntropy
original_glrlm_RunLengthNonUniformity
original_glrlm_RunLengthNonUniformityNormalized
original_glrlm_RunPercentage
original_glrlm_RunVariance
original_glrlm_ShortRunEmphasis
original_glrlm_ShortRunHighGrayLevelEmphasis
original_glrlm_ShortRunLowGrayLevelEmphasis
original_glszm_GrayLevelNonUniformity
original_glszm_GrayLevelNonUniformityNormalized
original_glszm_GrayLevelVariance
original_glszm_HighGrayLevelZoneEmphasis
original_glszm_LargeAreaEmphasis
original_glszm_LargeAreaHighGrayLevelEmphasis
original_glszm_LargeAreaLowGrayLevelEmphasis
original_glszm_LowGrayLevelZoneEmphasis
original_glszm_SizeZoneNonUniformity
original_glszm_SizeZoneNonUniformityNormalized

original_glszm_SmallAreaEmphasis
original_glszm_SmallAreaHighGrayLevelEmphasis
original_glszm_SmallAreaLowGrayLevelEmphasis
original_glszm_ZoneEntropy
original_glszm_ZonePercentage
original_glszm_ZoneVariance
original_ngtdm_Busyness
original_ngtdm_Coarseness
original_ngtdm_Complexity
original_ngtdm_Contrast
original_ngtdm_Strength
original_gldm_DependenceEntropy
original_gldm_DependenceNonUniformity
original_gldm_DependenceNonUniformityNormalized
original_gldm_DependenceVariance
original_gldm_GrayLevelNonUniformity
original_gldm_GrayLevelVariance
original_gldm_HighGrayLevelEmphasis
original_gldm_LargeDependenceEmphasis
original_gldm_LargeDependenceHighGrayLevelEmphasis
original_gldm_LargeDependenceLowGrayLevelEmphasis
original_gldm_LowGrayLevelEmphasis
original_gldm_SmallDependenceEmphasis
original_gldm_SmallDependenceHighGrayLevelEmphasis
original_gldm_SmallDependenceLowGrayLevelEmphasis
log-sigma-1-0-mm-3D_firstorder_10Percentile
log-sigma-1-0-mm-3D_firstorder_90Percentile
log-sigma-1-0-mm-3D_firstorder_Energy
log-sigma-1-0-mm-3D_firstorder_Entropy
log-sigma-1-0-mm-3D_firstorder_InterquartileRange
log-sigma-1-0-mm-3D_firstorder_Kurtosis
log-sigma-1-0-mm-3D_firstorder_Maximum
log-sigma-1-0-mm-3D_firstorder_MeanAbsoluteDeviation
log-sigma-1-0-mm-3D_firstorder_Mean
log-sigma-1-0-mm-3D_firstorder_Median
log-sigma-1-0-mm-3D_firstorder_Minimum
log-sigma-1-0-mm-3D_firstorder_Range
log-sigma-1-0-mm-3D_firstorder_RobustMeanAbsoluteDeviation
log-sigma-1-0-mm-3D_firstorder_RootMeanSquared
log-sigma-1-0-mm-3D_firstorder_Skewness
log-sigma-1-0-mm-3D_firstorder_TotalEnergy
log-sigma-1-0-mm-3D_firstorder_Uniformity
log-sigma-1-0-mm-3D_firstorder_Variance
log-sigma-1-0-mm-3D_glcm_Autocorrelation
log-sigma-1-0-mm-3D_glcm_JointAverage

log-sigma-1-0-mm-3D_glcm_ClusterProminence
log-sigma-1-0-mm-3D_glcm_ClusterShade
log-sigma-1-0-mm-3D_glcm_ClusterTendency
log-sigma-1-0-mm-3D_glcm_Contrast
log-sigma-1-0-mm-3D_glcm_Correlation
log-sigma-1-0-mm-3D_glcm_DifferenceAverage
log-sigma-1-0-mm-3D_glcm_DifferenceEntropy
log-sigma-1-0-mm-3D_glcm_DifferenceVariance
log-sigma-1-0-mm-3D_glcm_JointEnergy
log-sigma-1-0-mm-3D_glcm_JointEntropy
log-sigma-1-0-mm-3D_glcm_Imc1
log-sigma-1-0-mm-3D_glcm_Imc2
log-sigma-1-0-mm-3D_glcm_Idm
log-sigma-1-0-mm-3D_glcm_Idmn
log-sigma-1-0-mm-3D_glcm_Id
log-sigma-1-0-mm-3D_glcm_Idn
log-sigma-1-0-mm-3D_glcm_InverseVariance
log-sigma-1-0-mm-3D_glcm_MaximumProbability
log-sigma-1-0-mm-3D_glcm_SumEntropy
log-sigma-1-0-mm-3D_glcm_SumSquares
log-sigma-1-0-mm-3D_glrlm_GrayLevelNonUniformity
log-sigma-1-0-mm-3D_glrlm_GrayLevelNonUniformityNormalized
log-sigma-1-0-mm-3D_glrlm_GrayLevelVariance
log-sigma-1-0-mm-3D_glrlm_HighGrayLevelRunEmphasis
log-sigma-1-0-mm-3D_glrlm_LongRunEmphasis
log-sigma-1-0-mm-3D_glrlm_LongRunHighGrayLevelEmphasis
log-sigma-1-0-mm-3D_glrlm_LongRunLowGrayLevelEmphasis
log-sigma-1-0-mm-3D_glrlm_LowGrayLevelRunEmphasis
log-sigma-1-0-mm-3D_glrlm_RunEntropy
log-sigma-1-0-mm-3D_glrlm_RunLengthNonUniformity
log-sigma-1-0-mm-3D_glrlm_RunLengthNonUniformityNormalized
log-sigma-1-0-mm-3D_glrlm_RunPercentage
log-sigma-1-0-mm-3D_glrlm_RunVariance
log-sigma-1-0-mm-3D_glrlm_ShortRunEmphasis
log-sigma-1-0-mm-3D_glrlm_ShortRunHighGrayLevelEmphasis
log-sigma-1-0-mm-3D_glrlm_ShortRunLowGrayLevelEmphasis
log-sigma-1-0-mm-3D_glszm_GrayLevelNonUniformity
log-sigma-1-0-mm-3D_glszm_GrayLevelNonUniformityNormalized
log-sigma-1-0-mm-3D_glszm_GrayLevelVariance
log-sigma-1-0-mm-3D_glszm_HighGrayLevelZoneEmphasis
log-sigma-1-0-mm-3D_glszm_LargeAreaEmphasis
log-sigma-1-0-mm-3D_glszm_LargeAreaHighGrayLevelEmphasis
log-sigma-1-0-mm-3D_glszm_LargeAreaLowGrayLevelEmphasis
log-sigma-1-0-mm-3D_glszm_LowGrayLevelZoneEmphasis
log-sigma-1-0-mm-3D_glszm_SizeZoneNonUniformity

log-sigma-1-0-mm-3D_glszm_SizeZoneNonUniformityNormalized
log-sigma-1-0-mm-3D_glszm_SmallAreaEmphasis
log-sigma-1-0-mm-3D_glszm_SmallAreaHighGrayLevelEmphasis
log-sigma-1-0-mm-3D_glszm_SmallAreaLowGrayLevelEmphasis
log-sigma-1-0-mm-3D_glszm_ZoneEntropy
log-sigma-1-0-mm-3D_glszm_ZonePercentage
log-sigma-1-0-mm-3D_glszm_ZoneVariance
log-sigma-1-0-mm-3D_ngtdm_Busyness
log-sigma-1-0-mm-3D_ngtdm_Coarseness
log-sigma-1-0-mm-3D_ngtdm_Complexity
log-sigma-1-0-mm-3D_ngtdm_Contrast
log-sigma-1-0-mm-3D_ngtdm_Strength
log-sigma-1-0-mm-3D_gldm_DependenceEntropy
log-sigma-1-0-mm-3D_gldm_DependenceNonUniformity
log-sigma-1-0-mm-3D_gldm_DependenceNonUniformityNormalized
log-sigma-1-0-mm-3D_gldm_DependenceVariance
log-sigma-1-0-mm-3D_gldm_GrayLevelNonUniformity
log-sigma-1-0-mm-3D_gldm_GrayLevelVariance
log-sigma-1-0-mm-3D_gldm_HighGrayLevelEmphasis
log-sigma-1-0-mm-3D_gldm_LargeDependenceEmphasis
log-sigma-1-0-mm-3D_gldm_LargeDependenceHighGrayLevelEmphasis
log-sigma-1-0-mm-3D_gldm_LargeDependenceLowGrayLevelEmphasis
log-sigma-1-0-mm-3D_gldm_LowGrayLevelEmphasis
log-sigma-1-0-mm-3D_gldm_SmallDependenceEmphasis
log-sigma-1-0-mm-3D_gldm_SmallDependenceHighGrayLevelEmphasis
log-sigma-1-0-mm-3D_gldm_SmallDependenceLowGrayLevelEmphasis
log-sigma-2-0-mm-3D_firstorder_10Percentile
log-sigma-2-0-mm-3D_firstorder_90Percentile
log-sigma-2-0-mm-3D_firstorder_Energy
log-sigma-2-0-mm-3D_firstorder_Entropy
log-sigma-2-0-mm-3D_firstorder_InterquartileRange
log-sigma-2-0-mm-3D_firstorder_Kurtosis
log-sigma-2-0-mm-3D_firstorder_Maximum
log-sigma-2-0-mm-3D_firstorder_MeanAbsoluteDeviation
log-sigma-2-0-mm-3D_firstorder_Mean
log-sigma-2-0-mm-3D_firstorder_Median
log-sigma-2-0-mm-3D_firstorder_Minimum
log-sigma-2-0-mm-3D_firstorder_Range
log-sigma-2-0-mm-3D_firstorder_RobustMeanAbsoluteDeviation
log-sigma-2-0-mm-3D_firstorder_RootMeanSquared
log-sigma-2-0-mm-3D_firstorder_Skewness
log-sigma-2-0-mm-3D_firstorder_TotalEnergy
log-sigma-2-0-mm-3D_firstorder_Uniformity
log-sigma-2-0-mm-3D_firstorder_Variance
log-sigma-2-0-mm-3D_glcm_Autocorrelation

log-sigma-2-0-mm-3D_glcm_JointAverage
log-sigma-2-0-mm-3D_glcm_ClusterProminence
log-sigma-2-0-mm-3D_glcm_ClusterShade
log-sigma-2-0-mm-3D_glcm_ClusterTendency
log-sigma-2-0-mm-3D_glcm_Contrast
log-sigma-2-0-mm-3D_glcm_Correlation
log-sigma-2-0-mm-3D_glcm_DifferenceAverage
log-sigma-2-0-mm-3D_glcm_DifferenceEntropy
log-sigma-2-0-mm-3D_glcm_DifferenceVariance
log-sigma-2-0-mm-3D_glcm_JointEnergy
log-sigma-2-0-mm-3D_glcm_JointEntropy
log-sigma-2-0-mm-3D_glcm_Imc1
log-sigma-2-0-mm-3D_glcm_Imc2
log-sigma-2-0-mm-3D_glcm_Idm
log-sigma-2-0-mm-3D_glcm_Idmn
log-sigma-2-0-mm-3D_glcm_Id
log-sigma-2-0-mm-3D_glcm_Idn
log-sigma-2-0-mm-3D_glcm_InverseVariance
log-sigma-2-0-mm-3D_glcm_MaximumProbability
log-sigma-2-0-mm-3D_glcm_SumEntropy
log-sigma-2-0-mm-3D_glcm_SumSquares
log-sigma-2-0-mm-3D_glrlm_GrayLevelNonUniformity
log-sigma-2-0-mm-3D_glrlm_GrayLevelNonUniformityNormalized
log-sigma-2-0-mm-3D_glrlm_GrayLevelVariance
log-sigma-2-0-mm-3D_glrlm_HighGrayLevelRunEmphasis
log-sigma-2-0-mm-3D_glrlm_LongRunEmphasis
log-sigma-2-0-mm-3D_glrlm_LongRunHighGrayLevelEmphasis
log-sigma-2-0-mm-3D_glrlm_LongRunLowGrayLevelEmphasis
log-sigma-2-0-mm-3D_glrlm_LowGrayLevelRunEmphasis
log-sigma-2-0-mm-3D_glrlm_RunEntropy
log-sigma-2-0-mm-3D_glrlm_RunLengthNonUniformity
log-sigma-2-0-mm-3D_glrlm_RunLengthNonUniformityNormalized
log-sigma-2-0-mm-3D_glrlm_RunPercentage
log-sigma-2-0-mm-3D_glrlm_RunVariance
log-sigma-2-0-mm-3D_glrlm_ShortRunEmphasis
log-sigma-2-0-mm-3D_glrlm_ShortRunHighGrayLevelEmphasis
log-sigma-2-0-mm-3D_glrlm_ShortRunLowGrayLevelEmphasis
log-sigma-2-0-mm-3D_glszm_GrayLevelNonUniformity
log-sigma-2-0-mm-3D_glszm_GrayLevelNonUniformityNormalized
log-sigma-2-0-mm-3D_glszm_GrayLevelVariance
log-sigma-2-0-mm-3D_glszm_HighGrayLevelZoneEmphasis
log-sigma-2-0-mm-3D_glszm_LargeAreaEmphasis
log-sigma-2-0-mm-3D_glszm_LargeAreaHighGrayLevelEmphasis
log-sigma-2-0-mm-3D_glszm_LargeAreaLowGrayLevelEmphasis
log-sigma-2-0-mm-3D_glszm_LowGrayLevelZoneEmphasis

log-sigma-2-0-mm-3D_glszm_SizeZoneNonUniformity
log-sigma-2-0-mm-3D_glszm_SizeZoneNonUniformityNormalized
log-sigma-2-0-mm-3D_glszm_SmallAreaEmphasis
log-sigma-2-0-mm-3D_glszm_SmallAreaHighGrayLevelEmphasis
log-sigma-2-0-mm-3D_glszm_SmallAreaLowGrayLevelEmphasis
log-sigma-2-0-mm-3D_glszm_ZoneEntropy
log-sigma-2-0-mm-3D_glszm_ZonePercentage
log-sigma-2-0-mm-3D_glszm_ZoneVariance
log-sigma-2-0-mm-3D_ngtdm_Busyness
log-sigma-2-0-mm-3D_ngtdm_Coarseness
log-sigma-2-0-mm-3D_ngtdm_Complexity
log-sigma-2-0-mm-3D_ngtdm_Contrast
log-sigma-2-0-mm-3D_ngtdm_Strength
log-sigma-2-0-mm-3D_gldm_DependenceEntropy
log-sigma-2-0-mm-3D_gldm_DependenceNonUniformity
log-sigma-2-0-mm-3D_gldm_DependenceNonUniformityNormalized
log-sigma-2-0-mm-3D_gldm_DependenceVariance
log-sigma-2-0-mm-3D_gldm_GrayLevelNonUniformity
log-sigma-2-0-mm-3D_gldm_GrayLevelVariance
log-sigma-2-0-mm-3D_gldm_HighGrayLevelEmphasis
log-sigma-2-0-mm-3D_gldm_LargeDependenceEmphasis
log-sigma-2-0-mm-3D_gldm_LargeDependenceHighGrayLevelEmphasis
log-sigma-2-0-mm-3D_gldm_LargeDependenceLowGrayLevelEmphasis
log-sigma-2-0-mm-3D_gldm_LowGrayLevelEmphasis
log-sigma-2-0-mm-3D_gldm_SmallDependenceEmphasis
log-sigma-2-0-mm-3D_gldm_SmallDependenceHighGrayLevelEmphasis
log-sigma-2-0-mm-3D_gldm_SmallDependenceLowGrayLevelEmphasis
log-sigma-3-0-mm-3D_firstorder_10Percentile
log-sigma-3-0-mm-3D_firstorder_90Percentile
log-sigma-3-0-mm-3D_firstorder_Energy
log-sigma-3-0-mm-3D_firstorder_Entropy
log-sigma-3-0-mm-3D_firstorder_InterquartileRange
log-sigma-3-0-mm-3D_firstorder_Kurtosis
log-sigma-3-0-mm-3D_firstorder_Maximum
log-sigma-3-0-mm-3D_firstorder_MeanAbsoluteDeviation
log-sigma-3-0-mm-3D_firstorder_Mean
log-sigma-3-0-mm-3D_firstorder_Median
log-sigma-3-0-mm-3D_firstorder_Minimum
log-sigma-3-0-mm-3D_firstorder_Range
log-sigma-3-0-mm-3D_firstorder_RobustMeanAbsoluteDeviation
log-sigma-3-0-mm-3D_firstorder_RootMeanSquared
log-sigma-3-0-mm-3D_firstorder_Skewness
log-sigma-3-0-mm-3D_firstorder_TotalEnergy
log-sigma-3-0-mm-3D_firstorder_Uniformity
log-sigma-3-0-mm-3D_firstorder_Variance

log-sigma-3-0-mm-3D_glcm_Autocorrelation
log-sigma-3-0-mm-3D_glcm_JointAverage
log-sigma-3-0-mm-3D_glcm_ClusterProminence
log-sigma-3-0-mm-3D_glcm_ClusterShade
log-sigma-3-0-mm-3D_glcm_ClusterTendency
log-sigma-3-0-mm-3D_glcm_Contrast
log-sigma-3-0-mm-3D_glcm_Correlation
log-sigma-3-0-mm-3D_glcm_DifferenceAverage
log-sigma-3-0-mm-3D_glcm_DifferenceEntropy
log-sigma-3-0-mm-3D_glcm_DifferenceVariance
log-sigma-3-0-mm-3D_glcm_JointEnergy
log-sigma-3-0-mm-3D_glcm_JointEntropy
log-sigma-3-0-mm-3D_glcm_Imc1
log-sigma-3-0-mm-3D_glcm_Imc2
log-sigma-3-0-mm-3D_glcm_Idm
log-sigma-3-0-mm-3D_glcm_Idmn
log-sigma-3-0-mm-3D_glcm_Id
log-sigma-3-0-mm-3D_glcm_Idn
log-sigma-3-0-mm-3D_glcm_InverseVariance
log-sigma-3-0-mm-3D_glcm_MaximumProbability
log-sigma-3-0-mm-3D_glcm_SumEntropy
log-sigma-3-0-mm-3D_glcm_SumSquares
log-sigma-3-0-mm-3D_glrlm_GrayLevelNonUniformity
log-sigma-3-0-mm-3D_glrlm_GrayLevelNonUniformityNormalized
log-sigma-3-0-mm-3D_glrlm_GrayLevelVariance
log-sigma-3-0-mm-3D_glrlm_HighGrayLevelRunEmphasis
log-sigma-3-0-mm-3D_glrlm_LongRunEmphasis
log-sigma-3-0-mm-3D_glrlm_LongRunHighGrayLevelEmphasis
log-sigma-3-0-mm-3D_glrlm_LongRunLowGrayLevelEmphasis
log-sigma-3-0-mm-3D_glrlm_LowGrayLevelRunEmphasis
log-sigma-3-0-mm-3D_glrlm_RunEntropy
log-sigma-3-0-mm-3D_glrlm_RunLengthNonUniformity
log-sigma-3-0-mm-3D_glrlm_RunLengthNonUniformityNormalized
log-sigma-3-0-mm-3D_glrlm_RunPercentage
log-sigma-3-0-mm-3D_glrlm_RunVariance
log-sigma-3-0-mm-3D_glrlm_ShortRunEmphasis
log-sigma-3-0-mm-3D_glrlm_ShortRunHighGrayLevelEmphasis
log-sigma-3-0-mm-3D_glrlm_ShortRunLowGrayLevelEmphasis
log-sigma-3-0-mm-3D_glszm_GrayLevelNonUniformity
log-sigma-3-0-mm-3D_glszm_GrayLevelNonUniformityNormalized
log-sigma-3-0-mm-3D_glszm_GrayLevelVariance
log-sigma-3-0-mm-3D_glszm_HighGrayLevelZoneEmphasis
log-sigma-3-0-mm-3D_glszm_LargeAreaEmphasis
log-sigma-3-0-mm-3D_glszm_LargeAreaHighGrayLevelEmphasis
log-sigma-3-0-mm-3D_glszm_LargeAreaLowGrayLevelEmphasis

log-sigma-3-0-mm-3D_glszm_LowGrayLevelZoneEmphasis
log-sigma-3-0-mm-3D_glszm_SizeZoneNonUniformity
log-sigma-3-0-mm-3D_glszm_SizeZoneNonUniformityNormalized
log-sigma-3-0-mm-3D_glszm_SmallAreaEmphasis
log-sigma-3-0-mm-3D_glszm_SmallAreaHighGrayLevelEmphasis
log-sigma-3-0-mm-3D_glszm_SmallAreaLowGrayLevelEmphasis
log-sigma-3-0-mm-3D_glszm_ZoneEntropy
log-sigma-3-0-mm-3D_glszm_ZonePercentage
log-sigma-3-0-mm-3D_glszm_ZoneVariance
log-sigma-3-0-mm-3D_ngtdm_Busyness
log-sigma-3-0-mm-3D_ngtdm_Coarseness
log-sigma-3-0-mm-3D_ngtdm_Complexity
log-sigma-3-0-mm-3D_ngtdm_Contrast
log-sigma-3-0-mm-3D_ngtdm_Strength
log-sigma-3-0-mm-3D_gldm_DependenceEntropy
log-sigma-3-0-mm-3D_gldm_DependenceNonUniformity
log-sigma-3-0-mm-3D_gldm_DependenceNonUniformityNormalized
log-sigma-3-0-mm-3D_gldm_DependenceVariance
log-sigma-3-0-mm-3D_gldm_GrayLevelNonUniformity
log-sigma-3-0-mm-3D_gldm_GrayLevelVariance
log-sigma-3-0-mm-3D_gldm_HighGrayLevelEmphasis
log-sigma-3-0-mm-3D_gldm_LargeDependenceEmphasis
log-sigma-3-0-mm-3D_gldm_LargeDependenceHighGrayLevelEmphasis
log-sigma-3-0-mm-3D_gldm_LargeDependenceLowGrayLevelEmphasis
log-sigma-3-0-mm-3D_gldm_LowGrayLevelEmphasis
log-sigma-3-0-mm-3D_gldm_SmallDependenceEmphasis
log-sigma-3-0-mm-3D_gldm_SmallDependenceHighGrayLevelEmphasis
log-sigma-3-0-mm-3D_gldm_SmallDependenceLowGrayLevelEmphasis
log-sigma-4-0-mm-3D_firstorder_10Percentile
log-sigma-4-0-mm-3D_firstorder_90Percentile
log-sigma-4-0-mm-3D_firstorder_Energy
log-sigma-4-0-mm-3D_firstorder_Entropy
log-sigma-4-0-mm-3D_firstorder_InterquartileRange
log-sigma-4-0-mm-3D_firstorder_Kurtosis
log-sigma-4-0-mm-3D_firstorder_Maximum
log-sigma-4-0-mm-3D_firstorder_MeanAbsoluteDeviation
log-sigma-4-0-mm-3D_firstorder_Mean
log-sigma-4-0-mm-3D_firstorder_Median
log-sigma-4-0-mm-3D_firstorder_Minimum
log-sigma-4-0-mm-3D_firstorder_Range
log-sigma-4-0-mm-3D_firstorder_RobustMeanAbsoluteDeviation
log-sigma-4-0-mm-3D_firstorder_RootMeanSquared
log-sigma-4-0-mm-3D_firstorder_Skewness
log-sigma-4-0-mm-3D_firstorder_TotalEnergy
log-sigma-4-0-mm-3D_firstorder_Uniformity

log-sigma-4-0-mm-3D_firstorder_Variance
log-sigma-4-0-mm-3D_glcm_Autocorrelation
log-sigma-4-0-mm-3D_glcm_JointAverage
log-sigma-4-0-mm-3D_glcm_ClusterProminence
log-sigma-4-0-mm-3D_glcm_ClusterShade
log-sigma-4-0-mm-3D_glcm_ClusterTendency
log-sigma-4-0-mm-3D_glcm_Contrast
log-sigma-4-0-mm-3D_glcm_Correlation
log-sigma-4-0-mm-3D_glcm_DifferenceAverage
log-sigma-4-0-mm-3D_glcm_DifferenceEntropy
log-sigma-4-0-mm-3D_glcm_DifferenceVariance
log-sigma-4-0-mm-3D_glcm_JointEnergy
log-sigma-4-0-mm-3D_glcm_JointEntropy
log-sigma-4-0-mm-3D_glcm_Imc1
log-sigma-4-0-mm-3D_glcm_Imc2
log-sigma-4-0-mm-3D_glcm_Idm
log-sigma-4-0-mm-3D_glcm_Idmn
log-sigma-4-0-mm-3D_glcm_Id
log-sigma-4-0-mm-3D_glcm_Idn
log-sigma-4-0-mm-3D_glcm_InverseVariance
log-sigma-4-0-mm-3D_glcm_MaximumProbability
log-sigma-4-0-mm-3D_glcm_SumEntropy
log-sigma-4-0-mm-3D_glcm_SumSquares
log-sigma-4-0-mm-3D_glrlm_GrayLevelNonUniformity
log-sigma-4-0-mm-3D_glrlm_GrayLevelNonUniformityNormalized
log-sigma-4-0-mm-3D_glrlm_GrayLevelVariance
log-sigma-4-0-mm-3D_glrlm_HighGrayLevelRunEmphasis
log-sigma-4-0-mm-3D_glrlm_LongRunEmphasis
log-sigma-4-0-mm-3D_glrlm_LongRunHighGrayLevelEmphasis
log-sigma-4-0-mm-3D_glrlm_LongRunLowGrayLevelEmphasis
log-sigma-4-0-mm-3D_glrlm_LowGrayLevelRunEmphasis
log-sigma-4-0-mm-3D_glrlm_RunEntropy
log-sigma-4-0-mm-3D_glrlm_RunLengthNonUniformity
log-sigma-4-0-mm-3D_glrlm_RunLengthNonUniformityNormalized
log-sigma-4-0-mm-3D_glrlm_RunPercentage
log-sigma-4-0-mm-3D_glrlm_RunVariance
log-sigma-4-0-mm-3D_glrlm_ShortRunEmphasis
log-sigma-4-0-mm-3D_glrlm_ShortRunHighGrayLevelEmphasis
log-sigma-4-0-mm-3D_glrlm_ShortRunLowGrayLevelEmphasis
log-sigma-4-0-mm-3D_glszm_GrayLevelNonUniformity
log-sigma-4-0-mm-3D_glszm_GrayLevelNonUniformityNormalized
log-sigma-4-0-mm-3D_glszm_GrayLevelVariance
log-sigma-4-0-mm-3D_glszm_HighGrayLevelZoneEmphasis
log-sigma-4-0-mm-3D_glszm_LargeAreaEmphasis
log-sigma-4-0-mm-3D_glszm_LargeAreaHighGrayLevelEmphasis

log-sigma-4-0-mm-3D_glszm_LargeAreaLowGrayLevelEmphasis
log-sigma-4-0-mm-3D_glszm_LowGrayLevelZoneEmphasis
log-sigma-4-0-mm-3D_glszm_SizeZoneNonUniformity
log-sigma-4-0-mm-3D_glszm_SizeZoneNonUniformityNormalized
log-sigma-4-0-mm-3D_glszm_SmallAreaEmphasis
log-sigma-4-0-mm-3D_glszm_SmallAreaHighGrayLevelEmphasis
log-sigma-4-0-mm-3D_glszm_SmallAreaLowGrayLevelEmphasis
log-sigma-4-0-mm-3D_glszm_ZoneEntropy
log-sigma-4-0-mm-3D_glszm_ZonePercentage
log-sigma-4-0-mm-3D_glszm_ZoneVariance
log-sigma-4-0-mm-3D_ngtdm_Busyness
log-sigma-4-0-mm-3D_ngtdm_Coarseness
log-sigma-4-0-mm-3D_ngtdm_Complexity
log-sigma-4-0-mm-3D_ngtdm_Contrast
log-sigma-4-0-mm-3D_ngtdm_Strength
log-sigma-4-0-mm-3D_gldm_DependenceEntropy
log-sigma-4-0-mm-3D_gldm_DependenceNonUniformity
log-sigma-4-0-mm-3D_gldm_DependenceNonUniformityNormalized
log-sigma-4-0-mm-3D_gldm_DependenceVariance
log-sigma-4-0-mm-3D_gldm_GrayLevelNonUniformity
log-sigma-4-0-mm-3D_gldm_GrayLevelVariance
log-sigma-4-0-mm-3D_gldm_HighGrayLevelEmphasis
log-sigma-4-0-mm-3D_gldm_LargeDependenceEmphasis
log-sigma-4-0-mm-3D_gldm_LargeDependenceHighGrayLevelEmphasis
log-sigma-4-0-mm-3D_gldm_LargeDependenceLowGrayLevelEmphasis
log-sigma-4-0-mm-3D_gldm_LowGrayLevelEmphasis
log-sigma-4-0-mm-3D_gldm_SmallDependenceEmphasis
log-sigma-4-0-mm-3D_gldm_SmallDependenceHighGrayLevelEmphasis
log-sigma-4-0-mm-3D_gldm_SmallDependenceLowGrayLevelEmphasis
log-sigma-5-0-mm-3D_firstorder_10Percentile
log-sigma-5-0-mm-3D_firstorder_90Percentile
log-sigma-5-0-mm-3D_firstorder_Energy
log-sigma-5-0-mm-3D_firstorder_Entropy
log-sigma-5-0-mm-3D_firstorder_InterquartileRange
log-sigma-5-0-mm-3D_firstorder_Kurtosis
log-sigma-5-0-mm-3D_firstorder_Maximum
log-sigma-5-0-mm-3D_firstorder_MeanAbsoluteDeviation
log-sigma-5-0-mm-3D_firstorder_Mean
log-sigma-5-0-mm-3D_firstorder_Median
log-sigma-5-0-mm-3D_firstorder_Minimum
log-sigma-5-0-mm-3D_firstorder_Range
log-sigma-5-0-mm-3D_firstorder_RobustMeanAbsoluteDeviation
log-sigma-5-0-mm-3D_firstorder_RootMeanSquared
log-sigma-5-0-mm-3D_firstorder_Skewness
log-sigma-5-0-mm-3D_firstorder_TotalEnergy

log-sigma-5-0-mm-3D_firstorder_Uniformity
log-sigma-5-0-mm-3D_firstorder_Variance
log-sigma-5-0-mm-3D_glcm_Autocorrelation
log-sigma-5-0-mm-3D_glcm_JointAverage
log-sigma-5-0-mm-3D_glcm_ClusterProminence
log-sigma-5-0-mm-3D_glcm_ClusterShade
log-sigma-5-0-mm-3D_glcm_ClusterTendency
log-sigma-5-0-mm-3D_glcm_Contrast
log-sigma-5-0-mm-3D_glcm_Correlation
log-sigma-5-0-mm-3D_glcm_DifferenceAverage
log-sigma-5-0-mm-3D_glcm_DifferenceEntropy
log-sigma-5-0-mm-3D_glcm_DifferenceVariance
log-sigma-5-0-mm-3D_glcm_JointEnergy
log-sigma-5-0-mm-3D_glcm_JointEntropy
log-sigma-5-0-mm-3D_glcm_Imc1
log-sigma-5-0-mm-3D_glcm_Imc2
log-sigma-5-0-mm-3D_glcm_Idm
log-sigma-5-0-mm-3D_glcm_Idmn
log-sigma-5-0-mm-3D_glcm_Id
log-sigma-5-0-mm-3D_glcm_Idn
log-sigma-5-0-mm-3D_glcm_InverseVariance
log-sigma-5-0-mm-3D_glcm_MaximumProbability
log-sigma-5-0-mm-3D_glcm_SumEntropy
log-sigma-5-0-mm-3D_glcm_SumSquares
log-sigma-5-0-mm-3D_glrlm_GrayLevelNonUniformity
log-sigma-5-0-mm-3D_glrlm_GrayLevelNonUniformityNormalized
log-sigma-5-0-mm-3D_glrlm_GrayLevelVariance
log-sigma-5-0-mm-3D_glrlm_HighGrayLevelRunEmphasis
log-sigma-5-0-mm-3D_glrlm_LongRunEmphasis
log-sigma-5-0-mm-3D_glrlm_LongRunHighGrayLevelEmphasis
log-sigma-5-0-mm-3D_glrlm_LongRunLowGrayLevelEmphasis
log-sigma-5-0-mm-3D_glrlm_LowGrayLevelRunEmphasis
log-sigma-5-0-mm-3D_glrlm_RunEntropy
log-sigma-5-0-mm-3D_glrlm_RunLengthNonUniformity
log-sigma-5-0-mm-3D_glrlm_RunLengthNonUniformityNormalized
log-sigma-5-0-mm-3D_glrlm_RunPercentage
log-sigma-5-0-mm-3D_glrlm_RunVariance
log-sigma-5-0-mm-3D_glrlm_ShortRunEmphasis
log-sigma-5-0-mm-3D_glrlm_ShortRunHighGrayLevelEmphasis
log-sigma-5-0-mm-3D_glrlm_ShortRunLowGrayLevelEmphasis
log-sigma-5-0-mm-3D_glszm_GrayLevelNonUniformity
log-sigma-5-0-mm-3D_glszm_GrayLevelNonUniformityNormalized
log-sigma-5-0-mm-3D_glszm_GrayLevelVariance
log-sigma-5-0-mm-3D_glszm_HighGrayLevelZoneEmphasis
log-sigma-5-0-mm-3D_glszm_LargeAreaEmphasis

log-sigma-5-0-mm-3D_glszm_LargeAreaHighGrayLevelEmphasis
log-sigma-5-0-mm-3D_glszm_LargeAreaLowGrayLevelEmphasis
log-sigma-5-0-mm-3D_glszm_LowGrayLevelZoneEmphasis
log-sigma-5-0-mm-3D_glszm_SizeZoneNonUniformity
log-sigma-5-0-mm-3D_glszm_SizeZoneNonUniformityNormalized
log-sigma-5-0-mm-3D_glszm_SmallAreaEmphasis
log-sigma-5-0-mm-3D_glszm_SmallAreaHighGrayLevelEmphasis
log-sigma-5-0-mm-3D_glszm_SmallAreaLowGrayLevelEmphasis
log-sigma-5-0-mm-3D_glszm_ZoneEntropy
log-sigma-5-0-mm-3D_glszm_ZonePercentage
log-sigma-5-0-mm-3D_glszm_ZoneVariance
log-sigma-5-0-mm-3D_ngtdm_Busyness
log-sigma-5-0-mm-3D_ngtdm_Coarseness
log-sigma-5-0-mm-3D_ngtdm_Complexity
log-sigma-5-0-mm-3D_ngtdm_Contrast
log-sigma-5-0-mm-3D_ngtdm_Strength
log-sigma-5-0-mm-3D_gldm_DependenceEntropy
log-sigma-5-0-mm-3D_gldm_DependenceNonUniformity
log-sigma-5-0-mm-3D_gldm_DependenceNonUniformityNormalized
log-sigma-5-0-mm-3D_gldm_DependenceVariance
log-sigma-5-0-mm-3D_gldm_GrayLevelNonUniformity
log-sigma-5-0-mm-3D_gldm_GrayLevelVariance
log-sigma-5-0-mm-3D_gldm_HighGrayLevelEmphasis
log-sigma-5-0-mm-3D_gldm_LargeDependenceEmphasis
log-sigma-5-0-mm-3D_gldm_LargeDependenceHighGrayLevelEmphasis
log-sigma-5-0-mm-3D_gldm_LargeDependenceLowGrayLevelEmphasis
log-sigma-5-0-mm-3D_gldm_LowGrayLevelEmphasis
log-sigma-5-0-mm-3D_gldm_SmallDependenceEmphasis
log-sigma-5-0-mm-3D_gldm_SmallDependenceHighGrayLevelEmphasis
log-sigma-5-0-mm-3D_gldm_SmallDependenceLowGrayLevelEmphasis
wavelet-LLH_firstorder_10Percentile
wavelet-LLH_firstorder_90Percentile
wavelet-LLH_firstorder_Energy
wavelet-LLH_firstorder_Entropy
wavelet-LLH_firstorder_InterquartileRange
wavelet-LLH_firstorder_Kurtosis
wavelet-LLH_firstorder_Maximum
wavelet-LLH_firstorder_MeanAbsoluteDeviation
wavelet-LLH_firstorder_Mean
wavelet-LLH_firstorder_Median
wavelet-LLH_firstorder_Minimum
wavelet-LLH_firstorder_Range
wavelet-LLH_firstorder_RobustMeanAbsoluteDeviation
wavelet-LLH_firstorder_RootMeanSquared
wavelet-LLH_firstorder_Skewness

wavelet-LLH_firstorder_TotalEnergy
wavelet-LLH_firstorder_Uniformity
wavelet-LLH_firstorder_Variance
wavelet-LLH_glcm_Autocorrelation
wavelet-LLH_glcm_JointAverage
wavelet-LLH_glcm_ClusterProminence
wavelet-LLH_glcm_ClusterShade
wavelet-LLH_glcm_ClusterTendency
wavelet-LLH_glcm_Contrast
wavelet-LLH_glcm_Correlation
wavelet-LLH_glcm_DifferenceAverage
wavelet-LLH_glcm_DifferenceEntropy
wavelet-LLH_glcm_DifferenceVariance
wavelet-LLH_glcm_JointEnergy
wavelet-LLH_glcm_JointEntropy
wavelet-LLH_glcm_Imc1
wavelet-LLH_glcm_Imc2
wavelet-LLH_glcm_Idm
wavelet-LLH_glcm_Idmn
wavelet-LLH_glcm_Id
wavelet-LLH_glcm_Idn
wavelet-LLH_glcm_InverseVariance
wavelet-LLH_glcm_MaximumProbability
wavelet-LLH_glcm_SumEntropy
wavelet-LLH_glcm_SumSquares
wavelet-LLH_glrlm_GrayLevelNonUniformity
wavelet-LLH_glrlm_GrayLevelNonUniformityNormalized
wavelet-LLH_glrlm_GrayLevelVariance
wavelet-LLH_glrlm_HighGrayLevelRunEmphasis
wavelet-LLH_glrlm_LongRunEmphasis
wavelet-LLH_glrlm_LongRunHighGrayLevelEmphasis
wavelet-LLH_glrlm_LongRunLowGrayLevelEmphasis
wavelet-LLH_glrlm_LowGrayLevelRunEmphasis
wavelet-LLH_glrlm_RunEntropy
wavelet-LLH_glrlm_RunLengthNonUniformity
wavelet-LLH_glrlm_RunLengthNonUniformityNormalized
wavelet-LLH_glrlm_RunPercentage
wavelet-LLH_glrlm_RunVariance
wavelet-LLH_glrlm_ShortRunEmphasis
wavelet-LLH_glrlm_ShortRunHighGrayLevelEmphasis
wavelet-LLH_glrlm_ShortRunLowGrayLevelEmphasis
wavelet-LLH_glszm_GrayLevelNonUniformity
wavelet-LLH_glszm_GrayLevelNonUniformityNormalized
wavelet-LLH_glszm_GrayLevelVariance
wavelet-LLH_glszm_HighGrayLevelZoneEmphasis

wavelet-LLH_glszm_LargeAreaEmphasis
wavelet-LLH_glszm_LargeAreaHighGrayLevelEmphasis
wavelet-LLH_glszm_LargeAreaLowGrayLevelEmphasis
wavelet-LLH_glszm_LowGrayLevelZoneEmphasis
wavelet-LLH_glszm_SizeZoneNonUniformity
wavelet-LLH_glszm_SizeZoneNonUniformityNormalized
wavelet-LLH_glszm_SmallAreaEmphasis
wavelet-LLH_glszm_SmallAreaHighGrayLevelEmphasis
wavelet-LLH_glszm_SmallAreaLowGrayLevelEmphasis
wavelet-LLH_glszm_ZoneEntropy
wavelet-LLH_glszm_ZonePercentage
wavelet-LLH_glszm_ZoneVariance
wavelet-LLH_ngtdm_Busyness
wavelet-LLH_ngtdm_Coarseness
wavelet-LLH_ngtdm_Complexity
wavelet-LLH_ngtdm_Contrast
wavelet-LLH_ngtdm_Strength
wavelet-LLH_gldm_DependenceEntropy
wavelet-LLH_gldm_DependenceNonUniformity
wavelet-LLH_gldm_DependenceNonUniformityNormalized
wavelet-LLH_gldm_DependenceVariance
wavelet-LLH_gldm_GrayLevelNonUniformity
wavelet-LLH_gldm_GrayLevelVariance
wavelet-LLH_gldm_HighGrayLevelEmphasis
wavelet-LLH_gldm_LargeDependenceEmphasis
wavelet-LLH_gldm_LargeDependenceHighGrayLevelEmphasis
wavelet-LLH_gldm_LargeDependenceLowGrayLevelEmphasis
wavelet-LLH_gldm_LowGrayLevelEmphasis
wavelet-LLH_gldm_SmallDependenceEmphasis
wavelet-LLH_gldm_SmallDependenceHighGrayLevelEmphasis
wavelet-LLH_gldm_SmallDependenceLowGrayLevelEmphasis
wavelet-LHL_firstorder_10Percentile
wavelet-LHL_firstorder_90Percentile
wavelet-LHL_firstorder_Energy
wavelet-LHL_firstorder_Entropy
wavelet-LHL_firstorder_InterquartileRange
wavelet-LHL_firstorder_Kurtosis
wavelet-LHL_firstorder_Maximum
wavelet-LHL_firstorder_MeanAbsoluteDeviation
wavelet-LHL_firstorder_Mean
wavelet-LHL_firstorder_Median
wavelet-LHL_firstorder_Minimum
wavelet-LHL_firstorder_Range
wavelet-LHL_firstorder_RobustMeanAbsoluteDeviation
wavelet-LHL_firstorder_RootMeanSquared

wavelet-LHL_firstorder_Skewness
wavelet-LHL_firstorder_TotalEnergy
wavelet-LHL_firstorder_Uniformity
wavelet-LHL_firstorder_Variance
wavelet-LHL_glcm_Autocorrelation
wavelet-LHL_glcm_JointAverage
wavelet-LHL_glcm_ClusterProminence
wavelet-LHL_glcm_ClusterShade
wavelet-LHL_glcm_ClusterTendency
wavelet-LHL_glcm_Contrast
wavelet-LHL_glcm_Correlation
wavelet-LHL_glcm_DifferenceAverage
wavelet-LHL_glcm_DifferenceEntropy
wavelet-LHL_glcm_DifferenceVariance
wavelet-LHL_glcm_JointEnergy
wavelet-LHL_glcm_JointEntropy
wavelet-LHL_glcm_Imc1
wavelet-LHL_glcm_Imc2
wavelet-LHL_glcm_Idm
wavelet-LHL_glcm_Idmn
wavelet-LHL_glcm_Id
wavelet-LHL_glcm_Idn
wavelet-LHL_glcm_InverseVariance
wavelet-LHL_glcm_MaximumProbability
wavelet-LHL_glcm_SumEntropy
wavelet-LHL_glcm_SumSquares
wavelet-LHL_glrlm_GrayLevelNonUniformity
wavelet-LHL_glrlm_GrayLevelNonUniformityNormalized
wavelet-LHL_glrlm_GrayLevelVariance
wavelet-LHL_glrlm_HighGrayLevelRunEmphasis
wavelet-LHL_glrlm_LongRunEmphasis
wavelet-LHL_glrlm_LongRunHighGrayLevelEmphasis
wavelet-LHL_glrlm_LongRunLowGrayLevelEmphasis
wavelet-LHL_glrlm_LowGrayLevelRunEmphasis
wavelet-LHL_glrlm_RunEntropy
wavelet-LHL_glrlm_RunLengthNonUniformity
wavelet-LHL_glrlm_RunLengthNonUniformityNormalized
wavelet-LHL_glrlm_RunPercentage
wavelet-LHL_glrlm_RunVariance
wavelet-LHL_glrlm_ShortRunEmphasis
wavelet-LHL_glrlm_ShortRunHighGrayLevelEmphasis
wavelet-LHL_glrlm_ShortRunLowGrayLevelEmphasis
wavelet-LHL_glszm_GrayLevelNonUniformity
wavelet-LHL_glszm_GrayLevelNonUniformityNormalized
wavelet-LHL_glszm_GrayLevelVariance

wavelet-LHL_glszm_HighGrayLevelZoneEmphasis
wavelet-LHL_glszm_LargeAreaEmphasis
wavelet-LHL_glszm_LargeAreaHighGrayLevelEmphasis
wavelet-LHL_glszm_LargeAreaLowGrayLevelEmphasis
wavelet-LHL_glszm_LowGrayLevelZoneEmphasis
wavelet-LHL_glszm_SizeZoneNonUniformity
wavelet-LHL_glszm_SizeZoneNonUniformityNormalized
wavelet-LHL_glszm_SmallAreaEmphasis
wavelet-LHL_glszm_SmallAreaHighGrayLevelEmphasis
wavelet-LHL_glszm_SmallAreaLowGrayLevelEmphasis
wavelet-LHL_glszm_ZoneEntropy
wavelet-LHL_glszm_ZonePercentage
wavelet-LHL_glszm_ZoneVariance
wavelet-LHL_ngtdm_Busyness
wavelet-LHL_ngtdm_Coarseness
wavelet-LHL_ngtdm_Complexity
wavelet-LHL_ngtdm_Contrast
wavelet-LHL_ngtdm_Strength
wavelet-LHL_gldm_DependenceEntropy
wavelet-LHL_gldm_DependenceNonUniformity
wavelet-LHL_gldm_DependenceNonUniformityNormalized
wavelet-LHL_gldm_DependenceVariance
wavelet-LHL_gldm_GrayLevelNonUniformity
wavelet-LHL_gldm_GrayLevelVariance
wavelet-LHL_gldm_HighGrayLevelEmphasis
wavelet-LHL_gldm_LargeDependenceEmphasis
wavelet-LHL_gldm_LargeDependenceHighGrayLevelEmphasis
wavelet-LHL_gldm_LargeDependenceLowGrayLevelEmphasis
wavelet-LHL_gldm_LowGrayLevelEmphasis
wavelet-LHL_gldm_SmallDependenceEmphasis
wavelet-LHL_gldm_SmallDependenceHighGrayLevelEmphasis
wavelet-LHL_gldm_SmallDependenceLowGrayLevelEmphasis
wavelet-LHH_firstorder_10Percentile
wavelet-LHH_firstorder_90Percentile
wavelet-LHH_firstorder_Energy
wavelet-LHH_firstorder_Entropy
wavelet-LHH_firstorder_InterquartileRange
wavelet-LHH_firstorder_Kurtosis
wavelet-LHH_firstorder_Maximum
wavelet-LHH_firstorder_MeanAbsoluteDeviation
wavelet-LHH_firstorder_Mean
wavelet-LHH_firstorder_Median
wavelet-LHH_firstorder_Minimum
wavelet-LHH_firstorder_Range
wavelet-LHH_firstorder_RobustMeanAbsoluteDeviation

wavelet-LHH_firstorder_RootMeanSquared
wavelet-LHH_firstorder_Skewness
wavelet-LHH_firstorder_TotalEnergy
wavelet-LHH_firstorder_Uniformity
wavelet-LHH_firstorder_Variance
wavelet-LHH_glcm_Autocorrelation
wavelet-LHH_glcm_JointAverage
wavelet-LHH_glcm_ClusterProminence
wavelet-LHH_glcm_ClusterShade
wavelet-LHH_glcm_ClusterTendency
wavelet-LHH_glcm_Contrast
wavelet-LHH_glcm_Correlation
wavelet-LHH_glcm_DifferenceAverage
wavelet-LHH_glcm_DifferenceEntropy
wavelet-LHH_glcm_DifferenceVariance
wavelet-LHH_glcm_JointEnergy
wavelet-LHH_glcm_JointEntropy
wavelet-LHH_glcm_Imc1
wavelet-LHH_glcm_Imc2
wavelet-LHH_glcm_Idm
wavelet-LHH_glcm_Idmn
wavelet-LHH_glcm_Id
wavelet-LHH_glcm_Idn
wavelet-LHH_glcm_InverseVariance
wavelet-LHH_glcm_MaximumProbability
wavelet-LHH_glcm_SumEntropy
wavelet-LHH_glcm_SumSquares
wavelet-LHH_glrlm_GrayLevelNonUniformity
wavelet-LHH_glrlm_GrayLevelNonUniformityNormalized
wavelet-LHH_glrlm_GrayLevelVariance
wavelet-LHH_glrlm_HighGrayLevelRunEmphasis
wavelet-LHH_glrlm_LongRunEmphasis
wavelet-LHH_glrlm_LongRunHighGrayLevelEmphasis
wavelet-LHH_glrlm_LongRunLowGrayLevelEmphasis
wavelet-LHH_glrlm_LowGrayLevelRunEmphasis
wavelet-LHH_glrlm_RunEntropy
wavelet-LHH_glrlm_RunLengthNonUniformity
wavelet-LHH_glrlm_RunLengthNonUniformityNormalized
wavelet-LHH_glrlm_RunPercentage
wavelet-LHH_glrlm_RunVariance
wavelet-LHH_glrlm_ShortRunEmphasis
wavelet-LHH_glrlm_ShortRunHighGrayLevelEmphasis
wavelet-LHH_glrlm_ShortRunLowGrayLevelEmphasis
wavelet-LHH_glszm_GrayLevelNonUniformity
wavelet-LHH_glszm_GrayLevelNonUniformityNormalized

wavelet-LHH_glszm_GrayLevelVariance
wavelet-LHH_glszm_HighGrayLevelZoneEmphasis
wavelet-LHH_glszm_LargeAreaEmphasis
wavelet-LHH_glszm_LargeAreaHighGrayLevelEmphasis
wavelet-LHH_glszm_LargeAreaLowGrayLevelEmphasis
wavelet-LHH_glszm_LowGrayLevelZoneEmphasis
wavelet-LHH_glszm_SizeZoneNonUniformity
wavelet-LHH_glszm_SizeZoneNonUniformityNormalized
wavelet-LHH_glszm_SmallAreaEmphasis
wavelet-LHH_glszm_SmallAreaHighGrayLevelEmphasis
wavelet-LHH_glszm_SmallAreaLowGrayLevelEmphasis
wavelet-LHH_glszm_ZoneEntropy
wavelet-LHH_glszm_ZonePercentage
wavelet-LHH_glszm_ZoneVariance
wavelet-LHH_ngtdm_Busyness
wavelet-LHH_ngtdm_Coarseness
wavelet-LHH_ngtdm_Complexity
wavelet-LHH_ngtdm_Contrast
wavelet-LHH_ngtdm_Strength
wavelet-LHH_gldm_DependenceEntropy
wavelet-LHH_gldm_DependenceNonUniformity
wavelet-LHH_gldm_DependenceNonUniformityNormalized
wavelet-LHH_gldm_DependenceVariance
wavelet-LHH_gldm_GrayLevelNonUniformity
wavelet-LHH_gldm_GrayLevelVariance
wavelet-LHH_gldm_HighGrayLevelEmphasis
wavelet-LHH_gldm_LargeDependenceEmphasis
wavelet-LHH_gldm_LargeDependenceHighGrayLevelEmphasis
wavelet-LHH_gldm_LargeDependenceLowGrayLevelEmphasis
wavelet-LHH_gldm_LowGrayLevelEmphasis
wavelet-LHH_gldm_SmallDependenceEmphasis
wavelet-LHH_gldm_SmallDependenceHighGrayLevelEmphasis
wavelet-LHH_gldm_SmallDependenceLowGrayLevelEmphasis
wavelet-HLL_firstorder_10Percentile
wavelet-HLL_firstorder_90Percentile
wavelet-HLL_firstorder_Energy
wavelet-HLL_firstorder_Entropy
wavelet-HLL_firstorder_InterquartileRange
wavelet-HLL_firstorder_Kurtosis
wavelet-HLL_firstorder_Maximum
wavelet-HLL_firstorder_MeanAbsoluteDeviation
wavelet-HLL_firstorder_Mean
wavelet-HLL_firstorder_Median
wavelet-HLL_firstorder_Minimum
wavelet-HLL_firstorder_Range

wavelet-HLL_firstorder_RobustMeanAbsoluteDeviation
wavelet-HLL_firstorder_RootMeanSquared
wavelet-HLL_firstorder_Skewness
wavelet-HLL_firstorder_TotalEnergy
wavelet-HLL_firstorder_Uniformity
wavelet-HLL_firstorder_Variance
wavelet-HLL_glcm_Autocorrelation
wavelet-HLL_glcm_JointAverage
wavelet-HLL_glcm_ClusterProminence
wavelet-HLL_glcm_ClusterShade
wavelet-HLL_glcm_ClusterTendency
wavelet-HLL_glcm_Contrast
wavelet-HLL_glcm_Correlation
wavelet-HLL_glcm_DifferenceAverage
wavelet-HLL_glcm_DifferenceEntropy
wavelet-HLL_glcm_DifferenceVariance
wavelet-HLL_glcm_JointEnergy
wavelet-HLL_glcm_JointEntropy
wavelet-HLL_glcm_Imc1
wavelet-HLL_glcm_Imc2
wavelet-HLL_glcm_Idm
wavelet-HLL_glcm_Idmn
wavelet-HLL_glcm_Id
wavelet-HLL_glcm_Idn
wavelet-HLL_glcm_InverseVariance
wavelet-HLL_glcm_MaximumProbability
wavelet-HLL_glcm_SumEntropy
wavelet-HLL_glcm_SumSquares
wavelet-HLL_glrlm_GrayLevelNonUniformity
wavelet-HLL_glrlm_GrayLevelNonUniformityNormalized
wavelet-HLL_glrlm_GrayLevelVariance
wavelet-HLL_glrlm_HighGrayLevelRunEmphasis
wavelet-HLL_glrlm_LongRunEmphasis
wavelet-HLL_glrlm_LongRunHighGrayLevelEmphasis
wavelet-HLL_glrlm_LongRunLowGrayLevelEmphasis
wavelet-HLL_glrlm_LowGrayLevelRunEmphasis
wavelet-HLL_glrlm_RunEntropy
wavelet-HLL_glrlm_RunLengthNonUniformity
wavelet-HLL_glrlm_RunLengthNonUniformityNormalized
wavelet-HLL_glrlm_RunPercentage
wavelet-HLL_glrlm_RunVariance
wavelet-HLL_glrlm_ShortRunEmphasis
wavelet-HLL_glrlm_ShortRunHighGrayLevelEmphasis
wavelet-HLL_glrlm_ShortRunLowGrayLevelEmphasis
wavelet-HLL_glszm_GrayLevelNonUniformity

wavelet-HLL_glszm_GrayLevelNonUniformityNormalized
wavelet-HLL_glszm_GrayLevelVariance
wavelet-HLL_glszm_HighGrayLevelZoneEmphasis
wavelet-HLL_glszm_LargeAreaEmphasis
wavelet-HLL_glszm_LargeAreaHighGrayLevelEmphasis
wavelet-HLL_glszm_LargeAreaLowGrayLevelEmphasis
wavelet-HLL_glszm_LowGrayLevelZoneEmphasis
wavelet-HLL_glszm_SizeZoneNonUniformity
wavelet-HLL_glszm_SizeZoneNonUniformityNormalized
wavelet-HLL_glszm_SmallAreaEmphasis
wavelet-HLL_glszm_SmallAreaHighGrayLevelEmphasis
wavelet-HLL_glszm_SmallAreaLowGrayLevelEmphasis
wavelet-HLL_glszm_ZoneEntropy
wavelet-HLL_glszm_ZonePercentage
wavelet-HLL_glszm_ZoneVariance
wavelet-HLL_ngtdm_Busyness
wavelet-HLL_ngtdm_Coarseness
wavelet-HLL_ngtdm_Complexity
wavelet-HLL_ngtdm_Contrast
wavelet-HLL_ngtdm_Strength
wavelet-HLL_gldm_DependenceEntropy
wavelet-HLL_gldm_DependenceNonUniformity
wavelet-HLL_gldm_DependenceNonUniformityNormalized
wavelet-HLL_gldm_DependenceVariance
wavelet-HLL_gldm_GrayLevelNonUniformity
wavelet-HLL_gldm_GrayLevelVariance
wavelet-HLL_gldm_HighGrayLevelEmphasis
wavelet-HLL_gldm_LargeDependenceEmphasis
wavelet-HLL_gldm_LargeDependenceHighGrayLevelEmphasis
wavelet-HLL_gldm_LargeDependenceLowGrayLevelEmphasis
wavelet-HLL_gldm_LowGrayLevelEmphasis
wavelet-HLL_gldm_SmallDependenceEmphasis
wavelet-HLL_gldm_SmallDependenceHighGrayLevelEmphasis
wavelet-HLL_gldm_SmallDependenceLowGrayLevelEmphasis
wavelet-HLH_firstorder_10Percentile
wavelet-HLH_firstorder_90Percentile
wavelet-HLH_firstorder_Energy
wavelet-HLH_firstorder_Entropy
wavelet-HLH_firstorder_InterquartileRange
wavelet-HLH_firstorder_Kurtosis
wavelet-HLH_firstorder_Maximum
wavelet-HLH_firstorder_MeanAbsoluteDeviation
wavelet-HLH_firstorder_Mean
wavelet-HLH_firstorder_Median
wavelet-HLH_firstorder_Minimum

wavelet-HLH_firstorder_Range
wavelet-HLH_firstorder_RobustMeanAbsoluteDeviation
wavelet-HLH_firstorder_RootMeanSquared
wavelet-HLH_firstorder_Skewness
wavelet-HLH_firstorder_TotalEnergy
wavelet-HLH_firstorder_Uniformity
wavelet-HLH_firstorder_Variance
wavelet-HLH_glcm_Autocorrelation
wavelet-HLH_glcm_JointAverage
wavelet-HLH_glcm_ClusterProminence
wavelet-HLH_glcm_ClusterShade
wavelet-HLH_glcm_ClusterTendency
wavelet-HLH_glcm_Contrast
wavelet-HLH_glcm_Correlation
wavelet-HLH_glcm_DifferenceAverage
wavelet-HLH_glcm_DifferenceEntropy
wavelet-HLH_glcm_DifferenceVariance
wavelet-HLH_glcm_JointEnergy
wavelet-HLH_glcm_JointEntropy
wavelet-HLH_glcm_Imc1
wavelet-HLH_glcm_Imc2
wavelet-HLH_glcm_Idm
wavelet-HLH_glcm_Idmn
wavelet-HLH_glcm_Id
wavelet-HLH_glcm_Idn
wavelet-HLH_glcm_InverseVariance
wavelet-HLH_glcm_MaximumProbability
wavelet-HLH_glcm_SumEntropy
wavelet-HLH_glcm_SumSquares
wavelet-HLH_glrlm_GrayLevelNonUniformity
wavelet-HLH_glrlm_GrayLevelNonUniformityNormalized
wavelet-HLH_glrlm_GrayLevelVariance
wavelet-HLH_glrlm_HighGrayLevelRunEmphasis
wavelet-HLH_glrlm_LongRunEmphasis
wavelet-HLH_glrlm_LongRunHighGrayLevelEmphasis
wavelet-HLH_glrlm_LongRunLowGrayLevelEmphasis
wavelet-HLH_glrlm_LowGrayLevelRunEmphasis
wavelet-HLH_glrlm_RunEntropy
wavelet-HLH_glrlm_RunLengthNonUniformity
wavelet-HLH_glrlm_RunLengthNonUniformityNormalized
wavelet-HLH_glrlm_RunPercentage
wavelet-HLH_glrlm_RunVariance
wavelet-HLH_glrlm_ShortRunEmphasis
wavelet-HLH_glrlm_ShortRunHighGrayLevelEmphasis
wavelet-HLH_glrlm_ShortRunLowGrayLevelEmphasis

wavelet-HLH_glszm_GrayLevelNonUniformity
wavelet-HLH_glszm_GrayLevelNonUniformityNormalized
wavelet-HLH_glszm_GrayLevelVariance
wavelet-HLH_glszm_HighGrayLevelZoneEmphasis
wavelet-HLH_glszm_LargeAreaEmphasis
wavelet-HLH_glszm_LargeAreaHighGrayLevelEmphasis
wavelet-HLH_glszm_LargeAreaLowGrayLevelEmphasis
wavelet-HLH_glszm_LowGrayLevelZoneEmphasis
wavelet-HLH_glszm_SizeZoneNonUniformity
wavelet-HLH_glszm_SizeZoneNonUniformityNormalized
wavelet-HLH_glszm_SmallAreaEmphasis
wavelet-HLH_glszm_SmallAreaHighGrayLevelEmphasis
wavelet-HLH_glszm_SmallAreaLowGrayLevelEmphasis
wavelet-HLH_glszm_ZoneEntropy
wavelet-HLH_glszm_ZonePercentage
wavelet-HLH_glszm_ZoneVariance
wavelet-HLH_ngtdm_Busyness
wavelet-HLH_ngtdm_Coarseness
wavelet-HLH_ngtdm_Complexity
wavelet-HLH_ngtdm_Contrast
wavelet-HLH_ngtdm_Strength
wavelet-HLH_gldm_DependenceEntropy
wavelet-HLH_gldm_DependenceNonUniformity
wavelet-HLH_gldm_DependenceNonUniformityNormalized
wavelet-HLH_gldm_DependenceVariance
wavelet-HLH_gldm_GrayLevelNonUniformity
wavelet-HLH_gldm_GrayLevelVariance
wavelet-HLH_gldm_HighGrayLevelEmphasis
wavelet-HLH_gldm_LargeDependenceEmphasis
wavelet-HLH_gldm_LargeDependenceHighGrayLevelEmphasis
wavelet-HLH_gldm_LargeDependenceLowGrayLevelEmphasis
wavelet-HLH_gldm_LowGrayLevelEmphasis
wavelet-HLH_gldm_SmallDependenceEmphasis
wavelet-HLH_gldm_SmallDependenceHighGrayLevelEmphasis
wavelet-HLH_gldm_SmallDependenceLowGrayLevelEmphasis
wavelet-HHL_firstorder_10Percentile
wavelet-HHL_firstorder_90Percentile
wavelet-HHL_firstorder_Energy
wavelet-HHL_firstorder_Entropy
wavelet-HHL_firstorder_InterquartileRange
wavelet-HHL_firstorder_Kurtosis
wavelet-HHL_firstorder_Maximum
wavelet-HHL_firstorder_MeanAbsoluteDeviation
wavelet-HHL_firstorder_Mean
wavelet-HHL_firstorder_Median

wavelet-HHL_firstorder_Minimum
wavelet-HHL_firstorder_Range
wavelet-HHL_firstorder_RobustMeanAbsoluteDeviation
wavelet-HHL_firstorder_RootMeanSquared
wavelet-HHL_firstorder_Skewness
wavelet-HHL_firstorder_TotalEnergy
wavelet-HHL_firstorder_Uniformity
wavelet-HHL_firstorder_Variance
wavelet-HHL_glcm_Autocorrelation
wavelet-HHL_glcm_JointAverage
wavelet-HHL_glcm_ClusterProminence
wavelet-HHL_glcm_ClusterShade
wavelet-HHL_glcm_ClusterTendency
wavelet-HHL_glcm_Contrast
wavelet-HHL_glcm_Correlation
wavelet-HHL_glcm_DifferenceAverage
wavelet-HHL_glcm_DifferenceEntropy
wavelet-HHL_glcm_DifferenceVariance
wavelet-HHL_glcm_JointEnergy
wavelet-HHL_glcm_JointEntropy
wavelet-HHL_glcm_Imc1
wavelet-HHL_glcm_Imc2
wavelet-HHL_glcm_Idm
wavelet-HHL_glcm_Idmn
wavelet-HHL_glcm_Id
wavelet-HHL_glcm_Idn
wavelet-HHL_glcm_InverseVariance
wavelet-HHL_glcm_MaximumProbability
wavelet-HHL_glcm_SumEntropy
wavelet-HHL_glcm_SumSquares
wavelet-HHL_glrlm_GrayLevelNonUniformity
wavelet-HHL_glrlm_GrayLevelNonUniformityNormalized
wavelet-HHL_glrlm_GrayLevelVariance
wavelet-HHL_glrlm_HighGrayLevelRunEmphasis
wavelet-HHL_glrlm_LongRunEmphasis
wavelet-HHL_glrlm_LongRunHighGrayLevelEmphasis
wavelet-HHL_glrlm_LongRunLowGrayLevelEmphasis
wavelet-HHL_glrlm_LowGrayLevelRunEmphasis
wavelet-HHL_glrlm_RunEntropy
wavelet-HHL_glrlm_RunLengthNonUniformity
wavelet-HHL_glrlm_RunLengthNonUniformityNormalized
wavelet-HHL_glrlm_RunPercentage
wavelet-HHL_glrlm_RunVariance
wavelet-HHL_glrlm_ShortRunEmphasis
wavelet-HHL_glrlm_ShortRunHighGrayLevelEmphasis

wavelet-HHL_glrlm_ShortRunLowGrayLevelEmphasis
wavelet-HHL_glszm_GrayLevelNonUniformity
wavelet-HHL_glszm_GrayLevelNonUniformityNormalized
wavelet-HHL_glszm_GrayLevelVariance
wavelet-HHL_glszm_HighGrayLevelZoneEmphasis
wavelet-HHL_glszm_LargeAreaEmphasis
wavelet-HHL_glszm_LargeAreaHighGrayLevelEmphasis
wavelet-HHL_glszm_LargeAreaLowGrayLevelEmphasis
wavelet-HHL_glszm_LowGrayLevelZoneEmphasis
wavelet-HHL_glszm_SizeZoneNonUniformity
wavelet-HHL_glszm_SizeZoneNonUniformityNormalized
wavelet-HHL_glszm_SmallAreaEmphasis
wavelet-HHL_glszm_SmallAreaHighGrayLevelEmphasis
wavelet-HHL_glszm_SmallAreaLowGrayLevelEmphasis
wavelet-HHL_glszm_ZoneEntropy
wavelet-HHL_glszm_ZonePercentage
wavelet-HHL_glszm_ZoneVariance
wavelet-HHL_ngtdm_Busyness
wavelet-HHL_ngtdm_Coarseness
wavelet-HHL_ngtdm_Complexity
wavelet-HHL_ngtdm_Contrast
wavelet-HHL_ngtdm_Strength
wavelet-HHL_gldm_DependenceEntropy
wavelet-HHL_gldm_DependenceNonUniformity
wavelet-HHL_gldm_DependenceNonUniformityNormalized
wavelet-HHL_gldm_DependenceVariance
wavelet-HHL_gldm_GrayLevelNonUniformity
wavelet-HHL_gldm_GrayLevelVariance
wavelet-HHL_gldm_HighGrayLevelEmphasis
wavelet-HHL_gldm_LargeDependenceEmphasis
wavelet-HHL_gldm_LargeDependenceHighGrayLevelEmphasis
wavelet-HHL_gldm_LargeDependenceLowGrayLevelEmphasis
wavelet-HHL_gldm_LowGrayLevelEmphasis
wavelet-HHL_gldm_SmallDependenceEmphasis
wavelet-HHL_gldm_SmallDependenceHighGrayLevelEmphasis
wavelet-HHL_gldm_SmallDependenceLowGrayLevelEmphasis
wavelet-HHH_firstorder_10Percentile
wavelet-HHH_firstorder_90Percentile
wavelet-HHH_firstorder_Energy
wavelet-HHH_firstorder_Entropy
wavelet-HHH_firstorder_InterquartileRange
wavelet-HHH_firstorder_Kurtosis
wavelet-HHH_firstorder_Maximum
wavelet-HHH_firstorder_MeanAbsoluteDeviation
wavelet-HHH_firstorder_Mean

wavelet-HHH_firstorder_Median
wavelet-HHH_firstorder_Minimum
wavelet-HHH_firstorder_Range
wavelet-HHH_firstorder_RobustMeanAbsoluteDeviation
wavelet-HHH_firstorder_RootMeanSquared
wavelet-HHH_firstorder_Skewness
wavelet-HHH_firstorder_TotalEnergy
wavelet-HHH_firstorder_Uniformity
wavelet-HHH_firstorder_Variance
wavelet-HHH_glcm_Autocorrelation
wavelet-HHH_glcm_JointAverage
wavelet-HHH_glcm_ClusterProminence
wavelet-HHH_glcm_ClusterShade
wavelet-HHH_glcm_ClusterTendency
wavelet-HHH_glcm_Contrast
wavelet-HHH_glcm_Correlation
wavelet-HHH_glcm_DifferenceAverage
wavelet-HHH_glcm_DifferenceEntropy
wavelet-HHH_glcm_DifferenceVariance
wavelet-HHH_glcm_JointEnergy
wavelet-HHH_glcm_JointEntropy
wavelet-HHH_glcm_Imc1
wavelet-HHH_glcm_Imc2
wavelet-HHH_glcm_Idm
wavelet-HHH_glcm_Idmn
wavelet-HHH_glcm_Id
wavelet-HHH_glcm_Idn
wavelet-HHH_glcm_InverseVariance
wavelet-HHH_glcm_MaximumProbability
wavelet-HHH_glcm_SumEntropy
wavelet-HHH_glcm_SumSquares
wavelet-HHH_glrlm_GrayLevelNonUniformity
wavelet-HHH_glrlm_GrayLevelNonUniformityNormalized
wavelet-HHH_glrlm_GrayLevelVariance
wavelet-HHH_glrlm_HighGrayLevelRunEmphasis
wavelet-HHH_glrlm_LongRunEmphasis
wavelet-HHH_glrlm_LongRunHighGrayLevelEmphasis
wavelet-HHH_glrlm_LongRunLowGrayLevelEmphasis
wavelet-HHH_glrlm_LowGrayLevelRunEmphasis
wavelet-HHH_glrlm_RunEntropy
wavelet-HHH_glrlm_RunLengthNonUniformity
wavelet-HHH_glrlm_RunLengthNonUniformityNormalized
wavelet-HHH_glrlm_RunPercentage
wavelet-HHH_glrlm_RunVariance
wavelet-HHH_glrlm_ShortRunEmphasis

wavelet-HHH_glrlm_ShortRunHighGrayLevelEmphasis
wavelet-HHH_glrlm_ShortRunLowGrayLevelEmphasis
wavelet-HHH_glszm_GrayLevelNonUniformity
wavelet-HHH_glszm_GrayLevelNonUniformityNormalized
wavelet-HHH_glszm_GrayLevelVariance
wavelet-HHH_glszm_HighGrayLevelZoneEmphasis
wavelet-HHH_glszm_LargeAreaEmphasis
wavelet-HHH_glszm_LargeAreaHighGrayLevelEmphasis
wavelet-HHH_glszm_LargeAreaLowGrayLevelEmphasis
wavelet-HHH_glszm_LowGrayLevelZoneEmphasis
wavelet-HHH_glszm_SizeZoneNonUniformity
wavelet-HHH_glszm_SizeZoneNonUniformityNormalized
wavelet-HHH_glszm_SmallAreaEmphasis
wavelet-HHH_glszm_SmallAreaHighGrayLevelEmphasis
wavelet-HHH_glszm_SmallAreaLowGrayLevelEmphasis
wavelet-HHH_glszm_ZoneEntropy
wavelet-HHH_glszm_ZonePercentage
wavelet-HHH_glszm_ZoneVariance
wavelet-HHH_ngtdm_Busyness
wavelet-HHH_ngtdm_Coarseness
wavelet-HHH_ngtdm_Complexity
wavelet-HHH_ngtdm_Contrast
wavelet-HHH_ngtdm_Strength
wavelet-HHH_gldm_DependenceEntropy
wavelet-HHH_gldm_DependenceNonUniformity
wavelet-HHH_gldm_DependenceNonUniformityNormalized
wavelet-HHH_gldm_DependenceVariance
wavelet-HHH_gldm_GrayLevelNonUniformity
wavelet-HHH_gldm_GrayLevelVariance
wavelet-HHH_gldm_HighGrayLevelEmphasis
wavelet-HHH_gldm_LargeDependenceEmphasis
wavelet-HHH_gldm_LargeDependenceHighGrayLevelEmphasis
wavelet-HHH_gldm_LargeDependenceLowGrayLevelEmphasis
wavelet-HHH_gldm_LowGrayLevelEmphasis
wavelet-HHH_gldm_SmallDependenceEmphasis
wavelet-HHH_gldm_SmallDependenceHighGrayLevelEmphasis
wavelet-HHH_gldm_SmallDependenceLowGrayLevelEmphasis
wavelet-LLL_firstorder_10Percentile
wavelet-LLL_firstorder_90Percentile
wavelet-LLL_firstorder_Energy
wavelet-LLL_firstorder_Entropy
wavelet-LLL_firstorder_InterquartileRange
wavelet-LLL_firstorder_Kurtosis
wavelet-LLL_firstorder_Maximum
wavelet-LLL_firstorder_MeanAbsoluteDeviation

wavelet-LLL_firstorder_Mean
wavelet-LLL_firstorder_Median
wavelet-LLL_firstorder_Minimum
wavelet-LLL_firstorder_Range
wavelet-LLL_firstorder_RobustMeanAbsoluteDeviation
wavelet-LLL_firstorder_RootMeanSquared
wavelet-LLL_firstorder_Skewness
wavelet-LLL_firstorder_TotalEnergy
wavelet-LLL_firstorder_Uniformity
wavelet-LLL_firstorder_Variance
wavelet-LLL_glcm_Autocorrelation
wavelet-LLL_glcm_JointAverage
wavelet-LLL_glcm_ClusterProminence
wavelet-LLL_glcm_ClusterShade
wavelet-LLL_glcm_ClusterTendency
wavelet-LLL_glcm_Contrast
wavelet-LLL_glcm_Correlation
wavelet-LLL_glcm_DifferenceAverage
wavelet-LLL_glcm_DifferenceEntropy
wavelet-LLL_glcm_DifferenceVariance
wavelet-LLL_glcm_JointEnergy
wavelet-LLL_glcm_JointEntropy
wavelet-LLL_glcm_Imc1
wavelet-LLL_glcm_Imc2
wavelet-LLL_glcm_Idm
wavelet-LLL_glcm_Idmn
wavelet-LLL_glcm_Id
wavelet-LLL_glcm_Idn
wavelet-LLL_glcm_InverseVariance
wavelet-LLL_glcm_MaximumProbability
wavelet-LLL_glcm_SumEntropy
wavelet-LLL_glcm_SumSquares
wavelet-LLL_glrlm_GrayLevelNonUniformity
wavelet-LLL_glrlm_GrayLevelNonUniformityNormalized
wavelet-LLL_glrlm_GrayLevelVariance
wavelet-LLL_glrlm_HighGrayLevelRunEmphasis
wavelet-LLL_glrlm_LongRunEmphasis
wavelet-LLL_glrlm_LongRunHighGrayLevelEmphasis
wavelet-LLL_glrlm_LongRunLowGrayLevelEmphasis
wavelet-LLL_glrlm_LowGrayLevelRunEmphasis
wavelet-LLL_glrlm_RunEntropy
wavelet-LLL_glrlm_RunLengthNonUniformity
wavelet-LLL_glrlm_RunLengthNonUniformityNormalized
wavelet-LLL_glrlm_RunPercentage
wavelet-LLL_glrlm_RunVariance

wavelet-LLL_glrlm_ShortRunEmphasis
wavelet-LLL_glrlm_ShortRunHighGrayLevelEmphasis
wavelet-LLL_glrlm_ShortRunLowGrayLevelEmphasis
wavelet-LLL_glszm_GrayLevelNonUniformity
wavelet-LLL_glszm_GrayLevelNonUniformityNormalized
wavelet-LLL_glszm_GrayLevelVariance
wavelet-LLL_glszm_HighGrayLevelZoneEmphasis
wavelet-LLL_glszm_LargeAreaEmphasis
wavelet-LLL_glszm_LargeAreaHighGrayLevelEmphasis
wavelet-LLL_glszm_LargeAreaLowGrayLevelEmphasis
wavelet-LLL_glszm_LowGrayLevelZoneEmphasis
wavelet-LLL_glszm_SizeZoneNonUniformity
wavelet-LLL_glszm_SizeZoneNonUniformityNormalized
wavelet-LLL_glszm_SmallAreaEmphasis
wavelet-LLL_glszm_SmallAreaHighGrayLevelEmphasis
wavelet-LLL_glszm_SmallAreaLowGrayLevelEmphasis
wavelet-LLL_glszm_ZoneEntropy
wavelet-LLL_glszm_ZonePercentage
wavelet-LLL_glszm_ZoneVariance
wavelet-LLL_ngtdm_Busyness
wavelet-LLL_ngtdm_Coarseness
wavelet-LLL_ngtdm_Complexity
wavelet-LLL_ngtdm_Contrast
wavelet-LLL_ngtdm_Strength
wavelet-LLL_gldm_DependenceEntropy
wavelet-LLL_gldm_DependenceNonUniformity
wavelet-LLL_gldm_DependenceNonUniformityNormalized
wavelet-LLL_gldm_DependenceVariance
wavelet-LLL_gldm_GrayLevelNonUniformity
wavelet-LLL_gldm_GrayLevelVariance
wavelet-LLL_gldm_HighGrayLevelEmphasis
wavelet-LLL_gldm_LargeDependenceEmphasis
wavelet-LLL_gldm_LargeDependenceHighGrayLevelEmphasis
wavelet-LLL_gldm_LargeDependenceLowGrayLevelEmphasis
wavelet-LLL_gldm_LowGrayLevelEmphasis
wavelet-LLL_gldm_SmallDependenceEmphasis
wavelet-LLL_gldm_SmallDependenceHighGrayLevelEmphasis
wavelet-LLL_gldm_SmallDependenceLowGrayLevelEmphasis
square_firstorder_10Percentile
square_firstorder_90Percentile
square_firstorder_Energy
square_firstorder_Entropy
square_firstorder_InterquartileRange
square_firstorder_Kurtosis
square_firstorder_Maximum

square_firstorder_MeanAbsoluteDeviation
square_firstorder_Mean
square_firstorder_Median
square_firstorder_Minimum
square_firstorder_Range
square_firstorder_RobustMeanAbsoluteDeviation
square_firstorder_RootMeanSquared
square_firstorder_Skewness
square_firstorder_TotalEnergy
square_firstorder_Uniformity
square_firstorder_Variance
square_glcm_Autocorrelation
square_glcm_JointAverage
square_glcm_ClusterProminence
square_glcm_ClusterShade
square_glcm_ClusterTendency
square_glcm_Contrast
square_glcm_Correlation
square_glcm_DifferenceAverage
square_glcm_DifferenceEntropy
square_glcm_DifferenceVariance
square_glcm_JointEnergy
square_glcm_JointEntropy
square_glcm_Imc1
square_glcm_Imc2
square_glcm_Idm
square_glcm_Idmn
square_glcm_Id
square_glcm_Idn
square_glcm_InverseVariance
square_glcm_MaximumProbability
square_glcm_SumEntropy
square_glcm_SumSquares
square_glrlm_GrayLevelNonUniformity
square_glrlm_GrayLevelNonUniformityNormalized
square_glrlm_GrayLevelVariance
square_glrlm_HighGrayLevelRunEmphasis
square_glrlm_LongRunEmphasis
square_glrlm_LongRunHighGrayLevelEmphasis
square_glrlm_LongRunLowGrayLevelEmphasis
square_glrlm_LowGrayLevelRunEmphasis
square_glrlm_RunEntropy
square_glrlm_RunLengthNonUniformity
square_glrlm_RunLengthNonUniformityNormalized
square_glrlm_RunPercentage

square_glrlm_RunVariance
square_glrlm_ShortRunEmphasis
square_glrlm_ShortRunHighGrayLevelEmphasis
square_glrlm_ShortRunLowGrayLevelEmphasis
square_glszm_GrayLevelNonUniformity
square_glszm_GrayLevelNonUniformityNormalized
square_glszm_GrayLevelVariance
square_glszm_HighGrayLevelZoneEmphasis
square_glszm_LargeAreaEmphasis
square_glszm_LargeAreaHighGrayLevelEmphasis
square_glszm_LargeAreaLowGrayLevelEmphasis
square_glszm_LowGrayLevelZoneEmphasis
square_glszm_SizeZoneNonUniformity
square_glszm_SizeZoneNonUniformityNormalized
square_glszm_SmallAreaEmphasis
square_glszm_SmallAreaHighGrayLevelEmphasis
square_glszm_SmallAreaLowGrayLevelEmphasis
square_glszm_ZoneEntropy
square_glszm_ZonePercentage
square_glszm_ZoneVariance
square_ngtdm_Busyness
square_ngtdm_Coarseness
square_ngtdm_Complexity
square_ngtdm_Contrast
square_ngtdm_Strength
square_gldm_DependenceEntropy
square_gldm_DependenceNonUniformity
square_gldm_DependenceNonUniformityNormalized
square_gldm_DependenceVariance
square_gldm_GrayLevelNonUniformity
square_gldm_GrayLevelVariance
square_gldm_HighGrayLevelEmphasis
square_gldm_LargeDependenceEmphasis
square_gldm_LargeDependenceHighGrayLevelEmphasis
square_gldm_LargeDependenceLowGrayLevelEmphasis
square_gldm_LowGrayLevelEmphasis
square_gldm_SmallDependenceEmphasis
square_gldm_SmallDependenceHighGrayLevelEmphasis
square_gldm_SmallDependenceLowGrayLevelEmphasis
squareroot_firstorder_10Percentile
squareroot_firstorder_90Percentile
squareroot_firstorder_Energy
squareroot_firstorder_Entropy
squareroot_firstorder_InterquartileRange
squareroot_firstorder_Kurtosis

squareroot_firstorder_Maximum
squareroot_firstorder_MeanAbsoluteDeviation
squareroot_firstorder_Mean
squareroot_firstorder_Median
squareroot_firstorder_Minimum
squareroot_firstorder_Range
squareroot_firstorder_RobustMeanAbsoluteDeviation
squareroot_firstorder_RootMeanSquared
squareroot_firstorder_Skewness
squareroot_firstorder_TotalEnergy
squareroot_firstorder_Uniformity
squareroot_firstorder_Variance
squareroot_glcm_Autocorrelation
squareroot_glcm_JointAverage
squareroot_glcm_ClusterProminence
squareroot_glcm_ClusterShade
squareroot_glcm_ClusterTendency
squareroot_glcm_Contrast
squareroot_glcm_Correlation
squareroot_glcm_DifferenceAverage
squareroot_glcm_DifferenceEntropy
squareroot_glcm_DifferenceVariance
squareroot_glcm_JointEnergy
squareroot_glcm_JointEntropy
squareroot_glcm_Imc1
squareroot_glcm_Imc2
squareroot_glcm_Idm
squareroot_glcm_Idmn
squareroot_glcm_Id
squareroot_glcm_Idn
squareroot_glcm_InverseVariance
squareroot_glcm_MaximumProbability
squareroot_glcm_SumEntropy
squareroot_glcm_SumSquares
squareroot_glrlm_GrayLevelNonUniformity
squareroot_glrlm_GrayLevelNonUniformityNormalized
squareroot_glrlm_GrayLevelVariance
squareroot_glrlm_HighGrayLevelRunEmphasis
squareroot_glrlm_LongRunEmphasis
squareroot_glrlm_LongRunHighGrayLevelEmphasis
squareroot_glrlm_LongRunLowGrayLevelEmphasis
squareroot_glrlm_LowGrayLevelRunEmphasis
squareroot_glrlm_RunEntropy
squareroot_glrlm_RunLengthNonUniformity
squareroot_glrlm_RunLengthNonUniformityNormalized

squareroot_glrlm_RunPercentage
squareroot_glrlm_RunVariance
squareroot_glrlm_ShortRunEmphasis
squareroot_glrlm_ShortRunHighGrayLevelEmphasis
squareroot_glrlm_ShortRunLowGrayLevelEmphasis
squareroot_glszm_GrayLevelNonUniformity
squareroot_glszm_GrayLevelNonUniformityNormalized
squareroot_glszm_GrayLevelVariance
squareroot_glszm_HighGrayLevelZoneEmphasis
squareroot_glszm_LargeAreaEmphasis
squareroot_glszm_LargeAreaHighGrayLevelEmphasis
squareroot_glszm_LargeAreaLowGrayLevelEmphasis
squareroot_glszm_LowGrayLevelZoneEmphasis
squareroot_glszm_SizeZoneNonUniformity
squareroot_glszm_SizeZoneNonUniformityNormalized
squareroot_glszm_SmallAreaEmphasis
squareroot_glszm_SmallAreaHighGrayLevelEmphasis
squareroot_glszm_SmallAreaLowGrayLevelEmphasis
squareroot_glszm_ZoneEntropy
squareroot_glszm_ZonePercentage
squareroot_glszm_ZoneVariance
squareroot_ngtdm_Busyness
squareroot_ngtdm_Coarseness
squareroot_ngtdm_Complexity
squareroot_ngtdm_Contrast
squareroot_ngtdm_Strength
squareroot_gldm_DependenceEntropy
squareroot_gldm_DependenceNonUniformity
squareroot_gldm_DependenceNonUniformityNormalized
squareroot_gldm_DependenceVariance
squareroot_gldm_GrayLevelNonUniformity
squareroot_gldm_GrayLevelVariance
squareroot_gldm_HighGrayLevelEmphasis
squareroot_gldm_LargeDependenceEmphasis
squareroot_gldm_LargeDependenceHighGrayLevelEmphasis
squareroot_gldm_LargeDependenceLowGrayLevelEmphasis
squareroot_gldm_LowGrayLevelEmphasis
squareroot_gldm_SmallDependenceEmphasis
squareroot_gldm_SmallDependenceHighGrayLevelEmphasis
squareroot_gldm_SmallDependenceLowGrayLevelEmphasis
logarithm_firstorder_10Percentile
logarithm_firstorder_90Percentile
logarithm_firstorder_Energy
logarithm_firstorder_Entropy
logarithm_firstorder_InterquartileRange

logarithm_firstorder_Kurtosis
logarithm_firstorder_Maximum
logarithm_firstorder_MeanAbsoluteDeviation
logarithm_firstorder_Mean
logarithm_firstorder_Median
logarithm_firstorder_Minimum
logarithm_firstorder_Range
logarithm_firstorder_RobustMeanAbsoluteDeviation
logarithm_firstorder_RootMeanSquared
logarithm_firstorder_Skewness
logarithm_firstorder_TotalEnergy
logarithm_firstorder_Uniformity
logarithm_firstorder_Variance
logarithm_glcm_Autocorrelation
logarithm_glcm_JointAverage
logarithm_glcm_ClusterProminence
logarithm_glcm_ClusterShade
logarithm_glcm_ClusterTendency
logarithm_glcm_Contrast
logarithm_glcm_Correlation
logarithm_glcm_DifferenceAverage
logarithm_glcm_DifferenceEntropy
logarithm_glcm_DifferenceVariance
logarithm_glcm_JointEnergy
logarithm_glcm_JointEntropy
logarithm_glcm_Imc1
logarithm_glcm_Imc2
logarithm_glcm_Idm
logarithm_glcm_Idmn
logarithm_glcm_Id
logarithm_glcm_Idn
logarithm_glcm_InverseVariance
logarithm_glcm_MaximumProbability
logarithm_glcm_SumEntropy
logarithm_glcm_SumSquares
logarithm_glrlm_GrayLevelNonUniformity
logarithm_glrlm_GrayLevelNonUniformityNormalized
logarithm_glrlm_GrayLevelVariance
logarithm_glrlm_HighGrayLevelRunEmphasis
logarithm_glrlm_LongRunEmphasis
logarithm_glrlm_LongRunHighGrayLevelEmphasis
logarithm_glrlm_LongRunLowGrayLevelEmphasis
logarithm_glrlm_LowGrayLevelRunEmphasis
logarithm_glrlm_RunEntropy
logarithm_glrlm_RunLengthNonUniformity

logarithm_glrlm_RunLengthNonUniformityNormalized
logarithm_glrlm_RunPercentage
logarithm_glrlm_RunVariance
logarithm_glrlm_ShortRunEmphasis
logarithm_glrlm_ShortRunHighGrayLevelEmphasis
logarithm_glrlm_ShortRunLowGrayLevelEmphasis
logarithm_glszm_GrayLevelNonUniformity
logarithm_glszm_GrayLevelNonUniformityNormalized
logarithm_glszm_GrayLevelVariance
logarithm_glszm_HighGrayLevelZoneEmphasis
logarithm_glszm_LargeAreaEmphasis
logarithm_glszm_LargeAreaHighGrayLevelEmphasis
logarithm_glszm_LargeAreaLowGrayLevelEmphasis
logarithm_glszm_LowGrayLevelZoneEmphasis
logarithm_glszm_SizeZoneNonUniformity
logarithm_glszm_SizeZoneNonUniformityNormalized
logarithm_glszm_SmallAreaEmphasis
logarithm_glszm_SmallAreaHighGrayLevelEmphasis
logarithm_glszm_SmallAreaLowGrayLevelEmphasis
logarithm_glszm_ZoneEntropy
logarithm_glszm_ZonePercentage
logarithm_glszm_ZoneVariance
logarithm_ngtdm_Busyness
logarithm_ngtdm_Coarseness
logarithm_ngtdm_Complexity
logarithm_ngtdm_Contrast
logarithm_ngtdm_Strength
logarithm_gldm_DependenceEntropy
logarithm_gldm_DependenceNonUniformity
logarithm_gldm_DependenceNonUniformityNormalized
logarithm_gldm_DependenceVariance
logarithm_gldm_GrayLevelNonUniformity
logarithm_gldm_GrayLevelVariance
logarithm_gldm_HighGrayLevelEmphasis
logarithm_gldm_LargeDependenceEmphasis
logarithm_gldm_LargeDependenceHighGrayLevelEmphasis
logarithm_gldm_LargeDependenceLowGrayLevelEmphasis
logarithm_gldm_LowGrayLevelEmphasis
logarithm_gldm_SmallDependenceEmphasis
logarithm_gldm_SmallDependenceHighGrayLevelEmphasis
logarithm_gldm_SmallDependenceLowGrayLevelEmphasis
exponential_firstorder_10Percentile
exponential_firstorder_90Percentile
exponential_firstorder_Energy
exponential_firstorder_Entropy

exponential_firstorder_InterquartileRange
exponential_firstorder_Kurtosis
exponential_firstorder_Maximum
exponential_firstorder_MeanAbsoluteDeviation
exponential_firstorder_Mean
exponential_firstorder_Median
exponential_firstorder_Minimum
exponential_firstorder_Range
exponential_firstorder_RobustMeanAbsoluteDeviation
exponential_firstorder_RootMeanSquared
exponential_firstorder_Skewness
exponential_firstorder_TotalEnergy
exponential_firstorder_Uniformity
exponential_firstorder_Variance
exponential_glcm_Autocorrelation
exponential_glcm_JointAverage
exponential_glcm_ClusterProminence
exponential_glcm_ClusterShade
exponential_glcm_ClusterTendency
exponential_glcm_Contrast
exponential_glcm_Correlation
exponential_glcm_DifferenceAverage
exponential_glcm_DifferenceEntropy
exponential_glcm_DifferenceVariance
exponential_glcm_JointEnergy
exponential_glcm_JointEntropy
exponential_glcm_Imc1
exponential_glcm_Imc2
exponential_glcm_Idm
exponential_glcm_Idmn
exponential_glcm_Id
exponential_glcm_Idn
exponential_glcm_InverseVariance
exponential_glcm_MaximumProbability
exponential_glcm_SumEntropy
exponential_glcm_SumSquares
exponential_glrlm_GrayLevelNonUniformity
exponential_glrlm_GrayLevelNonUniformityNormalized
exponential_glrlm_GrayLevelVariance
exponential_glrlm_HighGrayLevelRunEmphasis
exponential_glrlm_LongRunEmphasis
exponential_glrlm_LongRunHighGrayLevelEmphasis
exponential_glrlm_LongRunLowGrayLevelEmphasis
exponential_glrlm_LowGrayLevelRunEmphasis
exponential_glrlm_RunEntropy

exponential_glrlm_RunLengthNonUniformity
exponential_glrlm_RunLengthNonUniformityNormalized
exponential_glrlm_RunPercentage
exponential_glrlm_RunVariance
exponential_glrlm_ShortRunEmphasis
exponential_glrlm_ShortRunHighGrayLevelEmphasis
exponential_glrlm_ShortRunLowGrayLevelEmphasis
exponential_glszm_GrayLevelNonUniformity
exponential_glszm_GrayLevelNonUniformityNormalized
exponential_glszm_GrayLevelVariance
exponential_glszm_HighGrayLevelZoneEmphasis
exponential_glszm_LargeAreaEmphasis
exponential_glszm_LargeAreaHighGrayLevelEmphasis
exponential_glszm_LargeAreaLowGrayLevelEmphasis
exponential_glszm_LowGrayLevelZoneEmphasis
exponential_glszm_SizeZoneNonUniformity
exponential_glszm_SizeZoneNonUniformityNormalized
exponential_glszm_SmallAreaEmphasis
exponential_glszm_SmallAreaHighGrayLevelEmphasis
exponential_glszm_SmallAreaLowGrayLevelEmphasis
exponential_glszm_ZoneEntropy
exponential_glszm_ZonePercentage
exponential_glszm_ZoneVariance
exponential_ngtdm_Busyness
exponential_ngtdm_Coarseness
exponential_ngtdm_Complexity
exponential_ngtdm_Contrast
exponential_ngtdm_Strength
exponential_gldm_DependenceEntropy
exponential_gldm_DependenceNonUniformity
exponential_gldm_DependenceNonUniformityNormalized
exponential_gldm_DependenceVariance
exponential_gldm_GrayLevelNonUniformity
exponential_gldm_GrayLevelVariance
exponential_gldm_HighGrayLevelEmphasis
exponential_gldm_LargeDependenceEmphasis
exponential_gldm_LargeDependenceHighGrayLevelEmphasis
exponential_gldm_LargeDependenceLowGrayLevelEmphasis
exponential_gldm_LowGrayLevelEmphasis
exponential_gldm_SmallDependenceEmphasis
exponential_gldm_SmallDependenceHighGrayLevelEmphasis
exponential_gldm_SmallDependenceLowGrayLevelEmphasis

C | List of DE genes in Chapter 3

Gene Ensembl ID	log(Fold Change)	Likelihood Ratio	P Value	FDR P Value	External Gene ID
ENSG00000244734	-3.110942685	49.35568903	2.14E-12	2.23E-08	HBB
ENSG00000188536	-2.897419966	36.37983366	1.62E-09	8.48E-06	HBA2
ENSG00000206172	-2.848029829	33.89631621	5.81E-09	2.02E-05	HBA1
ENSG00000122862	-1.21208352	31.64301324	1.85E-08	4.84E-05	SRGN
ENSG00000163220	-2.528618623	31.18716865	2.34E-08	4.90E-05	S100A9
ENSG00000134531	-1.293697179	30.50609318	3.33E-08	5.80E-05	EMP1
ENSG00000025708	-1.743561908	28.22694215	1.08E-07	0.000161052	TYMP
ENSG00000122026	-1.724220274	27.94441809	1.25E-07	0.00016307	RPL21
ENSG00000143546	-2.663166532	27.30830729	1.73E-07	0.000201392	S100A8
ENSG00000264281	1.961256376	26.23470485	3.02E-07	0.000315915	CTD-2031P19.4
ENSG00000171051	-2.335443448	25.7695698	3.85E-07	0.000365436	FPR1
ENSG00000119535	-2.301094079	25.43939565	4.57E-07	0.000397497	CSF3R
ENSG00000136167	-1.286909849	25.09221272	5.47E-07	0.000439285	LCP1
ENSG00000162747	-2.848243562	24.84419271	6.22E-07	0.000463906	FCGR3B
ENSG00000011422	-1.797541232	24.24299168	8.49E-07	0.000591521	PLAUR
ENSG00000108691	-1.992618289	23.86485401	1.03E-06	0.000674884	CCL2
ENSG00000169908	-0.885702968	22.3397194	2.28E-06	0.001404055	TM4SF1
ENSG00000204577	-2.815282648	22.06495126	2.64E-06	0.001530074	LILRB3
ENSG00000158859	-2.687930018	21.74812927	3.11E-06	0.001709747	ADAMTS4
ENSG00000018280	-2.309409737	20.66666718	5.47E-06	0.002855675	SLC11A1
ENSG00000254087	-1.217205461	19.54634864	9.82E-06	0.004885566	LYN
ENSG00000015133	-1.276536209	18.93741685	1.35E-05	0.006247254	CCDC88C
ENSG00000116741	-1.094052551	18.83808726	1.42E-05	0.006247254	RGS2
ENSG00000169403	-1.290323197	18.82214543	1.43E-05	0.006247254	PTAFR
ENSG00000059728	-1.386718953	18.37978487	1.81E-05	0.007563729	MXD1
ENSG00000105835	-1.276093554	17.73004459	2.55E-05	0.010230934	NAMPT
ENSG00000166501	-1.137618702	17.41082568	3.01E-05	0.011652808	PRKCB
ENSG00000107562	-0.831516987	17.06252771	3.62E-05	0.013497487	CXCL12
ENSG00000082074	-1.485356534	16.87720421	3.99E-05	0.014068333	FYB
ENSG00000161570	-2.499010277	16.83076144	4.09E-05	0.014068333	CCL5
ENSG00000103196	-1.425594864	16.76056955	4.24E-05	0.014068333	CRISPLD2
ENSG00000178878	-1.233864922	16.73043834	4.31E-05	0.014068333	APOLD1
ENSG00000104290	0.680966495	16.6211611	4.56E-05	0.014450956	FZD3
ENSG00000000938	-2.072620842	16.54959329	4.74E-05	0.014565337	FGR
ENSG00000123689	-2.12103194	16.45376988	4.99E-05	0.014569639	G0S2
ENSG00000153317	-0.537427874	16.32276019	5.34E-05	0.014569639	ASAP1
ENSG00000072786	-1.390047433	16.31440157	5.37E-05	0.014569639	STK10
ENSG00000130066	-0.842249057	16.3014358	5.40E-05	0.014569639	SAT1
ENSG00000185650	-0.557913732	16.28895735	5.44E-05	0.014569639	ZFP36L1
ENSG00000137575	-0.594828951	16.12869577	5.92E-05	0.015141478	SDCBP
ENSG00000142347	-1.512436497	16.08993991	6.04E-05	0.015141478	MYO1F
ENSG00000059804	-1.478189902	16.04797772	6.18E-05	0.015141478	SLC2A3
ENSG00000166147	-0.521332318	16.02588249	6.25E-05	0.015141478	FBN1
ENSG00000163638	-1.291290952	15.96750666	6.44E-05	0.015141478	ADAMTS9
ENSG00000101096	-0.854565435	15.94502962	6.52E-05	0.015141478	NFATC2
ENSG00000017427	-0.908704362	15.89766155	6.69E-05	0.015187684	IGF1
ENSG00000178726	-1.079494121	15.85558346	6.84E-05	0.015198744	THBD

ENSG00000069702	-0.81751704	15.70530265	7.40E-05	0.016020612	TGFBR3
ENSG00000073756	-1.444972608	15.67711352	7.51E-05	0.016020612	PTGS2
ENSG00000210154	-1.697101896	15.63379032	7.69E-05	0.01606401	MT-TD
ENSG00000130755	-1.118661042	15.52002724	8.16E-05	0.016298859	GMFG
ENSG00000243829	-1.124336899	15.50710976	8.22E-05	0.016298859	CTB-33G10.1
ENSG00000197747	-0.620631593	15.4961841	8.27E-05	0.016298859	S100A10
ENSG00000139318	-0.948687802	15.41899	8.61E-05	0.016663931	DUSP6
ENSG00000111348	-0.636031234	15.3431595	8.96E-05	0.016862181	ARHGDIB
ENSG00000148840	-1.010175918	15.30296077	9.16E-05	0.016862181	PPRC1
ENSG00000198604	-0.892989957	15.29449187	9.20E-05	0.016862181	BAZ1A
ENSG00000130164	-0.985047875	15.14830556	9.94E-05	0.017905166	LDLR
ENSG00000163162	-0.527381479	15.00793618	0.00010706	0.018960507	RNF149
ENSG00000256618	-3.766531192	14.93519335	0.000111268	0.019100221	MTRNR2L1
ENSG00000010810	-1.121053796	14.91614218	0.000112397	0.019100221	FYN
ENSG00000069399	-0.996489025	14.90050355	0.000113333	0.019100221	BCL3
ENSG00000062716	-0.707467916	14.85438875	0.000116138	0.019262238	VMP1
ENSG00000076662	-1.16634052	14.68497223	0.000127055	0.020225171	ICAM3
ENSG00000163513	-0.671135513	14.68176331	0.000127272	0.020225171	TGFBR2
ENSG00000167703	-1.050722946	14.67469141	0.00012775	0.020225171	SLC43A2
ENSG00000113070	-1.209127966	14.59670805	0.000133147	0.02076496	HBEGF
ENSG00000125347	-1.218102122	14.35501364	0.000151376	0.023260712	IRF1
ENSG00000034971	-0.782275846	14.29676222	0.000156133	0.023643998	MYOC
ENSG00000141574	-1.457231481	14.07875633	0.000175313	0.026150809	SECTM1
ENSG00000196565	-3.132903321	14.05339929	0.000177692	0.026150809	HBG2
ENSG00000091592	-0.736784799	14.00906364	0.000181932	0.026367021	NLRP1
ENSG00000214548	-1.081793641	13.98567967	0.000184208	0.026367021	MEG3
ENSG00000155130	-0.566974335	13.84272418	0.000198765	0.028066134	MARCKS
ENSG00000176435	-1.41148724	13.68869395	0.000215749	0.030043597	CLEC14A
ENSG00000184557	-1.860252316	13.66473478	0.00021852	0.030043597	SOCS3
ENSG00000118515	-1.423181676	13.63120998	0.000222456	0.030187632	SGK1
ENSG00000115956	-1.593850545	13.59987666	0.0002262	0.030302152	PLEK
ENSG00000178695	-0.766068852	13.51420069	0.000236765	0.031161869	KCTD12
ENSG00000132334	-0.982759461	13.49984947	0.000238583	0.031161869	PTPRE
ENSG00000173334	-1.108157883	13.42420408	0.000248398	0.031750032	TRIB1
ENSG00000164920	-1.031902791	13.41101189	0.000250151	0.031750032	OSR2
ENSG00000183688	-1.012657146	13.37245123	0.000255347	0.031750032	FAM101B
ENSG00000162618	-1.574266612	13.34538204	0.00025906	0.031750032	ELTD1
ENSG00000129277	-1.513667661	13.34341114	0.000259332	0.031750032	CCL4
ENSG00000170323	-1.888183514	13.32911274	0.000261317	0.031750032	FABP4
ENSG00000118503	-1.461043422	13.22539425	0.000276182	0.032593295	TNFAIP3
ENSG00000165030	-1.087820461	13.21901952	0.000277123	0.032593295	NFIL3
ENSG00000164736	-1.952234457	13.18737678	0.000281841	0.032593295	SOX17
ENSG00000127954	-1.314992666	13.1761325	0.000283537	0.032593295	STEAP4
ENSG00000116679	-0.611665977	13.16309751	0.000285517	0.032593295	IVNS1ABP
ENSG00000112303	-1.642586547	13.15356178	0.000286973	0.032593295	VNN2
ENSG00000117289	-0.855811288	13.11660726	0.00029269	0.032633261	TXNIP
ENSG00000167470	-0.81502012	13.11097216	0.000293571	0.032633261	MIDN
ENSG00000163736	-3.024458895	13.03746967	0.00030532	0.033582022	PPBP

ENSG00000117143	-0.905708125	12.99319391	0.000312625	0.034027305	UAP1
ENSG00000099994	0.746466131	12.95545535	0.000318991	0.034362193	SUSD2
ENSG00000174059	-0.754559106	12.89695048	0.000329118	0.03509136	CD34
ENSG00000127445	0.461066286	12.81200752	0.000344402	0.036350047	PIN1
ENSG00000257337	0.502255665	12.70544848	0.000364592	0.038096191	RP11-983P16.4
ENSG00000128567	-1.271756136	12.68252039	0.00036909	0.038184342	PODXL
ENSG00000162511	-0.820352995	12.63048037	0.000379508	0.038507895	LAPTM5
ENSG00000127920	-0.797451789	12.62270583	0.000381089	0.038507895	GNG11
ENSG00000167604	-1.288350126	12.61202459	0.000383273	0.038507895	NFKBID
ENSG00000099860	-1.189596048	12.57946173	0.000390009	0.038811471	GADD45B
ENSG00000159200	-0.869054793	12.53628104	0.000399126	0.039096804	RCAN1
ENSG00000006652	-0.731107808	12.53051405	0.00040036	0.039096804	IFRD1
ENSG00000130600	-0.919677782	12.5029444	0.000406311	0.039310604	H19
ENSG00000137193	-1.221679399	12.45434012	0.000417022	0.039976693	PIM1
ENSG00000124762	-1.234524652	12.4163363	0.000425594	0.040317819	CDKN1A
ENSG00000101955	-0.869827325	12.40451409	0.000428297	0.040317819	SRPX
ENSG00000176170	-1.368211684	12.37220848	0.000435772	0.040655179	SPHK1
ENSG00000145824	-0.941807851	12.29722279	0.000453633	0.041946983	CXCL14
ENSG00000165685	-1.971384606	12.26418156	0.000461736	0.042321721	TMEM52B
ENSG00000117228	-1.001002833	12.24728116	0.000465937	0.042335402	GBP1
ENSG00000157557	-0.781743885	12.23016909	0.000470229	0.042357126	ETS2
ENSG00000248323	-2.912790629	12.19562019	0.000479018	0.042665514	LUCAT1
ENSG00000136826	-1.217183553	12.17971579	0.00048312	0.042665514	KLF4
ENSG00000184922	-1.289579168	12.16900349	0.000485903	0.042665514	FMNL1
ENSG00000111145	-0.798482309	12.13870562	0.00049386	0.043002895	ELK3
ENSG00000180447	-1.135148502	12.10872385	0.000501865	0.043338713	GAS1
ENSG00000221869	-0.825637086	12.0563155	0.000516172	0.044208871	CEBPD
ENSG00000183486	-1.080577052	11.82270843	0.000585127	0.049707238	MX2
ENSG00000233276	-0.490380439	11.71459291	0.000620119	0.052255007	GPX1
ENSG00000086061	-0.670888966	11.54654885	0.000678751	0.056107312	DNAJA1
ENSG00000134853	-0.618547067	11.54189179	0.000680454	0.056107312	PDGFRA
ENSG00000126878	0.650178835	11.53782539	0.000681944	0.056107312	AIF1L
ENSG00000167074	0.593582489	11.49230855	0.000698848	0.057048913	TEF
ENSG00000180871	-2.080222335	11.42240071	0.000725639	0.058776736	CXCR2
ENSG00000028137	-0.798607207	11.37061796	0.00074615	0.059973281	TNFRSF1B
ENSG00000234745	-0.541438771	11.34992365	0.000754511	0.060171657	HLA-B
ENSG00000198223	-1.200646987	11.33612971	0.000760136	0.060171657	CSF2RA
ENSG00000163132	-0.96838566	11.29150713	0.000778624	0.061171784	MSX1
ENSG00000182809	0.505787149	11.27286717	0.000786482	0.061327959	CRIP2
ENSG00000078596	-0.62486026	11.21447962	0.000811616	0.062514928	ITM2A
ENSG00000143850	-1.045533594	11.20475182	0.000815881	0.062514928	PLEKHA6
ENSG00000182378	-1.122212119	11.19619549	0.000819652	0.062514928	PLCXD1
ENSG00000121966	-1.41960017	11.15914938	0.000836183	0.063313561	CXCR4
ENSG00000184232	-0.78194939	11.09353406	0.000866292	0.065121503	OAF
ENSG00000198832	0.465739978	11.02977104	0.000896602	0.066918546	SELM
ENSG00000224743	-0.955674914	10.9496171	0.00093623	0.06921433	TEX26-AS1
ENSG00000134851	-0.518811013	10.94096808	0.00094061	0.06921433	TMEM165
ENSG00000163734	-1.504781677	10.91466629	0.000954059	0.069713025	CXCL3

ENSG00000125810	-0.557653486	10.8458847	0.000990156	0.071848167	CD93
ENSG00000057704	-1.187781216	10.82028507	0.00100394	0.071955512	TMCC3
ENSG00000130429	-0.510505431	10.81758096	0.001005408	0.071955512	ARPC1B
ENSG00000111859	-0.823465504	10.77293801	0.001029949	0.07321045	NEDD9
ENSG00000197019	-0.835308579	10.75348931	0.001040829	0.073483929	SERTAD1
ENSG00000198478	-0.834089942	10.63475502	0.00110982	0.07782891	SH3BGRL2
ENSG00000115590	-2.647277643	10.57486867	0.001146354	0.079855028	IL1R2
ENSG00000134899	-0.499011509	10.53254365	0.001172907	0.081163589	ERCC5
ENSG00000266402	0.490827998	10.49962369	0.001193989	0.081498268	SNORA76
ENSG00000186529	-2.364057275	10.48375977	0.001204284	0.081498268	CYP4F3
ENSG00000182463	-0.928501139	10.48210266	0.001205365	0.081498268	TSHZ2
ENSG00000168883	-0.484138999	10.47662864	0.001208942	0.081498268	USP39
ENSG00000099194	-1.500882252	10.40728762	0.00125519	0.084073573	SCD
ENSG00000005249	-1.247589622	10.34386754	0.001299055	0.086457515	PRKAR2B
ENSG00000103811	-0.704890294	10.29046019	0.001337197	0.088432755	CTSH
ENSG00000142634	-0.996260176	10.2657675	0.001355213	0.089060538	EFHD2
ENSG00000196262	0.728452486	10.1997132	0.001404625	0.09173079	PPIA
ENSG00000131459	-1.020246805	10.17646056	0.00142245	0.092317872	GFPT2
ENSG00000075234	-0.86588163	10.15211322	0.001441359	0.09296767	TTC38
ENSG00000176788	-0.662432238	10.10492739	0.001478734	0.094793212	BASP1
ENSG00000163221	-2.410423903	10.08311595	0.001496341	0.095336983	S100A12
ENSG00000178053	-1.072939036	10.06785879	0.001508783	0.095547096	MLF1
ENSG00000170955	0.446420404	10.05397647	0.001520195	0.095689835	PRKCDBP
ENSG00000152213	-2.147665644	9.969795051	0.001591292	0.097304687	ARL11
ENSG00000073060	-1.254493128	9.957719485	0.001601763	0.097304687	SCARB1
ENSG00000227507	-1.420303518	9.949447221	0.001608977	0.097304687	LTB
ENSG00000143384	-0.514023215	9.946518202	0.001611539	0.097304687	MCL1
ENSG00000166710	-0.379039311	9.940234177	0.00161705	0.097304687	B2M
ENSG00000112096	-0.620770378	9.938206603	0.001618832	0.097304687	SOD2
ENSG00000172403	0.546865601	9.937261714	0.001619663	0.097304687	SYNPO2
ENSG00000174697	-1.868015269	9.930868375	0.001625298	0.097304687	LEP
ENSG00000165997	-0.777708768	9.921908498	0.001633229	0.097304687	ARL5B
ENSG00000173559	-1.089248362	9.913203752	0.001640972	0.097304687	NABP1
ENSG00000213246	0.411433385	9.896195785	0.001656208	0.097304687	SUPT4H1
ENSG00000077420	-1.303301772	9.881329255	0.001669643	0.097304687	APBB1IP
ENSG00000179388	-1.126830886	9.877519072	0.001673104	0.097304687	EGR3
ENSG00000138207	-1.596744782	9.86329412	0.001686089	0.097304687	RBP4
ENSG00000111912	-0.653787212	9.843920838	0.001703939	0.097304687	NCOA7
ENSG00000091136	-0.762705752	9.841639168	0.001706054	0.097304687	LAMB1
ENSG00000236439	1.068167861	9.839037478	0.001708469	0.097304687	RP11-175B9.3
ENSG00000130844	-0.869491501	9.833659192	0.001713471	0.097304687	ZNF331
ENSG00000151422	0.469901306	9.798253188	0.001746777	0.098251752	FER
ENSG00000006638	0.482044042	9.79596242	0.001748955	0.098251752	TBXA2R
ENSG00000171608	-0.736693779	9.782094659	0.001762194	0.098466151	PIK3CD
ENSG00000163947	-0.936478525	9.733789821	0.001809111	0.100549997	ARHGEF3
ENSG00000160593	-1.539761686	9.711664531	0.001831021	0.101229302	AMICA1
ENSG00000112297	-1.114921389	9.664060529	0.001879078	0.103339416	AIM1
ENSG00000131042	-1.344618035	9.612915121	0.001932137	0.104816659	LILRB2

ENSG00000148926	-0.746233144	9.610523031	0.001934655	0.104816659	ADM
ENSG00000167657	0.516258439	9.6002785	0.001945479	0.104816659	DAPK3
ENSG00000185215	-0.890228594	9.599725235	0.001946065	0.104816659	TNFAIP2
ENSG00000075426	-0.576002331	9.576534202	0.001970801	0.105334199	FOSL2
ENSG00000069849	-0.695276274	9.57185042	0.001975835	0.105334199	ATP1B3
ENSG00000064932	-0.775500138	9.556440469	0.001992491	0.105392699	SBNO2
ENSG00000131981	-0.5340953	9.552194244	0.001997105	0.105392699	LGALS3
ENSG00000134802	-0.689745299	9.521460839	0.002030829	0.106303288	SLC43A3
ENSG00000173918	0.464788415	9.51795912	0.002034707	0.106303288	C1QTNF1
ENSG00000221963	-0.635916151	9.486933284	0.002069404	0.10757814	APOL6
ENSG00000151892	-0.79542476	9.422494603	0.002143397	0.110873066	GFRA1
ENSG00000125746	0.47050263	9.395172491	0.002175575	0.111937887	EML2
ENSG00000104213	-0.749697062	9.386905282	0.002185408	0.111937887	PDGFRL
ENSG00000168038	1.236530745	9.372256721	0.002202941	0.112285535	ULK4
ENSG00000169242	-0.97026958	9.354221521	0.002224724	0.112845367	EFNA1
ENSG00000163131	-0.915407881	9.336250446	0.002246647	0.113406852	CTSS
ENSG00000225630	-1.001076797	9.307447722	0.002282242	0.114649739	MTND2P28
ENSG00000100075	0.599692419	9.291969969	0.002301605	0.114924073	SLC25A1
ENSG00000086758	0.328602041	9.285538599	0.0023097	0.114924073	HUWE1
ENSG00000143333	-1.45424664	9.160952755	0.002472338	0.121539112	RGS16
ENSG00000111725	0.547149129	9.159987038	0.002473643	0.121539112	PRKAB1
ENSG00000102802	-0.645684035	9.136403678	0.002505731	0.121539112	MEDAG
ENSG00000135046	-0.423241012	9.13607022	0.002506188	0.121539112	ANXA1
ENSG00000138356	-0.692087947	9.135349798	0.002507175	0.121539112	AOX1
ENSG00000204482	-1.248958811	9.131514564	0.002512436	0.121539112	LST1
ENSG00000146540	0.318881116	9.102011309	0.002553286	0.122946003	C7orf50
ENSG00000144802	-0.956965709	9.053418101	0.002622042	0.125677583	NFKBIZ
ENSG00000110852	-1.043088768	9.008520479	0.002687239	0.128214414	CLEC2B
ENSG00000160255	-0.724202885	8.970784711	0.002743308	0.130294637	ITGB2
ENSG00000100417	0.424567335	8.953953987	0.002768697	0.130905484	PMM1
ENSG00000170525	-0.578318233	8.94023729	0.002789565	0.13129803	PFKFB3
ENSG00000186517	-0.955359332	8.925387146	0.002812337	0.131776293	ARHGAP30
ENSG00000136280	0.526852603	8.887440211	0.00287139	0.13394266	CCM2
ENSG00000100605	0.402578334	8.837239764	0.002951452	0.137065428	ITPK1
ENSG00000168214	-0.289145512	8.801059569	0.003010557	0.138626761	RBPJ
ENSG00000154734	-0.884839632	8.800423471	0.003011606	0.138626761	ADAMTS1
ENSG00000144655	-0.964354593	8.785262921	0.003036738	0.139170503	CSRNP1
ENSG00000108582	-0.417706158	8.761186498	0.003077088	0.140392007	CPD
ENSG00000162772	-1.21466762	8.751604715	0.003093297	0.140392007	ATF3
ENSG00000261669	0.862992971	8.74458436	0.003105229	0.140392007	CTD-2515A14.1
ENSG00000161835	-0.909213618	8.737605876	0.003117135	0.140392007	GRASP
ENSG00000206177	-2.379078465	8.681323981	0.003214874	0.143966947	HBM
ENSG00000158578	-2.598691687	8.676120306	0.003224066	0.143966947	ALAS2
ENSG00000121274	0.368406385	8.631898217	0.003303272	0.146876121	PAPD5
ENSG00000122420	-0.835370319	8.584353931	0.003390637	0.150121876	PTGFR
ENSG00000125817	0.342804572	8.552961568	0.003449606	0.152088307	CENPB
ENSG00000159128	-0.448484136	8.534615844	0.003484549	0.1529834	IFNGR2
ENSG00000163399	-0.412559606	8.51354211	0.003525132	0.153075772	ATP1A1

ENSG00000175416	0.38512012	8.506306377	0.003539177	0.153075772	CLTB
ENSG00000132780	-0.349556813	8.500932895	0.003549644	0.153075772	NASP
ENSG00000166228	0.557323305	8.496801545	0.003557713	0.153075772	PCBD1
ENSG00000250461	-0.920162643	8.495682739	0.003559902	0.153075772	RP11-631M6.2
ENSG00000106003	-1.024691977	8.479576551	0.003591557	0.15380401	LFNG
ENSG00000166741	-0.521990356	8.456256581	0.003637898	0.154243708	NNMT
ENSG00000116667	-0.725132158	8.449963871	0.003650507	0.154243708	C1orf21
ENSG00000204882	0.628885309	8.446806098	0.003656851	0.154243708	GPR20
ENSG00000102096	-0.710632017	8.43943373	0.003671706	0.154243708	PIM2
ENSG00000071967	-0.635042821	8.436976184	0.003676671	0.154243708	CYBRD1
ENSG00000113749	-0.98094316	8.424013353	0.003702975	0.154243708	HRH2
ENSG00000156427	-1.401642287	8.419556761	0.003712063	0.154243708	FGF18
ENSG00000100028	-0.273398917	8.413230981	0.003725001	0.154243708	SNRPD3
ENSG00000072195	0.35480791	8.4051174	0.003741662	0.154243708	SPEG
ENSG00000119508	-1.121413381	8.401342385	0.00374944	0.154243708	NR4A3
ENSG00000137822	0.456497823	8.39132704	0.003770156	0.154487669	TUBGCP4
ENSG00000132475	-0.286538317	8.374224918	0.003805798	0.15454152	H3F3B
ENSG00000077312	0.38683426	8.368210049	0.003818415	0.15454152	SNRPA
ENSG00000239218	-0.969428002	8.362023127	0.003831438	0.15454152	RPS20P22
ENSG00000126822	0.383728796	8.356068497	0.003844014	0.15454152	PLEKHG3
ENSG00000240771	0.473609198	8.355403739	0.00384542	0.15454152	ARHGEF25
ENSG00000164056	-0.625890909	8.335209784	0.003888399	0.154649894	SPRY1
ENSG00000140682	0.413532128	8.335076937	0.003888683	0.154649894	TGFB1I1
ENSG00000100365	-0.934787387	8.333286183	0.003892518	0.154649894	NCF4
ENSG00000107929	-0.462721208	8.312118809	0.003938142	0.155316324	LARP4B
ENSG00000074657	0.386046649	8.311713829	0.003939021	0.155316324	ZNF532
ENSG00000142910	0.444295146	8.301488362	0.00396126	0.155606042	TINAGL1
ENSG00000159176	0.510472254	8.281959789	0.004004089	0.156699344	CSRP1
ENSG00000103187	-0.696161106	8.27266188	0.004024646	0.156916131	COTL1
ENSG00000255928	0.73118713	8.205937173	0.004175354	0.162186882	RP11-456I15.2
ENSG00000122965	0.702763909	8.165525463	0.00426941	0.163776507	RBM19
ENSG00000204252	-0.969774204	8.15732522	0.004288758	0.163776507	HLA-DOA
ENSG00000149591	0.675784614	8.145964841	0.004315709	0.163776507	TAGLN
ENSG00000152332	-0.577203403	8.144670305	0.004318791	0.163776507	UHMK1
ENSG00000145423	-0.7725248	8.139759953	0.004330502	0.163776507	SFRP2
ENSG00000100335	0.374282689	8.138603143	0.004333265	0.163776507	MIEF1
ENSG00000112079	-0.460033248	8.136832963	0.004337498	0.163776507	STK38
ENSG00000182575	0.484960611	8.127197735	0.004360609	0.163776507	NXPH3
ENSG00000171303	0.581014619	8.120711956	0.004376237	0.163776507	KCNK3
ENSG00000188042	-1.127612906	8.119147062	0.004380016	0.163776507	ARL4C
ENSG00000079950	0.326731676	8.115560551	0.00438869	0.163776507	STX7
ENSG00000267121	-1.714815968	8.098584078	0.004429985	0.164729234	CTD-2020K17.1
ENSG00000110047	0.371192503	8.091791147	0.00444662	0.164761445	EHD1
ENSG00000137801	-1.036318039	8.061551432	0.004521445	0.166547215	THBS1
ENSG00000049246	0.562373103	8.059449956	0.004526692	0.166547215	PER3
ENSG00000103145	0.333703303	8.046323768	0.004559609	0.166988074	HCFC1R1
ENSG00000148290	0.454901844	8.041947443	0.004570637	0.166988074	SURF1
ENSG00000121067	0.343402494	8.02049613	0.00462509	0.167800716	SPOP

ENSG00000263391	-0.825170448	8.017065506	0.004633859	0.167800716	AL512428.1
ENSG00000163110	0.34687431	8.014254613	0.004641057	0.167800716	PDLIM5
ENSG00000120738	-0.904534096	8.004956509	0.004664948	0.168082913	EGR1
ENSG00000148700	-0.456488211	7.98889886	0.004706503	0.168525292	ADD3
ENSG00000104969	0.456506413	7.987753013	0.004709483	0.168525292	SGTA
ENSG00000235568	-1.546310722	7.981393589	0.004726055	0.168541112	NFAM1
ENSG00000169282	0.458937395	7.968806268	0.004759031	0.169139857	KCNAB1
ENSG00000129596	-0.777754479	7.960564664	0.00478075	0.169335775	CDO1
ENSG00000108669	-0.704079305	7.923161813	0.004880591	0.172288143	CYTH1
ENSG00000111404	0.590599295	7.869061614	0.005028774	0.176921423	RERGL
ENSG00000125354	-0.447274502	7.845910379	0.00509358	0.17855771	Sep-06
ENSG00000136630	-0.554507652	7.840282984	0.005109461	0.17855771	HLX
ENSG00000077157	0.361357239	7.822706567	0.005159387	0.179701463	PPP1R12B
ENSG00000096968	0.501381625	7.816654392	0.005176694	0.179705225	JAK2
ENSG00000165898	0.707758669	7.807256108	0.005203686	0.18004408	ISCA2
ENSG00000095380	-0.545619172	7.791708894	0.005248653	0.181000572	NANS
ENSG00000204161	-1.416296777	7.780948909	0.005280006	0.181039131	C10orf128
ENSG00000092964	-0.343219766	7.779438177	0.005284423	0.181039131	DPYSL2
ENSG00000198858	-0.521283722	7.7719342	0.00530642	0.181198633	R3HDM4
ENSG00000134697	-0.421714054	7.760082182	0.005341353	0.181797386	GNL2
ENSG00000180353	-0.639478328	7.740588547	0.00539932	0.183173685	HCLS1
ENSG00000166819	-1.675852574	7.685650162	0.005566162	0.188222752	PLIN1
ENSG00000243811	-1.24074075	7.678267219	0.005588981	0.188384714	APOBEC3D
ENSG00000205336	-1.26085814	7.66889098	0.005618098	0.188461357	GPR56
ENSG00000183779	0.416256362	7.665929175	0.005627327	0.188461357	ZNF703
ENSG00000109501	0.367872847	7.659442488	0.005647595	0.18853586	WFS1
ENSG00000163516	-0.881701302	7.610380673	0.005803323	0.192937905	ANKZF1
ENSG00000105819	-0.518129381	7.606325775	0.005816388	0.192937905	PMPCB
ENSG00000272574	-1.060293857	7.592013661	0.005862743	0.193860126	RP11-359K18.4
ENSG00000265150	-0.693609325	7.57828045	0.005907577	0.19423486	RN7SL2
ENSG00000168309	-0.826179446	7.574847373	0.005918839	0.19423486	FAM107A
ENSG00000101596	-0.427766973	7.564469755	0.005953017	0.19423486	SMCHD1
ENSG00000260054	0.352083403	7.560823343	0.005965073	0.19423486	RP11-611L7.1
ENSG00000163704	0.726212707	7.55830665	0.005973409	0.19423486	PRRT3
ENSG00000179776	-1.184875975	7.548494441	0.006006023	0.19423486	CDH5
ENSG00000158246	0.654317841	7.543565389	0.006022475	0.19423486	FAM46B
ENSG00000162783	-0.608669603	7.543472328	0.006022786	0.19423486	IER5
ENSG00000035664	-1.20984002	7.53195199	0.00606142	0.194879308	DAPK2
ENSG00000177663	-0.427993077	7.510875507	0.006132755	0.196567981	IL17RA
ENSG00000028277	-0.624972302	7.479942768	0.006239005	0.19904173	POU2F2
ENSG00000185947	-0.893894063	7.477339653	0.006248032	0.19904173	ZNF267
ENSG00000163660	-0.715545022	7.453892701	0.006329941	0.201038144	CCNL1
ENSG00000034510	-0.408807342	7.447128344	0.006353774	0.20118359	TMSB10
ENSG00000100906	-0.396582045	7.429569925	0.006416067	0.202542261	NFKBIA
ENSG00000139722	-0.857635198	7.416795238	0.006461781	0.203370924	VPS37B
ENSG00000050405	-0.502850874	7.3984403	0.006528045	0.204466539	LIMA1
ENSG00000107949	0.573047366	7.396324515	0.006535728	0.204466539	BCCIP
ENSG00000088356	0.623916568	7.377373013	0.006604958	0.206015538	PDRG1

ENSG00000174353	1.563538236	7.353407455	0.006693577	0.207711704	STAG3L3
ENSG00000140941	-0.449497068	7.347393293	0.006716006	0.207711704	MAP1LC3B
ENSG00000100055	-0.68484699	7.34659918	0.006718974	0.207711704	CYTH4
ENSG00000089057	-0.429418951	7.336554679	0.006756622	0.208259407	SLC23A2
ENSG00000113369	-0.347665034	7.31845221	0.006825017	0.209274938	ARRDC3
ENSG00000117020	0.377531386	7.312285738	0.006848476	0.209274938	AKT3
ENSG00000132205	-0.825173261	7.299731937	0.00689649	0.209274938	EMILIN2
ENSG00000095303	-0.985317459	7.298134276	0.006902625	0.209274938	PTGS1
ENSG00000138166	-1.193243183	7.295437766	0.006912992	0.209274938	DUSP5
ENSG00000184113	-0.983948202	7.292919795	0.006922688	0.209274938	CLDN5
ENSG00000204652	1.321244866	7.291083671	0.006929766	0.209274938	RPS26P8
ENSG00000145687	0.324885886	7.282922426	0.006961319	0.209278581	SSBP2
ENSG00000170776	-0.407018806	7.28069817	0.006969944	0.209278581	AKAP13
ENSG00000152518	-0.316536755	7.274112114	0.006995546	0.209445457	ZFP36L2
ENSG00000124126	-0.754059818	7.243558669	0.007115581	0.211985818	PREX1
ENSG00000101347	-0.573359828	7.231115663	0.007165067	0.211985818	SAMHD1
ENSG00000233901	-1.387589569	7.229306318	0.007172292	0.211985818	RP11-65J3.1
ENSG00000185339	-0.844677647	7.226277707	0.007184402	0.211985818	TCN2
ENSG00000196628	-0.316701201	7.22398659	0.007193577	0.211985818	TCF4
ENSG00000144476	-0.667326181	7.221855735	0.007202121	0.211985818	ACKR3
ENSG00000214485	0.684869211	7.21470845	0.007230856	0.212147589	RPL7P1
ENSG00000168874	0.341260366	7.210402525	0.007248224	0.212147589	ATOH8
ENSG00000177606	-0.658001085	7.20197568	0.007282337	0.212238683	JUN
ENSG00000103202	0.344805446	7.199605784	0.00729196	0.212238683	NME4
ENSG00000134369	-0.415250041	7.190308153	0.007329839	0.212748583	NAV1
ENSG00000163257	0.312305438	7.181342987	0.007366555	0.213221964	DCAF16
ENSG00000197766	-0.57092601	7.161650154	0.007447865	0.214979943	CFD
ENSG00000143226	-0.733972599	7.151869638	0.007488588	0.215559938	FCGR2A
ENSG00000163866	0.34826263	7.143330045	0.007524331	0.215993769	SMIM12
ENSG00000185862	-1.201397569	7.13293799	0.007568062	0.216653922	EVI2B
ENSG00000110079	-0.943388858	7.110728872	0.007662395	0.218755091	MS4A4A
ENSG00000171223	-0.81048531	7.104447939	0.00768929	0.218924781	JUNB
ENSG00000165152	0.402173563	7.089017519	0.007755775	0.220217656	TMEM246
ENSG00000141480	-0.538725534	7.078556234	0.007801184	0.220906699	ARRB2
ENSG00000120129	-0.687682604	7.036014781	0.007988659	0.225604062	DUSP1
ENSG00000121316	-0.666189418	7.017021994	0.00807384	0.227154306	PLBD1
ENSG00000198355	-0.518150095	7.013408738	0.00809015	0.227154306	PIM3
ENSG00000104765	-0.336424372	7.007291497	0.00811784	0.227154306	BNIP3L
ENSG00000081237	-0.973824561	7.000605338	0.008148216	0.227154306	PTPRC
ENSG00000204103	-0.453113716	6.999719168	0.00815225	0.227154306	MAFB
ENSG00000188404	-1.230921168	6.987377356	0.008208655	0.227970522	SELL
ENSG00000090861	0.284603457	6.983778258	0.008225178	0.227970522	AARS
ENSG00000160271	-0.419054149	6.978215961	0.008250782	0.228075183	RALGDS
ENSG00000159167	-1.306741536	6.967570658	0.00830001	0.228080124	STC1
ENSG00000147010	-0.539615703	6.964370147	0.00831487	0.228080124	SH3KBP1
ENSG00000155090	-0.653691974	6.964031322	0.008316444	0.228080124	KLF10
ENSG00000153815	-0.643209622	6.954115514	0.008362663	0.228245861	CMIP
ENSG00000144218	0.648462038	6.949956118	0.008382129	0.228245861	AFF3

ENSG00000167613	-0.945570149	6.937707763	0.00843972	0.228245861	LAIR1
ENSG00000110876	-1.008663678	6.935541709	0.008449947	0.228245861	SELPLG
ENSG00000146457	-0.348370338	6.933487702	0.008459656	0.228245861	WTAP
ENSG00000120899	-0.543089097	6.932013046	0.008466634	0.228245861	PTK2B
ENSG00000162733	-0.341301204	6.930163464	0.008475394	0.228245861	DDR2
ENSG00000165168	-0.537823299	6.91648288	0.008540479	0.229407359	CYBB
ENSG00000065413	-0.649222101	6.908468567	0.008578844	0.22952706	ANKRD44
ENSG00000071127	0.296029575	6.906283661	0.008589334	0.22952706	WDR1
ENSG00000067082	-0.455169822	6.901813845	0.008610834	0.22952706	KLF6
ENSG00000125730	-0.554763719	6.884556032	0.008694366	0.230636783	C3
ENSG00000198106	-1.055243267	6.88325279	0.008700708	0.230636783	SNX29P2
ENSG00000171940	-1.072264693	6.873170691	0.008749927	0.230636783	ZNF217
ENSG00000086062	-0.322418368	6.871048711	0.008760323	0.230636783	B4GALT1
ENSG00000214753	0.314591681	6.870537489	0.008762829	0.230636783	HNRNPUL2
ENSG00000095794	-0.646965261	6.860870947	0.00881036	0.230917619	CREM
ENSG00000158615	-0.590631616	6.859383167	0.008817698	0.230917619	PPP1R15B
ENSG00000124107	-0.868798471	6.852470026	0.008851881	0.231233264	SLPI
ENSG00000126458	0.348922584	6.838586485	0.00892094	0.232456118	RRAS
ENSG00000114541	-0.789800201	6.821836727	0.009004991	0.233705768	FRMD4B
ENSG00000138814	-0.448403308	6.820124099	0.00901363	0.233705768	PPP3CA
ENSG00000260859	-1.133481671	6.788136125	0.009176567	0.237062391	RP11-254F19.2
ENSG00000160801	0.447266072	6.785823183	0.009188465	0.237062391	PTH1R
ENSG00000135316	0.217296148	6.769951417	0.009270536	0.23799583	SYNCRIP
ENSG00000174099	0.353078331	6.763080406	0.009306298	0.23799583	MSRB3
ENSG00000236801	0.587799423	6.763007576	0.009306677	0.23799583	RPL24P8
ENSG00000168497	-0.868787249	6.76126838	0.009315752	0.23799583	SDPR
ENSG00000092969	0.52834471	6.740836333	0.009423044	0.240149722	TGFB2
ENSG00000160310	0.295035137	6.726888552	0.009497012	0.241445934	PRMT2
ENSG00000163701	0.608454201	6.714709795	0.009562085	0.242043627	IL17RE
ENSG00000169252	-1.057799823	6.710950437	0.009582264	0.242043627	ADRB2
ENSG00000165175	-0.702668792	6.706294452	0.009607316	0.242043627	MID1IP1
ENSG00000153707	0.378432046	6.700893501	0.009636461	0.242043627	PTPRD
ENSG00000085265	-1.817224449	6.700731049	0.009637339	0.242043627	FCN1
ENSG00000140832	1.4654645	6.69663448	0.009659507	0.242043627	MARVELD3
ENSG00000136158	-0.552658651	6.686700233	0.009713483	0.242813848	SPRY2
ENSG00000169896	-0.997006805	6.664838906	0.009833354	0.245223675	ITGAM
ENSG00000210140	-0.614473137	6.653001553	0.009898893	0.245609144	MT-TC
ENSG00000145022	0.479588318	6.650282629	0.00991401	0.245609144	TCTA
ENSG00000159388	-0.813004134	6.649327075	0.009919328	0.245609144	BTG2
ENSG00000189058	-0.604842181	6.637741657	0.009984042	0.246533512	APOD
ENSG00000145495	0.326683416	6.630750495	0.010023302	0.246533512	Mar-06
ENSG00000163874	-0.768544905	6.62859014	0.010035466	0.246533512	ZC3H12A
ENSG00000095637	0.310169335	6.625828835	0.010051036	0.246533512	SORBS1
ENSG00000124228	-0.408872313	6.614373975	0.010115889	0.246965913	DDX27
ENSG00000196411	-1.033239284	6.613606491	0.01012025	0.246965913	EPHB4
ENSG00000141564	1.275064155	6.605539124	0.010166202	0.246965913	RPTOR
ENSG00000204231	0.325483696	6.599070696	0.010203201	0.246965913	RXRB
ENSG00000119574	0.48498565	6.595922936	0.010221256	0.246965913	ZBTB45

ENSG00000012174	0.439516697	6.5938223	0.010233323	0.246965913	MBTPS2
ENSG00000087087	-0.303884132	6.593684908	0.010234112	0.246965913	SRRT
ENSG00000204592	-0.436899496	6.584766791	0.010285509	0.247634294	HLA-E
ENSG00000186480	-0.716427295	6.561127595	0.01042303	0.248484849	INSIG1
ENSG00000197405	-0.993164226	6.559389189	0.010433217	0.248484849	C5AR1
ENSG00000111880	-0.56334626	6.558630226	0.010437668	0.248484849	RNGTT
ENSG00000205682	0.919913925	6.558418622	0.010438909	0.248484849	RP11-798L4.1
ENSG00000169093	0.535149692	6.55827694	0.010439741	0.248484849	ASMTL
ENSG00000197471	-1.381977763	6.547988703	0.010500279	0.249357765	SPN
ENSG00000185049	0.383693163	6.533760809	0.010584593	0.25079006	NELFA
ENSG00000012822	0.469685097	6.520058977	0.010666447	0.251636019	CALCOCO1
ENSG00000145362	-0.591934309	6.518398788	0.010676408	0.251636019	ANK2
ENSG00000165424	-0.536052645	6.515713055	0.010692544	0.251636019	ZCCHC24
ENSG00000166250	-0.792733986	6.506393225	0.010748731	0.252128673	CLMP
ENSG00000242094	-0.714279752	6.499881451	0.010788169	0.252128673	FOXP1-IT1
ENSG00000008324	-0.640480898	6.497121916	0.010804926	0.252128673	SS18L2
ENSG00000035681	-0.693537916	6.493113106	0.010829317	0.252128673	NSMAF
ENSG00000167641	0.462470073	6.492324005	0.010834125	0.252128673	PPP1R14A
ENSG00000137076	0.336308078	6.485622361	0.010875046	0.252429219	TLN1
ENSG00000102755	-1.128878768	6.482305654	0.010895356	0.252429219	FLT1
ENSG00000115594	-0.640621286	6.477370319	0.010925651	0.252547321	IL1R1
ENSG00000167191	-0.770415	6.471865167	0.010959545	0.252547321	GPRC5B
ENSG00000172660	0.270174514	6.469141209	0.010976356	0.252547321	TAF15
ENSG00000104368	-0.742787725	6.465780695	0.010997132	0.252547321	PLAT
ENSG00000242247	-0.436981226	6.457356327	0.011049392	0.253190993	ARFGAP3
ENSG00000102901	-0.606003459	6.44602489	0.011120087	0.253807291	CENPT
ENSG00000113643	0.323087188	6.445261368	0.011124867	0.253807291	RARS
ENSG00000131116	0.325968753	6.4354289	0.011186614	0.254029236	ZNF428
ENSG00000133789	0.562165666	6.432760852	0.01120343	0.254029236	SWAP70
ENSG00000121297	-0.671318485	6.432110999	0.01120753	0.254029236	TSHZ3
ENSG00000196652	0.422613913	6.40779961	0.011362013	0.256357829	ZKSCAN5
ENSG00000128512	-0.912519104	6.405459532	0.011376998	0.256357829	DOCK4
ENSG00000273218	-0.590269263	6.404387743	0.011383868	0.256357829	LLNLR-246C6.1
ENSG00000168394	-0.857453286	6.39373687	0.011452369	0.256802998	TAP1
ENSG00000163823	-0.881826502	6.393671685	0.011452789	0.256802998	CCR1
ENSG00000136938	-0.289663856	6.366540127	0.011629212	0.260200497	ANP32B
ENSG00000130589	-0.765608761	6.344846943	0.011772277	0.261851529	HELZ2
ENSG00000129559	0.271898874	6.34472527	0.011773084	0.261851529	NEDD8
ENSG00000196924	0.431646139	6.343957406	0.011778182	0.261851529	FLNA
ENSG00000095906	0.33307444	6.325586089	0.011900815	0.26349945	NUBP2
ENSG00000175785	0.546776418	6.325299108	0.011902741	0.26349945	PRIMA1
ENSG00000065427	0.234324145	6.320385371	0.011935769	0.26367198	KARS
ENSG00000143322	-0.452584208	6.314829127	0.011973228	0.263941483	ABL2
ENSG00000087245	-0.423357809	6.310806125	0.012000426	0.263984117	MMP2
ENSG00000173546	0.412824427	6.303761299	0.012048207	0.26447839	CSPG4
ENSG00000168918	-0.62166194	6.293327207	0.012119334	0.264965255	INPP5D
ENSG00000184500	-0.621001228	6.293068652	0.012121102	0.264965255	PROS1
ENSG00000106397	-0.494929832	6.288662009	0.012151275	0.265070292	PLOD3

ENSG00000185022	-0.703112989	6.273326662	0.012256881	0.266268273	MAFF
ENSG00000166669	-0.534355386	6.273286708	0.012257158	0.266268273	ATF7IP2
ENSG00000081320	-0.728563148	6.256332607	0.012375012	0.268270751	STK17B
ENSG00000100292	-0.802904118	6.248079549	0.012432803	0.268914059	HMOX1
ENSG00000148450	0.313863474	6.244755301	0.012456159	0.268914059	MSRB2
ENSG00000270820	0.686709039	6.220375619	0.012628832	0.272079717	RP11-355B11.2
ENSG00000131016	-0.372318789	6.212972338	0.012681752	0.272657668	AKAP12
ENSG00000111962	-0.804394589	6.205037567	0.012738725	0.273320191	UST
ENSG00000152463	1.146313806	6.200574401	0.012770886	0.273448748	OLAH
ENSG00000141622	-1.392681743	6.170564112	0.012989318	0.276497786	RNF165
ENSG00000143442	0.338768803	6.163017795	0.013044847	0.276497786	POGZ
ENSG00000162407	-0.357559741	6.16299121	0.013045043	0.276497786	PPAP2B
ENSG00000198053	-0.509206007	6.161854207	0.01305343	0.276497786	SIRPA
ENSG00000169692	-0.661480704	6.153314202	0.013116608	0.276497786	AGPAT2
ENSG00000229715	0.374973307	6.153234333	0.0131172	0.276497786	EEF1DP3
ENSG00000086848	0.832599624	6.151159078	0.013132601	0.276497786	ALG9
ENSG00000170412	0.412578768	6.148991696	0.013148704	0.276497786	GPRC5C
ENSG00000205502	-1.653825012	6.147895349	0.013156858	0.276497786	C2CD4B
ENSG00000150779	0.389757263	6.144474352	0.013182334	0.276497786	TIMM8B
ENSG00000088247	0.270755108	6.141521686	0.013204364	0.276497786	KHSRP
ENSG00000198160	0.306634592	6.133174666	0.013266844	0.276862224	MIER1
ENSG00000123329	-0.940717016	6.132119918	0.013274761	0.276862224	ARHGAP9
ENSG00000127328	0.570687436	6.110066357	0.013441408	0.279779431	RAB3IP
ENSG00000166135	0.316605054	6.102854558	0.01349637	0.280364944	HIF1AN
ENSG00000023516	0.68855557	6.088852109	0.013603744	0.282034763	AKAP11
ENSG00000133424	0.486862332	6.081085086	0.013663682	0.282274299	LARGE
ENSG00000176194	-2.072002755	6.080355408	0.013669327	0.282274299	CIDEA
ENSG00000205362	-1.078460853	6.076173084	0.013701728	0.282291047	MT1A
ENSG00000255468	1.252426807	6.073282223	0.01372417	0.282291047	RP11-867G23.8
ENSG00000107130	0.498427105	6.062745114	0.013806291	0.282988723	NCS1
ENSG00000039319	-0.355819617	6.058782865	0.013837302	0.282988723	ZFYVE16
ENSG00000006468	-0.769566411	6.056865885	0.013852331	0.282988723	ETV1
ENSG00000113657	0.28298619	6.048606786	0.013917274	0.282988723	DPYSL3
ENSG00000184515	0.441476164	6.048217388	0.013920344	0.282988723	BEX5
ENSG00000132670	-0.390306817	6.044448819	0.013950087	0.282988723	PTPRA
ENSG00000171729	0.512357957	6.039471041	0.013989475	0.282988723	TMEM51
ENSG00000105221	0.378937862	6.037746478	0.014003148	0.282988723	AKT2
ENSG00000171056	-1.031164875	6.036306606	0.014014574	0.282988723	SOX7
ENSG00000264364	0.259577912	6.026077441	0.014096024	0.282988723	DYNLL2
ENSG00000266714	-0.911028732	6.018948247	0.014153079	0.282988723	MYO15B
ENSG00000100330	-0.430614495	6.018597968	0.014155888	0.282988723	MTMR3
ENSG00000106066	-1.03204906	6.017837403	0.01416199	0.282988723	CPVL
ENSG00000196263	0.809122123	6.017807447	0.014162231	0.282988723	ZNF471
ENSG00000268205	-0.35109848	6.017545633	0.014164332	0.282988723	CTC-444N24.11
ENSG00000188559	-0.504725549	6.010165576	0.014223693	0.283248102	RALGAPA2
ENSG00000108342	-3.235389883	6.009193623	0.01423153	0.283248102	CSF3
ENSG00000109065	0.624055936	6.003864688	0.014274576	0.283564727	NAT9
ENSG00000226525	-0.479987443	5.999741242	0.014307977	0.283688898	RPS7P10

ENSG00000107882	0.378970507	5.969737502	0.014553447	0.287353468	SUFU
ENSG00000264198	-1.311854258	5.963363186	0.014606153	0.287353468	RP11-94L15.2
ENSG00000197562	0.651157989	5.958982748	0.014642487	0.287353468	RAB40C
ENSG00000269113	0.75914682	5.956575102	0.014662497	0.287353468	TRABD2B
ENSG00000119812	0.301628197	5.956170292	0.014665864	0.287353468	FAM98A
ENSG00000054267	-0.357147209	5.952131517	0.014699502	0.287353468	ARID4B
ENSG00000090975	0.943369463	5.946167065	0.014749322	0.287353468	PITPNM2
ENSG00000074071	0.466376745	5.94273564	0.014778064	0.287353468	MRPS34
ENSG00000169744	-0.695199928	5.940736184	0.014794838	0.287353468	LDB2
ENSG00000197969	0.387498328	5.938887222	0.014810367	0.287353468	VPS13A
ENSG00000184160	0.450883221	5.938667745	0.014812211	0.287353468	ADRA2C
ENSG00000147164	0.298359141	5.935427369	0.01483947	0.287353468	SNX12
ENSG00000132326	-0.632029619	5.93414063	0.014850308	0.287353468	PER2
ENSG00000110324	-0.682132668	5.924301321	0.014933458	0.28800922	IL10RA
ENSG00000249617	-0.744067899	5.9217894	0.014954763	0.28800922	RP11-366M4.17
ENSG00000198585	0.343920632	5.916309341	0.01500135	0.28800922	NUDT16
ENSG00000179134	-0.299257761	5.915415409	0.015008964	0.28800922	SAMD4B
ENSG00000013588	-0.732589077	5.911405445	0.015043165	0.28800922	GPRC5A
ENSG00000115963	-0.578217281	5.909012817	0.015063611	0.28800922	RND3
ENSG00000173269	-0.637933668	5.906146446	0.015088142	0.28800922	MMRN2
ENSG00000159674	-0.580476416	5.904214021	0.015104704	0.28800922	SPON2
ENSG00000164403	-0.592252931	5.894083268	0.015191835	0.289131558	SHROOM1
ENSG00000154096	-0.739688547	5.890947851	0.015218907	0.289131558	THY1
ENSG00000204287	-0.443161403	5.873081792	0.015374115	0.290377447	HLA-DRA
ENSG00000150938	0.372956021	5.869533699	0.015405132	0.290377447	CRIM1
ENSG00000151689	-0.406413937	5.868276716	0.015416136	0.290377447	INPP1
ENSG00000160785	-0.590722257	5.867467316	0.015423226	0.290377447	SLC25A44
ENSG00000168734	0.318448641	5.867359208	0.015424173	0.290377447	PKIG
ENSG00000228393	-1.501365796	5.861625132	0.0154745	0.290377447	LINC01004
ENSG00000147454	-0.335055299	5.861111511	0.015479016	0.290377447	SLC25A37
ENSG00000151702	-0.735566482	5.853151423	0.015549182	0.290532196	FLI1
ENSG00000136689	-1.391653655	5.852207941	0.01555752	0.290532196	IL1RN
ENSG00000196972	0.82618574	5.850719994	0.015570679	0.290532196	LINC00087
ENSG00000069667	-0.517668241	5.845911145	0.015613287	0.290807914	RORA
ENSG00000142871	-0.685857795	5.836631699	0.015695846	0.291742418	CYR61
ENSG00000053702	0.687229175	5.834004535	0.015719301	0.291742418	NRIP2
ENSG00000184258	0.819121369	5.818189072	0.015861267	0.292423173	CDR1
ENSG00000161671	0.808227693	5.815364569	0.01588676	0.292423173	EMC10
ENSG00000111261	-0.700694117	5.814821739	0.015891664	0.292423173	MANSC1
ENSG00000165507	-0.533569878	5.809640671	0.015938551	0.292423173	C10orf10
ENSG00000169139	0.218537313	5.808337436	0.015950367	0.292423173	UBE2V2
ENSG00000210174	-0.882152617	5.808261921	0.015951052	0.292423173	MT-TR
ENSG00000210112	-0.675842809	5.808170457	0.015951881	0.292423173	MT-TM
ENSG00000205763	0.433816817	5.797557916	0.016048449	0.292627077	RP9P
ENSG00000165732	-0.324968556	5.794211498	0.016079025	0.292627077	DDX21
ENSG00000138193	0.42880122	5.792731307	0.016092568	0.292627077	PLCE1
ENSG00000105364	0.608711333	5.79253723	0.016094344	0.292627077	MRPL4
ENSG00000101938	-0.533042389	5.791588639	0.016103031	0.292627077	CHRDL1

ENSG00000161642	-1.150215781	5.787684037	0.016138837	0.29276859	ZNF385A
ENSG00000137124	0.397342773	5.780289291	0.016206874	0.293367814	ALDH1B1
ENSG00000110090	0.255566033	5.777997311	0.016228021	0.293367814	CPT1A
ENSG00000115946	-0.638442828	5.759302058	0.016401586	0.295836267	PNO1
ENSG00000154783	-0.847928019	5.75720303	0.016421192	0.295836267	FGD5
ENSG00000159840	0.404809366	5.751322565	0.016476248	0.296317238	ZYX
ENSG00000136770	-0.63289667	5.740050191	0.016582319	0.296660877	DNAJC1
ENSG00000102316	0.277416274	5.738495087	0.016597007	0.296660877	MAGED2
ENSG00000026297	-0.38895848	5.737614619	0.016605329	0.296660877	RNASET2
ENSG00000163520	-0.618550796	5.737234785	0.016608921	0.296660877	FBLN2
ENSG00000219222	0.3897516	5.729595974	0.01668132	0.297445586	RP11-480N24.3
ENSG00000164530	-0.501128229	5.719621899	0.016776343	0.298630333	PI16
ENSG00000169752	0.60034942	5.716071565	0.016810301	0.298725915	NRG4
ENSG00000213722	0.279016555	5.707081045	0.016896612	0.299051976	DDAH2
ENSG00000104332	-0.502807295	5.705905165	0.016907934	0.299051976	SFRP1
ENSG00000164967	-0.668881904	5.705222596	0.01691451	0.299051976	RPP25L
ENSG00000139637	0.43471325	5.685345314	0.017107173	0.301344153	C12orf10
ENSG00000118855	-0.646902738	5.676369024	0.017194917	0.301344153	MFSD1
ENSG00000242372	0.243682581	5.673499363	0.017223066	0.301344153	EIF6
ENSG00000137077	-1.692653176	5.669951192	0.017257936	0.301344153	CCL21
ENSG00000055044	-0.449459605	5.667226692	0.017284761	0.301344153	NOP58
ENSG00000228343	0.476108429	5.66587439	0.017298092	0.301344153	RP11-1148L6.5
ENSG00000173846	-0.729783992	5.665009825	0.01730662	0.301344153	PLK3
ENSG00000126012	-0.63990096	5.662255115	0.017333822	0.301344153	KDM5C
ENSG00000240065	-0.502709362	5.662231656	0.017334054	0.301344153	PSMB9
ENSG00000198399	-0.345292464	5.661835293	0.017337971	0.301344153	ITSN2
ENSG00000223274	-1.269329347	5.657801951	0.017377888	0.301344153	RNA5SP498
ENSG00000197381	0.421544182	5.656556751	0.017390231	0.301344153	ADARB1
ENSG00000131196	-0.552111679	5.620298107	0.017753629	0.307131901	NFATC1
ENSG00000126785	-0.903211854	5.61446909	0.017812777	0.307645792	RHOJ
ENSG00000185811	-1.051313995	5.609908462	0.017859196	0.307938512	IKZF1
ENSG00000043143	0.378171377	5.59991994	0.017961298	0.309188807	JADE2
ENSG00000000003	-0.56552432	5.59212946	0.018041351	0.309227506	TSPAN6
ENSG00000149357	-0.281184035	5.586281539	0.018101684	0.309227506	LAMTOR1
ENSG00000260025	0.440406331	5.584803505	0.018116966	0.309227506	RP11-490M8.1
ENSG00000138758	-0.313229147	5.583619454	0.018129217	0.309227506	Sep-11
ENSG00000100351	-2.105936509	5.578208747	0.018185313	0.309227506	GRAP2
ENSG00000181396	0.392733718	5.577643099	0.018191188	0.309227506	OGFOD3
ENSG00000128383	-1.96536678	5.576269286	0.018205465	0.309227506	APOBEC3A
ENSG00000159263	0.585413384	5.57212214	0.018248631	0.309227506	SIM2
ENSG00000136867	-1.067824129	5.571208522	0.018258155	0.309227506	SLC31A2
ENSG00000019144	-0.52262492	5.571080852	0.018259486	0.309227506	PHLDB1
ENSG00000248527	-0.554399727	5.563051558	0.018343413	0.309862888	MTATP6P1
ENSG00000260822	0.389241443	5.561820677	0.018356314	0.309862888	GS1-358P8.4
ENSG00000151726	-0.685674691	5.554461187	0.018433646	0.310072401	ACSL1
ENSG00000162692	-0.684701178	5.552191817	0.01845756	0.310072401	VCAM1
ENSG00000210195	-0.796569106	5.552173756	0.01845775	0.310072401	MT-TT
ENSG00000143387	-0.384216462	5.54913993	0.01848977	0.310111732	CTSK

ENSG00000164916	-0.348146897	5.542819265	0.018556665	0.310734917	FOXK1
ENSG00000151338	-0.735474356	5.539535519	0.018591517	0.310820411	MIPOL1
ENSG00000074410	-1.358515518	5.528440481	0.018709775	0.312297818	CA12
ENSG00000271811	-0.421796542	5.520841379	0.018791219	0.312400771	RP1-79C4.4
ENSG00000104756	0.369977285	5.519767335	0.018802759	0.312400771	KCTD9
ENSG00000026508	-0.327517295	5.51630472	0.018840015	0.312400771	CD44
ENSG00000054793	0.276683225	5.511185769	0.018895232	0.312400771	ATP9A
ENSG00000184785	0.377113355	5.508081124	0.018928803	0.312400771	SMIM10
ENSG00000197380	0.37880945	5.506371676	0.018947314	0.312400771	DACT3
ENSG00000260257	0.383206153	5.505501213	0.018956747	0.312400771	RP5-1085F17.3
ENSG00000011465	-0.443858872	5.504949071	0.018962732	0.312400771	DCN
ENSG00000129250	0.312271135	5.502894698	0.018985021	0.312400771	KIF1C
ENSG00000156587	0.345563352	5.495360864	0.019066992	0.313256293	UBE2L6
ENSG00000138326	-0.251014761	5.485024846	0.019180047	0.313907355	RPS24
ENSG00000008394	-0.946769515	5.484556912	0.019185182	0.313907355	MGST1
ENSG00000265113	-0.93972513	5.483503507	0.019196746	0.313907355	RP11-70O5.2
ENSG00000122335	0.419439981	5.472117633	0.019322199	0.315465097	SERAC1
ENSG00000148908	-0.661356197	5.455776047	0.019503739	0.317487063	RGS10
ENSG00000158352	-0.577723869	5.455500668	0.019506814	0.317487063	SHROOM4
ENSG00000090376	-0.784253164	5.449528948	0.019573604	0.318078671	IRAK3
ENSG00000184584	-0.346899377	5.422013429	0.019884417	0.322627753	TMEM173
ENSG00000170456	0.337345159	5.413333023	0.019983526	0.323486538	DENND5B
ENSG00000111203	0.47000855	5.411958726	0.019999263	0.323486538	ITFG2
ENSG00000220023	0.465907911	5.408908756	0.020034236	0.323551365	AL592183.1
ENSG00000175756	0.371082475	5.404729364	0.020082262	0.323826476	AURKAIP1
ENSG00000169895	-0.294502021	5.390255869	0.020249501	0.326020092	SYAP1
ENSG00000177363	-0.610643014	5.386366963	0.020294682	0.326197965	LRRN4CL
ENSG00000100908	0.7013937	5.383935341	0.020322985	0.326197965	EMC9
ENSG00000127951	-0.4212749	5.368385475	0.020504949	0.328340018	FGL2
ENSG00000125735	-1.354474858	5.366223773	0.020530378	0.328340018	TNFSF14
ENSG00000213523	-0.553108568	5.364497338	0.02055071	0.328340018	SRA1
ENSG00000160991	-0.559780217	5.339345141	0.020849304	0.332549546	ORAI2
ENSG00000033327	0.303412676	5.336961306	0.020877835	0.332549546	GAB2
ENSG00000145284	-0.755469292	5.332344727	0.020933205	0.332923988	SCD5
ENSG00000151612	0.361445467	5.326790307	0.021000024	0.333443637	ZNF827
ENSG00000117533	0.355634049	5.324329193	0.021029702	0.333443637	VAMP4
ENSG00000186314	0.5282928	5.314860531	0.021144286	0.334465697	PRELID2
ENSG00000113441	0.3732661	5.311214784	0.021188577	0.334465697	LNPEP
ENSG00000160888	-0.602695854	5.311082195	0.02119019	0.334465697	IER2
ENSG00000109881	-0.720894309	5.302561029	0.021294093	0.335130678	CCDC34
ENSG00000172889	-1.182141049	5.302366965	0.021296466	0.335130678	EGFL7
ENSG00000214176	-0.778648419	5.291208562	0.021433341	0.336777408	PLEKHM1P
ENSG00000204472	-0.551411644	5.284578478	0.0215151	0.337554471	AIF1
ENSG00000223396	-1.197668129	5.280472506	0.021565895	0.337844127	RPS10P7
ENSG00000177646	0.34459814	5.272812859	0.021660984	0.338825781	ACAD9
ENSG00000117016	0.506570936	5.266955412	0.021733993	0.339377653	RIMS3
ENSG00000145861	0.352622713	5.264775943	0.021761224	0.339377653	C1QTNF2
ENSG00000101265	-0.445141927	5.259782031	0.021823752	0.339755144	RASSF2

ENSG00000167797	0.315537422	5.25765345	0.02185046	0.339755144	CDK2AP2
ENSG00000112699	0.455760769	5.253440251	0.021903425	0.339876432	GMDS
ENSG00000026950	-0.54428245	5.249232246	0.021956457	0.339876432	BTN3A1
ENSG00000110693	0.400299795	5.246155696	0.021995314	0.339876432	SOX6
ENSG00000180771	0.241987927	5.244179429	0.022020311	0.339876432	SRSF8
ENSG00000041802	-0.316100958	5.244133217	0.022020896	0.339876432	LSG1
ENSG00000225137	0.451698757	5.231718402	0.02217861	0.341805751	DYNC1I2P1
ENSG00000108219	-0.438948659	5.224911641	0.022265578	0.342640678	TSPAN14
ENSG00000114742	-0.47642794	5.214966134	0.022393283	0.343441906	WDR48
ENSG00000143344	-0.450327166	5.212877865	0.022420194	0.343441906	RGL1
ENSG00000235162	0.348164371	5.2103704	0.022452551	0.343441906	C12orf75
ENSG00000112320	0.299030774	5.209918588	0.022458386	0.343441906	SOBP
ENSG00000163072	-0.993877228	5.208092674	0.022481985	0.343441906	NOSTRIN
ENSG00000136859	-0.527823489	5.201311967	0.022569847	0.344280778	ANGPTL2
ENSG00000110237	0.382038148	5.190499127	0.022710693	0.345798672	ARHGEF17
ENSG00000206503	-0.337359351	5.185158614	0.022780593	0.345798672	HLA-A
ENSG00000121858	-0.611424761	5.183712126	0.022799564	0.345798672	TNFSF10
ENSG00000066294	-0.553173776	5.183546977	0.022801731	0.345798672	CD84
ENSG00000252835	2.118687722	5.177554011	0.022880512	0.346490534	SCARNA21
ENSG00000100985	-1.482346074	5.170822304	0.022969341	0.347211111	MMP9
ENSG00000128016	-0.883140073	5.165008185	0.023046349	0.347211111	ZFP36
ENSG00000124772	-1.79610528	5.164898414	0.023047806	0.347211111	CPNE5
ENSG00000131669	0.360371461	5.163903442	0.023061012	0.347211111	NINJ1
ENSG00000121892	-0.274135025	5.160931447	0.023100505	0.347305295	PDS5A
ENSG00000172260	-0.303258652	5.156434252	0.0231604	0.347705488	NEGR1
ENSG00000163517	0.343063762	5.148363139	0.023268297	0.348490074	HDAC11
ENSG00000124181	0.412037791	5.145821506	0.023302382	0.348490074	PLCG1
ENSG00000135678	-0.79415254	5.143779387	0.023329806	0.348490074	CPM
ENSG00000204420	-0.909282023	5.141025235	0.023366845	0.348490074	C6orf25
ENSG00000153446	-0.737809888	5.140091324	0.023379418	0.348490074	C16orf89
ENSG00000116132	-0.353391846	5.126151138	0.023567933	0.350458889	PRRX1
ENSG00000230551	-0.389381443	5.125367184	0.023578582	0.350458889	CTB-89H12.4
ENSG00000114391	-0.198004053	5.121443904	0.023631945	0.35047591	RPL24
ENSG00000163788	-0.46894188	5.120352708	0.02364681	0.35047591	SNRK
ENSG00000156802	0.520880371	5.114424214	0.023727739	0.351177256	ATAD2
ENSG00000131446	-0.277580153	5.108755614	0.023805389	0.351266936	MGAT1
ENSG00000065357	-0.587469379	5.108651759	0.023806814	0.351266936	DGKA
ENSG00000163479	-0.238504524	5.106624447	0.02383465	0.351266936	SSR2
ENSG00000112769	-0.424200543	5.101304027	0.023907863	0.351849669	LAMA4
ENSG00000155380	-0.346092251	5.087921422	0.024093052	0.354076378	SLC16A1
ENSG00000137845	-0.484971007	5.07843322	0.024225252	0.355519179	ADAM10
ENSG00000128731	-0.349364283	5.075938435	0.024260136	0.355531789	HERC2
ENSG00000138777	0.493018132	5.070145311	0.024341343	0.356037486	PPA2
ENSG00000262380	-0.582935184	5.0685623	0.024363582	0.356037486	CTB-193M12.3
ENSG00000137522	0.309577784	5.066196035	0.024396865	0.356037486	RNF121
ENSG00000117500	-0.609842321	5.057847855	0.024514662	0.356889489	TMED5
ENSG00000115216	0.320623028	5.056982979	0.0245269	0.356889489	NRBP1
ENSG00000135218	-1.034596162	5.05288318	0.024584996	0.356889489	CD36

ENSG00000263740	-0.852027497	5.050722329	0.024615674	0.356889489	RN7SL4P
ENSG00000149596	0.37225412	5.049993992	0.024626024	0.356889489	JPH2
ENSG00000163531	0.533552502	5.047018235	0.024668355	0.357007807	NFASC
ENSG00000225746	-0.903639901	5.042202994	0.024737013	0.357506285	AL132709.5
ENSG00000060656	0.345656321	5.023122273	0.025011031	0.359526964	PTPRU
ENSG00000243335	0.376791	5.021500129	0.025034471	0.359526964	KCTD7
ENSG00000250069	-0.86252777	5.019981944	0.02505643	0.359526964	CTB-131B5.2
ENSG00000226688	0.421850165	5.019934067	0.025057123	0.359526964	ENTPD1-AS1
ENSG00000182534	0.450122565	5.019499848	0.025063407	0.359526964	MXRA7
ENSG00000087074	-0.552754035	5.01650512	0.025106794	0.359526964	PPP1R15A
ENSG00000175220	0.24607736	5.012210226	0.025169153	0.359526964	ARHGAP1
ENSG00000106211	0.295290874	5.008571146	0.025222117	0.359526964	HSPB1
ENSG00000029363	-0.237292819	5.007793402	0.025233451	0.359526964	BCLAF1
ENSG00000184381	0.733092944	5.005571538	0.02526586	0.359526964	PLA2G6
ENSG00000166436	-0.463636693	5.003111781	0.025301789	0.359526964	TRIM66
ENSG00000081087	0.30627948	5.002811073	0.025306185	0.359526964	OSTM1
ENSG00000128534	0.408312359	5.001584067	0.025324131	0.359526964	NAA38
ENSG00000174807	-0.645846971	4.988934501	0.025509912	0.361393019	CD248
ENSG00000165494	-0.402386603	4.987928745	0.025524744	0.361393019	PCF11
ENSG00000198959	0.368745055	4.980899686	0.025628652	0.362373183	TGM2
ENSG00000183696	-0.654683329	4.972243123	0.025757223	0.363405742	UPP1
ENSG00000100994	0.337654191	4.967832918	0.025822982	0.363405742	PYGB
ENSG00000067248	-0.359691542	4.965177463	0.025862661	0.363405742	DHX29
ENSG00000257151	0.41671393	4.964539555	0.025872202	0.363405742	PWAR6
ENSG00000178096	0.528760778	4.964314205	0.025875574	0.363405742	BOLA1
ENSG00000134363	-0.816279742	4.951646496	0.026065833	0.364813564	FST
ENSG00000177125	0.580979092	4.949239431	0.026102149	0.364813564	ZBTB34
ENSG00000122359	0.202154258	4.947497633	0.026128461	0.364813564	ANXA11
ENSG00000189067	-0.262353636	4.945738672	0.02615506	0.364813564	LITAF
ENSG00000072210	0.328133427	4.943447861	0.026189744	0.364813564	ALDH3A2
ENSG00000087365	0.212015937	4.943435974	0.026189924	0.364813564	SF3B2
ENSG00000168476	-0.611712149	4.941438178	0.026220211	0.364813564	REEP4
ENSG00000184840	0.326403165	4.932439469	0.026357085	0.366230289	TMED9
ENSG00000147130	0.300731844	4.927504889	0.026432456	0.366574031	ZMYM3
ENSG00000185236	0.276547628	4.924068729	0.026485073	0.366574031	RAB11B
ENSG00000204843	0.237662388	4.923938472	0.02648707	0.366574031	DCTN1
ENSG00000117000	0.303309083	4.91932322	0.026557919	0.366614651	RLF
ENSG00000112799	-0.915701514	4.915468523	0.026617243	0.366614651	LY86
ENSG00000171316	-0.69882569	4.915211245	0.026621208	0.366614651	CHD7
ENSG00000129824	-0.251322005	4.914618134	0.026630349	0.366614651	RPS4Y1
ENSG00000159733	-0.634390063	4.91203242	0.026670242	0.366680728	ZFYVE28
ENSG00000168404	-0.626723883	4.903672105	0.026799649	0.367847695	MLKL
ENSG00000100644	-0.357647313	4.902005262	0.026825528	0.367847695	HIF1A
ENSG00000130176	0.411828214	4.895503978	0.026926713	0.368414657	CNN1
ENSG00000137766	0.774128459	4.894819388	0.026937391	0.368414657	UNC13C
ENSG00000047188	-0.580059185	4.890842656	0.026999505	0.36858432	YTHDC2
ENSG00000106948	-0.516648793	4.889510541	0.027020345	0.36858432	AKNA
ENSG00000244462	-0.405679014	4.883321966	0.027117382	0.368983426	RBM12

ENSG00000184640	0.259117974	4.883140733	0.027120229	0.368983426	Sep-09
ENSG00000161960	-0.562844778	4.869952879	0.027328247	0.371330103	EIF4A1
ENSG00000131873	-0.383287108	4.863919449	0.027423967	0.37145315	CHSY1
ENSG00000128245	0.280013455	4.863434176	0.027431681	0.37145315	YWHAH
ENSG00000129657	-0.669221476	4.862662671	0.02744395	0.37145315	SEC14L1
ENSG00000119801	0.224061042	4.86042707	0.027479533	0.371453611	YPEL5
ENSG00000167378	0.29869546	4.857577544	0.027524958	0.371586928	IRGQ
ENSG00000169813	-0.423351349	4.851347513	0.027624543	0.372450133	HNRNPF
ENSG00000117640	0.30740163	4.848375579	0.027672181	0.372611622	MTFR1L
ENSG00000254184	-0.898552421	4.845437217	0.027719365	0.37276659	TYW1B
ENSG00000185515	0.3717416	4.83652701	0.027862955	0.373423661	BRCC3
ENSG00000029725	0.281691915	4.836381091	0.027865313	0.373423661	RABEP1
ENSG00000165724	0.521448363	4.835754644	0.027875438	0.373423661	ZMYND19
ENSG00000115306	-0.204421493	4.823739742	0.028070379	0.375553639	SPTBN1
ENSG00000197329	-0.50426891	4.819074861	0.028146448	0.376089819	PELI1
ENSG00000241990	0.433746181	4.816454143	0.028189278	0.376181053	RP6-109B7.3
ENSG00000080371	-0.253398787	4.808596205	0.028318105	0.377418208	RAB21
ENSG00000170145	-0.421270726	4.795214273	0.028538907	0.379408711	SIK2
ENSG00000105821	-0.438304046	4.795143726	0.028540075	0.379408711	DNAJC2
ENSG00000228634	-0.899881805	4.788012444	0.028658478	0.379807244	RP4-534N18.2
ENSG00000074054	-0.414955173	4.787046705	0.028674551	0.379807244	CLASP1
ENSG00000072274	-0.541417474	4.78583138	0.028694793	0.379807244	TFRC
ENSG00000213903	-0.766772282	4.781828963	0.028761558	0.379807244	LTB4R
ENSG00000138061	-0.637515602	4.780638939	0.02878144	0.379807244	CYP1B1
ENSG00000139289	-0.793248181	4.780237744	0.028788146	0.379807244	PHLDA1
ENSG00000114013	-0.914012871	4.777666579	0.028831163	0.379895106	CD86
ENSG00000037637	0.342098781	4.767680725	0.028998866	0.381623618	FBXO42
ENSG00000163565	-0.491048591	4.765320457	0.029038653	0.381666522	IFI16
ENSG00000256043	-0.384216249	4.761705406	0.029099702	0.381694042	CTSO
ENSG00000144136	-0.384983244	4.759992998	0.029128667	0.381694042	SLC20A1
ENSG00000091436	0.323328491	4.75871314	0.029150335	0.381694042	MLTK
ENSG00000196588	0.32624323	4.755594886	0.029203197	0.381907638	MKL1
ENSG00000214114	0.598790068	4.74864944	0.029321299	0.382525978	MYCBP
ENSG00000147257	-0.816872785	4.748508697	0.029323697	0.382525978	GPC3
ENSG00000181097	0.376101457	4.741684625	0.029440229	0.383567277	RP11-429J17.2
ENSG00000084623	-0.260067342	4.737862489	0.029505709	0.383941664	EIF3I
ENSG00000169442	-1.216639386	4.733353188	0.029583157	0.384451998	CD52
ENSG00000184014	-0.35008516	4.731298608	0.029618515	0.384451998	DENND5A
ENSG00000186111	0.365806143	4.727764362	0.029679439	0.384599238	PIP5K1C
ENSG00000130558	-0.55425286	4.72614375	0.02970742	0.384599238	OLFM1
ENSG00000119865	-0.356588383	4.724242525	0.02974028	0.384599238	CNRIP1
ENSG00000005884	0.384910001	4.71240816	0.029945675	0.38565984	ITGA3
ENSG00000198523	0.36764889	4.710561774	0.029977854	0.38565984	PLN
ENSG00000108654	-0.248489353	4.710516815	0.029978638	0.38565984	DDX5
ENSG00000178605	0.367919316	4.710471893	0.029979421	0.38565984	GTPBP6
ENSG00000225028	1.068730475	4.707589205	0.030029735	0.38565984	RP11-330M19.1
ENSG00000048707	0.291789081	4.706787328	0.030043747	0.38565984	VPS13D
ENSG00000111716	0.211939998	4.704239605	0.030088309	0.385757967	LDHB

ENSG00000119699	0.422495528	4.698255356	0.030193252	0.386629026	TGFB3
ENSG00000144747	-0.432002333	4.69501975	0.030250151	0.386883514	TMF1
ENSG00000066629	-0.427283429	4.689452948	0.030348308	0.387405945	EML1
ENSG00000159069	0.311728451	4.683970598	0.0304453	0.387405945	FBXW5
ENSG00000151967	-0.732094941	4.683330063	0.030456653	0.387405945	SCHIP1
ENSG00000116670	-0.565724699	4.677929992	0.030552543	0.387405945	MAD2L2
ENSG00000140105	-0.560991956	4.677381459	0.030562301	0.387405945	WARS
ENSG00000168802	0.262519781	4.676314623	0.030581288	0.387405945	CHTF8
ENSG00000179632	0.329597384	4.676249689	0.030582444	0.387405945	MAF1
ENSG00000159720	-0.348663787	4.675959759	0.030587607	0.387405945	ATP6V0D1
ENSG00000233117	0.384821793	4.671042269	0.030675306	0.388046334	LINC00702
ENSG00000021762	0.269390671	4.668106091	0.030727795	0.388240302	OSBPL5
ENSG00000140443	0.24970213	4.659466702	0.030882782	0.38927562	IGF1R
ENSG00000104976	0.36916738	4.658209012	0.030905413	0.38927562	SNAPC2
ENSG00000178607	-0.842690878	4.657315471	0.030921501	0.38927562	ERN1
ENSG00000134333	-0.256386364	4.652374834	0.031010617	0.389717108	LDHA
ENSG00000100504	-0.503498336	4.65123777	0.031031164	0.389717108	PYGL
ENSG00000168079	-0.465612557	4.646165924	0.031122988	0.390014484	SCARA5
ENSG00000077809	1.473649094	4.645584286	0.031133537	0.390014484	GTF2I
ENSG00000119977	-0.545777181	4.643750462	0.031166819	0.390014484	TCTN3
ENSG00000008853	0.514654326	4.633504548	0.031353458	0.391412053	RHOBTB2
ENSG00000213066	0.546429201	4.631345859	0.031392929	0.391412053	FGFR1OP
ENSG00000163344	0.320800234	4.629520326	0.031426349	0.391412053	PMVK
ENSG00000134287	0.232127565	4.629411674	0.031428339	0.391412053	ARF3
ENSG00000101335	0.810049052	4.626737352	0.031477367	0.391503808	MYL9
ENSG00000035403	0.358385509	4.62492481	0.031510642	0.391503808	VCL
ENSG00000156535	-0.702190037	4.616829751	0.031659701	0.392624452	CD109
ENSG00000128228	0.322161384	4.612602767	0.031737827	0.392624452	SDF2L1
ENSG00000099622	0.190005802	4.612083794	0.031747433	0.392624452	CIRBP
ENSG00000187288	-1.700808515	4.61188356	0.03175114	0.392624452	CIDEC
ENSG00000115042	0.788886453	4.607904657	0.031824897	0.393071332	FAHD2A
ENSG00000267659	-1.108106787	4.600162665	0.031968923	0.394045876	RP11-118B18.1
ENSG00000149346	0.787244729	4.599610372	0.031979223	0.394045876	SLX4IP
ENSG00000112658	0.288048129	4.59230963	0.03211571	0.395234022	SRF
ENSG00000168092	-0.190628551	4.590411272	0.032151299	0.395234022	PAFAH1B2
ENSG00000106268	-0.589748746	4.585276738	0.032247763	0.395807105	NUDT1
ENSG00000112473	0.263667274	4.58390016	0.032273677	0.395807105	SLC39A7
ENSG00000139974	-0.702805373	4.572783435	0.032483745	0.397916356	SLC38A6
ENSG00000101246	0.29318517	4.569732732	0.032541642	0.398158802	ARFRP1
ENSG00000019582	-0.374494999	4.562843969	0.032672775	0.398422281	CD74
ENSG00000255092	1.046507497	4.562079583	0.03268736	0.398422281	RP11-58K22.4
ENSG00000225921	0.648978579	4.560889756	0.032710076	0.398422281	NOL7
ENSG00000161940	-0.935137829	4.56059546	0.032715697	0.398422281	BCL6B
ENSG00000160753	0.28808229	4.547265887	0.032971356	0.400350997	RUSC1
ENSG00000128266	-0.664962112	4.545958474	0.032996544	0.400350997	GNAZ
ENSG00000103056	-0.669511888	4.542316995	0.033066805	0.400350997	SMPD3
ENSG00000154736	-0.723797537	4.542125547	0.033070503	0.400350997	ADAMTS5
ENSG00000187325	0.408457214	4.541394962	0.03308462	0.400350997	TAF9B

ENSG00000131779	0.420206582	4.538418411	0.0331422	0.400350997	PEX11B
ENSG00000224459	1.061850928	4.538414635	0.033142273	0.400350997	RP11-169K16.4
ENSG00000140350	-0.282349191	4.534733562	0.033213627	0.400749638	ANP32A
ENSG00000075618	-0.37999143	4.532662171	0.033253849	0.400772167	FSCN1
ENSG00000182752	-0.685961684	4.530256219	0.033300632	0.400873617	PAPPA
ENSG00000109062	-0.583570913	4.527393901	0.033356378	0.401082611	SLC9A3R1
ENSG00000173598	-0.536119264	4.524799624	0.033406987	0.401229439	NUDT4
ENSG00000136895	0.352327013	4.519228968	0.033515933	0.402075751	GARNL3
ENSG00000149532	0.264326613	4.5081429	0.033733848	0.404225894	CPSF7
ENSG00000106608	0.424121055	4.494359756	0.034006846	0.407030391	URGCP
ENSG00000203280	0.642261435	4.490961714	0.034074504	0.407373556	CTA-221G9.11
ENSG00000091409	-0.759207827	4.484933537	0.034194876	0.408345439	ITGA6
ENSG00000220804	0.733893625	4.482847323	0.034236638	0.408377427	AC093642.5
ENSG00000168056	0.24032097	4.473248646	0.034429471	0.410209283	LTBP3
ENSG00000137509	-0.349545811	4.46668994	0.034561885	0.411317925	PRCP
ENSG00000115461	-0.326604262	4.464251581	0.034611249	0.411436793	IGFBP5
ENSG00000215039	0.410800417	4.457006451	0.03475836	0.412581078	CD27-AS1
ENSG00000102753	0.613049395	4.455625214	0.03478648	0.412581078	KPNA3
ENSG00000106636	0.248299224	4.450329645	0.03489451	0.412985895	YKT6
ENSG00000177200	-0.244085248	4.45007765	0.03489966	0.412985895	CHD9
ENSG00000118194	-2.067637111	4.441942691	0.035066324	0.41435365	TNNT2
ENSG00000183955	-0.725179557	4.438714138	0.035132699	0.41435365	SETD8
ENSG00000070961	-0.385035925	4.43864084	0.035134207	0.41435365	ATP2B1
ENSG00000225972	-0.770934295	4.434615893	0.035217143	0.414863506	MTND1P23
ENSG00000151532	-0.526478722	4.432092304	0.035269247	0.415009421	VTI1A
ENSG00000229344	-0.699714038	4.426099004	0.035393313	0.415658317	RP5-857K21.7
ENSG00000101346	-0.522652047	4.425586072	0.035403953	0.415658317	POFUT1
ENSG00000166265	-1.118782331	4.419741389	0.03552542	0.416062736	CYYR1
ENSG00000101040	-0.369685622	4.418108348	0.035559437	0.416062736	ZMYND8
ENSG00000170801	-0.636602795	4.416980709	0.035582946	0.416062736	HTRA3
ENSG00000251417	0.941000558	4.416274684	0.035597673	0.416062736	RP11-1348G14.4
ENSG00000116774	-0.37951052	4.407258596	0.035786307	0.417800136	OLFML3
ENSG00000213465	0.258600393	4.401782739	0.035901383	0.418231349	ARL2
ENSG00000162654	-0.823322625	4.401031987	0.03591719	0.418231349	GBP4
ENSG00000213203	-0.64837582	4.398535028	0.035969816	0.418231349	GIMAP1
ENSG00000117713	-0.251308679	4.397893713	0.035983346	0.418231349	ARID1A
ENSG00000163430	-0.25010138	4.392024466	0.036107415	0.419207084	FSTL1
ENSG00000082146	-0.902509922	4.385756164	0.036240413	0.420172178	STRADB
ENSG00000064961	-0.357078358	4.383767266	0.03628272	0.420172178	HMG20B
ENSG00000214530	0.809532798	4.380451115	0.036353375	0.420172178	STARD10
ENSG00000104805	0.229070562	4.376814904	0.036431014	0.420172178	NUCB1
ENSG00000126709	-0.386913976	4.376689535	0.036433694	0.420172178	IFI6
ENSG00000181555	0.469249216	4.374189782	0.036487173	0.420172178	SETD2
ENSG00000257178	0.657964085	4.373390431	0.036504291	0.420172178	MIR10A
ENSG00000104142	0.349445471	4.370883849	0.036558025	0.420172178	VPS18
ENSG00000108773	-0.396382476	4.368113028	0.03661752	0.420172178	KAT2A
ENSG00000102524	-0.500715324	4.367428275	0.036632238	0.420172178	TNFSF13B
ENSG00000254429	-0.640345055	4.367398913	0.03663287	0.420172178	CTD-2562J17.7

ENSG00000025434	-0.583408848	4.360794896	0.036775142	0.421341508	NR1H3
ENSG00000115380	-0.334545826	4.355918622	0.036880564	0.422026943	EFEMP1
ENSG00000104093	-0.55173777	4.352671164	0.036950947	0.422026943	DMXL2
ENSG00000175595	0.811185779	4.352432074	0.036956135	0.422026943	ERCC4
ENSG00000164465	-0.407360029	4.344999184	0.037117785	0.422748415	DCBLD1
ENSG00000131871	-0.328942258	4.344151099	0.037136276	0.422748415	VIMP
ENSG00000176393	-0.455886171	4.342323387	0.037176159	0.422748415	RNPEP
ENSG00000267107	-0.867561231	4.342095011	0.037181146	0.422748415	AC011526.1
ENSG00000196230	0.234378642	4.337782578	0.03727544	0.423359862	TUBB
ENSG00000148175	-0.238873775	4.332261957	0.037396518	0.424273849	STOM
ENSG00000068831	0.310267534	4.328446596	0.037480437	0.424721644	RASGRP2
ENSG00000168310	-0.584792887	4.326774265	0.037517282	0.424721644	IRF2
ENSG00000167525	-0.777409943	4.322103334	0.037620394	0.424807653	PROCA1
ENSG00000048405	-0.397091451	4.321215036	0.037640037	0.424807653	ZNF800
ENSG00000148660	0.357314578	4.320068585	0.037665404	0.424807653	CAMK2G
ENSG00000181039	0.826274342	4.316175332	0.037751683	0.424807653	ANKRD34A
ENSG00000176595	-0.882191491	4.315128551	0.037774917	0.424807653	KBTBD11
ENSG00000198301	0.30880468	4.314404967	0.037790985	0.424807653	SDAD1
ENSG00000232079	-1.398615556	4.311851232	0.037847754	0.424807653	AL035610.1
ENSG00000145675	0.258730188	4.308358232	0.037925546	0.424807653	PIK3R1
ENSG00000188846	-0.251169863	4.30707553	0.037954155	0.424807653	RPL14
ENSG00000140374	-0.461886732	4.306067482	0.037976654	0.424807653	ETFA
ENSG00000127125	0.229019998	4.305805619	0.037982501	0.424807653	PPCS
ENSG00000163017	0.456406617	4.301675139	0.038074852	0.424807653	ACTG2
ENSG00000177374	-0.56809845	4.300019629	0.038111933	0.424807653	HIC1
ENSG00000160818	-0.266913912	4.299662286	0.038119942	0.424807653	GPATCH4
ENSG00000065135	0.266067606	4.297255656	0.038173926	0.424807653	GNAI3
ENSG00000198722	0.48556981	4.296754783	0.038185171	0.424807653	UNC13B
ENSG00000164904	0.255060651	4.29533878	0.038216981	0.424807653	ALDH7A1
ENSG00000178980	0.263417377	4.291515641	0.038303006	0.424807653	SEPW1
ENSG00000187091	0.535010503	4.290241142	0.038331729	0.424807653	PLCD1
ENSG00000253475	0.413667814	4.289963609	0.038337986	0.424807653	RP11-110G21.2
ENSG00000259426	0.957167971	4.285461089	0.038439655	0.424891843	RP11-253M7.1
ENSG00000112697	0.337395646	4.284963241	0.038450914	0.424891843	TMEM30A
ENSG00000259398	-0.948725662	4.284226838	0.038467574	0.424891843	RP11-430B1.1
ENSG00000108774	0.253642646	4.281609752	0.038526844	0.424942994	RAB5C
ENSG00000111816	0.428240771	4.280432288	0.038553542	0.424942994	FRK
ENSG00000125868	0.296035334	4.272279247	0.038738935	0.426536496	DSTN
ENSG00000149823	0.747907215	4.268458481	0.038826138	0.427046646	VPS51
ENSG00000139644	-0.183130983	4.264328453	0.03892063	0.427569154	TMBIM6
ENSG00000165572	0.347963733	4.262807813	0.038955482	0.427569154	KBTBD6
ENSG00000180354	0.247203442	4.260948518	0.038998141	0.427588216	MTURN
ENSG00000213949	0.288432201	4.256333372	0.039104239	0.427672736	ITGA1
ENSG00000176978	-0.293078244	4.255938999	0.039113319	0.427672736	DPP7
ENSG00000106524	0.362575874	4.252380168	0.03919536	0.427672736	ANKMY2
ENSG00000162174	-1.106166556	4.25186686	0.039207208	0.427672736	ASRGL1
ENSG00000093072	-0.639692867	4.251724414	0.039210497	0.427672736	CECR1
ENSG00000187134	-0.542325529	4.244913317	0.039368079	0.428534438	AKR1C1

ENSG00000166165	0.377191215	4.244200446	0.039384611	0.428534438	CKB
ENSG00000173267	0.449532628	4.242996943	0.039412537	0.428534438	SNCG
ENSG00000170852	-0.533690804	4.240622893	0.039467684	0.428687975	KBTBD2
ENSG00000170271	0.351345142	4.23804192	0.03952773	0.428700201	FAXDC2
ENSG00000130758	0.710736374	4.237048597	0.039550866	0.428700201	MAP3K10
ENSG00000133639	-0.306454543	4.232676429	0.039652865	0.428722557	BTG1
ENSG00000107290	-0.259242053	4.232383739	0.039659703	0.428722557	SETX
ENSG00000161813	-0.455849666	4.229002641	0.039738786	0.428722557	LARP4
ENSG00000136279	0.228909331	4.225526685	0.039820259	0.428722557	DBNL
ENSG00000165782	0.267995958	4.224099848	0.039853753	0.428722557	TMEM55B
ENSG00000157379	0.276843075	4.223498911	0.039867869	0.428722557	DHRS1
ENSG00000186642	-0.665347856	4.22323432	0.039874086	0.428722557	PDE2A
ENSG00000141753	-0.334962524	4.221741201	0.039909187	0.428722557	IGFBP4
ENSG00000134955	1.146375524	4.21961087	0.039959324	0.428722557	SLC37A2
ENSG00000175898	-0.547203556	4.219445092	0.039963228	0.428722557	CTD-2369P2.2
ENSG00000175183	0.443644106	4.21578289	0.040049581	0.429078925	CSRP2
ENSG00000092020	0.377181292	4.21339812	0.040105918	0.429078925	PPP2R3C
ENSG00000148180	-0.249817084	4.210943106	0.040164001	0.429078925	GSN
ENSG00000144118	-0.325103569	4.207658947	0.040241839	0.429078925	RALB
ENSG00000136451	0.243413069	4.206499172	0.040269364	0.429078925	VEZF1
ENSG00000169902	-0.610619036	4.206221376	0.04027596	0.429078925	TPST1
ENSG00000204264	-0.509799154	4.204002175	0.040328694	0.429078925	PSMB8
ENSG00000179136	1.033408608	4.203248856	0.040346611	0.429078925	LINC00670
ENSG00000034152	-0.389586142	4.201483624	0.040388629	0.429078925	MAP2K3
ENSG00000175395	0.451027002	4.200241626	0.04041822	0.429078925	ZNF25
ENSG00000263466	0.614460925	4.198986269	0.040448152	0.429078925	RP1-56K13.2
ENSG00000140836	0.272002181	4.195475398	0.040531987	0.429532186	ZFHX3
ENSG00000101846	0.541729039	4.187668793	0.040719054	0.431068947	STS
ENSG00000055483	-0.315968798	4.185985441	0.04075951	0.431068947	USP36
ENSG00000189241	0.202897068	4.180131223	0.040900534	0.432123031	TSPYL1
ENSG00000174151	0.490592423	4.178122292	0.040949045	0.432198562	CYB561D1
ENSG00000114115	0.315850892	4.173772291	0.041054297	0.432872195	RBP1
ENSG00000100129	0.187128673	4.170308698	0.041138304	0.4333207	EIF3L
ENSG00000157873	-0.440481139	4.166539985	0.041229916	0.433848334	TNFRSF14
ENSG00000253284	-0.65506643	4.160780378	0.041370339	0.434627732	RP11-282K24.3
ENSG00000183291	-0.444371346	4.160091212	0.041387175	0.434627732	Sep-15
ENSG00000064205	0.288413507	4.152562972	0.041571555	0.435159195	WISP2
ENSG00000104047	0.431432414	4.152513682	0.041572765	0.435159195	DTWD1
ENSG00000135899	-0.399071666	4.151662203	0.041593675	0.435159195	SP110
ENSG00000167772	-0.615302603	4.150181957	0.04163005	0.435159195	ANGPTL4
ENSG00000179583	-0.676715226	4.149532786	0.041646013	0.435159195	CIITA
ENSG00000083312	0.224333711	4.144186285	0.04177773	0.436099404	TNPO1
ENSG00000176142	0.400667132	4.141529513	0.041843345	0.43615309	TMEM39A
ENSG00000087077	0.277516331	4.138470146	0.041919038	0.43615309	TRIP6
ENSG00000166821	-0.79993985	4.137540184	0.041942075	0.43615309	PEX11A
ENSG00000003436	-0.415637193	4.137105225	0.041952854	0.43615309	TFPI
ENSG00000115464	0.43451417	4.133088884	0.042052526	0.43615309	USP34
ENSG00000177303	-0.407307977	4.131482126	0.04209247	0.43615309	CASKIN2

ENSG00000262814	0.627396144	4.130657007	0.042112998	0.43615309	MRPL12
ENSG00000157613	-0.595400907	4.130414818	0.042119025	0.43615309	CREB3L1
ENSG00000152104	0.210081114	4.128827809	0.042158543	0.43615309	PTPN14
ENSG00000173473	0.224031626	4.120899996	0.042356539	0.437019294	SMARCC1
ENSG00000134107	-0.752071936	4.1206653	0.042362416	0.437019294	BHLHE40
ENSG00000101109	-0.315427717	4.118923977	0.042406042	0.437019294	STK4
ENSG00000198252	-0.417862589	4.118783375	0.042409567	0.437019294	STYX
ENSG00000077458	0.577023647	4.112237839	0.042573993	0.438062303	FAM76B
ENSG00000002330	0.352873163	4.111303155	0.042597528	0.438062303	BAD
ENSG00000173726	0.232730214	4.109754351	0.042636555	0.438062303	TOMM20
ENSG00000115361	0.442141413	4.106621032	0.042715624	0.438443573	ACADL
ENSG00000105518	0.269802954	4.10375546	0.042788072	0.438456788	TMEM205
ENSG00000182919	0.4976252	4.103251166	0.042800835	0.438456788	C11orf54
ENSG00000106511	-0.821977986	4.099495363	0.042896015	0.439001431	MEOX2
ENSG00000120833	-1.035622402	4.093841145	0.043039725	0.439487834	SOCS2
ENSG00000153234	-0.764856947	4.092890495	0.043063937	0.439487834	NR4A2
ENSG00000150054	0.471680359	4.092178828	0.043082072	0.439487834	MPP7
ENSG00000112149	-0.800795018	4.091013489	0.043111784	0.439487834	CD83
ENSG00000236751	0.859698856	4.087410459	0.043203786	0.439524119	RP1-30G7.2
ENSG00000140939	0.44738816	4.086855689	0.04321797	0.439524119	NOL3
ENSG00000129009	0.269247604	4.08560047	0.043250081	0.439524119	ISLR
ENSG00000136710	0.347452999	4.084291334	0.043283598	0.439524119	CCDC115
ENSG00000129128	0.276848524	4.08161039	0.043352322	0.43979458	SPCS3
ENSG00000224660	-0.655241835	4.07973926	0.043400356	0.439854816	SH3BP5-AS1
ENSG00000165949	-0.708738892	4.077734282	0.043451887	0.439950353	IFI27
ENSG00000196586	-0.341649433	4.075672336	0.043504949	0.440061196	MYO6
ENSG00000160392	0.461841306	4.072297706	0.04359194	0.44051468	C19orf47
ENSG00000103005	0.42681365	4.05385596	0.044070571	0.444921159	USB1
ENSG00000185010	-0.798968132	4.051871992	0.044122391	0.445014348	F8
ENSG00000156265	-0.48139329	4.046539561	0.044261988	0.445570209	MAP3K7CL
ENSG00000113810	-0.538051486	4.046509046	0.044262788	0.445570209	SMC4
ENSG00000069535	0.292492416	4.044316555	0.044320321	0.44571996	MAOB
ENSG00000164741	-0.221663659	4.042367076	0.044371544	0.445766322	DLC1
ENSG00000102359	-0.678885988	4.038570902	0.044471466	0.445766322	SRPX2
ENSG00000163754	0.288377898	4.038250883	0.0444799	0.445766322	GYG1
ENSG00000205138	0.533733164	4.037656284	0.044495576	0.445766322	SDHAF1
ENSG00000253864	0.529777208	4.033106357	0.04461572	0.446541814	AC131025.8
ENSG00000196843	-0.446827589	4.02509856	0.044828	0.44663232	ARID5A
ENSG00000170471	-0.334883641	4.024844192	0.044834761	0.44663232	RALGAPB
ENSG00000042753	0.284979646	4.023615381	0.044867435	0.44663232	AP2S1
ENSG00000114853	0.244048194	4.020946934	0.044938475	0.44663232	ZBTB47
ENSG00000168564	-0.539224931	4.019425118	0.044979043	0.44663232	CDKN2AIP
ENSG00000173818	0.285940613	4.019357035	0.044980859	0.44663232	ENDOV
ENSG00000119938	0.374926958	4.01905405	0.04498894	0.44663232	PPP1R3C
ENSG00000015153	0.358500551	4.018786452	0.044996079	0.44663232	YAF2
ENSG00000172159	-0.722638377	4.018248502	0.045010435	0.44663232	FRMD3
ENSG00000154822	-0.499465908	4.016684303	0.045052203	0.44663232	PLCL2
ENSG00000157350	-0.493279899	4.013960763	0.045125025	0.446930228	ST3GAL2

ENSG00000185112	-0.835617568	4.010612682	0.045214717	0.446993613	FAM43A
ENSG00000101384	0.27223299	4.009954477	0.045232372	0.446993613	JAG1
ENSG00000161547	-0.231467563	4.008933897	0.045259761	0.446993613	SRSF2
ENSG00000081059	-1.250486999	4.001666334	0.045455304	0.447607927	TCF7
ENSG00000167004	-0.255800961	4.001576483	0.045457727	0.447607927	PDIA3
ENSG00000115468	0.419055653	4.000983479	0.045473723	0.447607927	EFHD1
ENSG00000134030	0.369835431	4.000257537	0.045493312	0.447607927	CTIF
ENSG00000165630	0.871810244	3.996155239	0.04560418	0.448276647	PRPF18
ENSG00000247157	0.664909747	3.991212381	0.045738143	0.448862734	RP11-434C1.1
ENSG00000113811	-0.333449756	3.99024801	0.045764328	0.448862734	SELK
ENSG00000012048	-0.549960295	3.989204608	0.045792676	0.448862734	BRCA1
ENSG00000260228	1.126077627	3.981444477	0.046004096	0.45009617	RP11-483P21.2
ENSG00000103199	0.325949288	3.981059574	0.046014609	0.45009617	ZNF500
ENSG00000166685	0.521049336	3.978771649	0.046077153	0.45009617	COG1
ENSG00000198771	-0.723001482	3.978272415	0.046090813	0.45009617	RCSD1
ENSG00000198231	0.243746881	3.974660334	0.046189768	0.450641353	DDX42
ENSG00000061918	0.510156427	3.971877212	0.046266167	0.450788037	GUCY1B3
ENSG00000161904	-0.297108414	3.970970447	0.046291087	0.450788037	LEMD2
ENSG00000091009	0.310719819	3.967963006	0.046373839	0.451173415	RBM27
ENSG00000132603	-0.698758041	3.963566591	0.046495092	0.451883316	NIP7
ENSG00000180917	0.578127663	3.96218374	0.0465333	0.451883316	CMTR2
ENSG00000164733	-0.21073519	3.957232071	0.046670385	0.45212806	CTSB
ENSG00000154330	0.316995835	3.956972199	0.046677591	0.45212806	PGM5
ENSG00000196352	-0.468625394	3.956239361	0.046697919	0.45212806	CD55
ENSG00000135269	0.361304197	3.955026499	0.046731582	0.45212806	TES
ENSG00000059378	-0.603097434	3.938923222	0.047180968	0.455672208	PARP12
ENSG00000126217	-0.503585037	3.937848618	0.047211118	0.455672208	MCF2L
ENSG00000171385	0.384242682	3.93692441	0.047237065	0.455672208	KCND3
ENSG00000172458	-0.72087866	3.935668826	0.047272339	0.455672208	IL17D
ENSG00000174839	0.390407974	3.927829516	0.047493204	0.456930839	DENND6A
ENSG00000168286	0.324057698	3.924836281	0.047577823	0.456930839	THAP11
ENSG00000140853	-0.527548617	3.922662687	0.04763937	0.456930839	NLRC5
ENSG00000175213	0.386317636	3.922178247	0.047653098	0.456930839	ZNF408
ENSG00000161638	-0.468398247	3.9208338	0.047691221	0.456930839	ITGA5
ENSG00000056998	-1.165072045	3.920522375	0.047700056	0.456930839	GYG2
ENSG00000137133	0.293960623	3.920206504	0.04770902	0.456930839	HINT2
ENSG00000198466	-0.48220549	3.912338465	0.047932857	0.457811513	ZNF587
ENSG00000263883	0.399443845	3.911868665	0.047946257	0.457811513	RP11-51F16.5
ENSG00000101400	0.339156739	3.911593051	0.047954121	0.457811513	SNTA1
ENSG00000120318	-0.602201559	3.91081843	0.047976228	0.457811513	ARAP3
ENSG00000151468	0.306591827	3.90333348	0.0481904	0.459435666	CCDC3
ENSG00000213015	0.339176821	3.901133097	0.048253553	0.45961839	ZNF580
ENSG00000212464	1.209206807	3.896491408	0.04838706	0.460113288	SNORA12
ENSG00000153993	-0.470857844	3.895684532	0.048410307	0.460113288	SEMA3D
ENSG00000119927	-0.60463139	3.893892126	0.048461992	0.460113288	GPAM
ENSG00000140931	-0.406455906	3.893211025	0.048481647	0.460113288	CMTM3
ENSG00000159202	0.228607893	3.88447236	0.048734574	0.462055416	UBE2Z
ENSG00000102119	0.246761985	3.883089452	0.048774727	0.462055416	EMD

ENSG00000112773	0.257617982	3.881194934	0.048829792	0.462158061	FAM46A
ENSG00000196396	0.209232569	3.874007302	0.049039302	0.463407644	PTPN1
ENSG00000231764	-2.02157743	3.873623461	0.049050517	0.463407644	DLX6-AS1
ENSG00000135999	0.353725939	3.871301488	0.049118419	0.463629951	EPC2
ENSG00000137103	0.287072055	3.867078316	0.049242171	0.464203462	TMEM8B
ENSG00000157020	-0.254419812	3.866197306	0.049268029	0.464203462	SEC13
ENSG00000224822	0.4324922	3.863682749	0.049341911	0.46448075	THRB-IT1
ENSG00000091732	-0.546006978	3.861893045	0.049394567	0.464557907	ZC3HC1
ENSG00000229164	-0.903588404	3.856219422	0.049561887	0.465708627	TRAC
ENSG00000103942	0.961159317	3.854725001	0.049606058	0.465708627	HOMER2
ENSG00000100060	-0.780473895	3.847849892	0.049809805	0.467012115	MFNG
ENSG00000141258	0.216941263	3.847025642	0.049834291	0.467012115	SGSM2
ENSG00000115504	-0.466489749	3.845466677	0.049880639	0.467027593	EHBP1
ENSG00000182326	-0.302622855	3.841526882	0.04999797	0.467707067	C1S